DEPARTAMENTO DE ASTROFÍSICA

Universidad de La Laguna

Distribución de las condiciones físicas y abundancias químicas en regiones H II a pequeñas escalas angulares

Memoria que presenta
Adal Mesa Delgado
para optar al grado de
Doctor en Ciencias Físicas

INSTITUTO Đ ASTROFÍSICA Đ CANARIAS
mayo de 2010

Fecha de examen: 16 de Julio de 2010
Director de Tesis: Dr. César Esteban López

Algunas de las figuras incluidas en este documento ya han sido publicadas en *The Astrophysical Journal* y *Monthly Notices of the Royal Astronomical Society.*
Parte del material incluido en este documento ya ha sido publicado en *The Astrophysical Journal* y *Monthly Notices of the Royal Astronomical Society.*

A mis padres: Amaro y María.
Gracias por la paciencia y por
no intentar entender lo inexplicable.

Agradecimientos

No es que en mi interior me considere un poco perro, que a veces lo soy, pero al empezar a escribir esta sección –indudablemente la más difícil y la escrita con más cariño– lo primero que pasa por mi cabeza es el ladrido de un perro: ¡Guau! Y esto es porque me resulta imposible creer que hayan pasado cuatro años de tesis. Que se dicen rápido, pero son cuatro tremendas vueltas al Sol. Durante estos años, he conocido muchas personas que han dejado su particular huella. Es difícil acordarse de todos ellos, y agradecerles sus grandes y/o pequeñas contribuciones, que han hecho que esta tesis haya llegado a buen puerto sin yo perder la cabeza en el camino (creo).

Remontándome a los inicios de esta tesis, en primer lugar me gustaría agradecer a Santiago Brouard la deposición de fe en mi persona. Gracias por el voto de confianza. Espero que se haya visto recompensado después de todo este tiempo.

A mi director de tesis, César Esteban. Muchísimas gracias por estos fantásticos cuatro años de tesis, por la paciencia que has tenido conmigo, por la ayuda prestada cuando fue necesaria tanto dentro como fuera del ámbito laboral y, por supuesto, por tratarme como una persona más y no como un "esclavo de tesis". Ha sido un placer aprender y trabajar contigo. Espero que siga siéndolo.

Muchas gracias al que yo considero, sobre todo durante los primeros años, mi pseudo-director de tesis: Jorge. ¡Yorch! Gracias por aguantar mis problemas para conseguir entrar en este mundo, por la motivación que me ofreces, aunque en ocasiones no saquemos nada en claro y por la ayuda prestada en la infinidad de problemas que me han surgido a lo largo de estos años.

Gracias también al árbitro interno de esta tesis, Valentina Luridiana. Gracias por la eficiencia en la revisión de la misma y por tus incontables sugerencias de estilo y redacción. En este mismo punto, también me gustaría agradecer la ayuda presestada por todos los pares de ojos que han dedicado su tiempo y esfuerzo en leer y releer esta tesis en busca de "ratas". Está clarísimo que cuatro ojos ven mejor que dos y yo tuve la suerte de contar con seis pares de ellos (Jorge, Luis, Jonay, Ana, Elena y Raúl).

Gracias a mis compañeros de "mini-grupo" de investigación: Luis, Manu, Valentina, Jorge, Sergio, Ángel y Leticia. Siempre dispuestos a ayudar casi sin pedirlo. Gracias por los comentarios en los artículos, por la ayuda prestada en los múltiples pasos anteriores a la temida redacción del artículo y, lo más importante, por los momentos cafeteros a media mañana que siempre sirvieron, sirven y servirán para olvidar que teníamos trabajo que hacer.

Siempre estaré agradecido a mis compañeros de corralín y de otros corralines. En especial a los que han soportado mis constantes charlas, quejas y divagaciones durante estos años: Julio, Jesús, Tobías, Christoph e Inés. Gracias por aguantarme, por hacer que el día a día fuera algo más que trabajar (salvo cuando en realidad trabajábamos), por los buenos momentos de risas dentro y fuera del trabajo (en especial, durante las cenas de navidad del IAC... ya va a ser imposible que me toque la pata de jamón), por escuchar y ayudarme cuando les planteaba cualquier problema. Gracias a todos.

Gracias a toda la gente del IAC con la que alguna vez he tenido el placer de hablar y conocer. Desde el CAU hasta Personal, pasando por secretarias y recepcionistas. Gracias por la ayuda prestada.

A mis queridos amigos, un millón de gracias. Desde los que han estado siempre, pasando por los más recientes, hasta los que ya no están: Jonay, Jonay ("Sexy" para los amigos), Elena, Ana, Kike, Pilar, Héctor, Felipe, Marga y Fernando (*"Probablemente ya, de mi te has olvidado"*; no te hemos olvidado). Gracias también a los amigos que veo una vez cada cuatro años y aún así es como si les hubiera visto el día anterior. A todos, muchas gracias por ser como son, por haberme dejado entrar en sus vidas, por los buenos momentos que hemos vivido y seguiremos viviendo, por sacarme una sonrisa, por las incontables cervezas compartidas y los intentos de arreglar el mundo tras una barra en una noche. Gracias, sencillamente, por escuchar mis lamentos de tesis.

Mil gracias a mi familia. A mis padres por la infinita ayuda que he recibido de ellos toda mi vida, que no es poca. A mis abuelos porque nunca entendieron por qué me interesaba tanto mirar al cielo si todo eso estaba tan lejos. Gracias a ellos nunca olvidaré cuál es el auténtico sabor de unas buenas papas guisadas y lo que cuesta que lleguen a la mesa.

En definitiva, muchas gracias. A todos y cada uno de ustedes mis más sinceros e infinitos agradecimientos porque al final lo conseguí y aquí está el egendro tras cuatro años de trabajo.

"When you've got nothing,
you've got nothing to lose"
Bob Dylan.

"Vamos comear,
colocando um ponto final,
pelo menos já é um sinal,
de que tudo na vida tem fim"
Paulinho Moska.

Resumen

Las regiones H II son nubes de gas interestelar, ionizadas por estrellas masivas jóvenes de tipos espectrales OB, cuyo espectro de líneas de emisión puede observarse a grandes distancias en el Universo. El análisis del espectro de las regiones H II permite determinar las condiciones físicas del gas ionizado y las abundancias químicas de algunos de los elementos más importantes (He, C, N, O, Ne, S, Ar, Cl y Fe). Este último aspecto hace de las regiones H II objetos indispensables para el estudio de la composición química del medio interestelar, desde la cercanía solar hasta galaxias a alto desplazamiento al rojo.

En nebulosas fotoionizadas, las abundancias de elementos más pesados que el He clásicamente se han determinado a partir de las brillantes líneas excitadas colisionalmente (LECs). Sin embargo, hace ya más de 20 años que se midió la primera línea de recombinación (LR) pura de elementos pesados y, desde entonces, persiste un gran problema en la comprensión de la física que tiene lugar en el seno de las nebulosas fotoionizadas: las abundancias químicas de un mismo ión obtenidas a partir de LRs suelen ser significativamente mayores a las determinadas a partir de LECs. Este problema se conoce en la actualidad como Discrepancia de Abundancias (DA) y continúa siendo un reto en el ámbito de las nebulosas gaseosas, todavía sin una solución satisfactoria.

El objetivo principal de la presente tesis doctoral es explorar, desde distintas vertientes observacionales, cuáles son las variables, o procesos físicos, de los que depende la DA en regiones H II, si existiera alguna dependencia. Una de las vertientes más prometedoras es el estudio del comportamiento de la DA en regiones H II galácticas brillantes y cercanas a pequeñas escalas espaciales, su posible dependencia con distintos parámetros nebulares (tales como temperatura y densidad electrónica, estado de ionización local del gas o la presencia de material a alta velocidad) y su correlación con estructuras morfológicas particulares (frentes de ionización, objetos Herbig-Haro, discos protoplanetarios o glóbulos). Este es el punto de inicio de esta tesis doctoral, ya que dicha técnica, utilizada en el estudio de la DA en contadas nebulosas planetarias y en la región H II extragaláctica 30 Doradus, aún no ha sido explorada en profundidad en regiones H II galácticas. Para ello, las regiones H II seleccionadas son: la Nebulosa de Orión, M8, M17 y NGC 7635.

La aplicación de la técnica anterior se consigue a partir del muestreo de espectros de rendija larga que cubren diferentes partes de las regiones H II. Para todos los objetos hemos determinado las distribuciones espaciales de un gran número de flujos de líneas de emisión, los coeficientes de extinción, las condiciones físicas y las abundancias químicas a partir de LECs y LRs. Entre otros resultados, en general, la DA parece no depender de ninguna de las propiedades nebulares del gas y, excluyendo la Nebulosa de Orión, la DA permanece básicamente constante a lo largo de las posiciones de rendija.

Debido a su cercanía y alto brillo superficial, el análisis llevado a cabo en la Nebulosa de Orión nos ha permitido relacionar algunos aumentos locales de la DA con la presencia de objetos Herbig-Haro. Este resultado nos ha llevado a aplicar nuevas técnicas observacionales, centradas en el estudio del rol de los objetos Herbig-Haro en el problema de la DA. Más concretamente, hemos analizado uno de los objetos Herbig-Haro más prominentes de la Nebulosa de Orión: HH 202. Por un lado, hemos abordado el problema de la DA en el objeto HH 202 haciendo uso de la espectroscopia de campo integral, encontrando un aumento progresivo de la DA en las zonas donde el flujo de gas alcanza su máxima veloci-

dad, que además coinciden con la localización del nudo sur de dicho objeto (HH 202-S). Por otro lado, ya contábamos con observaciones *echelle* de muy alta resolución espectral en la posición del HH 202-S que nos permitieron resolver las componentes cinemáticas asociadas al gas de fondo y al flujo de gas a alta velocidad. Los resultados indican que la mayor contribución a la DA, en el objeto HH 202, observada en los trabajos de rendija larga y espectroscopia de campo integral, proviene de la componente a alta velocidad. Esta es la principal conclusión de la presente tesis, ya que es la primera evidencia observacional obtenida que relaciona el problema de DA en regiones H II con la presencia de flujos de gas a alta velocidad.

CÓDIGOS UNESCO: 2101.06, 2103.03

Summary

H II regions are clouds of interstellar gas ionized by young and massive OB-type stars whose emission line spectra can be observed at large distances in the Universe. The analysis of H II region spectra allows us to determine the physical conditions of ionized gas and the chemical abundances of several important elements (He, C, N, O, Ne, S, Ar, Cl and Fe). This aspect makes H II regions essential objects to study the chemical composition of the interstellar medium, from the solar vicinity to high redshift galaxies.

Traditionally, in photoionized nebulae, abundances of elements heavier than He have been determined from the bright collisionally excited lines (CELs). However, there is a major problem in the comprehension of the physical processes which take place inside photoionized nebulae. Since the first abundance determination using recombination lines (RLs) of heavy elements, it is known that, for the same ion, the chemical abundances derived from RLs are significantly higher than those determined from CELs. This problem is known today as Abundance Discrepancy (AD) and remains a challenge in the field of the physics of the gaseous nebulae, without a satisfactory solution yet.

The main goal of this PhD thesis is to explore the dependences of the AD, if those dependences exist, with the different nebular variables or physical processes in H II regions from different points of view. One promising technique is the study of the AD distribution at small spatial scales in near and bright Galactic H II regions, its possible dependence with different nebular parameters (such as electron temperature and density, local ionization state of the gas and the presence of high velocity material) and its correlation with different morphological structures (ionization fronts, Herbig-Haro objects, protoplanetary disks or globules). The initial motivation for the present thesis is that this technique has not been explored in depth to study the AD problem in gaseous nebulae, excluding a few works carried out in planetary nebulae and the extragalactic H II region 30 Doradus. With this aim, the following Galactic H II regions have been selected: the Orion Nebula, M8, M17 and NGC 7635.

The application of this technique is made possible by a sample of long-slit spectra that covers different areas of the H II regions. For all objects, we have determined the spatial distributions of a large number of emission line fluxes, extinction coefficients, physical conditions and chemical abundances from CELs and RLs. Among other results, in general, the AD does not show any apparent correlation with the nebular properties of the ionized gas and, excluding the Orion Nebula, the AD remains rather constant along slit positions.

Because of its proximity and high surface brightness, the analysis carried out in the Orion Nebula has allowed us to relate some of the AD increases with the presence of Herbig-Haro objects. This result let us to implement new observational techniques focused on the study of the role of Herbig-Haro objects in the AD problem. Specifically, we have focused our attention on one of the most prominent Herbig-Haro objects of the Orion Nebula: HH 202. On the one hand, we have addressed the AD problem in HH 202 object using integral field spectroscopy, finding a progressive increase of the AD in areas where the gas flow reaches its maximum velocity, which coincide with the position of the southern knot of the object (HH 202-S). On the other hand, echelle spectroscopy at high spectral resolution has enabled us to resolve the kinematical components associated with the background gas and the high-velocity gas flow. Our results indicate that the greatest part of the contribution

to the AD in HH 202 –observed both in long-slit and integral field spectroscopy works– comes from the high velocity component. This is the main result of the present thesis as it is the first observational evidence obtained that relates the AD problem with the presence of high-velocity gas flows in H II regions.

UNESCO CODES: 2101.06, 2103.03

Índice

1

Introducción

1.1 Nebulosas gaseosas

Las nebulosas gaseosas son objetos extensos y brillantes que pueblan el cielo. Las de mayor brillo superficial, como la Nebulosa de Orión (NGC 1976 o M42) o la Nebulosa Anular (NGC 6720), pueden incluso observarse a través de telescopios de pequeña abertura.

En un primer intento de clasificar las nebulosas gaseosas fotoionizadas, podríamos distinguir dos tipos: las regiones H II o nebulosas difusas y las nebulosas planetarias (NPs). Las principales diferencias que podemos encontrar entre estos dos tipos de objetos están relacionadas con su origen, masa, evolución y edad de las estrellas que contienen, aunque los procesos físicos que en ellas tienen lugar son muy parecidos.

Las regiones H II o nebulosas difusas son nubes de gas ionizado localizadas principalmente en los brazos de las galaxias espirales y en las galaxias irregulares. La geometría típica de una región H II es resultado de la nube molecular progenitora. Este tipo de nebulosas están asociadas a brotes recientes de formación estelar y presentan un espectro de emisión que puede observarse a grandes distancias en el Universo. Además, su relación con objetos jóvenes y su corto tiempo de vida –del orden de 10^6-10^7 años– hacen de las regiones H II unos indicadores esenciales de la tasa de formación estelar, del contenido de estrellas masivas y de la composición química actual de las zonas donde se encuentran. En ellas, el gas está siendo ionizado y calentado por la radiación ultravioleta (UV) procedente de una, varias, o un cúmulo de estrellas masivas de tipos espectrales O y B temprano. Las temperaturas efectivas, T_*, de estas estrellas ionizantes se encuentran en torno a $3\text{–}5 \times 10^4$ K. A estas temperaturas, la nebulosa está compuesta por hidrógeno totalmente ionizado, helio una vez ionizado y otros elementos en diferentes estados de ionización. Dicha masa ionizada presenta densidades electrónicas típicas entre 10 y 100 cm^{-3}, pudiendo también alcanzar valores tan altos como 10^4 cm^{-3}.

Las NPs son nebulosas aisladas que representan la etapa final de la vida de una estrella de masa baja-intermedia –masas inferiores a unas $8\mathrm{M}_\odot$– tras haber salido de la rama asintótica de gigantes (o AGB, acrónimo del inglés *asymptotic giant branch*) expulsando al medio interestelar circundante sus capas más externas. El remanente estelar que queda después de la expulsión de material se conoce como estrella central de la NP. Las estre-

llas centrales de las NPs son viejas y tienen temperaturas efectivas del orden de 5×10^4 K. Estas estrellas evolucionan rápidamente hacia la fase de enana blanca, mientras las capas expulsadas al espacio continúan expandiéndose a velocidades supersónicas. Debido a la progresiva expansión, y la consecuente disminución de la densidad, las NPs pierden progresivamente brillo hasta que dejan de ser detectadas. Este tipo de nebulosas gaseosas tienen tiempos de vida relativamente cortos, del orden de unos pocos 10^4 años. El material ionizado por las estrellas centrales tiene densidades electrónicas que van desde 100 hasta 10^4 cm^{-3}.

El análisis del espectro de emisión de las nebulosas gaseosas, en especial las regiones H II, permite determinar las condiciones físicas del gas ionizado y las abundancias de algunos de los elementos más importantes (He, C, N, O, Ne, S, Ar, Cl y Fe). Este último aspecto las hace objetos indispensables para el estudio de la composición química del medio interestelar (desde la cercanía solar hasta galaxias con alto desplazamiento al rojo), para la determinación de los gradientes radiales de abundancias en galaxias espirales e incluso para determinar el helio de origen primordial (ver revisiones de Peimbert 1975; Stasińska 2004).

1.2 Física básica de las nebulosas gaseosas

1.2.1 Equilibrio de fotoionización

Ionización y recombinación

La fuente de energía que posibilita la emisión en una nebulosa gaseosa es, en la mayoría de los casos, la radiación UV procedente de las estrellas ionizantes. Generalmente, hay una o más estrellas calientes en los interiores o cercanías de las nebulosas, con temperaturas $T_* \gtrsim 3\times10^4$ K. Las partículas de gas son ionizadas por los fotones UV con energías por encima del umbral de ionización del hidrógeno, y el exceso de energía de cada fotón absorbido con energía superior a dicho umbral se transforma en energía cinética del fotoelectrón liberado. Las colisiones entre electrones y entre electrones e iones establecen un estado de equilibrio termodinámico (ET), y la energía se distribuye según la distribución *maxwelliana* de velocidades, la cual está definida por la temperatura electrónica del gas ionizado, T_e, que típicamente se sitúa en el rango 5000 K $< T_e <$ 20000 K (Osterbrock y Ferland 2006). Este proceso es conocido como *termalización* del gas de electrones, donde los fotoelectrones pasan a ser electrones térmicos. Por otro lado, las partículas de gas, una vez ionizadas, tienden a recombinarse con los electrones térmicos libres, y se establece un estado de equilibrio, en el cual la tasa de ionizaciones es igual a la tasa de recombinaciones para cada ion. De este modo, el grado de ionización en cada punto de la nebulosa dependerá de dicho equilibrio.

Si hay suficiente material molecular en torno a las estrellas ionizantes, todos los fotones ionizantes pueden ser absorbidos, produciendo una nebulosa que presentará un contorno bien definido conocido como frente de ionización. A este tipo de nebulosas se las denomina limitadas en radiación. En este caso, el elemento más abundante, el hidrógeno, absorbe la mayoría de los fotones del continuo Lyman, que provienen de la fuente ionizante, y define el tamaño de la región ionizada. El caso opuesto, donde los fotones procedentes del continuo Lyman ionizan todo el medio circundante y parte de ellos escapan de la nebulosa sin ser absorbidos, se conoce como nebulosa limitada en densidad.

En una nebulosa idealmente compuesta sólo por hidrógeno, el equilibrio entre el número de fotoionizaciones y recombinaciones por unidad de tiempo y volumen viene dado por:

$$n(H^0)\int_{\nu_0}^{\infty}\frac{4\pi J_\nu}{h\nu}a_\nu(H^0)d\nu = n_p n_e \alpha(H^0,T_e), \tag{1.1}$$

donde J_ν es la intensidad media del campo de radiación (en unidades de energía por unidad de área, tiempo, ángulo sólido e intervalo de frecuencias) en cada punto, $a_\nu(H^0)$ es la sección eficaz de fotoionización del H para fotones con energía $h\nu$ –donde h de aquí en adelante es la constante de Planck– superior a su umbral de ionización ($h\nu_0 = 13.6$ eV), $n(H^0)$, n_p y n_e son las densidades de átomos neutros, protones y electrones por unidad de volumen respectivamente y $\alpha(H^0,T_e)$ es el coeficiente de recombinación del H, el cual es aproximadamente proporcional a la inversa de la T_e. La integración representa el número de fotoionizaciones por átomo de H y tiempo, y se extiende a todas las frecuencias por encima del umbral que ioniza el hidrógeno, es decir, para $\nu > \nu_0$ o, en términos de longitud de onda, $\lambda < \lambda_0$ donde $\lambda_0 = 911$ Å.

Un concepto importante que surge en el estudio de esta primera aproximación es el denominado radio de Strömgren, R_s. Este da el tamaño de una nebulosa esférica limitada en radiación asumiendo que una fracción ϵ (*factor de llenado*) del volumen total de la nebulosa posee una n_e uniforme y una densidad de protones $n_p \approx n_e$. En estas condiciones, R_s se puede estimar como:

$$R_s = \Big(\frac{3Q(H^0)}{4\pi\epsilon n_e^2 \alpha_B(H^0,T_e)}\Big)^{1/3}, \tag{1.2}$$

donde $Q(H^0)$ es el número total de fotones emitidos por la estrella ionizante con energía superior a 13.6 eV por unidad de tiempo y $\alpha_B(H^0,T_e)$ es el coeficiente de recombinación del H para todos los estados excitados. El significado físico de esta relación es que el número total de fotones ionizantes emitidos por unidad de tiempo por la estrella central se equilibra con el número total de recombinaciones a niveles excitados, dentro del volumen ionizado $\frac{4}{3}\pi R_s^3$, en la misma unidad de tiempo.

Estructura de ionización

Una nebulosa real está compuesta por H, He y diferentes elementos pesados (C, N, O...). De este modo, la tasa de fotoionizaciones por unidad de volumen dependerá de la presencia de los otros elementos, que competirán con el hidrógeno en la absorción de fotones ionizantes. Por ejemplo, el helio, aunque es diez veces menos abundante que el hidrógeno, es la fuente dominante de absorción de fotones con energías superiores a 24.4 eV. Con ello, la nebulosa adoptará una estructura de capas acopladas, dependiendo de los potenciales de ionización de cada una de las especies iónicas.

A una distancia r de la fuente ionizante, las densidades $n(X^{+i+1})$ y $n(X^{+i})$ de los iones X^{+i+1} y X^{+i}, respectivamente, están relacionadas por la expresión:

$$\frac{n(X^{+i})Q(H^0)}{r^2 K} = n(X^{+i+1})n_e\alpha(X^{+i},T_e), \tag{1.3}$$

donde K es un factor que tiene en cuenta la distribución en frecuencias del campo de radiación ionizante y la sección eficaz de absorción. De acuerdo con la ecuación, los iones X^{+i} sólo pueden existir si el campo de radiación contiene fotones capaces de producir estos iones, y el cociente $n(X^{+i+1})/n(X^{+i})$ será mayor para nebulosas donde las fuentes ionizantes posean temperaturas efectivas mayores, es decir, mayor $Q(H^0)$.

A partir de la integración de la ecuación anterior a todo el volumen de la nebulosa y haciendo uso de la relación (1.2), se puede ver que para una nebulosa esférica de densidad constante, con un cierto factor de llenado, y bañada por un campo de radiación proveniente de una fuente ionizante con una temperatura efectiva dada, el promedio del cociente iónico es proporcional al factor $(Q(H^0)/n_e\epsilon^2)^{1/3}$. Esto quiere decir que una nebulosa de densidad 10^4 cm^{-3}, ionizada por una estrella de $T_* = 5 \times 10^4$ K, tendrá la misma estructura de ionización que una nebulosa con densidad de 10^2 cm^{-3} ionizada por cien de esas estrellas.

El parámetro de ionización clásico se define como:

$$U = \frac{Q(H^0)}{4\pi R_s^2 n_e c}, \tag{1.4}$$

donde c es la velocidad de la luz. Este parámetro representa físicamente el cociente adimensional de la densidad de fotones ionizantes sobre la densidad de electrones, y describe la estructura de ionización en un punto dado de la nebulosa. Es importante tener en cuenta que la ecuación anterior muestra que, a una distancia dada de la fuente ionizante, la ionización cae cuando la densidad aumenta localmente. Por otro lado, en dos nebulosas con densidad uniforme, ionizadas por la misma estrella, la ionización promedio más alta ocurrirá para aquella con mayor densidad.

1.2.2 Equilibrio térmico

La temperatura en cada punto de la nebulosa viene determinada por el equilibrio entre el calentamiento, debido a la fotoionización, y el enfriamiento, producido por la recombinación y la radiación emitida por la nebulosa. Esto se expresa como:

$$G - L_R = L_{ff} + L_C, \tag{1.5}$$

donde G es la tasa de calentamiento y L_R, L_{ff} y L_C son las tasas de enfriamiento por recombinación, transiciones libre–libre y radiación emitida por excitaciones colisionales, respectivamente.

El calentamiento del gas nebular es debido básicamente a la fotoionización. Como hemos visto en §1.2.1, este mecanismo genera fotoelectrones libres, con energías cinéticas $\frac{1}{2}mu^2 = h(\nu - \nu_0)$, que a continuación chocan con el resto de electrones libres e iones presentes en el gas y se termalizan. En equilibrio de ionización, las fotoionizaciones se ven compensadas por un número igual de recombinaciones, y la diferencia entre la energía media ganada por la deposición energética por parte de los fotoelectrones, y la energía media perdida por medio de la recombinación de electrones térmicos, representa la ganancia neta de energía del gas nebular. Esto viene representado por el término izquierdo de la ecuación (1.5). Por otro lado, bajo condiciones de equilibrio térmico, dicha ganancia neta de energía se ve compensada, principalmente, por el enfriamiento radiativo proveniente de

las excitaciones colisionales de los niveles de energía más bajos de iones comunes, tales como O^+, O^{2+} o N^+. Estas excitaciones finalizan con la emisión de fotones que pueden escapar de la nebulosa. A pesar de su baja abundancia respecto al H o al He, estos iones de elementos pesados contribuyen significativamente al enfriamiento de las nebulosas, debido a que tienen niveles de energía con potenciales de excitación del orden de kT_e –siendo k la constante de Boltzmann–; al contrario que el H y He, cuyos niveles energéticos más bajos tienen mayores potenciales de excitación. Un proceso secundario, que se suma a la excitación colisional, es la pérdida de energía por radiación libre–libre debida, principalmente, a la interacción de los electrones libres con los núcleos de H^+ y He^+. Esta contribuye en menor medida al enfriamiento global de la nebulosa con respecto a la excitación colisional. Por lo tanto, una mayor abundancia de metales hará que el enfriamiento sea más eficiente.

1.2.3 Líneas de emisión y los mecanismos que las producen

La radiación emitida por cada elemento de volumen de una nebulosa gaseosa depende de las abundancias de los elementos que la componen, determinadas por la historia previa evolutiva del gas, y de las condiciones locales de ionización, densidad y temperatura, determinadas a su vez por el campo de radiación. Los rasgos espectrales más evidentes son las líneas de emisión. La intensidad de una línea de emisión observada se puede escribir como:

$$I(\lambda) = \int j_\lambda ds = \int N_i n_e \epsilon_\lambda(T_e) ds, \tag{1.6}$$

donde la integral se extiende a lo largo de la línea de visión, j_λ es la intensidad de la línea por unidad de superficie o tasa de emisión, $\epsilon_\lambda(T_e)$ es el coeficiente de emisión de la línea o emisividad, y N_i y n_e son la densidad del ion responsable de la emisión y la densidad electrónica, respectivamente.

Las líneas de emisión son el producto de fotones emitidos como consecuencia de transiciones radiativas de electrones que decaen hacia los niveles de energía más bajos de un átomo o ion. Las características de las líneas están definidas, principalmente, por los mecanismos que las producen, la composición química del gas, la forma del continuo ionizante y la distribución geométrica del gas en la nebulosa.

Podemos encontrar tres mecanismos principales que producen la emisión de líneas de átomos o iones: la recombinación, la excitación colisional y la fluorescencia. Cada línea de emisión se puede producir a través de los distintos procesos, pero generalmente existe un mecanismo predominante. Por ejemplo, la contribución de recombinación en los flujos medidos de las líneas [O II] 7320 y 7330 Å es muy importante a temperaturas por debajo de los 5000 K, y comienza a dominar sobre la excitación colisional a las temperaturas más bajas observadas en regiones H II (Stasińska 2005).

Recombinación

La recombinación es un proceso de captura de electrones. Si estos se recombinan hacia niveles excitados de iones, a continuación decaerán progresivamente a niveles cada vez menos energéticos mediante transiciones radiativas, finalizando ocasionalmente en el nivel fundamental. Las líneas de emisión que resultan de este proceso son conocidas como líneas

de recombinación (LRs). A este tipo de líneas se las denomina también permitidas, porque son transiciones que cumplen las reglas de selección de una interacción de tipo dipolar–eléctrica.

La tasa de emisión de una LR que se genera entre los niveles nL y $n'L'$[1] se puede escribir como (Osterbrock y Ferland 2006):

$$j_\lambda = j_{nn'} = \frac{h\nu_{nn'}}{4\pi} N_i n_e \alpha_{nn'}^{eff}, \tag{1.7}$$

donde $h\nu_{nn'}$ es la diferencia de energía que existe entre los niveles involucrados en la transición y $\alpha_{nn'}^{eff}$ es el coeficiente de recombinación efectivo, el cual expresa la probabilidad de que un electrón del nivel nL decaiga en cascada hasta el nivel $n'L'$, teniendo en cuenta todos los caminos posibles.

Las LRs más conocidas y comúnmente detectadas son las líneas de H I –que forman parte de las series del hidrógeno de Lyman, Balmer, Paschen, etc.– que son emitidas a partir de la recombinación de electrones con iones de H^+; las líneas de He I (*e.g.* 5876 Å) emitidas en la recombinación de He^+; y las líneas de He II (*e.g.* 4686 Å) de la recombinación de He^{2+}. También es posible detectar LRs emitidas por iones de elementos pesados (*e.g.* C II 4267 Å y O II 4650 Å), aunque estas líneas son varios órdenes de magnitud más débiles que las LRs del hidrógeno, debido a que los iones que las producen son mucho menos abundantes.

Excitación colisional

Las colisiones entre los electrones libres e iones pueden excitar los electrones ligados que ocupan los niveles de energía más bajos de los iones. El decaimiento radiativo de los electrones ligados hacia los niveles inferiores presenta probabilidades de transición muy bajas –entre 10^{-4} y 1 s^{-1}– aunque, a las densidades electrónicas típicas del medio interestelar –$\leq 10^4$ cm^{-3}–, la desexcitación de los electrones ligados por medio de las colisiones de electrones libres es incluso menos probable que la transición radiativa. Por tanto, casi todas las excitaciones colisionales producen un fotón y las líneas de emisión resultantes son conocidas como líneas excitadas colisionalmente (LECs).

Para una LEC dada, la tasa de emisión resultado de la transición radiativa entre el nivel superior i y el inferior k se puede calcular como:

$$j_\lambda = j_{ik} = \frac{h\nu_{ik}}{4\pi} n_i A_{ik} N(X^{+l}), \tag{1.8}$$

donde n_i es la población relativa en el nivel superior i del elemento X ionizado $+l$ veces y $N(X^{+l})$ es la densidad del ion responsable de la emisión. Como vemos, para determinar la emisividad de una LEC hay que tener información sobre la población del nivel de partida. Para ello, es necesario resolver las ecuaciones de equilibrio estadístico. Para cada nivel excitado i de un determinado ion, dichas ecuaciones se pueden escribir como:

$$\sum_{j\neq i} n_j n_e q_{ji} + \sum_{j>i} n_j A_{ij} = \sum_{j\neq i} n_i n_e q_{ij} + \sum_{j<i} n_i A_{ij}, \tag{1.9}$$

[1] n y n' son los números cuánticos principales de los niveles; L y L' denotan el momento angular total.

donde n_i y n_j son las poblaciones relativas de los niveles i y j, A_{ij} es la probabilidad de transición radiativa entre dichos niveles (s^{-1}), y q_{ij} y q_{ji} son las tasas de desexcitación y excitación colisional (cm^{-3} s^{-1}). Las A_{ij} son independientes de la T_e del gas e inversamente proporcionales a los tiempos de vida de los niveles superiores, mientras que las tasas colisionales dependen de la temperatura. La tasa de desexcitación colisional, para una transición de un nivel superior i a otro inferior j, viene dada por:

$$q_{ij} = \frac{8.629 \times 10^{-6}}{T_e^{1/2}} \frac{\Omega(j,i)}{\omega_i}, \tag{1.10}$$

donde ω_i es el peso estadístico del nivel i, y $\Omega(j,i)$ es la fuerza de colisión media entre los niveles j e i, variable que contiene la dependencia con la T_e. Asimismo, las tasas de excitación y desexcitación se relacionan a través de la expresión:

$$q_{ji} = q_{ij} \frac{\omega_i}{\omega_j} e^{-\chi_{ij}/kT_e}, \tag{1.11}$$

donde χ_{ij} es la diferencia de las energías de excitación de los niveles i y j.

La resolución de las ecuaciones de equilibrio estadístico no es trivial, ya que dependen de varios parámetros atómicos –A_{ij}, $\Omega(j,i)$, χ_{ij} y ω_i– y estos no siempre están disponibles, o no están calculados con la precisión suficiente para todos los niveles y/o todos los iones o átomos. Con el objetivo de minimizar la complejidad del problema se recurre a diversas aproximaciones. En el análisis nebular, muchos de los iones observados –*e.g.* O^+, O^{2+}, N^+, S^+, S^{2+}– presentan una estructura sencilla de cinco niveles de baja energía, con configuraciones electrónicas en el estado fundamental p^2, p^3 o p^4. Esta aproximación se basa en que estos cinco primeros niveles son los físicamente relevantes en el cálculo del espectro emitido, teniendo en cuenta que los niveles por encima no llegan a poblarse significativamente por colisiones u otros mecanismos. En la figura 1.1 presentamos los diagramas de Grotrian de los cinco primeros niveles de los iones O^+, S^+, O^{2+} y N^+, donde se muestran las principales líneas de emisión de los mismos. El programa FIVEL, desarrollado por De Robertis et al. (1987), aplica la aproximación de cinco niveles con el fin de determinar las poblaciones de los mismos y las emisividades de un amplio número de líneas de emisión provenientes de los iones típicos observados en ambientes nebulares. La última versión de FIVEL es el programa NEBULAR, desarrollado por Shaw y Dufour (1995), que actualmente opera dentro del grupo de paquetes STSDAS de IRAF.

Un concepto importante a la hora de estudiar ambientes donde las colisiones pueden ser relevantes, como las nebulosas gaseosas, es el de densidad crítica, $n_{i,c}$. Este es el valor para el cual las desexcitaciones colisionales son igual de probables que las desexcitaciones radiativas. Para una transición dada desde el nivel i se define como:

$$n_{i,c} = \frac{\sum_{j<i} A_{ij}}{\sum_{j \neq i} q_{ij}}. \tag{1.12}$$

El valor de la densidad crítica marca el punto en el cual pasamos de un régimen de baja densidad a otro de alta densidad y sus valores aumentan a medida que aumenta el nivel. De este modo, para densidades por encima de la crítica, las desexcitaciones colisionales pueden ser importantes y habrá que considerarlas.

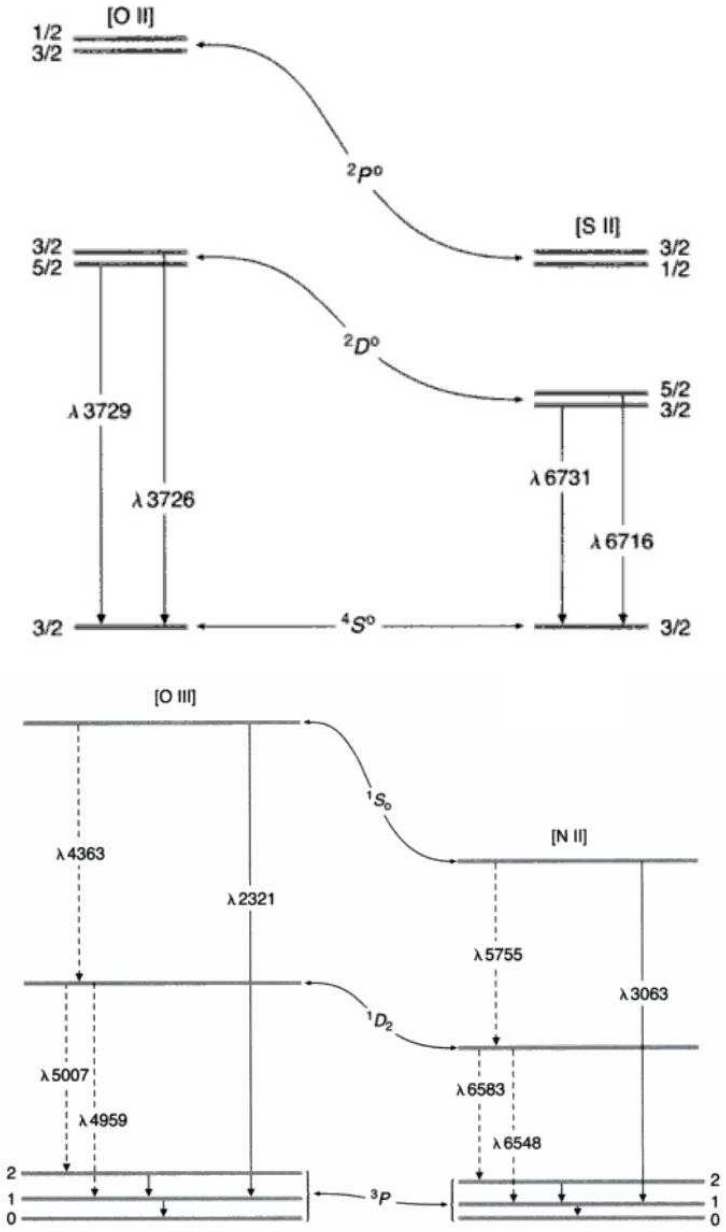

Figura 1.1: Diagramas de Grotrian que muestran las transiciones de las líneas más brillantes de [O II], [S II], [O III] y [N II] entre los cinco primeros niveles de energía de los respectivos iones. Las configuraciones electrónicas en el estado fundamental son: $2p^2$ para O^{2+} y N^+, $3p^3$ para S^+ y $2p^3$ para O^+. Los valores a izquierda y derecha de los niveles de energía, respresentan el momento angular total J de cada término espectral. La diferencia de energía entre los niveles ^3P de los iones O^{2+} y N^+, y de los niveles $^2D_0$ y $^2P_0$ de O^+ y S^+, ha sido exagerada para clarificar los niveles de llegada de las líneas nebulares. Figura adaptada de Osterbrock y Ferland (2006).

Tradicionalmente, las LECs se han dividido en tres grupos atendiendo al tipo de transición eléctronica involucrada: líneas prohibidas, semi-prohibidas y permitidas. Las líneas prohibidas –denominadas así porque violan las reglas de selección de una interacción dipolar-eléctrica– y semi-prohibidas presentan probabilidades de transición del orden 10^{-2} –o menores sobre todo en las LECs del infrarrojo–, mientras que las líneas permitidas tienen probabilidades de transición del orden de 10^8 s^{-1}. Atendiendo a estos valores, podemos inferir que la densidad crítica de las líneas prohibidas es menor que la misma en líneas semi-prohibidas y permitidas y, por tanto, las primeras serán más sensibles a los efectos de desexcitación colisional.

Fluorescencia

Otro mecanismo importante que da origen a líneas permitidas de elementos pesados es la fluorescencia, o fotoexcitación, por fotones del continuo estelar, o fotones procedentes de una recombinación previa (Grandi 1976). Las líneas de Bowen (Bowen 1934) son un caso particular de fluorescencia, donde el ion O^{3+} es excitado por la absorción de la línea He II Lyα. Tras ello, el O^{3+} vuelve al estado fundamental emitiendo las líneas O III 3133 y 3444 Å.

La interpretación de las líneas de emisión fluorescentes es bastante compleja y depende de distintos factores difíciles de conocer, por lo que habitualmente dichas líneas no se utilizan como diagnósticos en las nebulosas. Aún así, es muy importante saber qué líneas están afectadas por fluorescencia, con el fin de evitar análisis inapropiados. En Grandi (1976) y Esteban et al. (1998) podemos encontrar un extenso análisis de las líneas de elementos pesados que pueden, o no, estar afectadas por la excitación fluorescente.

Lucy (1995) y Rodríguez (1999) también presentan el análisis de los efectos de fluorescencia en líneas de elementos refractarios, tales como Fe o Ni. Las líneas emitidas por los iones de estos elementos están afectadas por la fluorescencia del continuo radiado por la fuente ionizante. Existe una vía para considerar los efectos de fluorescencia causados por la radiación del continuo estelar. Con ello, los flujos de líneas fluorescentes serían útiles en el análisis nebular. Para los iones afectados por este tipo de fluorescencia, las ecuaciones de equilibrio estadístico deben reescribirse teniendo en cuenta las emisiones estimuladas que el continuo puede producir. Esto es:

$$\sum_{j\neq i} n_j(n_e q_{ji} + UB_{ji}) + \sum_{j>i} n_j A_{ij} = \sum_{j\neq i} n_i(n_e q_{ij} + UB_{ij}) + \sum_{j<i} n_i A_{ij}. \tag{1.13}$$

Por un lado, B_{ij} es el coeficiente de Einstein de emisión estimulada, que se relaciona con A_{ij} como:

$$B_{ij} = \frac{c^3}{8\pi h\nu^3} A_{ij}, \tag{1.14}$$

y este a su vez se relaciona con B_{ji} por medio de los pesos estadísticos de los niveles i y j. Por otro lado, la variable U representa la emisión del continuo estelar. En una primera aproximación, esta variable podría estar representada por la emisión de un cuerpo negro, amortiguada por un factor relacionado con la distancia entre la fuente ionizante y el punto donde hemos medido la emisión de líneas fluorescentes. Está claro que utilizar funciones U

más realistas proporcionará mejores resultados a la hora de considerar la emisión fluorescente por continuo estelar. Bautista et al. (1996) realizan un análisis más extenso sobre los efectos del continuo estelar y su incorporación en las ecuaciones de equilibrio estadístico.

1.3 Polvo interestelar

Los granos de polvo juegan un papel importante en la física del medio interestelar, desde la termodinámica y la química del gas hasta la dinámica de la formación de estrellas. Aparte del gas, las nebulosas gaseosas contienen partículas de polvo cuyos efectos sobre las propiedades nebulares no deben menospreciarse. En base a observaciones que intentan cuantificar los efectos de la presencia del polvo, se ha conseguido identificar los posibles candidatos que conforman la mayor parte del polvo interestelar. Entre estos candidatos nos encontramos con: silicatos que se combinan con magnesio y/o hierro; piroxenos y olivinas; materiales carbonatados donde la masa predominante es de carbono; granos de SiC; combinaciones de oxígeno y hierro, tales como el óxido ferroso; y, en mucha menor medida, carbonatos como la calcita y la dolomita. Hay muchas evidencias que justifican la existencia de polvo en las nebulosas gaseosas y, como veremos a lo largo de esta sección, sus efectos sobre la determinación de las condiciones físicas y abundancias químicas pueden corregirse.

1.3.1 Extinción interestelar

El efecto más obvio de la presencia de polvo interestelar es la extinción de la luz procedente de nebulosas y estrellas distantes. Este efecto, el oscurecimiento de la luz estelar, fue el que llevó a Trumpler (1930) a inferir la existencia del polvo interestelar. Una gran parte de nuestro conocimiento acerca del polvo interestelar está basado en estudios que analizan la dependencia de la atenuación de la luz con la longitud de onda. Frecuentemente nos referimos a dicha atenuación como enrojecimiento, debido a que los efectos de extinción son más importantes en las longitudes de onda más azules respecto a las rojas.

En el regimen óptico, la extinción es básicamente debida a la dispersión de la luz por la presencia de polvo, aunque también puede haber efectos menos importantes de absorción. La reducción que sufre la luz procedente de una fuente distante debido a la presencia de polvo interestelar a lo largo de la línea de visión se cuantifica como:

$$F(\lambda) = I(\lambda)e^{-\tau_\lambda}, \tag{1.15}$$

donde $I(\lambda)$ es el flujo que recibiríamos en la Tierra en ausencia de extinción interestelar, a lo largo de la línea de visión (denominado también flujo corregido o desenrojecido, o intensidad en la astrofísica nebular), $F(\lambda)$ es el flujo observado, o enrojecido, y τ_λ es la profundidad óptica a la longitud de onda observada λ.

Clásicamente, el método utilizado para la caracterización de la extinción interestelar se basa en la comparación espectrofotométrica de pares de estrellas con el mismo tipo espectral y muy diferente grado de enrojecimiento. Durante años, este tipo de medidas se han realizado en muchas estrellas y ello nos ha dado una buena idea del comportamiento de la extinción interestelar. De forma general, los resultados obtenidos a lo largo de la línea

de visión en diferentes direcciones a través del medio interestelar difuso muestran que la dependencia de la extinción con la longitud de onda es:

$$\tau_\lambda = Cf(\lambda), \tag{1.16}$$

donde C es un factor constante que depende de la estrella observada y $f(\lambda)$ es una función conocida como curva o ley de extinción interestelar, cuyo comportamiendo es aproximadamente el mismo para una amplia mayoría de estrellas de la Galaxia.

De la ecuación anterior se desprende que la normalización de la función $f(\lambda)$, que contiene la dependencia en longitud de onda de la extinción, es arbitraria. Históricamente, en la astrofísica nebular, la normalización de $f(\lambda)$ se realiza a través de la longitud de onda de la línea de emisión de la serie de Balmer Hβ (H I 4861 Å). Con ello, haciendo uso de las relaciones anteriores y utilizando logaritmos decimales, el cociente de flujos observado relativo a Hβ queda expresado como:

$$\frac{F(\lambda)}{F(\mathrm{H}\beta)} = \frac{I(\lambda)}{I(\mathrm{H}\beta)} 10^{-c(\mathrm{H}\beta)\left[f(\lambda)-f(\mathrm{H}\beta)\right]}, \tag{1.17}$$

donde $c(\mathrm{H}\beta) = 0.434C$ es el denominado coeficiente de extinción, el cual representa la cantidad de extinción interestelar. Esta última relación es la que nos permite realizar la corrección de extinción, conocidos los parámetros $c(\mathrm{H}\beta)$ y $f(\lambda)$. Como podemos ver, esta corrección nos limita a la obtención de flujos intrínsecos, o intensidades, relativos a Hβ.

En primer lugar, para llevar a cabo una determinación práctica del coeficiente de extinción, hemos de conocer los valores de la función $f(\lambda)$. Para longitudes de onda mayores que 3030 Å, dicha función $f(\lambda)$ únicamente depende de la longitud de onda y del valor de la extinción selectiva, R_V, la cual se define como el cociente entre el número de magnitudes extinguidas en la banda V y el exceso de color entre las bandas B y V, es decir, $R_V = A_V/E(B-V)$. La variable R_V compara las propiedades de enrojecimiento y la extinción de los granos de polvo. Esta solamente es sensible a la composición, el tamaño y la forma de dichos granos. $R_V \approx 3.1$ es un valor típico encontrado para el medio interestelar difuso, aunque se pueden encontrar otros valores (*e.g.* $R_V \approx 5.5$ es para el caso particular de la Nebulosa de Orión). Muchos autores han obtenido empíricamente valores para la función $f(\lambda)$ y modelado su comportamiento en un amplio rango espectral. Algunos ejemplos de estos autores son: Whitford (1958), Seaton (1979) o Savage y Mathis (1979), quienes obtuvieron leyes de extinción para el valor típico de R_V en el medio interestelar difuso; Cardelli et al. (1989), cuya ley de extinción está parametrizada para cualquier valor de R_V; y Costero y Peimbert (1970) o Blagrave et al. (2007), cuyos trabajos analizan la extinción particular presente en la Nebulosa de Orión.

Una vez adoptada una ley de extinción, el valor de $c(\mathrm{H}\beta)$ se puede conseguir comparando los cocientes de flujos observados de las líneas de H I con los cocientes teóricos de las mismas líneas, que vienen dados por el modelo para el átomo de hidrógeno de Storey y Hummer (1995). El caso ideal consistiría en tener acceso a un gran conjunto de líneas de H I, aunque no es lo habitual, y el cociente clásicamente utilizado es F(Hα)/F(Hβ). Otro método menos usual para la obtención del coeficiente de extinción es el uso de las líneas en el UV e infrarrojo de [S II]. Estas líneas parten de los mismos niveles superiores de energía y, por tanto, su cociente relativo únicamente depende de las probabilidades de transición y las longitudes de onda (Miller 1968).

1.3.2 Formación y destrucción del polvo

Los datos observacionales obtenidos a partir de medidas de la emisión del continuo térmico en el infrarrojo y del continuo en el óptico debido a la dispersión de la radiación por la presencia de polvo, muestran que las partículas de polvo existen en las regiones H II y NPs.

Las investigaciones llevadas a cabo en el campo de la teoría y la experimentación indican que, tras su formación, los granos de polvo pueden crecer por acrecin de átomos individuales existentes en el gas interestelar. De todas formas, su formación no puede iniciarse apartir de colisiones entre átomos, incluso a las mayores densidades registradas en las nebulosas gaseosas. En NPs, las medidas en el rango infrarrojo han mostrado que muchas estrellas gigantes y supergigantes frías tienen capas externas de polvo que las rodean. Esto implicaría que el polvo debe estar presente en la atmósfera de estas estrellas, o que debió formarse durante las etapas más tempranas de expulsión de las capas externas debido a las altas densidades que se alcanzan en las cercanías de las mismas. En regiones H II se espera que las partículas de polvo originales se hayan formado por alguna de estas vías.

Los granos de polvo pueden llegar a ser destruidos por diferentes tipos de procesos. El paso de ondas de choque a través del gas interestelar es uno de los principales mecanismos que podría alterar, o destruir, el polvo presente en la fase gaseosa. Durante el paso de la onda de choque ocurren varios procesos –colisiones entre granos de polvo y entre granos de polvo e iones– que causan una mayor fragmentación de las partículas de polvo. La destrucción del polvo es un fenómeno muy relevante por varias razones. En especial, la principal razón que atañe a esta tesis, es la posible alteración de la composición química de la fase gaseosa después del paso de la onda de choque, ya que la destrucción de granos de polvo devuelve al medio interestelar parte del material que los conforma. Como vimos al principio de esta sección, el polvo contiene muchos elementos refractarios atrapados (*e.g.* Ca, Fe, o Si), los cuales son sustancialmente menos abundantes en el gas ionizado de la nebulosas, y cuya composición química es más susceptible de ser alterada por el efecto descrito aquí.

1.4 Determinaciones de parámetros físicos y químicos

La determinación de parámetros físicos –como la densidad y temperatura electrónica– a partir de espectros ópticos del gas de las nebulosas gaseosas, se realiza a través de cocientes de LECs, cuyas emisividades dependen fuertemente de las condiciones de temperatura y densidad. Por otro lado, las abundancias químicas se pueden determinar, bien a través del ajuste de ciertos observables espectroscópicos mediante modelos de fotoionización, o bien a partir de diagnósticos empíricos –método directo o calibraciones empíricas– basados en la medida del flujo de las líneas de emisión. Es importante destacar que para las determinaciones de los parámetros que aquí se presentan, la corrección de extinción es un paso necesario que nos permite calcular los flujos intrínsecos o desenrojecidos. En las siguientes secciones repasaremos cómo se obtienen dichos parámetros.

1.4.1 Condiciones físicas del gas

El cálculo de las condiciones físicas del gas ionizado se resume en la obtención de la densidad electrónica, n_e, y la temperatura electrónica, T_e.

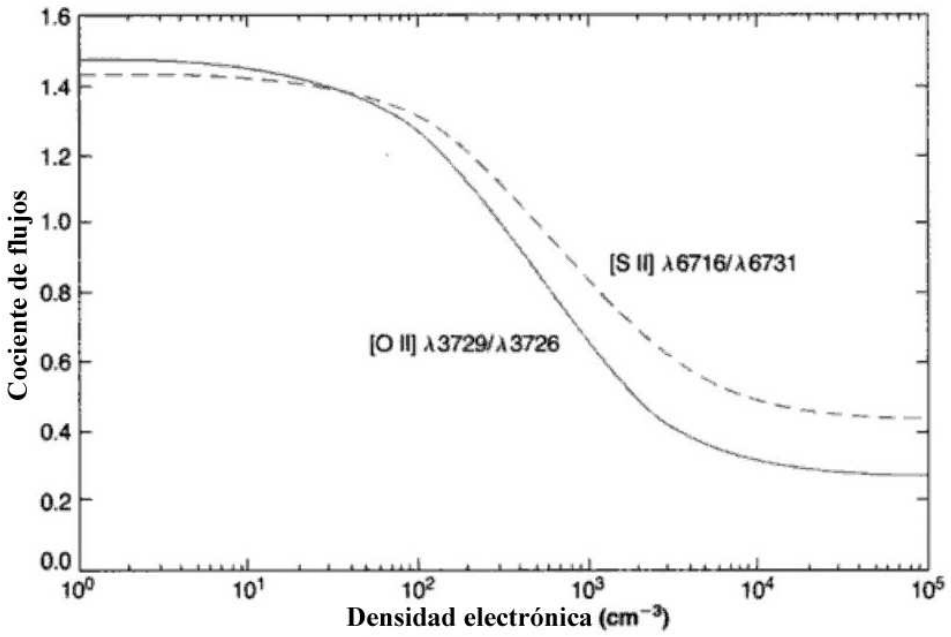

Figura 1.2: Variación de los cocientes de flujos con respecto a la densidad electrónica de las líneas de [O II] (línea continua) y [S II] (línea discontinua) para una temperatura típica de 10^4 K. Figura adaptada de Osterbrock y Ferland (2006).

La n_e promedio en una nebulosa puede ser medida a partir de la comparación de los flujos de dos LECs emitidas por un mismo ion desde niveles con energías de excitación similares. Esto da como resultado que las tasas de excitación relativas de los niveles de partida dependan únicamente del cociente de sus fuerzas de colisión. En el caso concreto de que los niveles implicados tengan diferentes probabilidades de transición, o diferentes tasas de desexcitación colisional, las poblaciones relativas de ambos niveles pasan a depender en gran medida de la n_e, así como del cociente de flujos de las líneas de emisión implicadas. Los cocientes de líneas más comúnmente utilizados en el rango óptico y para densidades intermedias entre 10^2 y 10^4 cm^{-3} son [O II] $\lambda3729/\lambda3726$ y [S II] $\lambda6716/\lambda6731$. En la figura 1.1 se presentan los diagramas de Grotrian de los cinco primeros niveles de los respectivos iones, donde se muestran las transiciones más relevantes en el rango óptico de las configuraciones electrónicas $2p^3$ para el [O II] y $3p^3$ para el [S II]. Existen otros cocientes de líneas para el cáculo de la densidad (ver Shaw y Dufour 1995), como pueden ser [Cl III] $\lambda5517/\lambda5537$ ó [Ar IV] $\lambda4711/\lambda4740$, que además permiten muestrear zonas de más alta densidad, aunque estas líneas son menos brillantes que las anteriores.

En el límite de baja densidad, donde cada excitación colisional produce la emisión de un fotón y las desexcitaciones colisionales son despreciables, el cociente de flujos coincide con el cociente de los pesos estadísticos de los niveles de partida de las líneas involucradas. En cambio, cuando tenemos densidades superiores a la densidad crítica de los niveles de partida, es decir, estamos en el límite de alta densidad, las poblaciones de dichos niveles comienzan a estar dominadas por las colisiones. En estas condiciones se establece el equili-

brio térmico y las poblaciones relativas de los niveles se rigen por la ecuación de Boltzmann. En una nebulosa gaseosa típicamente nos encontramos con densidades entre ambos límites, donde el cociente de líneas es muy sensible a la n_e y muy poco a la T_e. En estos casos, la obtención de la n_e se consigue a través de la resolución de las ecuaciones de equilibrio estadístico (ecuación 1.9) para cada uno de los cinco primeros niveles que se muestran en la figura 1.1. Con ello, obtenemos la variación del cociente de flujos de las líneas utilizadas como diagnóstico respecto a la densidad. En la figura 1.2 presentamos dicha variación para los cocientes de las líneas de [O II] y [S II], a una temperatura electrónica de 10^4 K. Para otro valor de temperatura, las curvas no presentan grandes cambios debido a la baja dependencia de los cocientes con la misma.

Otra manera de obtener la densidad electrónica es a través del análisis de líneas de elementos pesados como Fe o Ni. Concretamente, haciendo uso de un amplio conjunto de líneas de [Fe III] (Rodríguez 1998). La densidad que se obtiene a partir de dicho análisis es aquella que minimiza la dispersión de los cocientes observados, respecto a los teóricos de las líneas más brillantes de [Fe III]. Ambos cocientes, observados y teóricos, son normalizados respecto a la línea [Fe III] 4658 Å. Los cálculos para la determinación de los cocientes teóricos se realizan resolviendo las ecuaciones de equilibrio estadístico con un modelo atómico de 34 niveles para el ion de Fe^{2+}, haciendo uso de los datos atómicos –probabilidades de transición y fuerzas de colisión– más recientes disponibles en la literatura. La función de dispersión, F, que habría que minimizar se escribe como:

$$F = \sum_{i=1}^{n} \left(\frac{[I(\lambda_i)/I(\lambda 4658)]_{obs}}{[I(\lambda_i)/I(\lambda 4658)]_{teo}} - \frac{1}{n} \sum_{j=1}^{n} \frac{[I(\lambda_j)/I(\lambda 4658)]_{obs}}{[I(\lambda_j)/I(\lambda 4658)]_{teo}} \right)^2, \tag{1.18}$$

donde n es el número total de líneas de [Fe III] utilizadas.

En cuanto a la determinación de la temperatura, sabemos de la sección §1.2.2 que la T_e viene dada por el equilibrio que se establece entre los procesos de calentamiento y enfriamiento. La T_e se puede calcular solamente para unos pocos iones. Estos presentan una estructura de niveles de energía que producen LECs cuyas transiciones ocurren desde distintos niveles superiores con energías de excitación muy diferentes. Esta característica hace que el cociente de flujos de las LECs emitidas sea muy sensible a la temperatura. Dos de los mejores ejemplos son las LECs de [O III] y [N II], que se presentan también en la figura 1.1 sobre la estructura de cinco niveles de sus respectivos iones. El método clásico que nos permite determinar la T_e, es a partir de los cocientes de las intensidades de las líneas aurorales respecto a las nebulares de dichos iones. Las expresiones típicas que podemos encontrar para los cocientes de flujos son (Osterbrock y Ferland 2006):

$$[\text{O III}] : \frac{j_{\lambda 4959} + j_{\lambda 5007}}{j_{\lambda 4363}} = \frac{7.90 e^{(3.29\times 10^4/T_e)}}{1 + 4.5 \times 10^{-4} n_e / T_e^{1/2}}, \tag{1.19}$$

$$[\text{N II}] : \frac{j_{\lambda 6548} + j_{\lambda 6583}}{j_{\lambda 5755}} = \frac{8.23 e^{(2.50\times 10^4/T_e)}}{1 + 4.4 \times 10^{-3} n_e / T_e^{1/2}}. \tag{1.20}$$

Estas relaciones son válidas a primer orden, ya que la solución exacta la proporciona la resolución de las ecuaciones de equilibrio estadístico de los iones O^{2+} y N^+. Tanto los resultados obtenidos a partir de las ecuaciones como de la resolución numérica, son válidos

para un amplio rango de densidades, el cual está limitado por las densidades críticas de los niveles de partida de las líneas nebulares, del orden de 5×10^4 cm^{-3}, que son aproximadamente dos órdenes de magnitud más pequeñas que las densidades críticas de las líneas aurorales.

Existen más iones cuyas LECs emitidas son sensibles a los cambios de temperatura (ver Shaw y Dufour 1995). Algunas de ellas son: [S III] $(\lambda 9069 + \lambda 9532)/\lambda 6312$, [Ne III] $(\lambda 3869 + \lambda 3968)/\lambda 3343$ y [Ar III] $(\lambda 7136 + \lambda 7751)/\lambda 5192$. Otros cocientes de LECs como [O II] $(\lambda 3726+\lambda 3729)/(\lambda 7320+\lambda 7330)$ ó [S II] $(\lambda 6716+\lambda 6731)/(\lambda 4068+\lambda 4076)$ son también indicadores de T_e aunque, por contra, estos cocientes son bastante sensibles a la n_e.

Generalmente, el cálculo refinado de las condiciones físicas, n_e y T_e, se hace de forma conjunta ya que ambas variables, como hemos visto, dependen entre sí la una de la otra. En este sentido, un método iterativo con una temperatura inicial es una buena opción. El número de iteraciones necesarias para alcanzar la convergencia suele rondar entre 4 y 5.

Un último concepto importante, relacionado con el cálculo de las condiciones físicas, es que tanto las densidades como las temperaturas calculadas son representativas de las zonas nebulares ocupadas por los correspondientes iones y, por tanto, los valores obtenidos no tienen porque ser, en principio, característicos de toda la nebulosa.

1.4.2 Abundancias químicas

Siempre y cuando se hayan determinado con precisión las condiciones físicas del gas ionizado de la nebulosa, será posible obtener las abundancias químicas iónicas del mismo mediante el método empírico directo.

En general, como vimos en la sección §1.2.3, la intensidad de una línea de emisión se expresa según la ecuación (1.6). Suponiendo que la tasa de emisión, j_λ, es prácticamente constante a lo largo de la línea de visión, tendremos que la intensidad se puede escribir como:

$$I(\lambda) = j_\lambda \Delta s, \tag{1.21}$$

donde Δs es el recorrido a lo largo de la línea de visión.

La corrección de extinción permite la obtención de cocientes de flujos corregidos, o intensidades, como ya mencionamos en §1.3.1, relativos a Hβ. Por tanto, para un ion X^{+i} únicamente podemos determinar su abundancia química respecto al H^+, a partir del cociente relativo a Hβ. En términos de la relación anterior:

$$\frac{I(\lambda)}{I(H\beta)} = \frac{j_\lambda}{j_{H\beta}}, \tag{1.22}$$

donde la dependencia con Δs, imposible de determinar, se anula.

Abundancias iónicas a partir de LRs

De la sección §1.2.3, sabemos que la tasa de emisión de una LR se puede escribir como se muestra en la ecuación (1.7). En términos de la longitud de onda, y para un elemento X en el estado de ionización $+i$, dicha relación queda:

$$j_\lambda = \frac{hc}{4\pi\lambda} N(X^{+i}) n_e \alpha^{eff}(X^{+i}, T_e). \tag{1.23}$$

Por otro lado, la línea de emisión de referencia en el cociente de flujos, Hβ, es también una LR, por lo que su tasa de emisión, $j_{H\beta}$, se puede expresar como:

$$j_{H\beta} = \frac{hc}{4\pi\lambda_{H\beta}} N(\mathrm{H}^+) n_e \alpha^{eff}(\mathrm{H}^+, T_e), \tag{1.24}$$

aunque también cabe la posibilidad de utilizar la expresión aproximada para el cálculo de $j_{H\beta}$, obtenida por Aller (1984), y basada en el ajuste de los resultados obtenidos por Brocklehurst (1971) de las poblaciones de los niveles del átomo de hidrógeno. Dicha expresión tiene una precisión del 4% para densidades inferiores a 10^6 cm^{-3}, y se escribe como:

$$4\pi j_{H\beta} = 1.387 \times 10^{-25} n_e N(\mathrm{H}^+) T_4^{-0.983} 10^{-0.0424/T_4}, \tag{1.25}$$

donde T_4 es la temperatura electrónica en unidades de 10^4 K.

De este modo, a partir del uso de la expresión (1.22), podremos obtener de forma directa la abundancia química para el ion X^{+i} como:

$$\frac{N(X^{+i})}{N(\mathrm{H}^+)} = \frac{\lambda(\text{Å})}{4861} \frac{\alpha^{eff}(\mathrm{H}^+, T_e)}{\alpha^{eff}(X^{+i}, T_e)} \frac{I(\lambda)}{I(H\beta)}. \tag{1.26}$$

donde se puede ver que la dependencia con la T_e se encuentra en los coeficientes de recombinación efectivos. Estos coeficientes presentan dependencias muy débiles con la temperatura –$\alpha^{eff}(X^{+i}, T_e) \propto T_e^{-m}$, donde m es del orden de 1– y, por tanto, hacen que las abundancias químicas calculadas a partir de LRs sean casi independientes de las condiciones físicas del gas.

Abundancias iónicas a partir de LECs

Las abundancias iónicas a partir de LECs no presentan un cálculo tan sencillo como el caso de las LRs. La ecuación (1.8) nos da la tasa de emisión para una LEC cualquiera. Dicha ecuación, en términos de la longitud de onda de una LEC emitida entre los niveles i y j por el ion X^{+l}, se reescribe como:

$$j_\lambda = \frac{hc}{4\pi\lambda} n_i A_{ij} N(X^{+l}). \tag{1.27}$$

De tal modo que la abundancia química de dicho ion, respecto al H^+, se puede calcular a partir de la relación (1.22) como:

$$\frac{N(X^{+l})}{N(\mathrm{H}^+)} = \frac{\lambda(\text{Å})}{4861} \frac{n_e \alpha^{eff}(\mathrm{H}^+, T_e)}{n_i A_{ij}} \frac{I(\lambda)}{I(H\beta)}. \tag{1.28}$$

Como podemos ver, el cálculo de las abundancias iónicas a partir de LECs depende de la probabilidad de transición de dicha línea, A_{ij}, así como de la densidad electrónica del gas y la población del nivel de partida de la LEC, n_i. Así pues, el problema del cálculo de las abundancias a partir de LECs radica en la obtención de las poblaciones de los niveles energéticos y, por tanto, en la resolución de las ecuaciones de equilibrio estadístico. Contrariamente a lo que sucedía con las abundancias obtenidas a partir de

LRs, las calculadas a partir de LECs presentan una fuerte dependencia con las condiciones físicas, concretamente con la T_e a través del cálculo de las tasas de desexcitación colisional. La dependencia de dichas tasas con la temperatura suele ser: $q \propto T^{-1/2} e^{-\frac{\Delta E}{kT_e}}$. Por tanto, las abundancias que obtengamos a partir de estas líneas van a depender en gran medida de la temperatura adoptada.

Abundancias totales

El método directo del cálculo de abundancias químicas nos permite obtener con relativa simplicidad las abundancias iónicas a partir del cociente relativo de intensidades de líneas de emisión. El cálculo de la abundancia total, relativa al H, de un cierto elemento X se puede realizar sumando las abundancias iónicas del mismo elemento para cada uno de los posibles estados de ionización. Ahora bien, es habitual encontrarnos con que no todos los iones del elemento X producen líneas de emisión en el rango espectral cubierto por nuestro espectro. En estas condiciones, es posible la resolución del problema por medio de los llamados factores de corrección por ionización, ICFs (acrónimo de *ionization correction factor*). Estos factores tienen en cuenta la contribución de los estados de ionización no observados.

Típicamente, la obtención de ICFs se puede realizar por dos vías: a partir de un conjunto de modelos de fotoionización, o a partir de la similitud de los potenciales de ionización de iones observados y no observados.

Respecto al primer caso, podemos poner como ejemplo el ICF de S^{3+} obtenido por Stasińska (1978) para el cálculo de la abundancia total de S, debido a que en el rango óptico únicamente se observan líneas de [S II] y [S III]. La relación presentada por Stasińska (1978) se obtiene a partir del ajuste del cociente $S/(S^+ + S^{2+})$ en función de O^+/O, utilizando un amplio conjunto de modelos de fotoionización. Con el ICF(S^{3+}), la abundancia total de azufre sería:

$$\frac{S}{H} = \mathrm{ICF}(S^{3+}) \times \frac{S^+ + S^{2+}}{H^+} = \\ = \left[1 - \left(1 - \frac{O^+}{O}\right)^3\right]^{-1/3} \times \frac{S^+ + S^{2+}}{H^+}. \tag{1.29}$$

Por otro lado, un claro ejemplo de ICF obtenido a partir de la similitud de potenciales de ionización de distintos iones es el caso del He. Debido a la ausencia de líneas de emisión de helio neutro en el rango óptico, y basándose en la similitud de los potenciales de ionización del He^0 (24.6 eV) y el S^+ (23.3 eV), Peimbert et al. (1992) obtuvieron la siguiente expresión para el ICF(He^0) y el cálculo de la abundancia total de He:

$$\frac{He}{H} = \mathrm{ICF}(He^0) \times \frac{He^+}{H^+} = \left(1 + \frac{S^+}{S - S^+}\right) \times \frac{He^+}{H^+}. \tag{1.30}$$

1.5 La discrepancia de abundancias

1.5.1 Planteamiento del problema y antecedentes

El análisis de los espectros de líneas de emisión de las nebulosas gaseosas, regiones H II y NPs es una de las mejores herramientas para la obtención y el estudio de las abundancias

químicas a escala galáctica y extragaláctica. Para ello, un detallado conocimiento de las condiciones físicas y los mecanismos de excitación que producen la emisión de líneas es crucial para la fiabilidad y precisión de los resultados y, consecuentemente, para el estudio de la nucleosíntesis estelar y la evolución química de las galaxias. Históricamente, el análisis basado en LECs ha sido la mejor, e inicialmente la única, opción para la obtención de abundancias químicas de elementos más pesados que el He, dado su alto brillo y los eficientes diagnósticos de condiciones físicas que con ellas se pueden construir. Sin embargo, desde hace más de dos décadas, se han conseguido obtener abundancias químicas a partir de LRs de elementos pesados, las cuales presentan flujos varios órdenes de magnitud inferiores a las clásicas LECs –del orden de $0.001 \times F(\mathrm{H}\beta)$–. El resultado observacional más relevante que se obtiene a partir de la comparación de las abundancias químicas de un mismo ion calculadas a partir de los dos tipos de líneas es que las abundancias determinadas a partir de LRs son mayores que las abundancias que resultan del método tradicional basado en el análisis de LECs. Hoy en día, este hecho se conoce como problema de la discrepancia de abundancias (DA).

Las primeras nebulosas gaseosas donde se detectaron LRs de elementos pesados fueron las NPs debido a su alto grado de ionización y brillo superficial. Wyse (1942) fue el primero en detectar LRs de diferentes elementos pesados –C, O y N– en un amplio número de NPs. Particularmente, este autor detectó más de una veintena de LRs de O II en la nebulosa NGC 7009. Wyse (1942) argumentaba que dichas líneas de emisión se originaban en las capturas de electrones del ion O^{2+}, tal como ocurría con las líneas de Balmer, que se producen por la captura de electrones por parte del ion H^+, y por tanto el cociente relativo de las LRs de O II y H I daría cuenta de las tasas de recombinación, así como de la abundancia relativa de los iones que las producen, O^{2+}/H^+. La abundancia de O^{2+} obtenida por dicho autor a partir de LRs resultó significativamente mayor que la calculada por Menzel y Aller (1941), para la misma NP, a partir de las líneas de [O III]. A principios de los años cuarenta, esta discrepancia fue asociada a incertidumbres en los métodos utilizados en el cálculo de abundancias. Más tarde, Aller y Menzel (1945) y Torres-Peimbert y Peimbert (1977) encontraron que el cociente C^{2+}/H^+ era excesivamente alto en algunas NPs al calcularlo a partir del flujo de la LR C II 4267 Å.

La DA comenzó a ser un problema de interés científico con la puesta en órbita, en el año 1978, del satelite *IUE* (acrónimo de *International Ultraviolet Explorer*), que abrió la ventana al rango UV del espectro y permitió la medida de las LECs C III] 1907, 1909 Å. A partir de la medida de flujo de estas líneas, se obtuvieron abundancias químicas, relativas al H^+, de C^{2+} para un gran número de NPs, que resultaron ser sistemáticamente inferiores a las mismas obtenidas a partir de la LR C II 4267 Å (*e.g.* Harrington et al. 1980; Torres-Peimbert et al. 1980; French 1983; Kaler 1986; Rola y Stasińska 1994; Peimbert et al. 1995; Mathis y Liu 1999). Con el paso de los años, el mismo resultado ha sido una constante en el análisis de las abundancias químicas a partir de LRs de otros elementos pesados –N, O y Ne– para casi un centenar de NPs, localizadas tanto en el disco como en el bulbo galáctico (*e.g* Garnett y Dinerstein 2001; Liu et al. 1995, 2000, 2006; Tsamis et al. 2003a, 2004; Robertson-Tessi y Garnett 2005; Ruiz et al. 2003; Wesson et al. 2005; Zhang et al. 2005; García-Rojas et al. 2009).

En el caso de las regiones H II, la detección y medida de LRs de elementos pesados ha tenido un progreso mucho más lento, debido al bajo brillo superficial de estos objetos.

Torres-Peimbert et al. (1980) fueron los primeros en determinar la abundancia de C^{2+} a partir de LECs y LRs en la Nebulosa de Orión, encontrando el mismo resultado cualitativo. Peimbert et al. (1993) fueron los primeros que determinaron las abundancias de O^{2+} a partir de LRs, llegando nuevamente a la misma conclusión en las dos regiones H II estudiadas: las abundancias calculadas a partir de LRs son mayores que las que podemos obtener a partir de LECs para el mismo ion. En los últimos diez años, las contribuciones hechas por diversos autores ha aumentado significativamente la muestra de LRs de iones de elementos pesados –C, O, N o Ne– en regiones H II galácticas y extragalácticas (*e.g.* Esteban et al. 1999a,b, 2002, 2004, 2009; García-Rojas et al. 2004, 2005, 2006, 2007; López-Sánchez et al. 2007; Peimbert 2003; Peimbert et al. 2005; Tsamis et al. 2003b).

Hoy en día, la discrepancia de abundancias es uno de los mayores retos científicos en la comprensión de los procesos físicos que tienen lugar en el seno de las nebulosas gaseosas. Como veremos en las siguientes secciones, se han barajado varias teorías, pero ninguna de ellas presenta una solución completa y, por tanto, es un problema que continúa aún sin ser resuelto.

1.5.2 El factor de discrepancia de abundancias

La forma habitual que se ha adoptado en la astrofísica nebular para cuantificar la DA es a través del denominado factor de discrepancia de abundancias o ADF (acrónimo de *abundance discrepancy factor*). Dicho factor, para un determinado ion X^{+i}, se define como el cociente de las abundancias determinadas a partir de LRs y LECs. Por tanto, tiene la forma:

$$\mathrm{ADF}(X^{+i}) = (X^{+i}/\mathrm{H}^+)_{LR}/(X^{+i}/\mathrm{H}^+)_{LEC}. \tag{1.31}$$

En el estudio químico de las nebulosas gaseosas, es muy frecuente encontrarse las abundancias químicas expresadas en unidades logarítmicas. Por ello, puede encontrarse el ADF definido como[2]:

$$\mathrm{ADF}(X^{+i}) = log\Big(\frac{X^{+i}}{\mathrm{H}^+}\Big)_{LR} - log\Big(\frac{X^{+i}}{\mathrm{H}^+}\Big)_{LEC}. \tag{1.32}$$

Regiones H II *vs.* Nebulosas Planetarias

Los rápidos avances tecnológicos relacionados con telescopios de grandes aberturas y la mejora de la eficiencia cuántica de los detectores, han permitido aumentar la muestra de LRs de elementos pesados. Los principales iones para los cuales se han detectado y medido LRs son: C^{2+}, N^+, O^+, O^{2+} y Ne^{2+}. Para estos iones, se han podido determinar las abundancias químicas a partir de LRs y, a su vez, compararlas con las calculadas a partir de LECs, con el fin de muestrear sus posibles valores de ADF. Tanto en NPs como en regiones H II, la mayor muestra de ADFs está disponible para el ion O^{2+}, gracias a que las líneas de [O III] y O II se detectan con relativa facilidad en un estrecho rango del espectro óptico. Para el resto de iones, existen determinaciones de su ADF, aunque la muestra es más limitada por diferentes razones. En el caso del ion C^{2+}, son necesarias observaciones en el rango UV para la medida de las LECs C III] 1907, 1909 Å. Para el caso del N^+, las líneas de emisión pueden estar afectadas por efectos de fluorescencia. En cambio, la detección de

[2]Esta es la definición habitual de ADF que se ha considerado en esta tesis.

las LRs de los iones O^+ y Ne^{2+} requiere observaciones muy profundas, debido a que estas son incluso más débiles que las de O II. La muestra de ADFs en NPs de cualquiera de los iones anteriores es mucho más amplia que en regiones H II, debido al gran brillo superficial y alto grado de ionización de estos objetos.

Un análisis global de la muestra de ADF(O^{2+}) disponibles en la literatura muestra que las regiones H II, galácticas y extragálacticas, y las NPs presentan rangos de valores muy diferentes. Por un lado, en la mayoría de las NPs, podemos encontrar valores típicos de ADF(O^{2+}) entre 0.20 y 0.50 dex, con una clara tendencia a valores altos. Incluso, se han llegado a medir ADF(O^{2+}) superiores: ∼0.70 dex en NGC 7009 (Liu et al. 1995; Luo et al. 2001); ∼1.00 dex en NGC 6153 (Liu et al. 2000); ∼1.30 dex en M 1-42 (Liu et al. 2001); y el mayor ADF(O^{2+}) registrado en una NP, ∼1.85 dex en Hf2-2 (Liu et al. 2006). Por otro lado, los resultados más recientes encontrados en regiones H II galácticas y extragalácticas (Esteban et al. 2002, 2004, 2005; García-Rojas y Esteban 2007; López-Sánchez et al. 2007; Peimbert et al. 2005; Tsamis et al. 2003b) muestran que el rango de variación de los valores de ADF(O^{2+}) en este tipo de nebulosas gaseosas es mucho más estrecho, con valores entre 0.10 y 0.35 dex. Como veremos en las secciones posteriores, este hecho observacional es el que ha llevado a García-Rojas y Esteban (2007) a sugerir que el origen de la DA es diferente en ambos tipos de nebulosas gaseosas.

El estudio de la distribución espacial del ADF, más concretamente del ADF(O^{2+}), así como el flujo de las líneas de O II y [O III] a pequeñas escalas espaciales es una forma relativamente reciente de analizar el problema de la DA, mucho más explorada en NPs que en regiones H II. Liu et al. (2000), Garnett y Dinerstein (2001) y Krabbe y Copetti (2006), entre otros, han estudiado el comportamiento espacial del ADF(O^{2+}) en las NPs NGC 6153, NGC 6720 y NGC 7009, respectivamente. Los diferentes autores encuentran que el ADF(O^{2+}) no es constante a lo largo de la superficie nebular, disminuyendo desde el centro hacia los bordes de la nebulosa. El primer estudio en regiones H II, hasta la publicación de los artículos presentados en esta tesis, fue llevado a cabo por Tsamis et al. (2003b), quienes analizaron las variaciones espaciales de las propiedades nebulares de la región extragaláctica 30 Doradus, con una resolución angular de $3\farcs7$. Aunque la naturaleza extragaláctica de esta región añade una limitación adicional al muestreo, estos autores encontraron que el ADF(O^{2+}) permanecía prácticamente constante, en torno a 0.30 dex, a lo largo de la posición de rendija analizada. También observaron que los perfiles espaciales de las abundancias de O^{2+}, obtenidas a partir de LECs y LRs, eran similares y no presentaban variaciones significativas. Ambos resultados difieren de lo observado en NPs.

1.6 Hipótesis sobre el origen de la discrepancia de abundancias

Como ya se comentó anteriormente, las dicotomía en la determinación de abundancias a partir de LECs o LRs, tanto en regiones H II como en NPs, es un problema que lleva muchos años presente en la astrofísica de nebulosas fotoionizadas. A partir de los años 80, el problema de la DA se comenzó a relacionar con la posible existencia de variaciones en la estructura espacial de temperaturas de las nebulosas gasesosas, en la forma propuesta por Peimbert (1967). Sin embargo, en la última década han aparecido nuevas hipótesis, tales como los modelos químicamente inhomogéneos propuestos por Liu et al. (2000), Tsamis y Péquignot (2005) y Stasińska et al. (2007), o la presencia de regiones dentro de las nebulosas

con diferente grado de ionización (Ercolano 2009). A lo largo de esta sección, repasaremos las diferentes hipótesis existentes hasta la fecha que tratan de explicar el origen de la DA. Cabe destacar que ninguna de ellas proporciona una respuesta absolutamente satisfactoria a dicho problema.

1.6.1 Las fluctuaciones de temperatura

Algunos autores han asociado el problema de la DA a la presencia de fluctuaciones en la distribución espacial de temperaturas. Hace ya más de cuarenta años que estas fluctuaciones fueron propuestas por Peimbert (1967), quien intentaba proporcionar una explicación a la diferencia observada entre la temperatura determinada a partir de los diagnósticos basados en LECs y la temperatura obtenida a partir del salto de Balmer en las regiones H II galácticas M17, M8 y la Nebulosa de Orión. Peimbert (1967) fue el primero en explorar el impacto de la presencia de fluctuaciones en la distribución espacial de la temperatura electrónica de las nebulosas gaseosas sobre la determinación de la misma. Posteriormente, Peimbert y Costero (1969) estudiaron las implicaciones de la existencia de dichas fluctuaciones sobre el cálculo de abundancias químicas basado en LECs. No fue hasta 1980 que Torres-Peimbert et al. (1980) relacionaron el problema de la DA con la presencia de fluctuaciones de temperatura en el gas ionizado. En este contexto, la DA se produciría por la diferente dependencia de las emisividades de las LRs y las LECs con respecto a la T_e, mucho más débil en las primeras. Con ello, las abundancias obtenidas a partir de LECs estarían más afectadas por la presencia de fluctuaciones de temperatura, siendo menores a las reales; mientras que las determinadas a partir de LRs serían las representativas de la composición química real del gas ionizado.

El planteamiento propuesto por Peimbert (1967) se basa en que, si las fluctuaciones de temperatura son relativamente pequeñas, la emisividad de una línea de emisión se puede escribir como una serie de Taylor hasta segundo orden, en torno a la temperatura promedio del gas, T_0. Esto es:

$$\epsilon_\lambda(T_e) = \epsilon_\lambda(T_0) + (T_e - T_0)\left(\frac{d\epsilon_\lambda}{dT_e}\right)_{T_0} + \frac{1}{2}(T_e - T_0)^2\left(\frac{d^2\epsilon_\lambda}{dT_e^2}\right)_{T_0}, \tag{1.33}$$

donde la T_0 se puede definir como:

$$T_0 = \frac{\int T_e n_e N_i ds}{\int n_e N_i ds}. \tag{1.34}$$

Escogiendo adecuadamente la definición de la desviación cuadrática media de la distribución de temperaturas como:

$$t^2 = \frac{\int (T_e - T_0)^2 n_e N_i ds}{T_0^2 \int n_e N_i ds}, \tag{1.35}$$

la intensidad de una LR, o una LEC en el límite de baja densidad, se puede reescribir a partir de la ecuación (1.6) como:

$$I(\lambda) = \left[\epsilon_\lambda(T_0) + \frac{1}{2}\left(\frac{d^2\epsilon_\lambda}{dT_e^2}\right)_{T_0} T_0^2 t^2\right] \int n_e N_i ds. \tag{1.36}$$

Con ello, la estructura de temperaturas de una nebulosa gaseosa queda determinada a partir de su temperatura media, T_0, y su fluctuación cuadrática media, t^2. Es importante llamar la atención sobre el hecho de que cada ion presente en la nebulosa debería tener sus propios valores para T_0 y t^2, debido a que ocupan volúmenes diferentes en la nebulosa.

Determinación práctica de t^2

Existen varios procedimientos que permiten la determinación de T_0 y t^2 bajo ciertas hipótesis. La comparación directa de las T_e obtenidas a partir de LECs y LRs es el método comúnmente utilizado debido a la diferente dependencia funcional con la T_e de estas líneas. Siguiendo a Peimbert (1967), las temperaturas calculadas haciendo uso de LECs y LRs se pueden escribir formalmente en términos de T_0 y t^2 como:

$$T_{LEC} = T_0\left[1 + \left(\frac{(\Delta E/kT_0)^2 - 3\Delta E/kT_0 + 3/4}{\Delta E/kT_0 - 1/2}\right)\frac{t^2}{2}\right] \tag{1.37}$$

y

$$T_{LR} = T_0\left[1 - (1-\alpha)\frac{t^2}{2}\right], \tag{1.38}$$

donde ΔE es la energía de excitación de la LEC y α la potencia de la temperatura de la que depende la emisividad de una LR. Estas expresiones se pueden particularizar para las temperaturas calculadas con las líneas de [O III] y el continuo de Balmer (ver Peimbert et al. 2004, y las referencias que allí citan) como:

$$T_e([\text{O III}]) = T_0(\text{O}^{2+})\left[1 + \left(\frac{91300}{T_0(\text{O}^{2+})} - 3\right)\frac{t^2(\text{O}^{2+})}{2}\right] \tag{1.39}$$

y

$$T_e(\text{Bac}) = T_0(\text{H}^+)\left[1 - 1.67t^2(\text{H}^+)\right]. \tag{1.40}$$

De forma sencilla, estas ecuaciones nos permiten inferir los valores de T_0 y t^2 suponiendo que $T_0(\text{O}^{2+}) \approx T_0(\text{H}^+)$ y $t^2(\text{O}^{2+}) \approx t^2(\text{H}^+)$.

Otro procedimiento para el cálculo de t^2 fue propuesto por Peimbert et al. (2000). Este método es bastante similar al anterior, sólo que en este caso, la temperatura de la LR es aquella obtenida a partir de las líneas de He I, T_e(He I). Esta temperatura no es posible calcularla directamente, por lo que hemos de seguir el método propuesto por estos autores, que permite determinar de forma simultánea, y autoconsistente, los valores de He^+/H^+, T_e(He I), n_e(He I) y la profundidad óptica de la línea He I 3889 Å, haciendo uso de un amplio conjunto de cocientes de flujos de líneas de He I, relativos a una línea de H I. Dicho método se basa en que cada uno de los cocientes de línea depende unívocamente de las cuatro variables anteriores, y ello nos permite calcular los valores óptimos de estas cuatro incógnitas, minimizando el parámetro χ^2 de la distribución estadística de cocientes de línea. Es importante destacar que un mayor conjunto de líneas de He I, junto con una buena medida del flujo de la línea He I 3889 Å, hará que el procedimiento descrito sea más robusto. Como en el caso anterior, la comparación de la T_e(He I) con la T_e([O III]) bajo las suposiciones de que $T_0(\text{O}^{2+}) \approx T_0(\text{He}^+)$ y $t^2(\text{O}^{2+}) \approx t^2(\text{He}^+)$, permitirá obtener

el parámetro t^2. La expresión formal que relaciona la T_e(He I) con T_0 y t^2 es:

$$T_e(\text{He I}) = T_0\left[1 - (\langle\alpha\rangle + \beta - 1)\frac{t^2}{2}\right] = T_0(\text{He}^+)\left[1 - 1.43t^2(\text{He}^+)\right], \qquad (1.41)$$

donde $\langle\alpha\rangle$ es el valor promedio de la potencia de la dependencia de la emisividad con la temperatura para las líneas de He I y β el mismo factor para Hβ.

Sin embargo, en base al análisis de una amplia muestra de modelos de fotoionización, Kingdon y Ferland (1995) mostraron que los valores de t^2 obtenidos a partir de la comparación de temperaturas observadas no están relacionados con los t^2 calculados formalmente a partir de la ecuación (1.35). Esto se debe a que las suposiciones que facilitan la determinación del t^2 en los casos anteriores no son generalmente válidas, ya que la dependencia radial de la T_e no es la misma en los iones implicados (H^+ y O^{2+} ó He^+ y O^{2+}). Según Kingdon y Ferland (1995), dicha hipótesis puede proporcionar estimaciones razonables en nebulosas gaseosas con estrellas centrales más bien frías, tales como las regiones H II, mientras que en NPs, cuyas estrellas centrales tienen una mayor temperatura efectiva, los valores de t^2 resultarían ser estimaciones muy burdas.

Un camino para evitar el problema anterior en la estimación de t^2, es la comparación de temperaturas obtenidas a partir de cocientes de líneas de emisión de un mismo ion que se emitan desde niveles superiores con energías de excitación diferentes. Este es el caso de las líneas de estructura fina en el infrarrojo lejano y las líneas en el óptico de [O III]. Dinerstein et al. (1985) fueron los primeros en aplicar esta técnica, comparando las temperaturas calculadas a partir de los cocientes [O III] $\lambda5007/\lambda4363$ y [O III] $\lambda5007/52\mu$m. Sin embargo, este procedimiento también tiene dos grandes limitaciones: (1) es necesario tener una buena calibración en flujo relativa entre los rangos observados; y (2) es esencial utilizar aberturas con las mismas dimensiones, tanto en el espectro óptico como en el infrarrojo, con el fin de cerciorarnos de que estamos recibiendo el mismo flujo total y de los mismos volúmenes de la nebulosa.

Relación entre t^2 y DA

Suponiendo válida la propuesta de Torres-Peimbert et al. (1980), es decir, que el problema de la DA es consecuencia directa de la presencia de fluctuaciones de temperatura en el gas ionizado, tendríamos una relación directa entre el parámetro t^2 y el ADF. Peimbert y Costero (1969) expresaron formalmente dicha relación como:

$$\frac{X^{+i}}{\text{H}^+}^{LR} = \frac{X^{+i}}{\text{H}^+}_{t^2>0}^{LEC} = \frac{T_{\text{H}\beta}^{\alpha} T_{LEC}^{1/2}}{T_e([\text{O III}])^{\alpha+0.5}} \times e^{-\left(\frac{\Delta E}{kT_e([\text{O III}])} - \frac{\Delta E}{kT_{LEC}}\right)} \times \frac{X^{+i}}{\text{H}^+}_{t^2=0}^{LEC}, \qquad (1.42)$$

donde $T_{\text{H}\beta}$ es la temperatura para Hβ cuya potencia es $\alpha = -0.827$ según la definición (1.38), ΔE y T_{LEC} son la energía de excitación y la temperatura específica –definida por la ecuación (1.37)– de la LEC utilizada en el cálculo de la abundancia, respectivamente. A partir de la relación anterior, podemos obtener los valores de t^2 y T_0 que hacen que la abundancia iónica calculada a partir de LECs y LRs sea la misma. Suponiendo nebulosas químicamente homogéneas, nótese que la ecuación anterior también puede ser utilizada para el cálculo de abundancias químicas a partir de LECs con $t^2 > 0$, donde el parámetro

t^2 provendría de la comparación entre temperaturas, comentada en la sección previa (*e.g.* Peimbert et al. 2000, 2004, 2005).

Un argumento a favor de la relación entre la DA y la presencia de fluctuaciones de temperatura resultaría de la coincidencia entre los valores de t^2 deducidos a partir de la comparación de temperaturas y la comparación de abundancias. Torres-Peimbert y Peimbert (2003) encontraron que hay un buen acuerdo entre ambos tipos de valores de t^2 en tres de las NPs con mayores fluctuaciones de temperatura disponibles hasta esa fecha en la literatura. Dentro de los posibles errores, Peimbert (2003) también encuentra valores similares de t^2 a partir de la comparación de temperaturas –calculadas a partir del salto de Balmer y la combinación de los cocientes clásicos de las LECs de [N II] y [O III]– y la comparación de las abundancias de varios iones (O^+, O^{2+} y C^{2+}) en el análisis químico de la región extragaláctica 30 Doradus. Por contra, en un estudio paralelo de la misma región H II, Tsamis et al. (2003b) llegan a la conclusión de que los valores del parámetro t^2 determinados a partir de la comparación de temperaturas, en la forma propuesta por Peimbert (1967), no son suficientes para explicar la DA observada en este objeto (ver §1.6.2).

Si las fluctuaciones en la distribución espacial de temperaturas de las nebulosas gaseosas son el origen de la DA, el factor que la cuantifica, el ADF, debería presentar un determinado comportamiento respecto a las propiedades locales del gas ionizado y las características atómicas de los niveles de energía de los iones involucrados en la emisión. García-Rojas y Esteban (2007) han explorado estas correlaciones utilizando la muestra más amplia de valores de ADF(O^{2+}) obtenida hasta ahora en regiones H II, concluyendo que sus resultados parecen ser más consistentes con las predicciones del paradigma de las fluctuaciones de temperatura frente a las predicciones de los modelos químicamente inhomogéneos que describiremos en la siguiente sección.

Por definición, dentro del formalismo de las fluctuaciones de temperatura, el ADF debe estar relacionado con la energía de excitación, E_{ex}, del nivel superior del cual parte la línea de emisión, así como con la densidad crítica, $n_{i,c}$, de dicho nivel energético. En NPs, los estudios llevados a cabo por Liu et al. (2000, 2001), en los que se comparan las abundancias químicas de un mismo ion deteminadas a partir de LECs en distintos rangos espectrales (UV, óptico e infrarrojo lejano) muestran que el ADF no está relacionado con la E_{ex}, o la $n_{i,c}$. En cambio, el análisis presentado por García-Rojas y Esteban (2007) muestra ligeras correlaciones entre dichos parámetros con coeficientes de correlación $r = 0.7$. En la misma línea, la presencia de fluctuaciones de temperatura también predice que el ADF debe estar relacionado con la diferencia entre las temperaturas T_e([O III]) y T_e(Bac) (Peimbert y Costero 1969; Torres-Peimbert et al. 1980). En la figura 1.3 se muestran los ajustes lineales que relacionan el ADF(O^{2+}) y dicha diferencia obtenidos para NPs (Liu et al. 2001) y regiones H II (García-Rojas y Esteban 2007). En los datos de NPs, Liu et al. (2001) encuentra una fuerte correlación con un coeficiente $r = 0.95$ en el ajuste que no puede ser explicada por el paradigma de las fluctuaciones de temperatura. Ante esta correlación, Ferland (2003) señala que si los errores determinados para los valores de ADF(O^{2+}) de las NPs son representativos de las nebulosas gaseosas, entonces no estamos entendiendo la física del gas ionizado. En el caso de las regiones H II, la correlación entre dichas variables presenta una menor pendiente y un coeficiente de correlación $r = 0.58$. Contrariamente a lo que ocurre en NPs, García-Rojas y Esteban (2007) argumentan que la relación encontrada en regiones H II parece ser consistente con la hipótesis de las fluctuaciones de temperatura,

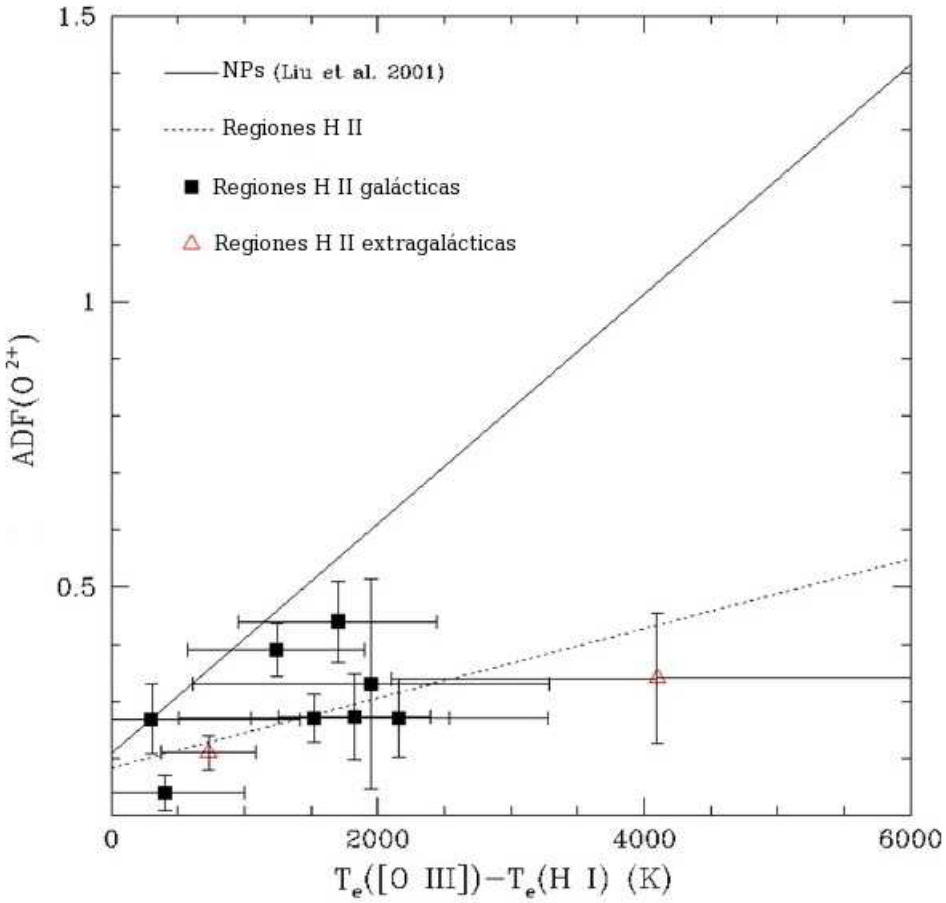

Figura 1.3: Correlación entre el ADF(O^{2+}) y la diferencia de temperaturas T_e([O III])−T_e(Bac). La línea discontinua corresponde al ajuste de los ADF(O^{2+}) encontrados en regiones H II, mientras que la línea continua representa el ajuste para NPs. Figura adaptada de García-Rojas y Esteban (2007).

que se traduce en valores similares y moderados del parámetro t^2, sin llegar a alcanzar los valores extremos encontrados en NPs. Otra correlación importante es aquella que se puede establecer en NPs entre el ADF(O^{2+}) y la n_e, según los resultados de Robertson-Tessi y Garnett (2005), mientras que en regiones H II no se observa (García-Rojas y Esteban 2007). Todos estos resultados han llevado a sugerir a García-Rojas y Esteban (2007) que la DA puede tener un origen distinto en las regiones H II y las NPs.

Origen de las fluctuaciones de temperatura

A pesar de que los procedimientos descritos a lo largo de esta sección permiten cuantificar las fluctuaciones de temperatura y considerando además los resultados positivos en favor de esta teoría –al menos en regiones H II– encontrados por García-Rojas y Esteban (2007), la existencia y origen de dichas fluctuaciones es, hoy por hoy, un campo todavía controvertido (ver revisiones de Esteban 2002; Liu 2002; Ferland 2003; Torres-Peimbert y Peimbert 2003;

Peimbert y Peimbert 2006; Liu 2006). A todo ello, se suma también uno de los principales problemas a los que se enfrenta el paradigma de las fluctuaciones de temperatura: la inconsistencia encontrada entre los t^2 teóricos y observacionales. Mientras que los valores del parámetro t^2 calculados en una amplia muestra de nebulosas gasesosas, son relativamente grandes, los modelos de fotoionización para nebulosas químicamente homogéneas predicen pequeñas fluctuaciones de temperatura en el rango $0.002 \leq t^2 \leq 0.03$, con un valor típico en torno a 0.005 (Gruenwald y Viegas 1992; Kingdon y Ferland 1995; Pérez 1997). Dados estos valores, parece muy razonable suponer la ausencia de fluctuaciones de temperatura, $t^2 = 0$, en el cálculo de las abundancias químicas a partir de LECs. Con el objetivo de explicar las diferencias encontradas entre la teoría y la observación y, consecuentemente, el origen de las fluctuaciones de temperatura, muchos autores han recurrido a la presencia de mecanismos físicos alternativos a la fotoionización. A continuación, expondremos los principales mecanismos considerados hasta la fecha.

- **Inhomogeneidades químicas**. Torres-Peimbert et al. (1990) fueron los primeros en proponer que la presencia de inhomogeneidades químicas podría explicar el origen de las fluctuaciones de temperatura en NPs. Estos autores encontraron que, suponiendo una zona interna rica en carbono en la NP NGC 4361, las abundancias obtenidas a partir de LECs coincidían con las determinadas a partir de LRs. Diferentes autores han presentado nuevos modelos químicamente inhomogéneos de nebulosas gaseosas para estudiar el origen de las fluctuaciones de temperatura. Por su parte, los resultados de los modelos calculados por Kingdon y Ferland (1998) sugieren que, aunque las inhomogeneidades químicas pueden producir sesgos despreciables en las determinaciones de las abundancias de algunos objetos, es muy poco probable que puedan resolver las discrepancias observadas en la mayoría de las nebulosas entre las fluctuaciones de temperatura observadas y las teóricas.

- **Deposición de energía mecánica**. Algunos autores han propuesto la deposición de energía mecánica por choques como fuente extra de calentamiento de las nebulosas y, a su vez, mecanismo de producción de fluctuaciones de temperatura. A partir de modelos compuestos por choques y fotoionización, Peimbert et al. (1991) exploraron el efecto de la presencia de choques sobre la estructura de temperaturas en las nebulosas gaseosas. Dichos autores concluyeron que podrían originarse grandes fluctuaciones de temperatura en regiones H II que contengan remanentes de supernova. El efecto neto de los choques aumentaría significativamente el flujo de las líneas aurorales utilizadas en el cálculo de la temperatura, más concretamente la línea [O III] 4363 Å, mientras que las líneas nebulares no se verían afectadas. Ello implicaría una sobreestimación de la T_e y, por tanto, una subestimación en las abundancias obtenidas a partir de LECs.

  Las estrellas centrales de las NPs depositan energía mecánica en las capas en expansión por medio de los vientos estelares, los flujos bipolares o multipolares y las eyecciones asimétricas. Todo ello contribuye a la generación de choques, turbulencia y un aumento de la velocidad de expansión de las capas externas. Estos procesos están más presentes en unas NPs que en otras y, por tanto, podrían dar cuenta del amplio rango de valores de t^2 que se observa en estos objetos. En algunas NPs hay

evidencias de que la presencia de choques puede afectar a las propiedades espectrales de las mismas. Peimbert et al. (1995) encontraron que las NPs bipolares tipo I de su muestra, donde se determinaban las mayores fluctuaciones en la temperatura, mostraban complejos movimientos de gas, con velocidades que podían superar los 100 km s^{-1}, corroborando la presencia de ondas de choque. Por su parte, Guerrero et al. (2005) observaron que algunas NPs emiten fuertemente en rayos X, y concluyeron que dicha emisión provendría de la excitación por choques producida por vientos estelares supersónicos.

Para las regiones H II, Peimbert (1995) sugirió que los vientos de las estrellas ionizantes inyectan energía mecánica al gas ionizado mediante choques y turbulencias subsónicas. En este sentido, utilizando modelos de síntesis evolutivos para la región H II gigante NGC 2363, Luridiana et al. (2001) compararon la tasa de energía cinética inyectada por vientos estelares con la luminosidad necesaria para reproducir los valores del parámetro t^2 observados. Los autores concluyen, incluso en el caso más favorable, que la luminosidad asociada al viento es más pequeña que la necesaria para obtener las fluctuaciones de temperatura observadas.

Si el problema de la DA está directamente relacionado con las fluctuaciones de temperatura, y estas, a su vez, se originan por la deposición de energía por medio de choques, una de las manifestaciones más claras de la presencia de dichos choques es el ensanchamiento de las líneas de emisión debido a la aparición de diferentes componentes cinemáticas. García-Rojas y Esteban (2007) estudiaron este efecto con la mayor muestra de regiones H II observadas hasta el momento, buscando correlaciones entre el ADF(O^{2+}) y las anchuras a media altura de diferentes líneas de emisión, pero sin encontrar claras relaciones entre las variables. En cambio, en la NP NGC 4361 la correlación encontrada por Liu (1998) entre la variación espacial de la T_e([O III]) y la velocidad radial y anchura a media altura de la línea He II 4686 Å, puede dar cuenta de los efectos de los choques.

- **Condensaciones de alta densidad**. Viegas y Clegg (1994) propusieron que los efectos de desexcitación colisional podrían ser relevantes en las líneas nebulares de [O III] bajo la presencia de condensaciones con densidades mayores a la densidad crítica de dichas líneas ($\sim 7\times10^5$ cm^{-3}) mientras que, en la mismas condiciones, la línea auroral [O III] 4363 Å no se vería afectada por las colisiones, ya que tiene una densidad crítica mucho mayor ($\sim 2.5\times10^7$ cm^{-3}). Con ello, la T_e([O III]) se sobreestimaría y, por tanto, las abundancias de O^{2+} a partir de LECs resultarían subestimadas. Uno de los caminos propuestos por los autores para detectar las condensaciones de alta densidad, es a través del uso de indicadores de densidad que involucran cocientes de líneas con densidades críticas altas, como [O II] λ7325/λ3727 ó [S II] λ4079/λ6725, y su comparación con los clásicos cocientes sensibles a la densidad (*e.g.* [S II] λ6731/λ6717).

  Varios autores han llevado a cabo diversos trabajos con el objetivo de detectar la presencia de condensaciones de alta densidad en NPs. A partir de imágenes con el telescopio espacial Hubble, Torres-Peimbert et al. (1997) encontraron que la NP M 2-29 presentaba dos componentes en densidad: por un lado, una de baja densidad ($\sim 10^4$ cm^{-3}) y menor temperatura a la determinada desde telescopios terrestres; y,

por otro lado, otra componente mucho más densa ($\sim 10^6$ cm^{-3}). Por su parte, Mathis et al. (1998) compilaron datos de las diez NPs con mayores ADFs, con el objetivo de encontrar evidencias de dichas condensaciones aplicando los diagnósticos propuestos por Viegas y Clegg (1994); pero no encontraron ninguna evidencia que ratificara la existencia de tales grumos. Liu (1998) también llevó a cabo un estudio similar al anterior, nuevamente con resultados negativos. Por otra parte, Liu et al. (2000) sugirieron el uso de los diagnósticos de densidad basados en las líneas de infrarrojo lejano, que tienen densidades críticas bajas, y su comparación con indicadores de densidad que hagan uso de líneas con densidades críticas altas (*e.g.* [Cl III] λ5537/λ5517 o [Ar IV] λ4740/λ4711). Utilizando estos diagnósticos se ha verificado la presencia de condensaciones muy densas en varias NPs (Liu et al. 2000, 2001). Las imágenes presentadas por Liu et al. (2000) de la NP NGC 6153, obtenidas con el telescopio espacial, muestran la existencia de muchos filamentos y grumos de material que han colisionado con el viento estelar de la estrella central.

En el campo de las regiones H II, y a partir de observaciones con el telescopio espacial, Walsh y Rosa (1999) encontraron un amplio rango de variación de las condiciones físicas del gas ionizado de la Nebulosa de Orión. Dichas variaciones estaban asociadas con la presencia de discos protoplanetarios, o *proplyds*[3], y filamentos embebidos dentro de la región H II. Los autores concluyen que este tipo de objetos podrían explicar las fluctuaciones de temperatura encontradas en la Nebulosa de Orión, en la forma propuesta por Viegas y Clegg (1994). Por otra parte, Peimbert (1995) afirma que, aunque la Nebulosa de Orión tiene regiones con densidades del orden de $\sim 10^6$ cm^{-3}, dichas zonas presentan bajo grado de ionización y, por tanto, la distribución espacial de temperaturas calculada a partir de las líneas de [O III] no se vería afectada.

- **Frentes de conducción**. Maciejewski et al. (1996) han sido los únicos que han estudiado los efectos de la contribución de los frentes de conducción en los espectros nebulares. Dichos frentes se localizan en la capa de transición conductiva entre el plasma visible y el gas calentado mediante choques por el viento estelar. El efecto de estos frentes es cualitativamente similar al producido por los choques sobre la línea auroral de [O III] utilizada en el cálculo de la temperatura. Los autores aplican su modelo a la Nebulosa de Orión, observando que este mecanismo, aunque predice un aumento en el flujo de la línea [O III] 4363 Å, no es suficiente para conseguir explicar el t^2 observado en esta región.

- **Calentamiento por la presencia de polvo**. Stasińska y Szczerba (2001) modelizaron los efectos del calentamiento fotoeléctrico del gas debido a la fotoionización de granos de polvo en NPs. Los autores encontraron que este proceso es especialmente importante en NPs ricas en filamentos, que además contienen una cantidad apreciable de granos de polvo. La estructura de temperaturas de este tipo particular de NPs estaría afectada por grandes variaciones de temperatura, sobre todo en las zonas más cercanas a la estrella central. En el supuesto caso de que una NP presente una

[3]Término que surge de la palabra inglesa *protoplanetary disks*. Este fue acuñado por O'Dell y Wen (1994) para referirse a las estrellas jóvenes observadas con el telescopio espacial Hubble que presentaban material circumestelar alrededor de ellas.

distribución de densidad inhomogénea, la fluctuación del parámetro de ionización inducida por la variación en densidad generaría fluctuaciones de temperatura debido al diferente calentamiento que sufren los granos de polvo y el hidrógeno.

Nuevamente, considerando la relación unívoca entre la DA y las fluctuaciones de temperatura, una vía para explorar la influencia de este proceso en la generación de fluctuaciones de temperatura es buscar correlaciones entre el ADF y las temperaturas efectivas de las estrellas ionizantes de las nebulosas. En NPs dicha correlación ha sido estudiada por Robertson-Tessi y Garnett (2005), sin ningún resultado positivo. García-Rojas y Esteban (2007) también han explorado esta posibilidad en regiones H II, llegando a la misma conclusión que en NPs: no se encuentra correlación entre el ADF y las temperaturas efectivas de las estrellas ionizantes. Sin embargo, en el caso de las regiones H II este estudio es algo más complicado, ya que dichas regiones generalmente son ionizadas por asociaciones de estrellas OB.

- **Reconexión magnética**. Ferland (2001) propuso que la reconexión magnética podría proporcionar variaciones en la estructura de temperaturas del plasma ionizado. La hipótesis descrita por este autor considera que una fracción del campo magnético del gas se destruye por la reconexión de líneas de campo magnético, suministrando la energía adicional necesaria para explicar las fluctuaciones de temperatura observadas. Ferland (2009) cita algunas referencias sobre la detección de campos magnéticos en nebulosas gaseosas. Abel et al. (2004) detectaron campos magnéticos del orden de 100μG en el velo de hidrógeno neutro localizado entre nosotros y las principales estrellas ionizantes de la Nebulosa de Orión. Por otra parte, Torres-Peimbert y Peimbert (2003) citan varias NPs en la que se han medido, e inferido, campos magnéticos del orden de mG. Aunque es sin duda una hipótesis interesante, hoy por hoy siguen sin existir modelos detallados que relacionen las fluctuaciones de temperatura con la reconexión magnética.

- **Variabilidad de la fuente ionizante**. Partiendo de la base de que las fluctuaciones de temperatura no pueden ser reproducidas mediante modelos de fotoionización en equilibrio y estacionarios en el tiempo, Binette et al. (2003) propusieron que la variabilidad de la fuente ionizante podría dar como resultado fluctuaciones de temperatura. Para ello, los autores investigaron la respuesta temporal de la estructura de ionización y de temperatura de una nebulosa fotoionizada por una fuente variable con un cierto periodo, así como el comportamiento del valor promedio de t^2 en función del periodo y la amplitud de las variaciones de flujo que experimenta la fuente ionizante. El análisis concluye que la amplitud de variación debería ser demasiado grande para alcanzar valores del parámetro t^2 similares a los observados y, por tanto, la variabilidad de la fuente ionizante no es un mecanismo viable para explicar los t^2 observados.

  Por otro lado, es bien conocido que los flujos ionizantes de las estrellas centrales de NPs no son constantes en el tiempo. Más concretamente, este efecto es más importante en las NPs producidas por las estrellas de masa intermedia, debido a que estas evolucionan relativamente rápido (Torres-Peimbert y Peimbert 2003). Un posible ejemplo de este mecanismo podría ser la nebulosa N66, en la pequeña Nube de Magallanes, donde el flujo ionizante ha disminuido un factor dos en un periodo de

casi diez años (Torres-Peimbert y Peimbert 2003, y las referencias que allí se citan).

- **Zonas con diferente grado de ionización**. Mathis (1976) sugirió la existencia de regiones en sombra en el interior de las nebulosas con el objetivo de explicar los flujos de líneas emitidas por iones con bajo potencial de ionización. Estas regiones estarían en sombra porque la radiación ionizante de la estrella central no incide directamente sobre ellas, siendo ionizadas por la radiación difusa. Consecuentemente, dichas zonas presentan un menor grado de ionización y una temperatura algunos miles de grados menor que la del material directamente ionizado por la estrella central. La presencia de regiones en sombra como único mecanismo generador de fluctuaciones de temperatura, produce valores para t^2 del orden de 0.01 en NPs similares a NGC 7293 y NGC 6720. La presencia de glóbulos moleculares ha sido confirmada en estas últimas nebulosas y, por ello, se espera que la presencia de este tipo de glóbulos sea normal en una amplia mayoría de nebulosas. De acuerdo con los resultados de Huggins y Frank (2006), los glóbulos moleculares en NGC 7293 mantienen en sombra un 5% del volumen de la nebulosa.

  En la línea de la presencia de zonas embedidas en las nebulosas con diferente grado de ionización, Giammanco y Beckman (2005) han propuesto que la mayor parte del hidrógeno que forma las regiones H II no está fotoionizado por la fuente central y se mantiene en estado neutro. Este modelo está compuesto por dos fases: la primera, llamada fase caliente, representa al gas ionizado normal de las nebulosas, y está siendo directamente ionizada por la estrella central; mientras que la otra componente, denominada fase fría, está compuesta por el hidrógeno neutro y puede ser ionizada por rayos cósmicos de baja energía, emitidos también por la fuente central. Esta nueva hipótesis es aplicada por los autores en las regiones analizadas por Esteban et al. (2002), concluyendo que se reproduce el orden de magnitud de los valores de t^2 observados en esas regiones. Sin embargo, Zhang et al. (2005) han revisado este modelo de dos fases, concluyendo que la tasa de rayos cósmicos que pueden ionizar el hidrógeno neutro está sobrestimada debido a la discrepancia que encuentran entre los t^2 recalculados por ellos mismos y los valores de t^2 obtenidos por Giammanco y Beckman (2005). Según Zhang et al. (2005), las elevadas diferencias de temperaturas entre las dos fases del modelo de Giammanco y Beckman sugieren que los valores de t^2 y T_0 hallados por Esteban et al. (2002) no son aplicables directamente a los modelos de dos fases.

1.6.2 Inhomogeneidades en la composición química

La propuesta realizada por Torres-Peimbert et al. (1990) sobre la existencia de inhomogeneidades químicas embebidas en el gas ionizado de las NPs para explicar el origen de las fluctuaciones de temperatura, junto con el conocimiento previo de que contadas NPs contenían grumos internos deficientes en hidrógeno con una fuerte emisión en LRs de elementos pesados (*e.g.* Abell 30, Harrington y Feibelman 1984), llevó a Liu et al. (2000) a proponer una nueva hipótesis alternativa a la existencia de fluctuaciones de temperatura para explicar el problema de la DA.

En el análisis de la NP NGC 6153, Liu et al. (2000) concluyen que las fluctuaciones

de temperatura no son suficientes para dar cuenta de la DA encontrada. Estos autores presentan una nueva propuesta basada en modelos empíricos químicamente inhomógeneos. Estos modelos se sustentan en el hecho observacional de que las densidades electrónicas, determinadas a partir de las LECs con densidades críticas bajas del infrarrojo lejano, [O III] 88-μm y 52-μm, son en torno a un factor 2 más pequeñas que las densidades electrónicas que se obtienen a partir de los cocientes de LECs en el óptico, [Ar IV] λ4740/λ4711 y [Cl III] λ5537/λ5517. Más aún, para un gran número de NPs observadas con el instrumento *LWS* (acrónimo de *Long Wavelength Spectrometer*), del telescopio espacial *ISO* (acrónimo de *Infrared Space Observatory*), Liu (1997) encuentra resultados similares: para una misma NP, las densidades calculadas a partir del cociente [O III] 88 μm/52 μm son sistemáticamente menores a las determinadas a partir de los cocientes de las líneas de [Ar IV] y [Cl III].

El mejor acuerdo encontrado entre los resultados observacionales y los resultados extraídos de los diferentes modelos empíricos propuestos por Liu et al. se obtiene para un escenario donde el gas está compuesto por dos componentes, o fases, con condiciones físicas bien diferenciadas. Por un lado, la primera componente se correspondería con el gas ionizado que presenta las condiciones físicas observadas a partir de los diagnósticos clásicos basados en LECs. Por otro lado, la otra componente está formada por grumos, embebidos en el gas ionizado normal, deficientes en hidrógeno y, por tanto, con una metalicidad mayor que la fase normal, más fríos y mucho más densos. Dichos grumos son los que producirían principalmente la emisión de LRs, mientras la mayor parte de la emisión de LECs provendría de la componente menos metálica. Por tanto, bajo la visión de este nuevo paradigma, las abundancias químicas representativas del gas ionizado corresponderían a las determinadas a partir del análisis clásico basado en LECs.

A pesar de que la propuesta de Liu et al. explica razonablemente la DA observada en NPs, el problema que presenta esta nueva hipótesis es que el origen de los grumos es incierto, dado que su composición química descarta que puedan formarse a partir de las eyecciones de material que sufren la estrellas progenitoras de NPs (Liu et al. 2000; Ercolano et al. 2004; Wesson et al. 2005; García-Rojas et al. 2009). La única sugerencia aportada hasta hoy día, para explicar la naturaleza de los grumos deficientes en hidrógeno, es la evaporación de cuerpos sólidos (tales como asteroides, cometas y planetas) que pertenecían al sistema planetario de la estrella progenitora (Liu 2003). Sin embargo, muy recientemente, Henney y Stasińska (2010) han llevado a cabo un minucioso análisis de las implicaciones de esta propuesta, concluyendo que la destrucción de cuerpos sólidos no puede explicar la DA observada en NPs. Aunque una población suficiente de cuerpos sólidos pudiera encontrarse en torno a las estrellas centrales de NPs, los autores calculan que la tasa de astillamiento de estos objetos es muy baja para llegar a extraer algo más que una pequeña fracción de sus masas durante el tiempo de vida de las NPs. Por contra, parece que la evaporación de cuerpos volátiles durante las fases finales que preceden a la etapa de AGB de las estrellas progenitoras podría proporcionar la cantidad necesaria de material en forma de gas con una alta metalicidad para explicar la DA, aunque esto únicamente ocurriría si la mezcla de material es ineficiente y la población de cometas en los sistemas planetarios de las estrellas progenitoras es mucho mayor a la que tenemos en nuestro sistema solar.

La presencia de inhomogeneidades químicas también ha sido postulada recientemente para el caso de las regiones H II. Tsamis et al. (2003b) consideran que la DA en regiones H II no puede ser debida a las fluctuaciones de temperatura, apoyándose en el hecho de que

las abundancias de O^{2+} obtenidas a partir de las LECs de estructura fina en el infrarrojo, son similares a las calculadas a partir de las LECs en el óptico y, por tanto, inferiores a las determinadas a partir de LRs. Bajo los postulados del paradigma de las fluctuaciones de temperatura, se esperaría que las líneas en el infrarrojo y las LRs del mismo ion proporcionen abundancias químicas similares, dado que ambos tipos de línea presentan una dependencia del mismo orden con la temperatura. Tsamis et al. (2003b) llegan a la conclusión de que la resolución del problema de la DA requiere la existencia de una componente rica en metales, menos densa y más fría que la componente de gas nebular normal. Los autores señalan que las bajas temperaturas –del orden de unos cientos de grados– de esta nueva componente ionizada, donde predomina la emisión de LRs, es la única forma de suprimir colectivamente la emisión de LECs –tanto la emisión en el óptico como la emisión de líneas en el infrarrojo–. Sin embargo, esta nueva propuesta necesita la existencia de una componente no observada hasta hoy día en ninguna región H II.

Posteriormente, y basándose en la idea propuesta por Tsamis et al., Tsamis y Péquignot (2005) desarrollaron modelos de fotoionización para la región extragaláctica 30 Doradus, ajustando toda la información espectroscópica disponible para este objeto desde el UV a las ondas de radio. Los resultados de estos autores favorecen un modelo de dos fases, que incorpora inhomogeneidades químicas a pequeña escala en forma de grumos deficientes en hidrógeno, más frios y densos, embebidos en el gas ionizado con la composición química típica de 30 Doradus. Los grumos están distribuidos uniformente, y se encuentran en equilibrio de presión con el gas de ambiente que los rodea. Según las estimaciones de los autores, estos grumos representan un 2% de la masa nebular de 30 Doradus y emiten cerca de un 8% del flujo total de Hβ. En cuanto a su composición química, los grumos presentan abundancias de helio relativas al hidrógeno normales con respecto al gas de ambiente, mientras que las abundancias de otros elementos para los cuales había información disponible (C, N, O, Ne, S y Ar), son un orden de magnitud mayores que las del gas nebular. Más tarde, Stasińska et al. (2007) generalizaron el modelo de Tsamis y Péquignot (2005) para cualquier región H II.

Este nuevo escenario para explicar la DA propone como origen de los grumos pobres en hidrógeno el modelo químico para la mezcla de elementos pesados de Tenorio-Tagle (1996). Según este modelo, las supernovas de tipo II que se originan dentro de asociaciones de estrellas OB expulsan material rico en metales al medio interestelar. Tras un largo tiempo en la fase coronal caliente ($T \geq 10^6$ K) del medio interestelar, tarde o temprano este material vuelve a caer sobre el disco galáctico, en forma de lluvia de grumos fríos y densos, con un tamaño típico de $\sim 10^{17}$ cm. Estos grumos se irán incorporando paulatinamente al contenido de hidrógeno atómico y molecular del disco –sin un proceso de mezcla eficiente– hasta la próxima generación de estrellas masivas que fotoionicen el gas y completen la mezcla de elementos pesados. Según Tenorio-Tagle (1996), la homogeneidad química del disco galáctico no se alcanza de forma instantánea después de un evento explosivo de supernova, pero sí se consigue después del nacimiento de la siguiente generación de estrellas. Bajo esta hipótesis, la propuesta de Tsamis y Péquignot (2005) y Stasińska et al. (2007) presenta dos componentes, o fases gaseosas, bien diferenciadas en composición química y condiciones físicas en las regiones H II. La componente responsable de la mayor parte de la emisión de LRs estaría compuesta por los grumos ricos en metales, resultado de las eyecciones de supernova y aún no mezclados con el gas de ambiente de las regiones H II, de donde

provendría la mayor parte de la emisión de LECs. Bajo esta nueva visión del problema de la DA, las abundancias obtenidas a partir de LECs y LRs representarían únicamente límites inferiores y superiores, respectivamente, de la abundancia real del gas ionizado de la región H II.

Del modelo de dos fases para regiones H II es destacable que proporciona una explicación natural a la DA, sin recurrir a mecanismos alternativos a la fotoionización. Sin embargo, López-Sánchez et al. (2007) y García-Rojas y Esteban (2007) han presentado diversas objeciones en contra de este modelo a partir del análisis de la más amplia muestra de ADFs obtenida en regiones H II. Para todos los objetos analizados, galácticos y extragalácticos, los valores del ADF(O^{2+}) son muy similares entre sí y, también, similares a los ADFs obtenidos para otros iones (C^{2+}, O^{+} y Ne^{2+}). Dada la homogeneidad de los valores del ADF en las regiones H II extragalácticas, parece que el ADF no muestra dependencias con el tipo morfológico, la masa, la metalicidad, o incluso la historia de formación estelar de la galaxia. En el caso de los ADFs encontrados en las regiones H II galácticas, la homogeneidad sugiere que el proceso que genera la DA es independiente de las condiciones y propiedades del disco galáctico, al menos en el rango de distancias galactocéntricas estudiadas por los autores. Otro de los puntos importantes que discuten García-Rojas y Esteban (2007) es el acuerdo aparente entre las abundancias calculadas a partir de LECs en el óptico e infrarrojo lejano, el cual es la base de partida del modelo de dos fases propuesto por Tsamis et al. (2003b). En el caso de las NPs, los autores creen que la comparación (aunque puede estar sujeta a los problemas planteados por Kingdon & Ferland 1995 y comentados en la sección §1.6.1) es plausible en este tipo de objetos, debido a su pequeño tamaño angular, tanto en el rango óptico como en el UV e infrarrojo. En cambio, dicha comparación no es tan factible para las regiones H II galácticas. Estos objetos son muy extensos y cubren mayores áreas sobre el cielo que las NPs, por lo que pueden surgir incertidumbres debidas a la estratificación de los iones, cuando comparamos abundancias iónicas calculadas a partir de las estrechas rendijas utilizadas en la espectroscopia óptica y las observaciones en el infrarrojo lejano, que hacen uso de telescopios espaciales con mayores aberturas. García-Rojas et al. (2006) muestran las dificultadas encontradas a la hora de comparar las abundancias totales de su muestra de regiones H II, obtenidas a partir de espectroscopia en el óptico, con las mismas determinadas a partir de las observaciones en el infrarrojo realizadas por Simpson et al. (1995).

1.6.3 Zonas con diferente grado de ionización en las nebulosas

Recientemente, Ercolano (2009) ha propuesto una hipótesis alternativa a las expuestas hasta ahora para explicar el problema de la DA en regiones H II. Bajo este nuevo paradigma, la DA es debida a la existencia de grumos y/o filamentos cuasi-neutros, y muy densos ($n_e \geq 10^4$ cm^{-3}), que están siendo ionizados por rayos X procedentes de la estrella central. Estos grumos están embebidos en el gas nebular, que está siendo ionizado por la radiación UV de la misma estrella central, y posee una densidad menor ($\leq 10^3$ cm^{-3}). Nuevamente, nos encontramos con un modelo de dos fases: por un lado, la denominada por la autora fase X, que está formada por los grumos y/o filamentos; y, por otro lado, la llamada fase E, compuesta por el gas nebular. Sin embargo, la principal diferencia de esta propuesta con los anteriores modelos de dos fases, es que el medio interestelar es químicamente homogéneo.

En la sugerencia de Ercolano (2009), la mayor parte de la emisión de LECs provendría de la fase E, mientras las LRs son emitidas en diferentes proporciones en la fase X y E. En este sentido, las abundancias que podemos determinar a partir de los distintos tipos de líneas de emisión nunca coincidirán con las reales del gas ionizado, aunque las abundancias químicas que podemos inferir a partir de LECs son bastante más fáciles de corregir que las mismas a partir de LRs, siguiendo el procedimiento propuesto por la autora en su artículo. Básicamente, este procedimiento trata de resolver cuál es la contribución de emisión de LRs que hay en la fase X respecto a la E.

Parte de la idea de Ercolano (2009) se basa en uno de los principales resultados presentado en esta tesis. Concretamente en el análisis de las distribuciones espaciales de la Nebulosa de Orión (§2), donde hemos encontrado que el ADF(O^{2+}) aumenta en las posiciones de los objetos Herbig-Haro cubiertos por nuestras posiciones de rendija. En el marco del modelo de fases X-E, el aumento que experimenta el ADF(O^{2+}) en esas posiciones es debido a los rayos X que inciden sobre el material neutro frío, y son emitidos por los frentes de choque que generan los objetos Herbig-Haro. De acuerdo con este modelo, Ercolano (2009) también destaca los aumentos de ADF(O^{2+}) que hemos encontrado en el mismo estudio en las cercanías de θ^1Ori C, la cual emite casi un 60% del flujo total en rayos X del cúmulo del Trapecio.

Ercolano (2009) aplica esta nueva hipótesis a la Nebulosa de Orión, utilizando los resultados presentados por García-Rojas y Esteban (2007). La aplicación reproduce, simultáneamente, el ADF(O^{2+}) observado en esta nebulosa y la temperatura obtenida a partir del salto de Balmer. Sin embargo, el flujo de rayos X requerido para reproducir dichos valores es varios órdenes de magnitud mayor al observado en fuentes de rayos X difusas de la Nebulosa de Orión.

1.6.4 Incertidumbres en los parámetros atómicos

Constatada la ineficacia de los modelos de fotoionización para dar cuenta de la DA observada en las nebulosas gaseosas, algunos autores han sugerido que pueden existir errores importantes en los parámetros atómicos de los iones comúnmente utilizados, C^{2+} y O^{2+}.

A partir del análisis de modelos sencillos de regiones H II, Rodríguez y García-Rojas (2010) han encontrado que los valores observados de temperatura y la estructura de temperaturas medida a través del cociente T_e([N II])/T_e([O III]), se reproducen fácilmente cuando las metalicidades de entrada en los modelos coinciden con las abundancias determinadas a partir de LECs. En cambio, al introducir fluctuaciones de temperatura en los modelos, producidas por un mecanismo de calentamiento adicional arbitrario, el acuerdo anterior entre modelos y observaciones desaparece. Concretamente, los valores del cociente T_e([N II])/T_e([O III]) que se determinan a partir de los modelos son menores que los observados. Los autores concluyen que, dado el buen acuerdo encontrado entre los modelos simples y las observaciones, el efecto que puedan causar las posibles incertidumbres de los coeficientes de recombinación es una explicación plausible para el problema de la DA en regiones H II. Por contra, otros autores descartan esta posibilidad, ya que produciría los mismos valores de ADF en todos los objetos, tanto NPs como regiones H II. Rodríguez y García-Rojas (2010) señalan que si, además de los errores intrínsecos a la medida de las débiles LRs, los coeficientes de recombinación fueran subestimados por un factor del orden

de 1.5, los valores de ADF ≈ 0.30 dex, típicamente hallados en regiones H II y algunas NPs serían fácilmente explicados, y una explicación alternativa sería únicamente necesaria para las NPs con grandes ADFs.

Esteban (2002) argumenta que los parámetros atómicos de recombinación, al menos de los iones C^{2+} y O^{2+}, parecen estar bien determinados. Primero, no hay evidencias de mecanismos de excitación desconocidos que afecten a la emisión de las LRs de estos iones. Por otro lado, una prueba de la consistencia que hay entre las abundancias determinadas a partir de LRs y LECs, es que el valor promedio del cociente de C^{2+}/O^{2+} calculado a partir de LRs y a partir de LECs, es 1.2 ± 0.6 para un amplio número de objetos, independientemente de lo grande, o pequeño, que sea el valor de ADF que presenten. Una última comprobación es que las abundancias de un mismo ion a partir de las líneas que conforman un mismo multiplete, o a partir de las líneas de otros multipletes, concuerdan en las nebulosas gaseosas donde esto se ha determinado. Estas tres sencillas pruebas parecen indicar que el conocimiento que tenemos y aplicamos sobre la física de la líneas de recombinación es esencialmente correcto.

1.7 Objetivos de la tesis

Han pasado más de cuarenta años desde que Peimbert (1967) y Peimbert y Costero (1969) postularan la posible existencia de variaciones a pequeña escala en la distribución espacial de temperaturas de las nebulosas gaseosas y sus implicaciones sobre la determinación de abundancias químicas. Actualmente, el panorama no es más alentador debido a que la comprensión del problema de la DA es uno de los grandes desafíos de la física de las nebulosas gaseosas para el que aún no contamos con una explicación definitiva. Es importante señalar que el análisis basado en LECs es el método estándar para la determinación de abundancias en regiones H II y que buena parte de nuestro conocimiento de la composición y evolución química del universo extragaláctico proviene del mismo análisis. Por tanto, es esencial comprobar si el método estándar nos proporciona las abundancias correctas, saber si existen realmente fluctuaciones de temperatura y comprender cuáles son las causas que originan el renombrado problema de la DA.

En la presente tesis doctoral se ha propuesto realizar un estudio espectroscópico profundo en regiones H II galácticas brillantes y cercanas, a las menores escalas angulares posibles, con el fin de analizar y cuantificar la posible variación espacial de las condiciones físicas, y ahondar en la comprensión del fenómeno de la DA, a partir de tres aproximaciones observacionales:

- Observaciones espectroscópicas profundas de rendija larga y resolución espectral intermedia de las regiones H II galácticas M8, M17, NGC 7635 y la Nebulosa de Orión. La aplicación de esta técnica, relativamente extendida en los estudios de NPs, nos permitirá estudiar las distribuciones espaciales de un gran número de variables: perfiles de flujos de muchas líneas de emisión, entre las que se encontrarán las débiles LRs de O II y C II; el coeficiente de extinción; las temperaturas y densidades electrónicas del gas ionizado; las abundancias químicas de O^{2+} obtenidas a partir de LECs y LRs; y el ADF(O^{2+}). El muestreo de dichas variables se realizará a las escalas angulares más pequeñas posibles y accesibles desde telescopios terrestres, que además nos permitan

obtener una relación señal a ruido óptima para la detección y medida de las débiles LRs y las líneas aurorales para el cálculo de la temperatura electrónica. Otro punto importante que nos ofrece el análisis de las distribuciones espaciales es la búsqueda de correlaciones entre el ADF(O^{2+}), el resto de parámetros nebulares y las estructuras morfológicas (tales como discos protoplanetarios, objetos Herbig-Haro, frentes de ionización, glóbulos...) localizadas en los interiores de las regiones H II. Hay que tener presente que el trabajo realizado por Tsamis et al. (2003b), en la región 30 Doradus, es el único precedente en la aplicación de esta técnica en regiones H II; aunque la naturaleza extragaláctica de este objeto impone un límite de resolución angular y lineal mucho mayor que el que hemos utilizado en los trabajos que aquí presentamos.

- Observaciones espectroscópicas de campo integral o bidimensionales. Esta es una técnica que se está comenzando a explotar a la hora de estudiar el problema de la DA en nebulosas gaseosas. La espectroscopia de campo integral es tan eficiente como la comentada en el punto anterior, con el añadido de que permite obtener la información espectral de cada elemento espacial dentro del campo bidimensional de los parámetros nombrados anteriormente. Además, permite combinar la espectroscopia con la capacidad de obtener imágenes del campo a cualquier longitud de onda, a lo largo del rango espectral observado. En esta tesis, la espectrocopia de campo integral se ha utilizado en el análisis de las propiedades físicas y químicas del gas ionizado de estructuras localizadas en los interiores de las regiones H II. Concretamente, y en base a los resultados hallados a lo largo de la tesis, nos hemos centrado en el estudio de uno de los objetos Herbig-Haro (HH) más prominentes de la Nebulosa de Orión: el HH 202. Al inicio de esta tesis, el único trabajo disponible en la literatura que aplicara espectroscopia bidimensional en regiones H II era el de Sánchez et al. (2007), quienes construyeron un gran mapa centrado en la zona del Trapecio de la Nebulosa de Orión, aunque a escalas angulares de $2\farcs7$. Posteriormente, con el objetivo de estudiar la DA, Tsamis et al. (2008) y Tsamis et al. (2009) han sido los primeros en utilizar la espectroscopia de campo integral en tres NPs del disco galáctico y algunos discos protoplanetarios de la Nebulosa de Orión, respectivamente.

- Observaciones espectroscópicas *echelle* de muy alta resolución espectral y amplio rango espectral. La alta resolución espectral que nos permite alcanzar este tipo de observaciones hace posible la observación de diferentes componentes cinemáticas en el gas ionizado. Por ello, se han llevado a cabo este tipo de observaciones en el objeto HH 202 de la Nebulosa de Orión, con el objetivo de analizar las propiedades físicas y químicas, así como el problema de la DA, en las distintas componentes cinemáticas resueltas. Ello nos permite analizar los posibles efectos que pudiera producir la presencia de flujos de gas a alta velocidad sobre la DA.

2

Comportamiento a pequeña escala de las condiciones físicas y abundancias químicas en la Nebulosa de Orión

La primera parte de esta tesis se ocupa del estudio de las distribuciones espaciales de las propiedades físicoquímicas –y las correlaciones que entre ellas se pudieran encontrar– en cinco posiciones de rendija larga sobre la Nebulosa de Orión. Estas observaciones se obtuvieron con el telescopio William Herschel (WHT, acrónimo de *William Herschel Telescope*) de 4.2m de abertura, ubicado en el Observatorio del Roque de los Muchachos, y su instrumento ISIS (acrónimo de *Intermediate dispersion Spectrograph and Imaging System*). Las posiciones de rendija cubren diferentes estructuras morfológicas de la Nebulosa de Orión. Debido a su relativa cercanía y su alto brillo superficial, esta nebulosa es la región H II galáctica más estudiada y, por tanto, el objeto óptimo para el análisis que aquí se plantea. Por un lado, la cercanía ha permitido al telescopio espacial Hubble resolver una rica estructura a escalas espaciales por debajo de $0\farcs5$, tales como discos protoplanetarios, nuevos objetos Herbig-Haro, glóbulos, o frentes de choque que surgen de la interacción del viento estelar y los flujos de gas provenientes de los discos protoplanetarios. Por otro lado, el alto brillo superficial ayuda a obtener una relación señal a ruido satisfactoria en las líneas de emisión más débiles –típicamente las LRs de O II– utilizando telescopios de aberturas intermedias como el WHT (3 a 5 metros) y tiempos de exposición relativamente cortos.

En este primer estudio se desarrollaron nuevas tareas en IDL e IRAF que permitían agilizar el análisis del gran volumen de espectros que se pueden extraer a partir de las cinco posiciones de rendija observadas. Dichas tareas llevan a cabo la extracción de espectros unidimensionales, la medida del flujo de las líneas de emisión, la corrección de extinción y el cálculo de condiciones físicas y abundancias químicas, a partir de LECs y LRs. Estos procedimientos también son utilizados en la segunda y cuarta parte de la presente tesis (capítulos §3 y §5).

Esta primera parte de la tesis fue publicada en el artículo "Small-scale behavior of the physical conditions and the abundance discrepancy in the Orion Nebula" de la revista *The Astrophysical Journal*, Volumen 675, páginas 389 a 404, el cual se adjunta a continuación,

tras el resumen.

Resumen: Presentamos los resultados de espectroscopia de rendija larga en la Nebulosa de Orión. El principal objetivo es estudiar las distribuciones espaciales de un amplio número de parámetros nebulares, que incluyen flujos de líneas, condiciones físicas y abundancias iónicas, con una resolución espacial del orden de $1''$. En particular, hemos comparado las abundancias de O^{2+} determinadas a partir de líneas excitadas colisionalmente y líneas de recombinación en 671 espectros unidimensionales que cubren diferentes zonas de la nebulosa. Encontramos que los discos protoplanetarios muestran picos prominentes en la T_e([N II]), lo cual es debido probablemente a que las altas densidades electrónicas encontradas en estos objetos producen desexcitación colisional. Los objetos Herbig-Haro también muestran valores grandes en la T_e([N II]) pero, en este caso, es más probable que sean debidos al calentamiento local producido por la presencia de choques. Encontramos también que las distribuciones espaciales de las líneas de O II y [O III] son bastante parecidas. El factor de discrepancia de abundancias (ADF) de O^{2+} permanece básicamente constante a lo largo de las posiciones de rendija, salvo en algunas áreas localizadas de la nebulosa como las que contienen los objetos Herbig-Haro más prominentes. Aparentemente, también existe un ligero aumento del ADF en $40''$ en torno a θ^1Ori C. Además, el ADF de O^{2+} parece aumentar ligeramente con la temperatura electrónica. Finalmente, estimamos los valores de la fluctuación cuadrática media de la temperatura electrónica, el conocido parámetro t^2. Nuestros resultados indican que si las hipotéticas inhomogeneidades térmicas existen, estas deben ser más pequeñas que nuestro elemento de resolución espacial utilizado.

The Astrophysical Journal, 675:389–404, 2008 March 1

SMALL-SCALE BEHAVIOR OF THE PHYSICAL CONDITIONS AND THE ABUNDANCE DISCREPANCY IN THE ORION NEBULA[1]

Adal Mesa-Delgado, César Esteban, and Jorge García-Rojas[2]
Instituto de Astrofísica de Canarias, E-38200 La Laguna, Tenerife, Spain; amd@ll.iac.es, cel@ll.iac.es, jogarcia@ll.iac.es
Received 2007 August 20; accepted 2007 October 5

ABSTRACT

We present the results of long-slit spectroscopy, in several positions, of the Orion Nebula. Our goal is to study the spatial distributions of a large number of nebular quantities, including line fluxes, physical conditions, and ionic abundances, at a spatial resolution of about 1″. In particular, we have compared the O^{++} abundance determined from collisionally excited and recombination lines in 671 individual one-dimensional spectra covering different morphological zones of the nebula. We find that protoplanetary disks (proplyds) show prominent spikes of T_e([N II]), which is probably produced by collisional deexcitation due to the high electron densities found in these objects. Herbig-Haro objects show also relatively high values of T_e([N II]), but these are probably produced by local heating due to shocks. We also find that the spatial distribution of the pure recombination O II and [O III] lines is fairly similar. The abundance discrepancy factor (ADF) of O^{++} remains rather constant along the slit positions, except in some particular small areas of the nebula, such as at the locations of the most conspicuous Herbig-Haro objects. There is also an apparent slight increase of the ADF in the inner 40″ around θ^1 Ori C. We find a negative radial gradient of T_e([O III]) and T_e([N II]) in the nebula, based on the projected distance from θ^1 Ori C. In addition, the ADF of O^{++} seems to increase very slightly with the electron temperature. Finally, we estimate the value of the mean-square electron temperature fluctuation, the so-called t^2 parameter. Our results indicate that the hypothetical thermal inhomogeneities, if they exist, should be smaller than our spatial resolution element.

Subject headings: H II regions — ISM: abundances — ISM: individual (Orion Nebula)

1. INTRODUCTION

Analysis of the spectrum of H II regions makes it possible to determine the chemical composition of the ionized gas phase of the interstellar medium, from the solar neighborhood to the high-redshift universe. Therefore, this stands as an essential tool for our knowledge of the chemical evolution of the universe. In photoionized nebulae, the abundance of the elements heavier than He is usually determined from collisional excitation lines (CELs), whose intensity depends exponentially on the electron temperature, T_e, of the gas. It was about 20 years ago when the first determinations of the C^{++} abundance from the intensity of the weak recombination line (RL) of C II λ4267 were made available for planetary nebulae (PNs). The comparison of the abundance obtained from C II λ4267 and from the CELs of this ion in the ultraviolet (UV) showed a difference that could be as large as a order of magnitude in some objects (e.g., French 1983; Rola & Stasińska 1994; Mathis & Liu 1999). Peimbert et al. (1993) were the first to determine the O^{++} abundance from the very weak RLs, obtaining the same qualitative result: the abundances obtained from RLs are higher than those determined by making use of CELs. This observational fact is currently known as the "abundance discrepancy" (AD) problem. In the last few years, our group has obtained a large data set of intermediate- and high-resolution spectroscopy of Galactic and extragalactic H II regions using medium- and large-aperture telescopes (Esteban et al. 2002, 2005; García-Rojas et al. 2004, 2005, 2006, 2007; López-Sánchez et al. 2007). The general result of these works is that the O^{++}/H^+ ratio calculated from RLs is between 0.10 and 0.35 dex higher than the value obtained from CELs in the same objects. The value of the AD that we usually find in H II regions is rather similar for all objects and ions and is much lower than the most extreme values found in PNs. The H II region results obtained by our group are fairly different than those found for PNs, and they seem to be consistent with the predictions of the temperature fluctuations paradigm formulated by Peimbert (1967), as argued in García-Rojas (2006) and García-Rojas & Esteban (2007). In the presence of temperature fluctuations (parameterized by the mean square of the spatial variations of temperature, the so-called t^2 parameter), the AD can be naturally explained by the different temperature dependences of the intensity of RLs and CELs. The existence and origin of temperature fluctuations are still controversial problems and a challenge for our understanding of ionized nebulae. Recently, Tsamis & Péquignot (2005) and Stasińska et al. (2007) have proposed a hypothesis to the origin of the AD that is based on the presence of cold high-metallicity clumps of supernova ejecta still not mixed with the ambient gas of the H II regions. This cold gas would produce most of the emission of the RLs, whereas the ambient gas of normal abundances would emit most of the intensity of the CELs.

Our group is interested in exploring the question of on what variable or physical process the AD depends, using different approaches. One of the most promising approaches is based on the study of the behavior of the AD factor at small spatial scales, something that has still not been explored in depth in nearby bright Galactic H II regions. In this paper, we make use of deep intermediate-resolution long-slit spectroscopy of the Orion Nebula to study the dependence of the AD with respect to different nebular parameters: electron temperature and density, the local ionization state of the gas, the presence of high-velocity material, and its correlation with different morphological structures (e.g., proplyds, ionization fronts, globules, Herbig-Haro objects).

[1] Based on observations made with the 4.2 m William Herschel Telescope (WHT), operated on the island of La Palma by the Isaac Newton Group in the Spanish Observatorio del Roque de los Muchachos of the Instituto de Astrofísica de Canarias.

[2] Current address: Instituto de Astronomía, UNAM, Apdo. Postal 70-264, 04510 México D.F., Mexico.

The spatial distribution of the physical conditions in the Orion Nebula has been investigated by several authors. Baldwin et al. (1991) obtained the density and temperature distributions at 21 and 14 points, respectively, along a 5′ line west of θ^1 Ori C, finding a density gradient that decreases to the outskirts of the nebula and a constant value of T_e. Walter et al. (1992) determined electron densities, electron temperatures, and chemical abundances for 22 regions of the Orion Nebula. Using also data from the literature, these authors find radial gradients of the physical conditions, but with a positive slope in the case of the temperature determined from [O III] lines. Pogge et al. (1992) obtained Fabry-Pérot images of the inner 6′ of the nebula, covering several bright CELs, that were taken with an average seeing of about 1.8″. Those authors present a density map obtained from the ratio of the [S II] doublet that confirms the presence of a density gradient that reaches its highest point immediately south-southwest of the Trapezium stars, along with some localized density enhancements in the Orion bar and some Herbig-Haro objects. Very recently, Sánchez et al. (2007) have obtained an integral field spectroscopy mosaic of an area of 5′ × 6′ of the center of the Orion Nebula, with a spatial resolution of 2.7″. The electron density map that they obtain is consistent with that obtained by Pogge et al. (1992) but richer in substructures, some of which are possibly associated with Herbig-Haro objects. Sánchez et al. (2007) also obtain an electron temperature map (derived from the line ratio of [N II] lines) that shows clear spatial variations, which rise near the Trapezium and drop toward the outer zones of the nebula. However, an important drawback of the temperature map of Sánchez et al. is that it is based on non–flux calibrated spectra, and possible effects due to variations in the dust extinction distribution cannot be disregarded. O'Dell et al. (2003) obtained a high–spatial resolution map of the electron temperature (derived from the line ratio of [O III] lines) of a 160″ × 160″ field centered at the southwest of the Trapezium. The data were obtained from narrowband images taken with the WFPC of the *Hubble Space Telescope* (*HST*). Although they do not find a substantial radial gradient of T_e in the nebula, O'Dell et al. (2003) report the existence of small-scale temperature variations down to a few arcseconds, which is compatible with the values of the temperature fluctuations parameter calculated from the AD determinations by Esteban et al. (2004). Rubin et al. (2003) obtained *HST* STIS long-slit spectroscopy at several slit positions on the Orion Nebula, analyzing the electron temperature and density spatial profiles with resolution elements of 0.5″ × 0.5″. These last authors do not find large-scale gradients of the physical conditions along the slits, but rather a relatively large point-to-point variation and some correlation of such variations with several small-scale structures.

The spatial mapping of the AD factor has been performed in few ionized nebulae, but largely for PNs. Liu et al. (2000), Garnett & Dinerstein (2001), and Krabbe & Copetti (2006) have found significant differences in the spatial profiles of the O^{++}/H^+ ratio derived by making use of RLs and CELs, and this suggests the presence of chemical inhomogeneities or additional mechanisms for producing the O II lines in these objects. Tsamis et al. (2003) have performed the only available study so far of the spatial distribution of the AD factor in an H II region: 30 Doradus. However, considering the extragalactic nature of this object and the spatial sampling of 3.5″ used by those authors, their final spatial resolution is very low: about 1 pc. In any case, Tsamis et al. (2003) find a rather constant AD factor along the zone covered with their observations, which is a quite different behavior than that observed in PNs.

In §§ 2 and 3 of this paper, we describe the observations, the data reduction procedure, and the aperture extraction and measurement of the emission lines. In § 4 we derive the physical conditions and the ionic abundances from both kinds of lines, CELs and RLs. In § 5 we present and discuss the spatial profiles of the physical conditions, the line fluxes, and the abundance discrepancy factor along the slit positions. In § 6 we discuss the large-scale radial distribution of some nebular properties along the nebula. In § 7 we explore possible correlations between the AD and different nebular parameters. In § 8 we address and estimate the possible temperature fluctuations inside the nebula. Finally, in § 9 we summarize our main conclusions.

2. OBSERVATIONS, DATA REDUCTION, AND EXTRACTION OF ONE-DIMENSIONAL SPECTRA

Intermediate-resolution spectroscopy was obtained on 2002 December 27 with the ISIS spectrograph at the 4.2 m William Herschel Telescope (WHT) of the Observatorio del Roque de los Muchachos (La Palma, Spain). Two different CCDs were used for the blue and red arms of the spectrograph: an EEV CCD with a configuration of 4096 × 2048 pixels, with a pixel size of 13.5 μm, in the blue arm, and a Marconi CCD with 4700 × 2148 pixels, with a pixel size of 13.5 μm, in the red arm. The dichroic prism used to separate the blue and red beams was set at 5400 Å. The slit was 3.7′ long and 1.03″ wide. Two gratings were used, the R1200B in the blue arm and the R316R in the red arm. These gratings give reciprocal dispersions of 17 and 62 Å mm^{-1}, and effective spectral resolutions of 0.86 and 3.81 Å, for the blue and red arms, respectively. The blue spectra cover the range from 4198 to 5048 Å, and the red ones from 5370 to 8690 Å. The spatial scale is 0.20″ $pixel^{-1}$ in both arms. The average seeing during the observations was ∼1.2″.

We observed five slit positions, covering different zones of the nebula and different position angles (see Fig. 1). These positions were chosen in order to cover different morphological structures, such as proplyds (158−323, 158−326, 159−350, 170−337, and 177−341), Herbig-Haro objects (HH 202, HH 203, HH 204, HH 529, and HH 530), and the Orion bar. Due to the high surface brightness of the nebula, a large number of individual short exposures were taken for each slit position and in each spectral range in order to achieve a good signal-to-noise ratio in the faint C II and O II RLs and to avoid saturating the brightest emission lines. The journal of observations can be found in Table 1. Note that the five slit positions are numbered as 1, 3, 4, 5, and 6; there was not actually a slit position number 2.

The spectra were wavelength-calibrated with a CuNe+CuAr lamp. The correction for atmospheric extinction was performed using the average curve for continuous atmospheric extinction at the Observatorio del Roque de los Muchachos. The absolute flux calibration was achieved by observations of the standard stars Feige 15, Feige 110, H600, and Hz 44. All the CCD frames were reduced using the standard IRAF[3] TWODSPEC reduction package to perform bias correction, flat-fielding, cosmic-ray rejection, wavelength and flux calibration, and sky subtraction.

The extraction of one-dimensional spectra was done automatically through an IRAF script, using the `apall` task. First, we traced the apertures interactively by selecting the brightest object (star, proplyd, or Herbig-Haro object) in each two-dimensional (2D) spectrum. In all cases we adjusted a third-order spline function and obtained a typical rms value of the fit that was between 0.05 and 0.1 pixels. In the following step, we defined the apertures

[3] IRAF is distributed by the National Optical Astronomical Observatory, operated by the Associated Universities for Research in Astronomy, Inc., under contract to the National Science Foundation.

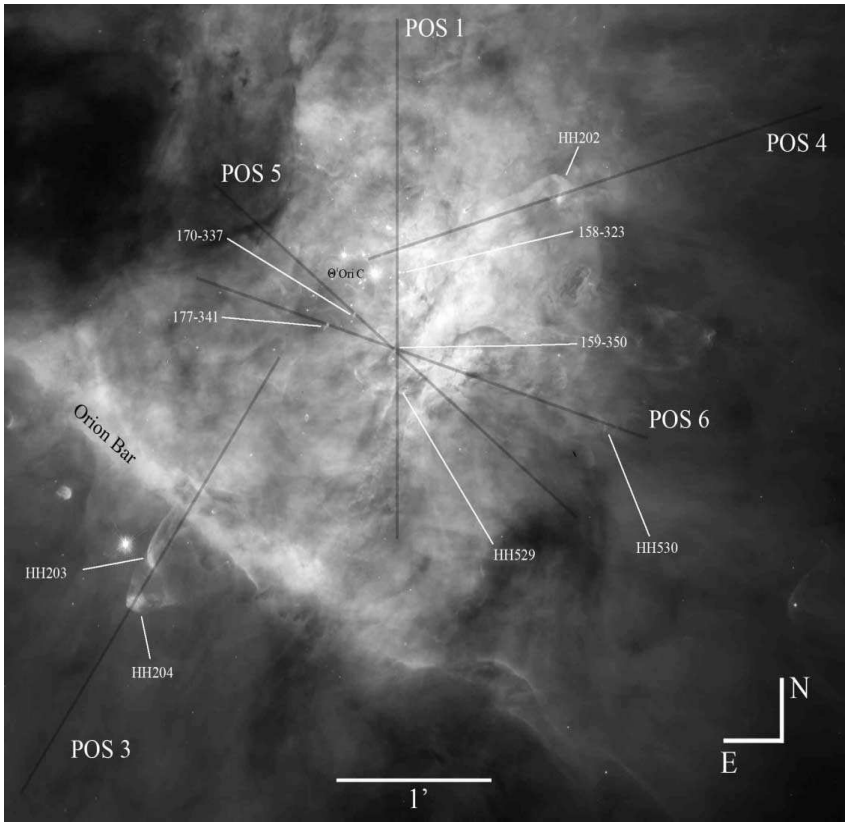

FIG. 1.—Our slit positions over a mosaic of a combination of WFPC2 images of the Orion Nebula, taken with different filters (O'Dell & Wong 1996).

to extract for each 2D spectrum by using the coefficients obtained in the aperture tracing. For all the slit positions, we extracted apertures with a size of 6 pixels in the spatial direction, which corresponds to an angular scale of 1.2″: the average seeing during the night. Therefore, each aperture covers a size of $1.2'' \times 1.03''$ in the spatial and spectral directions, respectively. At the distance of the Orion Nebula (450 pc; O'Dell 2001), 1″ corresponds to a linear size of 0.0022 pc, 6.8×10^{-15} cm, or 450 AU. The slit center in the red arm is some pixels displaced with respect to the slit center in the blue arm; this effect has been corrected in the extraction procedure, ensuring the same spatial coverage in the blue and red ranges. We have discarded the apertures located near the edges of the CCDs, resulting in a final number of 154 apertures extracted—individual one-dimensional spectra—for each slit position except numbers 1 and 4. In these two cases a star, θ^1 Ori A, fell into the slit, and we discarded the apertures that were contaminated by stellar emission (11 apertures in position 1 and 12 in position 4). In addition, the last 17 apertures at the northwest edge of position 4 were also discarded because the temperature-sensitive [O III] λ4363 line was not detected due to the faintness

TABLE 1
JOURNAL OF OBSERVATIONS

Slit Position	R.A.[a] (J2000,0)	Decl.[a] (J2000,0)	P.A. (deg)	$\Delta\lambda$ (Å)	Spectral Resolution (Å pixel^{-1})	Exposure Time (s)
1	05 35 15.0	−05 23 04	0	4198–5048	0.23	30 × 60
				5370–8690	0.84	40 × 30
3	05 35 22.4	−05 25 09	147	4198–5048	0.23	15 × 150
				5370–8690	0.84	25 × 60
4	05 35 12.4	−05 22 44	107	4198–5048	0.23	31 × 60
				5370–8690	0.84	40 × 30
5	05 35 15.8	−05 23 33	50	4198–5048	0.23	20 × 100
				5370–8690	0.84	39 × 30
6	05 35 15.3	−05 23 38	72	4198–5048	0.23	20 × 100
				5370–8690	0.84	41 × 30

NOTE.—Units of right ascension are hours, minutes, and seconds, and units of declination are degrees, arcminutes, and arcseconds.
[a] Coordinates of the slit center.

TABLE 2
NUMBER OF APERTURES EXTRACTED

Parameter	Position 1	Position 3	Position 4	Position 5	Position 6
Number of excluded apertures[a]	11	...	29	...	...
Number of extracted apertures[b]	143	154	125	154	154
Background-gas zones[c]	1–60, 72–84, 90–143	85–154	25–50, 75–85	1–57, 62–74, 79, 154	1–40, 45–63, 70–154

[a] Contaminated by stellar emission or nondetection of the [O III] λ4363 line.
[b] Summed for producing the whole-slit spectra.
[c] Summed for producing the background-gas spectra.

of the spectra. The final total number of apertures extracted was 730.

For each slit position, we extracted additional one-dimensional spectra by collapsing the whole slit—the whole extension of the 154 individual apertures—but excluding different particular zones: (1) only those apertures contaminated by stellar emission; these will be designated as "whole-slit" spectra, or (2) the same zones as before, but also those apertures covering proplyds, Herbig-Haro objects, or having a very low surface brightness; these spectra are designated as "background-gas." In Table 2, for each slit position, we summarize the number of apertures that are excluded due to stellar emission contamination or nondetection of the [O III] λ4363 line (first row), the total number of usable apertures (second row), and the apertures that we consider representative of the background gas (third row).

3. EMISSION LINE SELECTION, FLUX MEASUREMENTS, AND REDDENING CORRECTION

The emission lines considered in our analysis are listed in Table 3. Each line was selected in order to satisfy one of the following criteria:

1. H I lines (Hα, Hβ, and Hγ), which are used to compute the reddening correction and to rescale the line intensity ratios of the red spectral range with respect to the blue one.
2. Ratios of CELs of various species, which are used to compute both physical conditions, such as using the auroral lines [O III] λ4363 or [N II] λ5754 to derive T_e, or the [S II] lines to derive n_e, and ionic abundances.
3. Faint recombination lines of C II and O II, which are used to derive the C^{++} and O^{++} abundances and to compute the abundance discrepancy factor for O^{++} (via a comparison with the O^{++} abundances from the CELs).
4. Some lines that are blended with other lines of interest.

Line fluxes were measured by applying a single or multiple (in the case of line blending) Gaussian profile fitting procedure, except in some apertures of positions 3 and 4, where the complex velocity field of the Herbig-Haro objects affects the line profiles and the Gaussian fit was not feasible. In these cases, the line intensities were measured by integrating all the flux included in the line profile between two given limits and over a local continuum estimated by eye. All the measurements were made with the SPLOT routine of the IRAF package and by using our own scripts to automatize the process.

To accurately compute the line fluxes, we need to define the adjacent continuum of each line. This was also done by using the SPLOT routine. For each selected line, we define two small spectral zones, one at each side of the line, that are located as close as possible to the line and are free of any spectral feature. SPLOT fits the continuum between both zones and obtains the flux of the line. This automatic procedure was tested in randomly selected lines where we manually measured the flux using a local continuum estimated by eye. In general, there is a good agreement between both kinds of measurements within the adopted uncertainties. The observational errors associated with the line flux measurements was determined, following Castellanos et al. (2002), from the expression $\sigma_I = \sigma_c N^{1/2}[1 + \mathrm{EW}/(N\Delta)]^{1/2}$, where σ_I is the error in the line flux, σ_c represents the standard deviation of the continuum close to the measured emission line, N is the number of pixels used in the measurement of the line flux, EW is the line equivalent width, and Δ is the wavelength dispersion in units of Å pixel^{-1}. The final uncertainty of the line intensity ratios is estimated to be typically about 1% if the ratio $F(\lambda)/F(\mathrm{H}\beta) \geq 0.1$, about 2% if $0.01 \leq F(\lambda)/F(\mathrm{H}\beta) \leq 0.1$, about 10% if $0.005 \leq F(\lambda)/F(\mathrm{H}\beta) \leq 0.01$, about 25% if $0.001 \leq F(\lambda)/F(\mathrm{H}\beta) \leq 0.005$, and about 40% if $0.0001 \leq F(\lambda)/F(\mathrm{H}\beta) \leq 0.001$. We do not consider lines weaker than $0.0001F(\mathrm{H}\beta)$ (see below).

All the line intensities of a given aperture have been normalized to a particular H I recombination line present in each wavelength interval. For the blue spectra, the reference line was Hβ,

TABLE 3
SELECTED LINES

λ (Å)	Ion	Multiplet
4267.15	C II	6
4340.47	H I	Hγ
4363.21	[O III]	2F
4638.86	O II	1
4640.64	N III	2
4641.81	O II	1
4643.06	N II	5
4649.13	O II	1
4650.84	O II	1
4661.63	O II	1
4711.37	[Ar IV]	1F
4861.33	H I	Hβ
4881.00	[Fe III]	2F
4958.91	[O III]	1F
5006.94	[O III]	1F
5517.71	[Cl III]	1F
5537.88	[Cl III]	1F
5754.64	[N II]	3F
6300.30	[O I]	1F
6312.10	[S III]	3F
6363.78	[O I]	1F
6548.03	[N II]	1F
6562.82	H I	Hα
6583.41	[N II]	1F
6716.47	[S II]	2F
6730.85	[S II]	2F
7135.78	[Ar III]	1F
7319.19	[O II]	2F
7330.20	[O II]	2F
7751.10	[Ar III]	2F

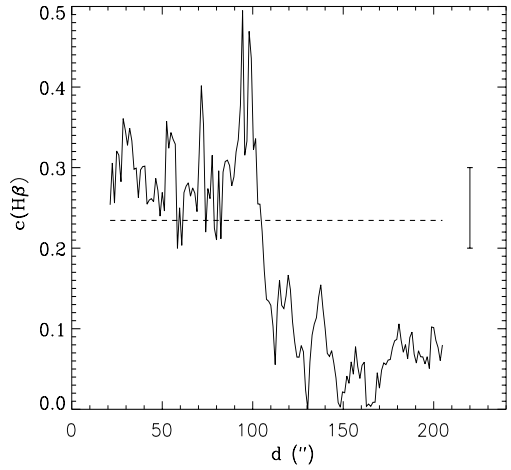

FIG. 2.—Spatial distribution of the reddening coefficient, $c(\mathrm{H}\beta)$, along slit position 6. Positional measurement along the slit goes from northeast to southwest (see Fig. 1). The dashed horizontal line represents the value of $c(\mathrm{H}\beta)$ obtained from the integrated spectrum along the whole slit. The typical error bar is included.

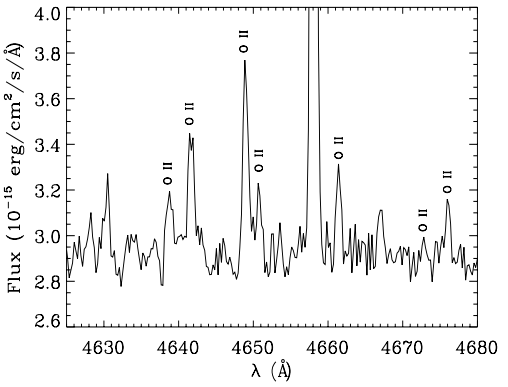

FIG. 3.—Portion of the blue spectrum of an aperture extracted from slit position 6, extending from positional measurements 151.4″ to 152.6″ (see Fig. 5). This is a representative example of the average quality of our one-dimensional spectra.

and for the red ones, the reference was Hα. To produce a final homogeneous set of line intensity ratios, all of them were rescaled to Hβ. The rescaling factor used in the red spectra was the theoretical Hα/Hβ ratio for the physical conditions of $T_e = 10{,}000$ K and $n_e = 1000$ cm^{-3}.

As can be expected, weak lines were not detected in all the apertures. To avoid bad weak-line measurements, we imposed three criteria to discriminate between real features and noise. The criteria are the following:

1. Line intensity peak over 2.5 times the sigma of the continuum (2.5 σ). The more usual criterion of 3 σ was not adopted because several important lines that were clearly detected were discarded using that constraint.
2. FWHM(λ) > 1.5FWHM(H I) or FWHM(λ) < FWHM(H I)/1.5. These inequalities were used to discriminate between true emission lines and spurious features.
3. $I(\lambda) < 0.0001I(\mathrm{H}\beta)$. This intensity was near the detection limit of our observations.

The reddening coefficient, $c(\mathrm{H}\beta)$, was obtained by fitting the observed Hγ/Hβ ratio to the theoretical one predicted by Storey & Hummer (1995) for the nebular conditions determined in the slit position observed by Esteban et al. (2004). Following Esteban et al. (1998), we have used the reddening function, $f(\lambda)$, normalized at Hβ as derived by Costero & Peimbert (1970) for the Orion Nebula. In Figure 2, as an example, we show the spatial distribution of $c(\mathrm{H}\beta)$ obtained for the apertures of slit position 6. The zone of the largest reddening at the left half of Figure 2 corresponds to the northeast portion of slit position 6. The reddening maps of O'Dell & Yusef-Zadeh (2000) and Sánchez et al. (2007) also show larger values at this zone, which is in the vicinity of the so-called Dark Bay. The typical uncertainty of $c(\mathrm{H}\beta)$ is estimated to be about 0.05.

4. PHYSICAL CONDITIONS AND CHEMICAL ABUNDANCES

4.1. *Electron Temperatures and Densities*

Nebular electron temperatures, T_e, and densities, n_e, have been derived from the usual CEL ratios, using the IRAF task `temden` of the package `nebular` (Shaw & Dufour 1995) with updated atomic data (see García-Rojas et al. 2005). We have computed n_e from the [S II] 6717/6731 line ratio and T_e from the nebular to auroral [O III] (4959 + 5007)/4363 and [N II] (6548 + 6584)/5754 line ratios. The spatial distributions of the physical conditions are presented and discussed in § 5.1. Although we include the [Cl III] doublet in our set of selected lines, we do not use the lines in the analysis because the number of apertures with good determinations of the density-sensitive line ratio is rather low.

The methodology for the determination of the physical conditions was the following: an initial T_e-value of 10,000 K was assumed in order to derive a first approximation to n_e([S II]); then the obtained n_e-value was used to compute T_e([O III]) and T_e([N II]); and finally, we iterated until convergence to compute the adopted values of n_e and T_e. Uncertainties in the physical conditions were computed by propagating the errors in the analytical expression of n_e computed by Castañeda et al. (1992) and the expression of T_e given by equations (5.4) and (5.5) of Osterbrock & Ferland (2006). Although the expression derived by Castañeda et al. (1992) is only valid to a limited range of densities lower than 10^4 cm^{-3}, it seems adequate for simply estimating the error propagation due to uncertainties in the computed temperatures and line ratios.

4.2. *Ionic Abundances from CELs and RLs*

Ionic abundances of N^+, O^+, O^{++}, S^+, S^{++}, and Ar^{++} have been derived from CELs by making use of the IRAF task `ionic` of the package `nebular`. We have assumed a two-zone scheme and a value of $t^2 = 0$, adopting T_e([N II]) for ions with a low ionization potential (N^+, O^+, and S^+) and T_e([O III]) for ions with a high ionization potential (O^{++}, S^{++}, and Ar^{++}). The errors in the ionic abundances are the quadratic sum of the independent contributions of n_e, T_e, and line flux uncertainties.

On the other hand, the high signal-to-noise ratio of the spectra has permitted us to detect and measure pure RLs of O II and C II in most of the apertures (see Fig. 3). These lines have the advantage that their relative intensity with respect to the H I lines depends weakly on T_e and n_e, which avoids the problem of the presence of temperature variations along the line of sight, which can actually affect the abundance determinations from CELs, whose emissivities depend strongly on the T_e-value of the nebula.

Let $I(\lambda)$ be the intensity of a RL of an element X, i times ionized, at wavelength λ; then the abundance of the ionization state $i+1$ of element X is given by

$$\frac{N(X^{i+1})}{N(H^+)} = \frac{\lambda(\text{Å})}{4861}\frac{\alpha_{\text{eff}}(H\beta)}{\alpha_{\text{eff}}(\lambda)}\frac{I(\lambda)}{I(H\beta)}, \quad (1)$$

where $\alpha_{\text{eff}}(\lambda)$ and $\alpha_{\text{eff}}(H\beta)$ are the effective recombination coefficients for the line and for Hβ, respectively. The $\alpha_{\text{eff}}(H\beta)/\alpha_{\text{eff}}(\lambda)$ ratio is almost independent of the adopted temperatures and densities.

Following Esteban et al. (1998), we have considered the abundances obtained from the intensity of each individual line of multiplet 1 of O II and the abundances from the estimated total intensity of the multiplet. This last quantity is obtained by multiplying the sum of the intensities of the individual lines observed by the multiplet correction factor, which is defined as

$$m_{\text{cf}} = \frac{\sum_{\text{all}} s_{ij}}{\sum_{\text{obs}} s_{ij}}, \quad (2)$$

where s_{ij} is the theoretical line strengths, which are constructed by assuming that they are proportional to the populations of their parent levels, if we assume LTE computation predictions. The upper sum runs over *all* the lines of the multiplet, and the lower sum runs over the *observed* lines of the multiplet.

The O^{++} and C^{++} abundances from RLs have been calculated using the representative T_e-values of these ions, T_e([O III]), and the effective recombination coefficients that are available in the literature (Storey [1994] for O II, assuming LS coupling, and Davey et al. [2000] for C II). The O^{++} abundance has only been computed when at least three lines of multiplet 1 were measured in a given one-dimensional spectrum. The final number of apertures with determinations of the O^{++}/H^+ ratio obtained from RLs was 671, 92% of the total number of available one-dimensional spectra. Non-LTE (NLTE) corrections are not taken into account for deriving the O^{++} abundances (see Tsamis et al. 2003; Ruiz et al. 2003; Peimbert et al. 2005), considering (1) that we use several lines of the multiplet and (2) the high densities, between 4000 and 6000 cm^{-3} (e.g., Esteban et al. 1998, 2004), of the Orion Nebula.

5. SPATIAL PROFILES ALONG THE SLIT POSITIONS

5.1. *Physical Conditions*

The first step in the analysis of our results was the obtaining of spatial profiles of several nebular parameters along the slit positions. The selected parameters were c(Hβ), n_e, T_e([N II]), T_e([O III]), the intensity of several selected lines (Hβ, C II λ4267, O II λ4649, [O III] λ4959, [Fe III] λ4881, [N II] λ5755 and λ6584, [O I] λ6300, and [S II] λ6717 and λ6731), the O^{++}/H^+ ratio obtained from CELs and RLs, and the C^{++}/H^+ ratio obtained from RLs. In Figures 4–8 we show some selected spatial profiles of slit positions 3, 6, 1, 4, and 5, respectively. Slit positions 3 and 6 are the most interesting ones, and we will focus our discussion on their main features. Slit position 3 crosses the Orion bar and the Herbig-Haro (HH) objects HH 203 and HH 204, and slit position 6 passes through the brightest part of the nebula at the southwest of the Trapezium cluster and crosses two proplyds, 159−350 and 177−341, as well as HH 530.

The spatial profiles of n_e show a large range of variation across the slits, with local maxima associated with the positions of proplyds, HH objects, the Orion bar, and the bright zone at the southwest of the Trapezium (see Figs. 4*a*–8*a*). The highest densities are found at the proplyd 159−350, which has been observed in slit positions 5 and 6 (see Figs. 8*a* and 5*a*, respectively). This object shows n_e-values on the order of 6×10^4 and 2×10^4 cm^{-3} in slit positions 5 and 6, respectively, whereas the proplyd 158−326, which is near θ^1 Ori C, shows values somewhat larger than 4×10^4 cm^{-3} (see Fig. 6*a*). The densities at the brightest zone of the nebula, at the southwest of the Trapezium, are about 2.5×10^4 cm^{-3} (see Fig. 5*a*). It is obvious that such high n_e determinations based on the [S II] doublet are not totally confident, because they are at the high-density limit of this indicator. The HH objects are also associated with local peaks of n_e, but not as high as those for the proplyds; in fact, HH 202, HH 203, and HH 204 show maxima of between 6000 and 1×10^4 cm^{-3}. In Figure 4*a*, the dashed line marks the n_e-value obtained from the whole-slit (integrated) spectrum, 2460 cm^{-3}, whereas the minimum and maximum values are about 700 and 8000 cm^{-3}, covering a range of 1 order of magnitude. In Figure 5*a*, we can see that the range of variation of n_e is also dramatic along slit position 6. In this figure we also compare the values corresponding to the whole-slit spectrum, 5500 cm^{-3}, and the background-gas spectrum, 4700 cm^{-3}, which corresponds to an integrated spectrum excluding the emission of the proplyds. As we can see, the measured density increases by 800 cm^{-3}, about 17%, when we include the emission of the proplyds in the integrated spectrum of the slit.

The spatial profiles of T_e([N II]) and T_e([O III]) show very interesting features (see Figs. 4*b*–8*b*). The proplyds observed in slit positions 1, 5, and 6 show quite prominent spikes of T_e([N II]) and lesser or almost absent ones of T_e([O III]). In slit position 6 (Fig. 5*b*), the value of T_e([N II]) increases locally by about 70% at the location of proplyd 177−341, and a similar spike shows the location of proplyd 170−337 in slit position 5 (Fig. 8*b*). The value of T_e([N II]) is also higher than the mean by 50% and 40% at the position of proplyd 159−250 in slit positions 5 and 6, respectively. For all the proplyds, the increase of T_e([O III]) is only of a few hundred kelvins at most. In Figure 5*b*, we can also see a relatively broad, about 5″ wide, spike of T_e([N II]) at 130″, where the temperature increases by about 15%. This feature is not related to any local structure reported by Bally et al. (2000), but rather with a conspicuous dark globule that can be seen at the edge of the bright zone at the southwest of the Trapezium. There are also less important temperature spikes related to some HH objects. In Figure 4*b*, we can see that the value of T_e([N II]) increases by about 15% at the location of HH 204, and that the increase is slightly lower for the case of T_e([O III]). In contrast, HH 203 does not show that behavior, and its temperatures are similar to those of the surrounding gas. In HH 202 (seen in slit position 4), the increase of the values of T_e([N II]) and T_e([O III]) are only about 8% and 5%, respectively (Fig. 7*b*). The other HH objects that we have observed, HH 529 and HH 530, do not show temperature variations with respect to the surrounding gas (Figs. 6*b* and 5*b*). The different behavior of the temperatures in the HH objects does not seem to be correlated with the velocity of their associated flows as reported by Henney et al. (2007). There is a final interesting feature regarding the temperature profiles that can be seen in Figure 4*b*. Although T_e([N II]) is almost always a few hundred kelvins larger than T_e([O III]) in all the slit positions (this has been also observed in previous works; e.g., Baldwin et al. 1991; Rubin et al. 2003), the zone around the Orion bar, between 130″ and 150″ in Figure 4*b*, shows a reversal of this relation in just the inner 10″ of the bar. In contrast, T_e([N II]) shows a local increase just outside the bar. This local increment of T_e([O III]) that we see in this particular zone could be related to the highly ionized jet, which is especially bright in [O III], that leads to HH 203 and HH 204 (see Doi et al. 2004). In fact, the position of this zone coincides with a knot of high–[O III] emission, which

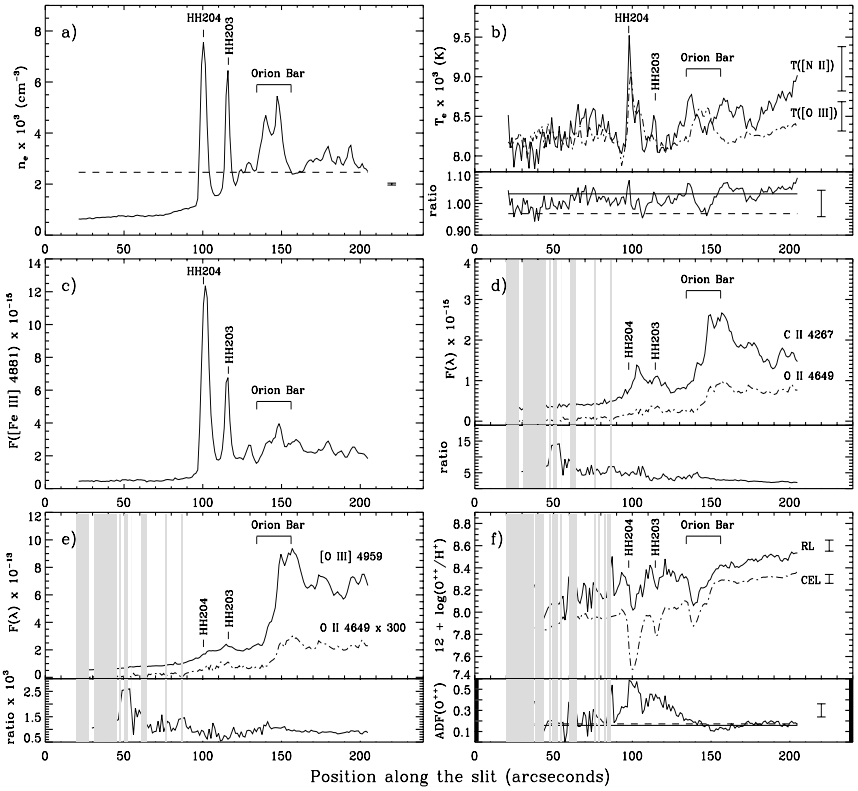

FIG. 4.—Spatial profiles of several nebular parameters along slit position 3. Positional measurement along the slit goes from southeast to northwest (see Fig. 1). The position of the Orion bar and the Herbig-Haro objects HH 203 and HH 204 are indicated. Typical error bars are included in some of the diagrams. (*a*) Profile of n_e. The horizontal dashed line gives the average value of n_e for the whole-slit (integrated) spectrum. (*b*) *Top*: Profiles of T_e([O III]) (*dash-dotted line*) and T_e([N II]) (*solid line*). *Bottom*: Profile of the T_e([N II])/T_e([O III]) ratio. The horizontal solid and dashed lines represent the values of this ratio for the background-gas and whole-slit spectra, respectively. (*c*) Profile of *F*([Fe III] λ4881). (*d*) *Top*: Profiles of *F*(C II λ4267) (*solid line*) and *F*(O II λ4649) (*dash-dotted line*). *Bottom*: Profile of the *F*(C II λ4267)/*F*(O II λ4649) ratio. The vertical gray bands indicate zones without a reliable measurement of the O II λ4649 line. (*e*) *Top*: Profiles of *F*([O III] λ4959) (*solid line*) and *F*(O II λ4649) (*dash-dotted line*). *Bottom*: Profile of the *F*([O III] λ4959)/*F*(O II λ4649) ratio. The vertical gray bands indicate zones without a reliable measurement of the O II λ4649 line. (*f*) *Top*: Profiles of $12 + \log(O^{++}/H^+)$ determined from RLs (*solid line*) and CELs (*dash-dotted line*). *Bottom*: Profile of ADF(O^{++}). The horizontal solid and dashed lines represent the values of the ADF for the background-gas and whole-slit spectra, respectively, and the vertical gray bands indicate zones without a reliable determination of the O^{++}/H^+ ratio from RLs.

can be seen in Figure 8 of Doi et al. (2004), that is crossed by our slit (their box with the position-based identifier 209−446).

Rubin et al. (2003) obtained *HST* STIS spectroscopy of a slit position very similar to our position 3—their slit 4—and show its T_e([O III]) spatial profile in their Figure 3*a*. If we compare that figure with our Figure 4*b*, we can see that the point-to-point dispersion of the temperature is substantially lower in our data. In fact, whereas T_e([O III]) varies from 6500 to 12,000 K in slit 4 of Rubin et al. (2003), the variations are only from 8000 to 9000 K in our slit position 3. This fact has two possible explanations: (1) the presence of real temperature variations with a typical spatial scale of between 0.5″ (the spatial resolution of the Rubin et al. data) and 1.2″ (our resolution) in the plane of the sky, or (2) that the temperature variations reported by Rubin et al. (2003) are spurious and are produced by the much lower signal-to-noise ratio of their data. We think that the second explanation is perhaps the most likely one, considering that the deepest exposures obtained by Rubin et al. for the spectral range containing [O III] λ4363 were about 1060 s long, and our exposures were between 1800 and 2200 s long. Moreover, an important factor should be added to correct for the different apertures of the telescopes used in this work and in Rubin et al. (4.2 and 2.4 m, respectively), as well as for the smallest element of spatial resolution used in Rubin et al.'s observations.

It is clear that the behavior of T_e([N II]) and T_e([O III]) at the positions of proplyds and HH objects is different. In Figures 4*b*–8*b* we also include the ratio of both temperatures, which shows clearly that the increase of T_e([N II]) is greater than that of T_e([O III]) in proplyds. The presence of T_e([N II]) enhancements in the proplyds of the Orion Nebula was previously reported by Rubin et al. (2003), and they interpret this as the effect of collisional deexcitation on the nebular lines of [N II] due to the high densities of these objects. We have explored that possibility, comparing the spatial profile of the intensity of the [N II] λ5755 and λ6584 lines. Both lines come from upper levels, but with very different critical densities: 7.9×10^6 cm^{-3} in the case of the [N II] λ5755 line, and 5.8×10^4 cm^{-3} in the case of the [N II] λ6584 line. In Figures 5*c* and 6*c*, we can see that the two proplyds with the largest electron densities ($n_e > 2$–6×10^4 cm^{-3}), 159−350 (also observed in Fig. 8*c*) and 158−323, show a spike in the brightness of the [N II] λ5755 line, whereas the [N II] λ6584 line does not show such a clear increase in its brightness with respect to the emission of the surroundings. However, the proplyds with the lowest electron densities ($n_e < 1 \times 10^4$ cm^{-3}), 177−341 and 170−337 (Figs. 5*c*

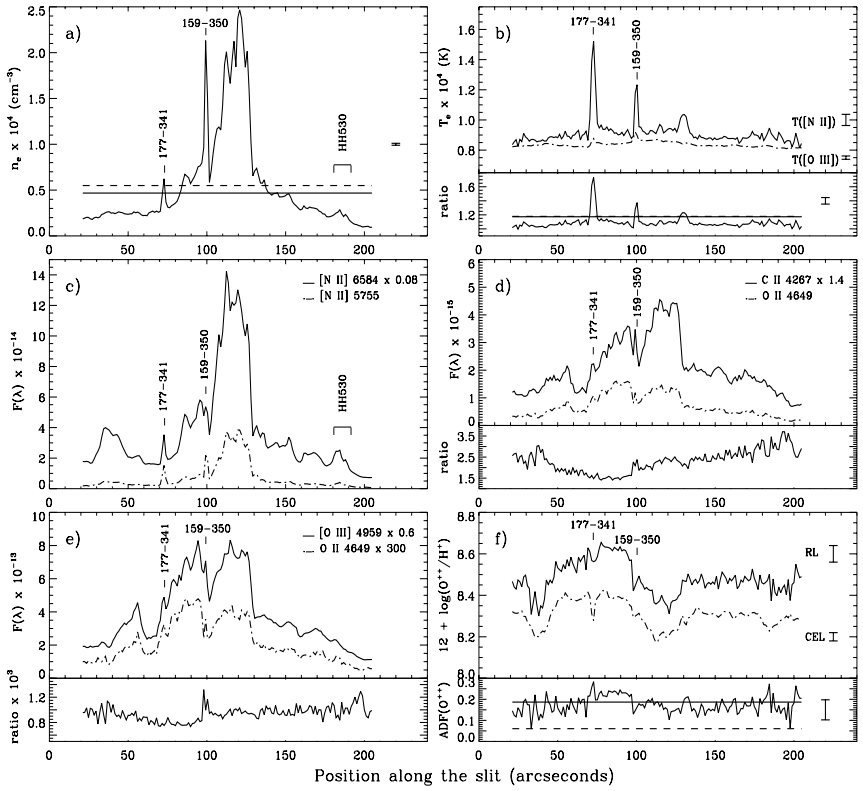

FIG. 5.—Spatial profiles of several nebular parameters along slit position 6. Positional measurement along the slit goes from northeast to southwest (see Fig. 1). The position of the proplyds 177−341 and 159−350 and the Herbig-Haro object HH 530 are indicated. Typical error bars are included in some of the diagrams. (*a*) Profile of n_e. The horizontal solid and dashed lines represent the values of n_e for the background-gas and whole-slit spectra, respectively. (*b*) *Top*: Profiles of T_e([O III]) (*dash-dotted line*) and T_e([N II]) (*solid line*). *Bottom*: Profile of the T_e([N II])/T_e([O III]) ratio. The horizontal solid and dashed lines represent the values of this ratio for the background-gas and whole-slit spectra, respectively. (*c*) Profiles of F([N II] λ6584) (*solid line*) and F([N II] λ5755) (*dash-dotted line*). (*d*) *Top*: Profiles of F(C II λ4267) (*solid line*) and F(O II λ4649) (*dash-dotted line*). *Bottom*: Profile of the F(C II λ4267)/F(O II λ4649) ratio. (*e*) *Top*: Profiles of F([O III] λ4959) (*solid line*) and F(O II λ4649) (*dash-dotted line*). *Bottom*: Profile of the F([O III] λ4959)/F(O II λ4649) ratio. (*f*) *Top*: Profiles of 12 + log(O^{++}/H^+) determined from RLs (*solid line*) and CELs (*dash-dotted line*). *Bottom*: Profile of ADF(O^{++}). The horizontal solid and dashed lines represent the values of the ADF for the background-gas and whole-slit spectra, respectively.

and 8*c*), show similar localized enhancements of the intensity of both [N II] lines, indicating that collisional deexcitation seems to be not so important in these two proplyds.

In order to further explore whether the different behavior of the auroral and nebular T_e([N II]) lines in some proplyds is due to collisional deexcitation, we have constructed Figure 9. In this figure, we show the theoretical curves of the n_e and T_e pairs that reproduce the observed range of values of the [N II] 5755/6584 line ratio in the proplyds, as well as the line of the lower limit of n_e, which corresponds to the lowest value of the [S II] 6731/6717 ratio measured in these objects. The theoretical predictions have been constructed with emissivities calculated by the photoionization code PHOTO as described in Stasińska (2005), kindly provided by G. Stasińska (2007, private communication). Unfortunately, the results of Figure 9 are not conclusive, but considering that the estimated n_e-value of the proplyds should be a lower limit of the true one, the permitted area of the diagram indicates that collisional deexcitation should be acting. Moreover, if that is correct, the true electron temperature should be lower than that actually indicated by T_e([N II]), but perhaps not too different from the values corresponding to the surrounding ionized gas (which are never lower than 3000 K). It is important to note that the T_e([N II])–values that we obtain for the whole-slit and the background-gas spectra of positions 5 and 6 only show differences on the order of a few tens of kelvins. This indicates that the contribution of proplyds in the integrated spectrum does not produce a substantial increase of the derived electron temperature. On the other hand, in contrast with what happens in proplyds, the increase of T_e([N II]) that we see in the HH objects does not seem to be related to collisional deexcitation. This is suggested because the HH objects show lower values of n_e and lower T_e([N II]) peaks than those of the proplyds, because their values of T_e([N II]) and T_e([O III]) show similar enhancements (see Figs. 4*b* and 7*b*), and because of the spatial coincidence of conspicuous similar peaks in both the [N II] λ5755 and λ6584 lines. Therefore, the [N II] emission of the HH objects should not be affected by substantial collisional deexcitation, and their electron temperature is higher, probably because the action of an additional source of heating, perhaps related to shock excitation.

5.2. *Line Fluxes*

One of the main spectral properties of HH objects is their strong emission in [Fe III] lines. In Figure 4*c*, we can see the spatial profile of the F([Fe III] λ4881)/I(Hβ) line ratio along slit position 3. For HH 204, the intensity of that line is a factor of 5 brighter than that for the Orion bar. This object also shows a similar enhancement

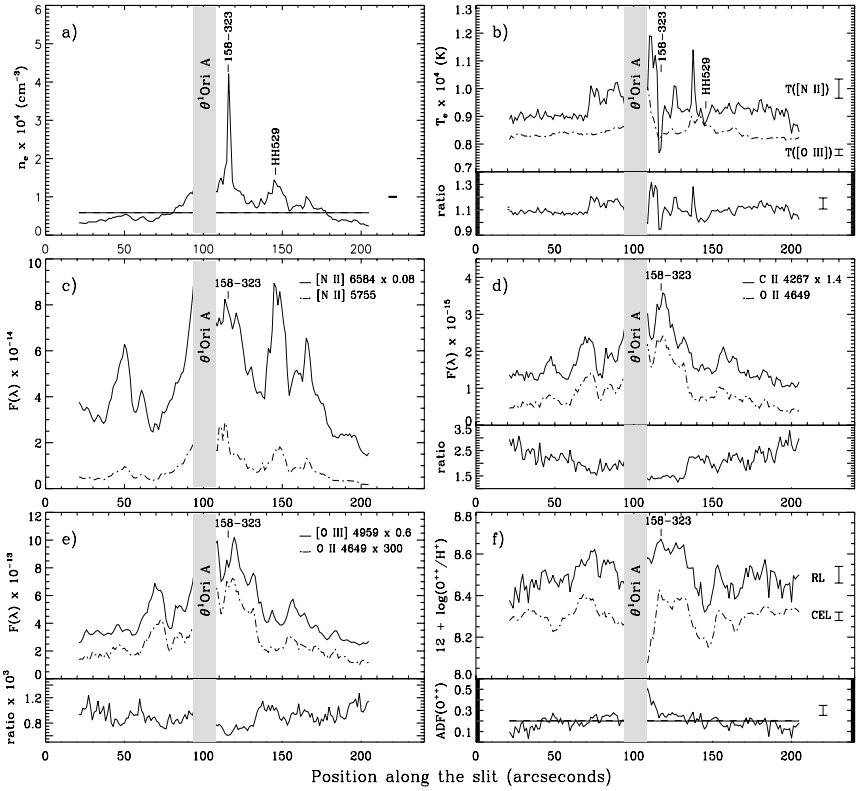

FIG. 6.—Same as Fig. 5, but for slit position 1. Positional measurement along the slit goes from north to south (see Fig. 1).

in the [O I] λ6300 line, as well as more moderate ones in the [S II] and [N II] lines. In the case of HH 202, observed in slit position 4, the intensity of the [Fe III] λ4881 line increases by a factor of 10 (Fig. 7*c*). The rest of the HH objects observed, HH 204, HH 529, and HH 530, also show enhancements in the [Fe III], [O I], [N II], and [S II] lines. These are common spectral features in shock-excited objects (see Hartigan et al. 1987). In contrast, the proplyds show [O I][4] spikes of moderate intensity and reversed spikes in the [S II] λ6717 and λ6731 lines, perhaps also due to collisional deexcitation because of the rather low critical densities of the upper levels of those [S II] transitions. The [O I] emission emerges from the photodissociation of OH in the H/H_2 front that lies close to the protoplanetary disk surface (Storzer & Hollenbach 1998).

In Figures 4*d*–8*d*, we show the spatial profiles of the pure RLs of C II λ4267 and O II λ4649 along the slit positions. The spatial distributions of the C II and O II lines are very similar. However, in the cases of the slit positions passing through the center, especially in positions 1 and 6, there is a slight decrease of the C II/O II ratio toward the central parts of the nebula. This variation could be due to the increase of the C^{3+} ionization fraction near the Trapezium stars.

In Figures 4*e*–8*e*, we show the spatial profiles of the O II λ4649 and [O III] λ4959 lines, which show a fairly similar spatial distribution in all the slit positions. This behavior is very different to that observed in PNs (Liu et al. 2000; Garnett & Dinerstein 2001; Krabbe & Copetti 2006), where the O II line emission peaks closer to the central star than does the [O III] line. We only find some localized enhancements of the [O III]/O II ratio, which are related to the positions of some proplyds (see Figs. 5*e* and 8*e*). These enhancements of the [O III]/O II ratio are correlated with the increase of the continuum due to the emission of proplyds that show a large number of absorption features that produce a decrease in the intensity of the O II λ4649 line (see § 5.3).

5.3. *The Abundance Discrepancy Factor*

Finally, Figures 4*f*–8*f* show the spatial variation of the O^{++}/H^+ ratios obtained from CELs and RLs, as well as the AD factor (ADF), which is defined as

$$\mathrm{ADF}(O^{++}) = \log(O^{++}/H^+)_{\mathrm{RLs}} - \log(O^{++}/H^+)_{\mathrm{CELs}} \quad (3)$$

for all the slit positions. The most interesting result concerning these figures is that the ADF remains fairly constant along most of the observed zones of the nebula, showing values between 0.15 and 0.20 dex, in agreement with the determinations by Esteban et al. (1998, 2004) that were based on deep echelle spectrophotometry of selected small areas of the Orion Nebula. It is necessary to note that the behavior of the ADF close to the proplyds is not confidently determined, because the O II lines are not properly measured in most of these objects due to the aforementioned strong increase of the continuum, which makes it difficult to measure of weak lines and the effects of possible absorption features of their spectra. In any case, Figure 5*f* shows a quite convincing

[4] The [O I] λ6300 line could not be corrected from the sky emission contribution. In any case, spatial variations of the intensity of this line along the slit can only be due to intrinsic nebular variations.

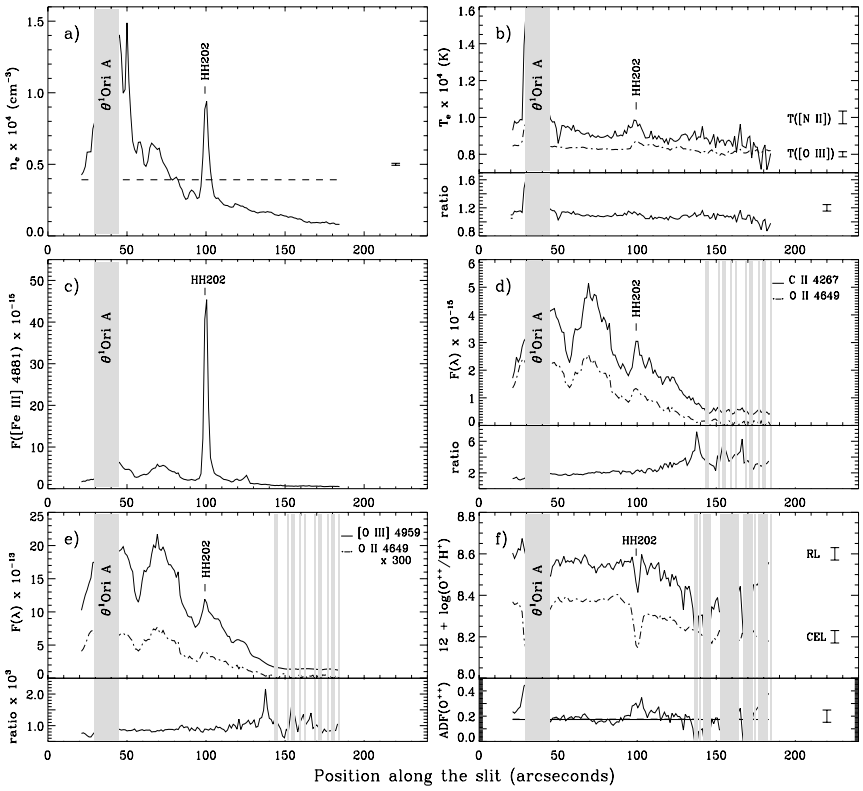

FIG. 7.—Same as Fig. 4, but for slit position 4. Positional measurement along the slit goes from southeast to northwest (see Fig. 1).

decrease of about 0.10 dex in the O^{++}/H^+ ratios obtained from CELs at the location of proplyd 177−341.

Another remarkable feature of the ADF along the slits can also be seen in Figure 5*f*, where we find a slightly higher ADF in an area between proplyds 159−350 and 177−341. It is interesting to note that slit position 5 (Fig. 8*f*) also shows the same higher values of the ADF between proplyd 159−350 and the area just at the north of proplyd 177−341. This common behavior in both slit positions indicates that the local increase of the ADF should be real. This enigmatic zone of relatively high values of the ADF has an apparent diameter of about 30″ and is located about 23″ south of the star θ^1 Ori C. There is no apparent morphological and/or kinematical feature related to this zone.

In Figures 5*f*–8*f*, we also include the values of the ADF that correspond to the whole-slit and background-gas spectra. It can be seen that the ADF of the background-gas spectrum is consistent with the average value of the different individual apertures extracted from the slit positions. However, the ADF obtained for the whole-slit spectrum, which is almost coincident with that of the background-gas spectrum in slit positions 1, 3, and 4, is substantially lower, about 0.1 dex, in slit positions 6 and 5 (Figs. 5*f* and 8*f*, respectively). The reason for this surprising result is most probably related to the strong contribution of the proplyds to the continuum of the integrated spectra, and that this contribution is producing some absorption in the O II lines. In fact, in slit positions 5 and 6, the continuum adjacent to the O II λ4649 line is about a factor of 1.7 higher in the whole-slit spectrum than in the background-gas one (see Fig. 10 for slit position 5). This higher continuum is also associated with a decrease of the intensity ratios of the O II lines with respect to Hβ. For example, the I(O II λ4649)/I(Hβ) ratio is about 25% lower in the whole-slit spectrum than in the background-gas spectrum of slit position 6.

In Figures 4*f* and 7*f*, we note that the ADF is particularly large, reaching even values up to 0.6 dex, at the locations of HH 203, HH 204, and HH 202. The large increase of the ADF is due to the low values of the O^{++}/H^+ ratios determined by CELs in these zones. In contrast, the O^{++} abundances determined by RLs do not show such a strong localized decrease. It is interesting to compare the behavior of the ADF at the HH objects and at the Orion bar in Figure 4. At the bar, we can see a similar decrease of the O^{++}/H^+ ratios determined from both kinds of lines, but which produce an ADF similar to the mean value along the slit. As has been discussed above, collisional deexcitation does not seem to affect the intensity of the nebular [N II] lines at HH 203 and HH 204, and therefore, if we consider the larger critical densities of the [O III] lines, this effect is even less likely to be producing the observed decrease of the O^{++}/H^+ ratios determined from CELs. The observed behavior of the ADF in the HH objects could be explained by the presence of localized heating due to a nonradiative process, most likely shock excitation, that would lead to the derivation of a lower O^{++}/H^+ (CELs) ratio, and this seems to be the case for HH 204, which shows a conspicuous spike of T_e([O III]) (Fig. 4*b*). However, this hypothesis fails to reproduce the presence of high ADFs in HH 203 and HH 202, where there are no spikes of T_e([O III]). Another explanation could be the presence of a localized high value of t^2 in those particular zones, but unfortunately, we cannot check this possibility with our data. Finally, the other HH objects that

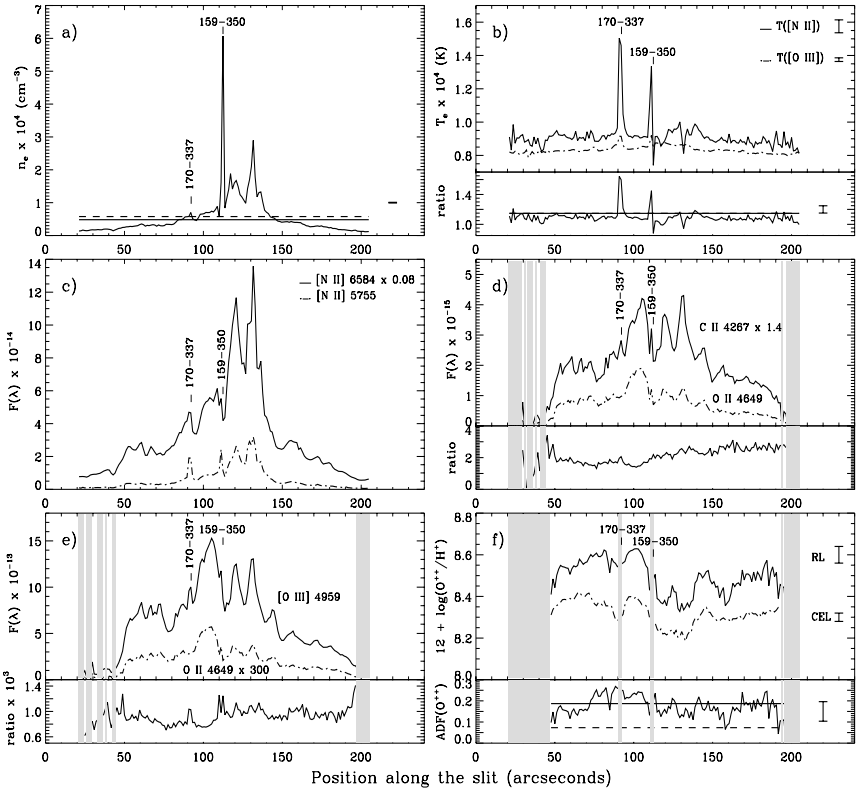

FIG. 8.—Same as Fig. 5, but for slit position 5. Positional measurement along the slit goes from northeast to southwest (see Fig. 1).

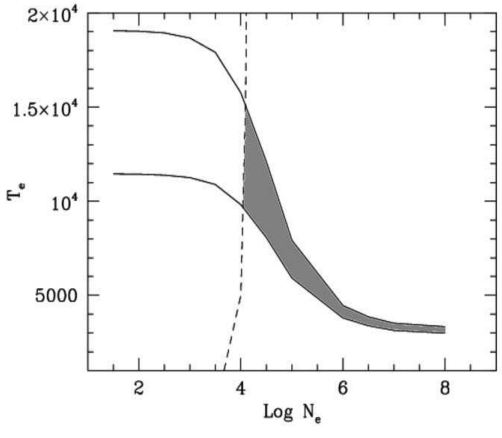

FIG. 9.—Plot of T_e vs. n_e. The solid lines represent the theoretical curves of the n_e and T_e pairs that reproduce the observed range of values of the [N II] 5755/6584 line ratio measured in the proplyds. The dashed line represents the lower limit of n_e, corresponding to the lowest value of the [S II] 6731/6717 ratio measured in the proplyds. The gray area represents the permitted zone for the average spectral properties of the proplyds. The theoretical predictions have been constructed with emissivities calculated by the photoionization code PHOTO as described in Stasińska (2005), kindly provided by G. Stasińska (2007, private communication).

are observed, HH 529 and HH 530, do not show any distinguishable enhancement of the ADF.

6. RADIAL DISTRIBUTIONS OF SOME RELEVANT NEBULAR PARAMETERS

We have constructed radial distribution diagrams of several nebular parameters, combining the data of the different slit positions

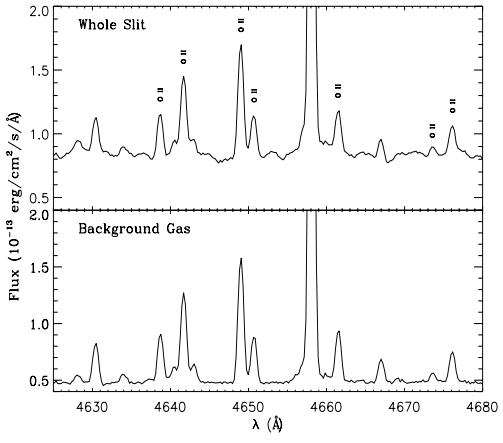

FIG. 10.—Comparison of the spectral area around multiplet 1 of O II for the whole-slit (*top*) and background-gas (*bottom*) spectra of slit position 5. Note the rather different contribution of the continuum emission. The whole-slit spectrum includes the emission of proplyds, and the background-gas spectrum does not.

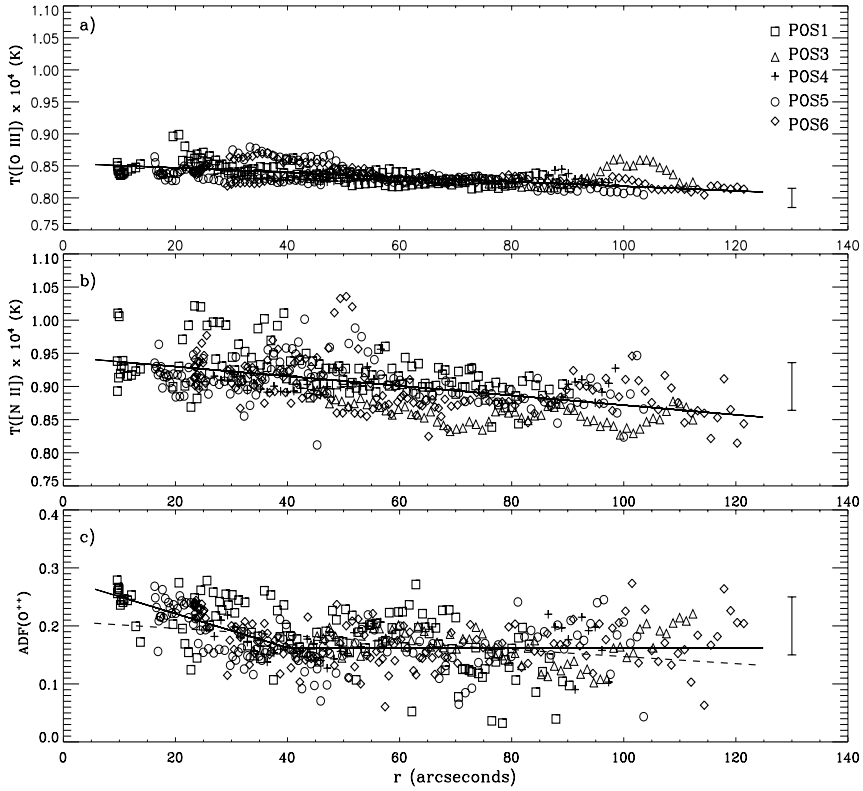

FIG. 11.—Radial distribution of the values of several nebular parameters along the Orion Nebula. We have included the data of the apertures of all slit positions, excluding those associated with proplyds or Herbig-Haro objects; i.e., the figures show the behavior of the featureless ionized gas. The abscissa axis indicates the projected angular distance of the center of each individual one-dimensional spectrum with respect to θ^1 Ori C. Symbols are described in panel (*a*). Typical error bars are included in the different diagrams. (*a*) Distribution of T_e([O III]). The solid line represents a least-squares linear fit to the data. (*b*) Distribution of T_e([N II]). The solid line represents a least-squares linear fit to the data. (*c*) Distribution of ADF(O^{++}). The dashed line represents a least-squares linear fit to the data, and the solid line represents a divided least-squares linear fit to the data into two regions, inside and outside of 40″. The fits to the data are given in the text.

and projecting the angular distance of the center of each individual one-dimensional spectrum with respect to θ^1 Ori C (Fig. 11). In these diagrams, we have only included the data of those apertures corresponding to the background gas; i.e., we have excluded all the points associated with proplyds or HH objects. We include the same points in all three panels of Figure 11, and only those for which the ADF was calculated. These diagrams permit us to study possible large-scale variations of the properties of the ionized gas across the nebula.

In Figure 11*a*, we show the radial distribution of T_e([O III]), which shows a slight but clear general decrease with increasing distance from θ^1 Ori C. In this figure, a bump can be seen in the temperature distribution of slit position 3 between 90″ and 120″. This bump corresponds to the local increase of T_e([O III]) that occurs at the inner part of the Orion bar (see also Fig. 4*b*). We have made a least-squares linear fit to the data shown in Figure 11*a*, but excluding those points belonging to the Orion bar. The result is

$$T_e([\mathrm{O\ III}])(\mathrm{K}) = 8540 - 3.6r, \qquad (4)$$

where r is the distance from θ^1 Ori C in units of arcseconds. The uncertainty of the slope is 0.2 K arcsec^{-1}, and the Spearman's correlation coefficient is 0.63 (hereafter, all the correlation coefficients we use are Spearman's). Walter et al. (1992) obtained a radial distribution of T_e([O III]) with a positive slope of 6.7 K arcsec^{-1} in the northwestern quadrant of the nebula, fitting their own data and others from the literature. The result of these authors disagrees with the clear behavior shown by our data in Figure 11*a*, which seems to be independent of the location of each slit position and even includes zones of the northwestern quadrant, our slit position 4. On the other hand, O'Dell et al. (2003) do not find significant spatial variations of T_e([O III]) across the nebula in their high-resolution map of the [O III] ratio obtained by the WFPC at the *HST*. As we can see, the different results regarding the large-scale temperature variations in the Orion Nebula are contradictory; however, we consider our data set to be more reliable than the previous ones, as it is based on homogeneous, higher signal-to-noise ratio spectroscopic observations.

In Figure 11*b*, it is evident that T_e([N II]) also shows a radial decrease. The least-squares linear fit to the data gives

$$T_e([\mathrm{N\ II}])(\mathrm{K}) = 9460 - 7.8r. \qquad (5)$$

We can see that the slope of the fit is larger than that obtained for T_e([O III]), and in this case, the result agrees qualitatively with the temperature gradient obtained by Walter et al. (1992) from the [N II] lines (−17.1 K arcsec^{-1}) in the inner 170″ of the nebula. The uncertainty of the slope of our fit is 0.6 K arcsec^{-1}, and its correlation coefficient is 0.52. Sánchez et al. (2007) obtain a bidimensional map of the spatial distribution of T_e([N II]), and they

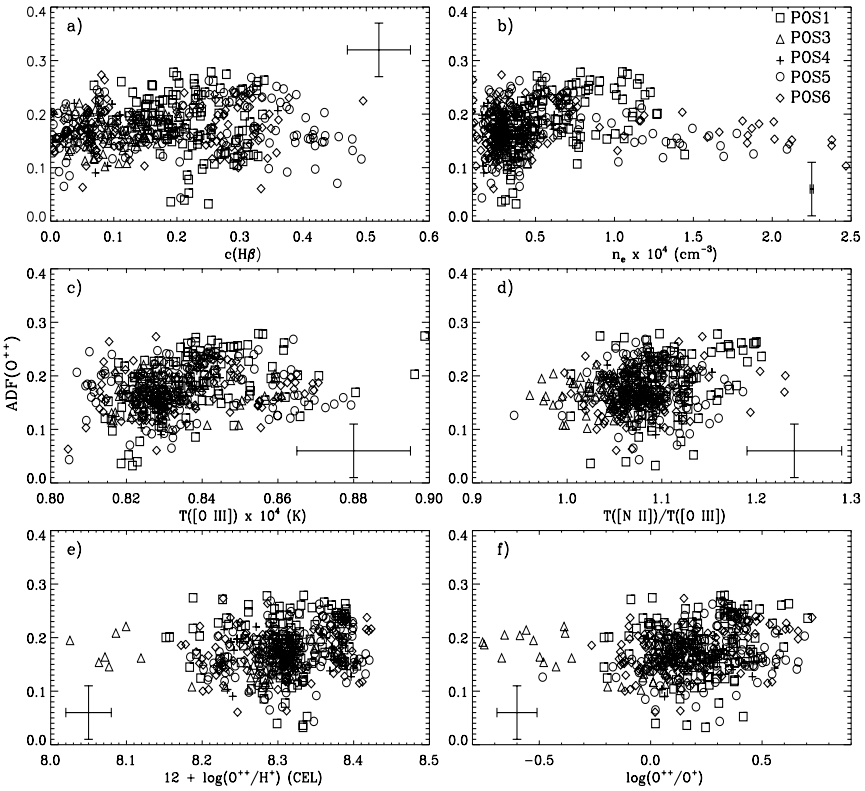

FIG. 12.—Abundance discrepancy factor of O^{++}, ADF(O^{++}), vs. several nebular parameters. We include the data from all slit positions. Symbols are described in panel (*b*). Typical error bars are included in each panel. (*a*) ADF(O^{++}) vs. $c(H\beta)$. (*b*) ADF(O^{++}) vs. n_e. (*c*) ADF(O^{++}) vs. T_e([O III]). (*d*) ADF(O^{++}) vs. the ratio T_e([N II])/T_e([O III]). (*e*) ADF(O^{++}) vs. the O^{++} abundance determined from CELs. (*f*) ADF(O^{++}) vs. the ratio O^{++}/O^{+}.

also find that this parameter is higher near the Trapezium stars and drops toward the outer zones of the nebula, in qualitative agreement with our result.

Finally, in Figure 11*c*, we show the radial distribution of the ADF(O^{++}) across the nebula. In this figure, part of the relatively large dispersion is due to the large observational uncertainty in several apertures. In fact, most of the data points with the highest and lowest values of the ADF correspond to low signal-to-noise ratio determinations at the edges of slit positions 1, 4, and 5. Despite the dispersion being relatively large, the first visual impression suggests that the ADF is rather constant or very slightly decreasing toward the outer parts of the nebula. In fact, the least-squares linear fit of all the points gives

$$\mathrm{ADF}(\mathrm{O}^{++}) = 0.2050 - 0.0005r, \qquad (6)$$

but with a very low correlation coefficient (0.32). However, other possibilities of fitting are possible. A more detailed inspection of Figure 11*c* shows that the ADF seems to increase toward the center, in the innermost 40″ of the nebula, and that this parameter becames basically constant for larger distances (the inner points of slit positions 1 and 5 consistently suggest the same tendency). We have divided the least-squares linear fit to the ADF into two regions, the first for the points in the inner 40″, and the second for the points outside this area, for which we have assumed a zero slope. The fits are the following:

$$\mathrm{ADF}(\mathrm{O}^{++}) = 0.279 - 0.003r \quad (r \leq 40''), \qquad (7)$$

with a correlation coefficient of 0.58, and

$$\mathrm{ADF}(\mathrm{O}^{++}) = 0.163 \quad (r > 40''). \qquad (8)$$

This apparent increase of the ADF toward the inner zones of the nebula can be ultimately related to two other tendencies that we have found in our data: first, the clear correlation illustrated in Figure 11*a*, which shows that T_e([O III]) is higher in the zones near the Trapezium stars; and second, the possible weak correlation between the ADF and T_e([O III]) that will be discussed in § 7. Therefore, the ADF seems to increase very slightly in the inner and systematically hotter zones of the nebula. If this behavior is real, it would indicate that whatever process is producing the ADF increases somehow with the local ionization of the gas, or that it depends on the distance between θ^1 Ori C and the ionization front, from which most of the nebular emission comes. This last possibility arises because, due to the blister geometry of the Orion Nebula, the smaller distance of the Trapezium stars to the main ionization front occurs precisely behind that massive star cluster (see Wen & O'Dell 1995).

7. CORRELATIONS BETWEEN THE ADF AND OTHER NEBULAR PROPERTIES

In order to shed some light on the physical nature of the ADF problem, we have explored the relationship of this parameter with other nebular properties determined from our one-dimensional spectra. Figure 12 illustrates the dependence of the ADF(O^{++})

TABLE 4
VALUES OF t^2_A, $t^2_{A,\mathrm{er}}$, AND t^2_I

Slit Position	$t^2_A(O^{++})$	$t^2_{A,\mathrm{er}}(O^{++})$	$t^2_A(N^+)$	$t^2_{A,\mathrm{er}}(N^+)$	$\langle t^2_I(O^{++})\rangle$
1.....	0.0013	0.0002	0.0127	0.0015	0.028
3.....	0.0004	0.0006	0.0010	0.0011	0.038
4.....	0.0008	0.0003	0.0055	0.0016	0.029
5.....	0.0004	0.0002	0.0126	0.0019	0.025
6.....	0.0005	0.0002	0.0024	0.0017	0.025

with respect to $c(\mathrm{H}\beta)$ (Fig. 12*a*), n_e (Fig. 12*b*), T_e([O III]) (Fig. 12*c*), the T_e([N II])/T_e([O III]) ratio (Fig. 12*d*), the O^{++} abundance determined from CELs (Fig. 12*e*), and the O^{++}/O^+ ratio (Fig. 12*f*). As in Figure 11, we have only included the data of the apertures corresponding to the background gas. Figure 12*a* indicates that the ADF does not depend on the amount of dust present in the line of sight of each individual one-dimensional spectrum. Also, there is no correlation between the ADF and n_e, as is shown in Figure 12*b*. However, from this figure it would seem that ADFs larger than about 0.15 dex are only found in zones with $n_e < 1.3\times10^4$ cm^{-3}. This apparent trend is incidentally produced by the apertures of slit position 1, which are located near θ^1 Ori C and show the largest values of the ADF, a behavior that does not seem to be related to n_e, but perhaps to the increase of T_e([O III]), as we will see below. The large dispersion of the ADF for the lowest densities shown in Figure 12*b* is an observational bias. The less dense zones show the lowest surface brightnesses and therefore have the faintest spectra, implying larger uncertainties in their ADF determinations. The behavior of the ADF with respect to T_e([O III]) is shown in Figure 12*c* and seems to show an apparent weak positive correlation, although T_e([O III]) shows a rather narrow interval of values in the nebula.

The other temperature indicator, T_e([N II]), shows similar behavior, and this is reflected in Figure 12*d*, where we plot the ADF versus the T_e([N II])/T_e([O III]) ratio. It is interesting to note that in Figure 12*d*, the data points are distributed in such a way that they delineate the cloud of uncertainty around the average value of the ADF and of the T_e([N II])/T_e([O III]) ratio, illustrating the conclusion that the portion of the nebula observed shows a tight proportionality between both quantities. The lack of correlation between the ADF and the ratio of electron temperatures of ions located in different zones of the nebula indicates that the natural temperature gradients that should exist in ionized nebulae, due to the different spatial locations of the main nebular coolants, do not play a significant role in producing the observed ADF in the Orion Nebula. This result is consistent with that found by García-Rojas & Esteban (2007) in their analysis of integrated spectra of a sample of Galactic and extragalactic H II regions. Figure 12*e* also shows a lack of correlation between the ADF and the O^{++}/H^+ ratio obtained from CELs; a similar diagram is found for the case of the O^{++} abundance obtained from RLs, although the range of variation of the O^{++}/H^+ ratio is very narrow. Only the points belonging to the Orion bar show values of the O^{++} abundance between 0.2 and 0.3 dex lower than the typical ones of the rest of the nebula, but their corresponding ADF is similar. Finally, Figure 12*f* represents the behavior of the ADF with respect to the O^{++}/O^+ ratio, and it is evident that, despite the relatively large range of values covered by the ionic ratio, there is not an apparent trend between these quantities.

8. TEMPERATURE FLUCTUATIONS

Following the formulation proposed by Peimbert (1967), the temperature fluctuation over the observed volume of a nebula can be parameterized in terms of the average temperature, T_0, and the mean-square electron temperature fluctuation, t^2, which are defined as

$$T_0 = \frac{\int T_e n_e n_i\, dV}{\int n_e n_i\, dV}, \tag{9}$$

$$t^2 = \frac{\int (T_e - T_0)^2 n_e n_i\, dV}{T_0^2 \int n_e n_i\, dV}, \tag{10}$$

where n_i is the ion density. The integrations are calculated over the entire volume, and the element of volume, dV, can be expressed as $dl\, dA$, the product of the elements of the length of the column along the line of sight and the surface area in the plane of the sky, respectively. Our spatially resolved spectroscopic data do not permit us to obtain a direct determination of t^2 along the line of sight. However, a discrete estimation of t^2 in the plane of the sky, t^2_A, can be obtained through the point-to-point determinations of T_e that we have obtained from the individual one-dimensional spectra extracted along the slit positions. Following a similar procedure as Liu (1998), Rubin et al. (2003), and Krabbe & Copetti (2005), and assuming that $n_e \approx n(\mathrm{H}^+)$ in all the points of the nebula, we can compute $T_{0,A}$ and t^2_A using the following equations:

$$T_{0,A} = \frac{\sum_j T_{e,j} n^2_{e,j} [n(\mathrm{X}^{+i})/n(\mathrm{H}^+)]_j}{\sum_j n^2_{e,j} [n(\mathrm{X}^{+i})/n(\mathrm{H}^+)]_j}, \tag{11}$$

$$t^2_A = \frac{\sum_j (T_{e,j} - T_{0,A})^2 n^2_{e,j} [n(\mathrm{X}^{+i})/n(\mathrm{H}^+)]_j}{T^2_{0,A} \sum_j n^2_{e,j} [n(\mathrm{X}^{+i})/n(\mathrm{H}^+)]_j}, \tag{12}$$

where $T_{e,j}$, $n_{e,j}$, and $[n(\mathrm{X}^{+i})/n(\mathrm{H}^+)]_j$ are the electron temperature, the electron density, and the ionic abundance of the X^{+i}th species in the jth aperture extracted from a given slit position. The quantity $T_{e,j}$ used in the equations above corresponds to the average temperatures along the line of sight that crosses the nebula at the jth aperture, and it can be expressed as

$$T_{e,j} = \frac{\int T_e n_e n_i\, dl}{\int n_e n_i\, dl}. \tag{13}$$

If we take this into account, it is likely that the value of t^2_A that we obtain is substantially lower than t^2, and, more strictly speaking, it should be considered a lower limit to t^2 (see further argumentation given by Rubin et al. [2003] and O'Dell et al. [2003]). In Table 4, we summarize the values of t^2_A that we obtain for each slit position and for each of the two ions for which we have determinations of T_e. We have included all the points for which T_e has been determined in the sums, even those belonging to proplyds or HH objects, in order to explore the effect of these structures into the derivation of t^2. Part of the value of t^2_A that we calculate for each ion comes from errors in the measurement of the emission-line ratios, so the intrinsic value of t^2_A must be corrected by the relative mean quadratic error of the T_e measurements, $t^2_{A,\mathrm{er}}$, with the simple relation $t^2_A - t^2_{A,\mathrm{er}}$ (see O'Dell et al. 2003; Krabbe & Copetti 2005). The values of $t^2_{A,\mathrm{er}}$ for each ion and slit position are also included in Table 4, and they are always lower than the corresponding values of t^2_A, except in the case of slit position 3, where the errors are slightly higher, indicating that most of the temperature variation along slit position 3 is produced by measurement uncertainties. The corrected value of t^2_A that we obtain is very low in all cases: $t^2_A(O^{++})$ ranges from $\sim$0 to 0.0011, and $t^2_A(N^+)$ goes from $\sim$0 to 0.0112. However, Rubin et al. (2003)

obtain $t^2_A(O^{++}) = 0.0068–0.0176$ and $t^2_A(N^+) = 0.0058–0.0175$ for the different slit positions they observe in the Orion Nebula, values that are relatively consistent with ours in the case of $t^2_A(N^+)$ but are considerably larger in the case of $t^2_A(O^{++})$. On the other hand, O'Dell et al. (2003) obtain $t^2_A(O^{++}) = 0.0050–0.0156$, which are values in good agreement with those obtained by Rubin et al. (2003), but also much higher than our determinations. The reason of this discrepancy is difficult to ascertain. The resolution element of each set of observations is rather different; our apertures are $1.2'' \times 1.03''$, and those of Rubin et al. (2003) and O'Dell et al. (2003) are $0.5'' \times 0.5''$ and $0.1'' \times 0.1''$, respectively. If the spatial resolution has something to do with the different values of $t^2_A(O^{++})$ obtained in this work and the previous works, this would imply that the small-scale spatial variations of T_e([O III]) have a characteristic size of between $0.5''$ and $1.0''$ and that those related to T_e([N II]) are larger: at least on the order of the size of our apertures. In any case, this seems to us to be a rather unlikely scenario. Another difference between our determinations and those of Rubin et al. (2003) and O'Dell et al. (2003) is that those authors use a relation for determining T_e from the [O III] line ratio that is valid in the low-density limit, while our calculations are based on solving the statistical equilibrium equations for the value of n_e measured for each particular aperture. We have explored the effect of this different procedure by applying equation (5) of Rubin et al. (2003), which was also used by O'Dell et al. (2003), to our data of slit position 6. In Figure 13, we show the ratio of the values of T_e([O III]) computed using the low-density limit approximation equation and our own determinations, and we find a systematical bias of about 1.12 and a small bump (∼5%) that is coincident with the zone of the highest density at the southwest of the Trapezium (see Fig. 5*a*). The use of both different procedures does not substantially increase the T_e dispersion. In fact, using the low-density limit approximation, we obtain $t^2_A(O^{++}) = 0.0008$ for slit position 6, which is only 60% larger than our calculations. Therefore, the use of a low-density limit approximation does not explain the large differences of $t^2_A(O^{++})$ that are found between our results and those of the other authors. A final possibility is the different signal-to-noise ratios of the data sets that we are comparing. As was mentioned in § 5.1, this is a likely source of discrepancies in the case of the long-slit data of Rubin et al. (2003), but this is more difficult to ascertain in the case of the data of O'Dell et al. (2003). These authors estimate a representative probable error of about 4.2% for their point-to-point T_e([O III]) determinations, which corresponds to a value of $t^2_{A,er}$ of about 0.0017, which is larger than our observational errors, but much lower than their nominal values of $t^2_A(O^{++})$, indicating that the temperature variations obtained by O'Dell et al. (2003) should be real if the errors are not largely underestimated. Only observations combining a very high signal-to-noise ratio and very high spatial resolution will be able to solve this puzzle.

As has been stated before, our spatially resolved spectroscopic data do not permit us to determine the value of t^2 along the line of sight, which we denote as t^2_l, but an indirect estimate can be obtained if we assume that the ADF is produced by the presence of such temperature variations. Although this is still a controversial possibility, there are some pieces of evidence that indicate that this may be correct, at least in the case of H II regions (see García-Rojas & Esteban 2007). O'Dell et al. (2003) show that the relation between t^2_A, t^2_l, and the total t^2 in three dimensions is

$$t^2 = t^2_A + \langle t^2_l \rangle, \tag{14}$$

where $\langle t^2_l \rangle$ is the average over all lines of sight. In Table 4, we include the values of $\langle t^2_l(O^{++}) \rangle$ that we obtain for each slit position. These values have been estimated from the average ADF(O^{++}) of the individual apertures of each slit position. From the table, it can be seen that the values of $\langle t^2_l(O^{++}) \rangle$ are rather similar for the different slit positions and are consistent with previous determinations, between 0.018 and 0.028 (Esteban et al. 1998, 2004), except in the case of slit position 3, which shows a rather higher value. This large temperature fluctuation comes from the also larger ADFs that we obtain at HH 203 and HH 204 (see Fig. 4*f*). If we take into account that the values of $t^2_A(O^{++})$ are much lower than the values of $\langle t^2_l(O^{++}) \rangle$, we may make the approximation that $t^2(O^{++}) \approx \langle t^2_l(O^{++}) \rangle$. To follow the arguments of O'Dell et al. (2003), this result would indicate that the hypothetical thermal inhomogeneities producing t^2 should be small-scale ones and unresolved by our data; i.e., smaller than our spatial resolution limit of about $1''$. On the other hand, our spatial resolution is unable to resolve the size of $10^{13}–10^{15}$ cm that Stasińska et al. (2007) derive for the metal-rich droplets they claim to be the most likely explanation of the AD.

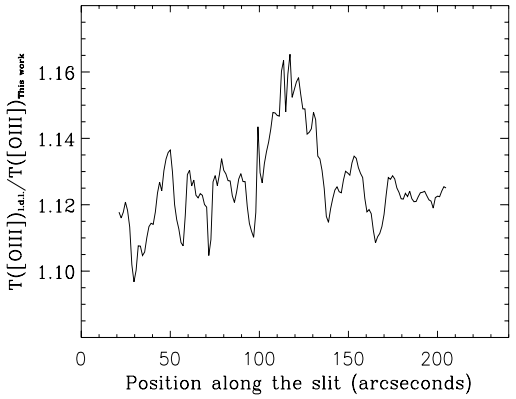

FIG. 13.—Ratio of the T_e([O III]) computed using the low-density limit approximation equation used by Rubin et al. (2003) to the value computed from our own determinations along slit position 6. Positional measurement along the slit goes from northeast to southwest (see Fig. 1).

9. CONCLUSIONS

We have studied the spatial distribution of a large number of nebular quantities along five slit positions covering different morphological zones of the Orion Nebula. The resolution element of the observations was $1.2'' \times 1.03''$. The studied quantities were $c(H\beta)$, n_e, T_e([N II]), T_e([O III]), the intensity of several selected lines (Hβ, C II λ4267, O II λ4649, [O III] λ4959, [Fe III] λ4881, [N II] λ5755 and λ6584, [O I] λ6300, and [S II] λ6717 and λ6731), the O^{++}/H^+ ratio obtained from collisionally excited lines (CELs) and recombination lines (RLs), and the C^{++}/H^+ ratio obtained from RLs. The total number of apertures or one-dimensional spectra extracted was 730. We have been able to determine the O^{++}/H^+ ratio from the faint RLs of this ion in 92% of the apertures.

The spatial distribution of n_e shows a large range of variation, larger than an order of magnitude, across the nebula, with local maxima associated with the positions of protoplanetary disks (proplyds), Herbig-Haro objects, the Orion bar, and the brightest area of the nebula at the southwest of the Trapezium. The proplyds show quite prominent spikes of T_e([N II]) and much lesser ones of T_e([O III]). This could be due to collisional deexcitation on the nebular lines of [N II] because of the high densities of these

objects. The Herbig-Haro objects also show somewhat higher values of T_e([N II]), but in this case, the origin could be related to extra heating of the gas due to shock excitation. The spatial distribution of the O II λ4949 and [O III] λ4959 lines is fairly similar along all the slit positions: a very different behavior from that observed in planetary nebulae. We have found that the abundance discrepancy factor (ADF) of O^{++}, which is the difference between the O^{++} abundance determined from RLs and that from CELs, remains, in general, rather constant along most of the observed areas of the nebula, showing values of between 0.15 and 0.20 dex. However, there are some localized enhancements of the ADF, especially at the position of the Herbig-Haro objects HH 202, HH 203, and HH 204.

The combined data of all slit positions indicate a clear decrease of T_e([N II]) and T_e([O III]) with increasing distance from the main ionizing source of the nebula, θ^1 Ori C. On the other hand, the radial distribution of the ADF shows a rather constant value across the nebula, except at the inner 40″, where the ADF seems to increase very slightly toward θ^1 Ori C.

We have explored possible correlations between the ADF of O^{++} and other nebular quantities, and we find a possible very weak increase of the ADF for higher electron temperatures. There are no apparent trends between the ADF and $c(H\beta)$, n_e, the T_e([N II])/T_e([O III]) ratio, the O^{++} abundance, or the O^{++}/O^{+} ratio.

Our spatially resolved spectroscopy allows us to estimate the value of the mean-square electron temperature fluctuation in the plane of the sky, which is a lower limit to the traditional t^2 parameter. We find very low values in all cases, a result that is in contradiction with previous estimates from the literature. Our results indicate that the hypothetical thermal inhomogeneities, if they exist, should be lower than our spatial resolution limit of about 1″.

It is clear that further studies on the T_e, chemical abundances, and ADF distributions at subarcsecond spatial scales are necessary in trying to disentangle (1) whether small spatial scale temperature fluctuations and/or metal-rich droplets are really present in the Orion Nebula in particular and H II regions in general and (2) the origin of the AD problem and its possible relation to t^2 and other nebular properties. The observations needed for this task are very difficult even for ground-based large-aperture telescopes and, at this time, are unfeasible with the current space telescopes and their available instrumentation.

We thank G. Stasińska and M. Rodríguez for their fruitful comments and help. We are grateful to the referee, Y. Tsamis, for his careful reading of the paper and his comments. This work has been funded by the Spanish Ministerio de Ciencia y Tecnología (MCyT) under project AYA2004-07466.

REFERENCES

Baldwin, J. A., Ferland, G. J., Martin, P. G., Corbin, M. R., Cota, S. A., Peterson, B. M., & Slettebak, A. 1991, ApJ, 374, 580
Bally, J., O'Dell, C. R., & McCaughrean, M. J. 2000, AJ, 119, 2919
Castañeda, H. O., Vilchez, J. M., & Copetti, M. V. F. 1992, A&A, 260, 370
Castellanos, M., Díaz, A. I., & Terlevich, E. 2002, MNRAS, 329, 315
Costero, R., & Peimbert, M. 1970, Bol. Obs. Tonantzintla Tacubaya, 5, 229
Davey, A. R., Storey, P. J., & Kisielius, R. 2000, A&AS, 142, 85
Doi, T., O'Dell, C. R., & Hartigan, P. 2004, AJ, 127, 3456
Esteban, C., García-Rojas, J., Peimbert, M., Peimbert, A., Ruiz, M. T., Rodríguez, M., & Carigi, L. 2005, ApJ, 618, L95
Esteban, C., Peimbert, M., García-Rojas, J., Ruiz, M. T., Peimbert, A., & Rodríguez, M. 2004, MNRAS, 355, 229
Esteban, C., Peimbert, M., Torres-Peimbert, S., & Escalante, V. 1998, MNRAS, 295, 401
Esteban, C., Peimbert, M., Torres-Peimbert, S., & Rodríguez, M. 2002, ApJ, 581, 241
French, H. B. 1983, ApJ, 273, 214
García-Rojas, J. 2006, Ph.D. thesis, Univ. La Laguna
García-Rojas, J., & Esteban, C. 2007, ApJ, 670, 457
García-Rojas, J., Esteban, C., Peimbert, A., Peimbert, M., Rodríguez, M., & Ruiz, M. T. 2005, MNRAS, 362, 301
García-Rojas, J., Esteban, C., Peimbert, A., Rodríguez, M., Peimbert, M., & Ruiz, M. T. 2007, Rev. Mex. AA, 43, 3
García-Rojas, J., Esteban, C., Peimbert, M., Costado, M. T., Rodríguez, M., Peimbert, A., & Ruiz, M. T. 2006, MNRAS, 368, 253
García-Rojas, J., Esteban, C., Peimbert, M., Rodríguez, M., Ruiz, M. T., & Peimbert, A. 2004, ApJS, 153, 501
Garnett, D. R., & Dinerstein, H. L. 2001, ApJ, 558, 145
Hartigan, P., Raymond, J., & Hartmann, L. 1987, ApJ, 316, 323
Henney, W. J., O'Dell, C. R., Zapata, L. A., García-Díaz, M. T., Rodríguez, L. F., & Robberto, M. 2007, AJ, 133, 2192
Krabbe, A. C., & Copetti, M. V. F. 2005, A&A, 443, 981
———. 2006, A&A, 450, 159
Liu, X.-W. 1998, MNRAS, 295, 699
Liu, X.-W., Storey, P. J., Barlow, M. J., Danziger, I. J., Cohen, M., & Bryce, M. 2000, MNRAS, 312, 585
López-Sánchez, A. R., Esteban, C., García-Rojas, J., Peimbert, M., & Rodríguez, M. 2007, ApJ, 656, 168
Mathis, J. S., & Liu, X.-W. 1999, ApJ, 521, 212
O'Dell, C. R. 2001, PASP, 113, 29
O'Dell, C. R., Peimbert, M., & Peimbert, A. 2003, AJ, 125, 2590
O'Dell, C. R., & Wong, K. 1996, AJ, 111, 846
O'Dell, C. R., & Yusef-Zadeh, F. 2000, AJ, 120, 382
Osterbrock, D. E., & Ferland, G. J. 2006, Astrophysics of Gaseous Nebulae and Active Galactic Nuclei (2nd ed.; Sausalito: University Science Books)
Peimbert, A., Peimbert, M., & Ruiz, M. T. 2005, ApJ, 634, 1056
Peimbert, M. 1967, ApJ, 150, 825
Peimbert, M., Storey, P. J., & Torres-Peimbert, S. 1993, ApJ, 414, 626
Pogge, R. W., Owen, J. M., & Atwood, B. 1992, ApJ, 399, 147
Rola, C., & Stasińska, G. 1994, A&A, 282, 199
Rubin, R. H., Martin, P. G., Dufour, R. J., Ferland, G. J., Blagrave, K. P. M., Liu, X.-W., Nguyen, J. F., & Baldwin, J. A. 2003, MNRAS, 340, 362
Ruiz, M. T., Peimbert, A., Peimbert, M., & Esteban, C. 2003, ApJ, 595, 247
Sánchez, S. F., Cardiel, N., Verheijen, M. A. W., Martín-Gordón, D., Vilchez, J. M., & Alves, J. 2007, A&A, 465, 207
Shaw, R. A., & Dufour, R. J. 1995, PASP, 107, 896
Stasińska, G. 2005, A&A, 434, 507
Stasińska, G., Tenorio-Tagle, G., Rodríguez, M., & Henney, W. J. 2007, A&A, 471, 193
Storey, P. J. 1994, A&A, 282, 999
Storey, P. J., & Hummer, D. G. 1995, MNRAS, 272, 41
Storzer, H., & Hollenbach, D. 1998, ApJ, 502, L71
Tsamis, Y. G., Barlow, M. J., Liu, X.-W., Danziger, I. J., & Storey, P. J. 2003, MNRAS, 338, 687
Tsamis, Y. G., & Péquignot, D. 2005, MNRAS, 364, 687
Walter, D. K., Dufour, R. J., & Hester, J. J. 1992, ApJ, 397, 196
Wen, Z., & O'Dell, C. R. 1995, ApJ, 438, 784

THE ASTROPHYSICAL JOURNAL, 685:679, 2008 September 20

ERRATUM: "SMALL-SCALE BEHAVIOR OF THE PHYSICAL CONDITIONS AND THE ABUNDANCE DISCREPANCY IN THE ORION NEBULA" (ApJ, 675, 389 [2008])

ADAL MESA-DELGADO, CÉSAR ESTEBAN, AND JORGE GARCÍA-ROJAS

In Table 1 of our original paper we include the coordinates of the centers of the 3.7′ long slits obtained in the observations. However, these do not correspond to the centers of the slits drawn in our Figure 1, which represents the extension of the portions of the slits that we finally analyze in the paper (we remove some sections, as indicated in Table 2). The central coordinates of these "effective" slits are given in Table E1 below.

In § 3 we indicate that the values of the reddening coefficient we obtain are somewhat low, lower than the values found in most of the literature (e.g. Esteban et al. 1998 [MNRAS, 295, 401]; O'Dell & Yusef-Zadeh 2000 [AJ, 120, 382]), but we do not discuss this fact in the paper. In particular, we find that our $c(\mathrm{H}\beta)$ values are in some regions about 0.3 or 0.4 dex lower than those found by O'Dell & Yusef-Zadeh for the same areas. We have investigated the reason of that discrepancy, and find that the data do not apparently suffer for flux calibration problems. The method we used involved measuring the $\mathrm{H}\beta$ and $\mathrm{H}\gamma$ flux ratios and comparing them with the theoretically expected values. This method demands very precise spectrophotometry, because one is using observations over a short wavelength base to determine reddening corrections over a much longer wavelength range. We have not found any error in our analysis, and hence cannot explain the differences in the extinction when compared with earlier results. However, the results of our paper are not particularly sensitive to the reddening correction.

We have calculated the effect on the $T([\mathrm{N\,II}])$ and $T([\mathrm{O\,III}])$ distributions of increasing the $c(\mathrm{H}\beta)$ by a constant value (0.3 and 0.7 dex) in all our slit positions, and the changes are not relevant for our conclusions. Obviously, the density maps are largely unaffected. In the case of an increment of 0.3 dex in $c(\mathrm{H}\beta)$, the temperatures change somewhat—about 100 K in $T([\mathrm{N\,II}])$, and considerably less for $T([\mathrm{O\,III}])$—for a given point, but the point-to-point variations are identical. The spatial behavior the abundance discrepancy factor, the main concern of the paper, is also not substantially affected, and its variation remains within the observational errors.

We are very grateful to C. R. O'Dell for his careful reading of our paper and for indicating the points discussed and corrected here, as well as the anonymous referee of this erratum.

TABLE E1
COORDINATES OF THE EFFECTIVE SLIT CENTERS

Slit Position	R.A.	Decl.
1	05 35 15.9	−05 23 25.2
3	05 35 22.2	−05 25 09.5
4	05 35 10.8	−05 22 51.3
5	05 35 15.9	−05 23 50.3
6	05 35 15.2	−05 23 53.1

3

Propiedades del gas ionizado en HH 202. I: resultados a partir de espectroscopia de campo integral con PMAS

Los objetos Herbig-Haro (HH) son fenómenos asociados con los primeros estadios de la evolución estelar. Se trata de flujos de gas a alta velocidad que interaccionan con el gas nebular y se detectan como pequeñas y brillantes nebulosidades. Los resultados encontrados en el capítulo anterior sugerirían que los objetos HH podrían jugar algún rol importante en el problema de la DA.

Por primera vez en regiones H II, y con el objetivo de estudiar el problema de la DA, se ha hecho uso de la espectroscopia de campo integral para el análisis de las distribuciones espaciales de las propiedades nebulares del gas ionizado de uno de los objetos HH más prominentes de la Nebulosa de Orión: HH 202. También, como en el capítulo anterior, se investiga la búsqueda de correlaciones entre el ADF, las condiciones físicas del gas y el parámetro de fluctuación de temperatura, t^2. Para ello, se llevan a cabo observaciones con el espectrógrafo PMAS (acrónimo de *Potsdam Multi-Aperture Spectrograph*) ubicado en el telescopio de 3.5m del Observatorio de Calar Alto.

Esta segunda parte de la tesis fue publicada en el artículo "Properties of the ionized gas in HH 202–I. Results from integral field spectroscopy with PMAS" de la revista *Monthly Notices of the Royal Astronomical Society*, Volumen 394, páginas 693 a 703, el cual se adjunta a continuación, tras el resumen.

Resumen: Presentamos los resultados obtenidos a partir de espectroscopia de campo integral con el *Potsdam Multi-Aperture Spectrograph* del objeto Herbig-Haro (HH) HH 202 con un muestreo espacial de $1''\times1''$. Hemos obtenido mapas de diferentes líneas de emisión, condiciones físicas –densidades y temperaturas electrónicas– y abundancias iónicas a partir de líneas de recombinación y líneas excitadas colisionalmente. Presentamos el primer mapa de la temperatura de Balmer y del parámetro de fluctuación de temperatura, t^2. También hemos calculado el t^2 sobre el plano del cielo, el cual es sustancialmente más pequeño que el determinado a lo largo de la línea de visión. Hemos mapeado el factor de discrepan-

cia de abundancias de O^{2+}, ADF(O^{2+}), encontrando su valor máximo en la posición del HH 202-S. Hemos explorado las relaciones entre el ADF(O^{2+}) y la densidad electrónica, las temperaturas de Balmer y [O III], el grado de ionización, así como el parámetro t^2. No hallamos correlaciones claras entre estas variables, y los resultados parecen indicar que el ADF y el t^2 son fenómenos independientes. Hemos encontrado una ligera correlación negativa entre las abundancias de O^{2+} determinadas a partir de líneas de recombinación y la temperatura, que es precisamente el comportamiento esperado en una nebulosa ionizada, por lo que parece que no hay evidencias de la presencia de grumos ricos en metales en las regiones H II.

Mon. Not. R. Astron. Soc. **394,** 693–703 (2009) doi:10.1111/j.1365-2966.2009.14392.x

Properties of the ionized gas in HH 202 – I. Results from integral field spectroscopy with PMAS⋆

A. Mesa-Delgado,[1]† L. López-Martín,[1] C. Esteban,[1] J. García-Rojas[2] and V. Luridiana[3]
[1]*Instituto de Astrofísica de Canarias, E-38200 La Laguna, Tenerife, Spain*
[2]*Instituto de Astronomía, UNAM, Apdo. Postal 70-264, 04510 México D.F., Mexico*
[3]*Instituto de Astrofísica de Andalucía (CSIC), Apdo. Correos 3004, E-18080 Granada, Spain*

Accepted 2008 December 12. Received 2008 December 10; in original form 2008 October 24

ABSTRACT

We present results from integral field spectroscopy with the Potsdam Multi-Aperture Spectrograph of the head of the Herbig–Haro (HH) object HH 202 with a spatial sampling of 1×1 arcsec^2. We have obtained maps of different emission lines, physical conditions – such as electron temperature and density – and ionic abundances from recombination and collisionally excited lines. We present the first map of the Balmer temperature and of the temperature fluctuation parameter, t^2. We have calculated the t^2 in the plane of the sky, which is substantially smaller than that determined along the line of sight. We have mapped the abundance discrepancy factor (ADF) of O^{2+}, ADF(O^{2+}), finding its maximum value at the HH 202-S position. We have explored the relations between the ADF(O^{2+}) and the electron density, the Balmer and [O III] temperatures, the ionization degree as well as the t^2 parameter. We do not find clear correlations between these properties and the results seem to support that the ADF and t^2 are independent phenomena. We have found a weak negative correlation between the O^{2+} abundance determined from recombination lines and the temperature, which is the expected behaviour in an ionized nebula, hence it seems that there is no evidence for the presence of supermetal-rich droplets in H II regions.

Key words: ISM: abundances – ISM: Herbig–Haro objects – ISM: individual: Orion Nebula – ISM: individual: HH 202.

1 INTRODUCTION

The Orion Nebula is the nearest, most observed and studied Galactic H II region. It is an active star-forming region where phenomena associated with the early stages of stellar evolution such as protoplanetary discs (proplyds) and Herbig–Haro (HH) objects can be observed in detail.

HH objects are bright nebulosities associated with high-velocity gas flows. The most prominent high-velocity feature in the nebula is the Becklin–Neugebauer/Kleinmann–Low (BN/KL) complex, which contains several HH objects (HH 201, 205, 206, 207 and 208). In addition, there are other important high-velocity flows that do not belong to the BN/KL complex, as is the case of HH 202, 203 and 204. The origin of these flows has been associated with infrared sources embedded within the Orion Molecular Cloud 1 South (see O'Dell & Henney 2008, and references therein).

HH 202 was one of the first HH objects identified in the Orion Nebula by Cantó et al. (1980) in their [S II] and [N II] images as an emission-line object showing two bright knots – the so-called HH 202-N and HH 202-S (see Fig. 1) – embedded in a more extended nebulosity with a long concave form. After its discovery, the spectroscopic work by Meaburn (1986) showed that the arc-shaped nebulosity emits in [O III] lines.

Furthermore, high spectral resolution spectroscopy in several emission lines ([O I], [S II], [N II], [O II], [S III] and Hα) has been performed in HH 202 by O'Dell, Wen & Hester (1991) who studied HH 202-S and found two velocity components. We can find in the recent literature extensive works on the gas kinematics in the Orion Nebula by Doi, O'Dell & Hartigan (2002) and O'Dell & Doi (2003), where tangential velocities have been measured, or by Doi, O'Dell & Hartigan (2004), who provide accurate radial velocity measurements, detecting up to three kinematic components in HH 202-S. In addition, the most detailed imaging study of the Orion Nebula in the [S II], [O III] and Hα lines has been carried out by O'Dell et al. (1997) with the *Hubble Space Telescope* (*HST*). These authors also detect an intense [O III] emission in the extended nebulosity of HH 202 and a strong [S II] emission at its knots. The extended [O III] emission found in all the works indicates that the main excitation

⋆Based on observations collected at the Centro Astronómico Hispano Alemán (CAHA) at Calar Alto, operated jointly by the Max-Planck Institut für Astronomie and the Instituto de Astrofísica de Andalucía (CSIC).
†E-mail: amd@iac.es

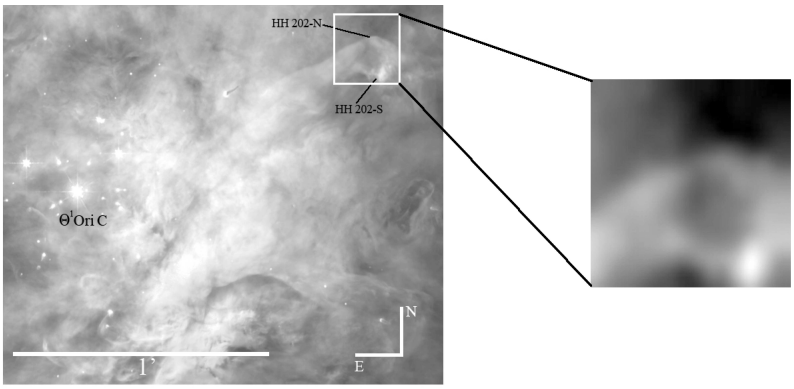

Figure 1. *HST* image of the central part of the Orion Nebula, which combines Wide-Field Planetary Camera 2 (WFPC2) images taken in different filters (O'Dell & Wong 1996). The white square corresponds to the FOV of PMAS IFU used, covering the head of HH 202. The separate close-up image on the right shows the Hα map obtained with PMAS. The original map is 16 × 16 pixel of 1 × 1 arcsec^2 size and has been rebinned to 160 × 160 pixel. Note the remarkable similarity between the *HST* image and our rebinned PMAS Hα map.

mechanism of HH 202 is the photoionization, most probably from the brightest and hottest star of the Trapezium cluster, θ^1 Ori C. This particular property – not very common in other HH objects, which are usually ionized by shocks – permits to derive the physical conditions and chemical abundances of the high-velocity gas associated with HH 202 making use of the standard techniques for the study of ionized nebulae.

Our group has studied in detail the chemical composition of the Orion Nebula in some previous papers (Esteban et al. 1998, 2004; Mesa-Delgado, Esteban & García-Rojas 2008) and is especially interested in studying the so-called abundance discrepancy (AD) problem in H II regions, which is the disagreement between the abundances of the same ion derived from collisionally excited lines (CELs) and recombination lines (RLs). From intermediate- and high-resolution spectroscopy of Galactic and extragalactic H II regions, our group has found that the O^{2+}/H^+ ratio calculated from RLs is always between 0.1 and 0.3 dex higher than the value obtained from CELs for the same region (see García-Rojas & Esteban 2007). The results obtained for H II regions are quite different to those obtained for planetary nebulae (PNe), where the AD shows a much wider range of values and could be substantially larger in some objects (e.g. Liu et al. 2000, 2006; Tsamis et al. 2003, 2004). As argued in García-Rojas & Esteban (2007), the AD problem in H II regions seems to be consistent with the predictions of the temperature fluctuation paradigm proposed by Peimbert (1967) and parametrized by the mean square of the spatial distributions of temperature, the so-called t^2 parameter. In this scenario, the AD would be produced by the very different temperature dependence of the emissivities of both kinds of lines. In any case, the existence and origin of such temperature fluctuations are still controversial. Tsamis & Péquignot (2005) and Stasińska et al. (2007) have proposed a different hypothesis in order to explain the AD in H II regions. Based on the model for heavy-element mixing of Tenorio-Tagle (1996), the presence of cold metal-rich droplets of supernova ejecta still not mixed with the ambient gas of the H II regions would produce most of the RL emission, while CEL emission would be produced by the ambient gas, which would have the typical electron temperature of an H II region and the expected composition of the local interstellar medium. In such case, the abundances from CELs would be the truly representative ones of the nebula.

Several authors have studied the spatial distribution of the physical conditions in the Orion Nebula. O'Dell, Peimbert & Peimbert (2003) have obtained a high spatial resolution map of the electron temperature in a field centred at the south-west of the Trapezium cluster from narrow-band images taken with the *HST*. They found small spatial scale temperature variations, which seem to be in quantitative agreement with the t^2 parameter determined using the AD factor (ADF) found by Esteban et al. (2004). However, Rubin et al. (2003) have taken long-slit spectroscopy making use of Space Telescope Imaging Spectrograph (STIS) at the *HST* in several positions and do not find substantial spatial variations or gradients of the physical conditions along their slits positions. More recently, Sánchez et al. (2007) have obtained a mosaic of the Orion Nebula from integral field spectroscopy with a spatial resolution of 2.7 arcsec, but lacking a confident absolute flux calibration due to bad transparency during the observations. Their electron temperature map shows clear spatial variations, and the electron density map is very rich in substructures, some of which could be related to HH objects. A more detailed view – but based on long-slit spectroscopy – has been obtained by Mesa-Delgado et al. (2008), who obtained spatial distributions – at spatial scales of 1.2 arcsec – of electron temperature, density, line intensities, ionic abundances and the ADF (defined as the difference between the abundances derived from RLs and CELs) for five slit positions crossing different morphological zones of the Orion Nebula, finding spikes in the distribution of the electron temperature and density which are related to the position of proplyds and HH objects. In particular, these authors found that the ADF shows larger values at the HH objects.

The use of the integral field spectroscopy is still in its infancy in the study of ionized nebulae and the number of works available is still rather small. In the case of PNe, Tsamis et al. (2008) have carried out the first deep study using this technique with Fibre Large Array Multi Element Spectrograph (FLAMES) at the Very Large Telescope (VLT) taking spectra of three PNe of the Galactic disc and covering the spectral range from 3964 to 5078 Å. For the Orion Nebula, Tsamis, Walsh & Péquignot (2009) have presented preliminary results of integral field spectroscopy with FLAMES for several proplyds with the aim of studying the behaviour of the physical conditions, chemical abundances and the ADF in and outside these kinds of objects. The first results show that the temperature

measured in the proplyds can be affected by collisional de-excitation as has been also suggested in previous works (Rubin et al. 2003; Mesa-Delgado et al. 2008).

The main goal of the present paper is to use integral field spectroscopy at spatial scales of 1 arcsec in order to explore the effect of HH objects on the derived ADF considering the results of Mesa-Delgado et al. (2008).

In Section 2 we describe the observations obtained with Potsdam Multi-Aperture Spectrometer (PMAS) and the reduction procedure. In Section 3 we describe the emission-line measurements and the reddening correction as well as some representative bidimensional maps of those quantities. In Section 4 we describe the determination of the physical conditions, chemical abundances – from both kinds of lines, CELs and RLs – and the ADF of O^{2+} as well as their corresponding maps. In Section 5 we calculate the t^2 parameter from different methods and present the first bidimensional map of this quantity. Furthermore, we show the possible correlations between the ADF and the rest of properties determined. Finally, in Section 6 we summarize our main conclusions.

2 OBSERVATIONS AND DATA REDUCTION

HH 202 was observed on 2007 October 14 at Calar Alto Observatory (Almería, Spain), using the 3.5-m telescope with the PMAS (Roth et al. 2005). The standard lens array integral field unit (IFU) of $16 \times 16\,\mathrm{arcsec}^2$ field of view (FOV) was used with a sampling of 1 arcsec. Most of the optical range was covered with the V600 grating using two grating rotator angles: −72, covering from 3500 to 5100 Å, and −68, covering from 5700 to 7200 Å. The effective spectral resolution was 3.6 Å. The position of the IFU covering HH 202 is shown in Fig. 1 where we can see the two bright knots HH 202-N and HH 202-S together with an Hα image obtained with PMAS rebinned to 160×160 pixels using the REBIN function of IDL which performs an expansion of the original map through a linear interpolation. The blue and red spectra have a total integration time of 1800 and 1000 s, respectively. Additional short exposures of 10 s were taken in order to avoid saturation of the brightest emission lines. Calibration images were obtained during the night: arc lamps for the wavelength calibration and a continuum lamp needed to extract the 256 individual spectra on the CCD. Observations of the spectrophotometric standard stars BD +28°4211, Feige 110 and G191−B2B (Oke 1990) were used for flux calibration. The error of this calibration is of the order of 5 per cent. The night was photometric and the typical seeing during the observations was 1 arcsec.

The data were reduced using the IRAF reduction package SPECRED. After bias subtraction, spectra were traced on the continuum lamp exposure obtained before each science exposure, and wavelength calibrated using a Hg–Ne arc lamp. The continuum lamp and sky flats were used to determine the response of the instrument for each fibre and wavelength. Finally, for the standard stars we have co-added the spectra of the central fibres and compared them with the tabulated one-dimensional spectra.

We have noticed the effect of the differential atmospheric refraction (DAR) in the monochromatic images of HH 202 obtained for Balmer lines at different wavelengths reaching the value of ∼1.3 arcsec between Hα and H11. We have measured offsets between all Balmer line images, and shifted with respect to Hα. The maximum coincident FOV resulting in the whole wavelength range is $15 \times 15\,\mathrm{arcsec}^2$. All the maps involving emission-line ratios analysed in this paper have been corrected for DAR.

Because of the relatively low spectral resolution of the observations, Hg 4358 Å telluric emission was somewhat blended with [O III] 4363 Å and a proper sky subtraction was necessary. We have taken a median value of the Hg 4358 Å line flux ($9.22 \times 10^{-16}\,\mathrm{erg\,cm^{-2}\,s^{-1}}$), which is in some regions approximately two orders of magnitude lower than the auroral line flux.

In previous works the background nebular emission in Orion proplyds has been determined, either using echelle data (Henney & O'Dell 1999) or integral field spectroscopy (Vasconcelos et al. 2005). In our case, the low spectral resolution of the data does not allow to separate the HH 202 emission from the background. Furthermore, as pointed out in both cited papers, this task is very challenging due to small-scale inhomogeneities in the nebular emission. As a result, only rough estimates can be given. Using the method proposed by Vasconcelos et al. (2005), we have assumed that the background emission is represented by the emission in the north-east corner of the FOV. The resulting background contribution is thus estimated to lie between 40 and 50 per cent in knot HH 202-S, and between 55 and 65 per cent in the rest of HH 202. If such a correction were applied to our data, we would obtain much larger densities, lower temperatures from the [N II] line ratio and higher temperatures from the [O III] line ratio with respect to the results presented in next sections. These results do not change the final conclusions of the paper because we are interested in how the presence of an HH object affects to the ADF when low spectral resolution observations are made and the contributions from the gas flows and the nebular background are mixed. In Paper II, we perform a complete analysis of the knot HH 202-S based on echelle spectrophotometry. The high resolution of these data has allowed us to resolve the kinematic component associated with the gas flow and the one associated with the background emission (in a small area included in the PMAS field). This analysis indicates that the background emission ranges from 30 per cent in the case of [N II] 5755 Å to 60 per cent for [O III] 5007 Å. In the case of H I lines, the background emission is about 50 per cent.

3 LINE MEASUREMENTS AND REDDENING CORRECTION

The emission lines considered in our analysis are the following: (a) Balmer lines, from Hα to H11, which are used to compute the reddening correction and correct the DAR shift (H8 and H10 were not used because they suffer from line blending); (b) CELs of various species, which are used to compute physical conditions and ionic abundances; (c) Faint RLs of C II and O II, which are used to derive the ionic abundances and to compute the ADF(O^{2+}). In Fig. 2, we show an example of the spectra of a given spaxel where we can see the blend of O II lines at 4649 and 4651 Å.

Line fluxes were measured applying a single or a multiple Gaussian profile fit procedure between two given limits and over the local continuum. All these measurements were made with the SPLOT routine of IRAF and using our own scripts to automatize the process. The errors associated with the line flux measurements were determined following Mesa-Delgado et al. (2008). The final error of a line was computed as the quadratic sum of the error in its flux measurement and the error in flux calibration. In order to avoid spurious weak line measurements, we imposed three criteria to discriminate between real features and noise: (1) line intensity peak over 2.5 times the σ of the continuum; (2) full width at half-maximum, FWHM(H I)/$1.5 < \mathrm{FWHM}(\lambda) < 1.5\,\mathrm{FWHM(H\,I)}$ and (3) $F(\lambda) > 0.0001\,F(\mathrm{H}\beta)$.

All line fluxes of a given spectrum have been normalized to Hβ and Hα for the blue and red range, respectively. To produce a final

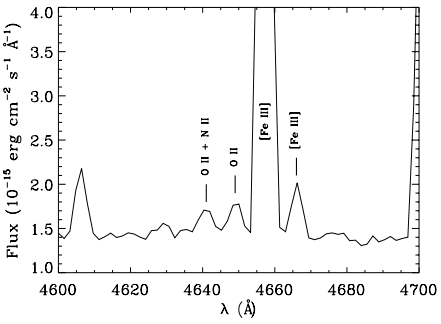

Figure 2. Section of a PMAS spectrum around O II lines of multiplet 1 corresponding to the spaxel position (−5.5, −6.5).

homogeneous set of line ratios, all of them were rescaled to Hβ. The rescaling factor used in the red spectra was the theoretical Hα/Hβ ratio for the physical conditions of $T_e = 10\,000$ K and $n_e = 1000\,\mathrm{cm}^{-3}$.

In Fig. 3, we show [O III] 5007, O II 4650, [N II] 6584 and [Fe III] 4881 Å emission-line maps with Hα contours overplotted. In Figs 3(a) and (b), it is possible to see that the [O III] 5007 and O II 4650 Å spatial distributions are quite similar. In particular, the O II flux map seems to peak at the position of the apex of HH 202, the zone also known as HH 202-S – spaxels (−5.5, −6.5) and (−6.5, −4.5). A similar spatial distribution of both kinds of lines was already observed using long-slit spectra in the Orion Nebula by Mesa-Delgado et al. (2008), as well as in the three PNe observed by Tsamis et al. (2008). Fig. 3 also shows that the spatial distributions of [N II] and [O III] are rather different. The [N II] map shows an enhancement in the bow shock of HH 202. HH objects are characterized by their strong emission in [Fe III] lines. In Fig. 3(d), we can see the spatial distribution of [Fe III] 4881 Å where the maximum emission is strongly concentrated at HH 202-S, which coincides with the maxima in radial velocity and electron density as we can see in Figs 4(b) and 5(a). This high [Fe III] emission at HH 202-S may be related to shock destruction of dust grains or to the particular excitation conditions of the gas in the knot.

The reddening coefficient, $c(\mathrm{H}\beta)$, has been obtained by fitting the observed Hγ/Hβ, Hδ/Hβ, H9/Hβ and H11/Hβ ratios to the theoretical ones predicted by Storey & Hummer (1995) for $n_e = 1000\,\mathrm{cm}^{-3}$ and $T_e = 10\,000$ K. We have used the reddening function, $f(\lambda)$, normalized to Hβ determined by Blagrave et al. (2007) for the Orion Nebula. The use of this extinction law instead of the classical one of Costero & Peimbert (1970) produces $c(\mathrm{H}\beta)$ values about 0.1 dex higher and dereddened fluxes with respect to Hβ about 3 per cent lower for lines in the range 5000 to 7500 Å, 4 per cent higher for wavelengths below 5000 Å and 2 per cent for wavelengths above 7500 Å. The final adopted $c(\mathrm{H}\beta)$ value for each spaxel is an average of the individual values derived from each Balmer line ratio weighted by their corresponding uncertainties. The typical error of $c(\mathrm{H}\beta)$ is about 0.14 dex for each spaxel. The resulting extinction map is shown in Fig. 4(a). The extinction coefficient varies approximately from 0.4 to 0.7 dex and reaches the highest values – between 0.8 and 0.9 dex – in a low surface brightness area at the north of HH 202. Excluding this zone – which shows the largest line intensity uncertainties – we obtain a mean value 0.56 ± 0.14 dex.

We have compared our $c(\mathrm{H}\beta)$ values with those obtained by O'Dell & Yusef-Zadeh (2000) and Mesa-Delgado et al. (2008) for

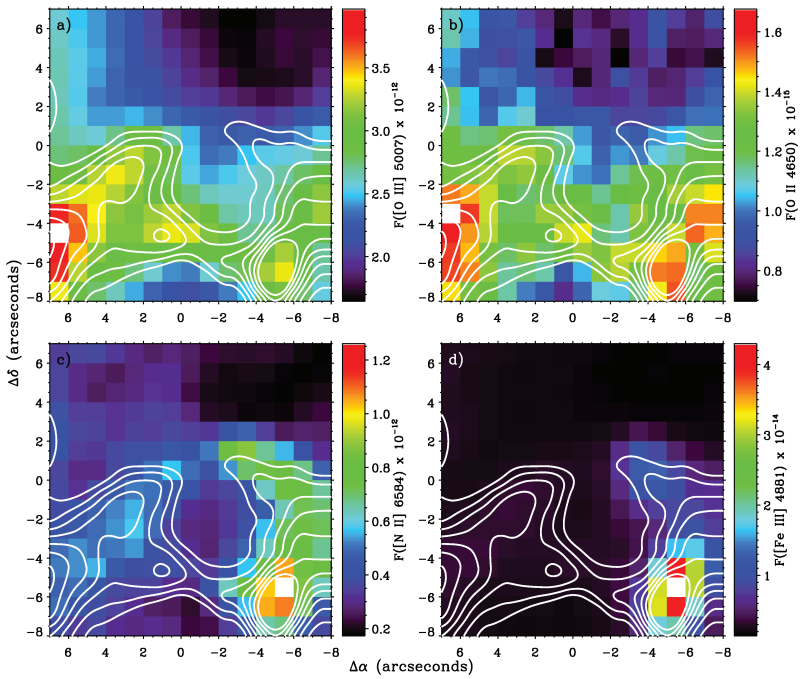

Figure 3. Emission-line flux maps with Hα contours overplotted on the HH 202 PMAS field of (a) [O III] 5007 Å, (b) O II 4650 Å, (c) [N II] 6584 Å and (d) [Fe III] 4881 Å (in units of erg cm^{-2} s^{-1}).

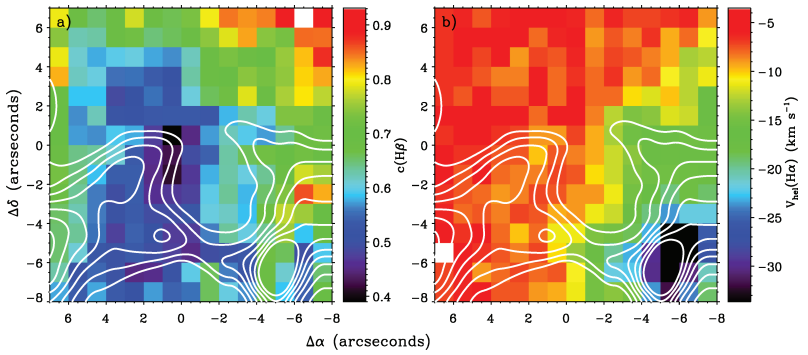

Figure 4. HH 202 PMAS maps with Hα contours overplotted: (a) c(Hβ), (b) Hα heliocentric velocity.

the area of HH 202. O'Dell & Yusef-Zadeh (2000) have obtained consistent c(Hβ) values from the Hα/Hβ line ratio using calibrated *HST* images and from radio to optical surface brightness ratio. HH 202 is located between the contour lines of 0.2 and 0.4 dex on the maps of O'Dell & Yusef-Zadeh (2000). However, Mesa-Delgado et al. (2008), from long-slit spectroscopy passing precisely through HH 202-S, derive a c(Hβ) value of about 0.4 $\pm$ 0.1 dex. Therefore, we find that our mean value of the reddening coefficient is consistent with the previous determinations taking into account the errors and the different extinction laws used.

The heliocentric velocity map obtained from the centroid of the Hα line profile is shown in Fig. 4(b). We observe that the gas around the head of HH 202 shows a velocity of about $-5\,\mathrm{km\,s^{-1}}$ and that the most negatives values are reached at HH 202-S position, where velocities of $-35\,\mathrm{km\,s^{-1}}$ are measured. These values of the velocity of HH 202-S agree within the errors with that determined by Doi et al. (2004) of $-39 \pm 2\,\mathrm{km\,s^{-1}}$ for this position. However, due to the lower spectral resolution of our data, the velocities we measure correspond to the blend of the emission of the background nebular gas and the gas flow of the HH object.

4 RESULTS

4.1 Physical conditions

Nebular electron densities, n_e, and temperatures, T_e, have been derived from the usual CEL ratios – [S II] 6717/6731 for n_e, and [O III] (4959+5007)/4363 and [N II] (6548+6584)/5755 for T_e, and using the TEMDEN task of the NEBULAR package of IRAF (Shaw & Dufour 1995) with updated atomic data (see García-Rojas et al. 2005). Following the same procedure as Mesa-Delgado et al. (2008) for the determination of the physical conditions, we have assumed an initial $T_e = 10\,000$ K to derive a first approximation of n_e, then we calculate T_e([O III]) and T_e([N II]), and iterate until convergence. We have not corrected the observed intensity of [N II] 5755 Å for contribution by recombination when determining T_e([N II]) because this contribution is expected to be rather small in H II regions with high ionization degree such as the Orion Nebula (e.g. Esteban et al. 2004). Bidimensional maps of n_e, T_e([O III]), T_e([N II])/T_e([O III]) ratio and T_e([N II]) are shown in Figs 5(a), (b), (c) and (d), respectively.

In Fig. 5(a), we can see that the highest densities are just reached at the positions of HH 202-N and HH 202-S with values of about $10\,000\,\mathrm{cm^{-3}}$. Similar values were obtained by Mesa-Delgado et al. (2008) for HH 202-S. For the gas outside the HH object, we find a n_e of about $4000\,\mathrm{cm^{-3}}$ and the lowest densities ($\sim$2500 cm^{-3}) at the low surface brightness region at the north-west corner of the FOV. The typical errors in our density determination are between 200 and $250\,\mathrm{cm^{-3}}$.

Fig. 5(b) shows that T_e([O III]) is rather constant in the whole FOV. However, the highest values of T_e([O III]) trace the form of HH 202 – with an almost constant temperature of 8500 K – reaching the peak value at the HH 202-S position where shock heating should be maximum. However, T_e([N II]) shows a much wider range of values across the FOV, but its spatial distribution is completely different to that of T_e([O III]). The maximum values of T_e([N II]) are found just behind HH 202-S or ahead of the north-west border of the bow shock of HH 202-N (see Fig. 5d). The lowest values are found in the inner part of HH 202 ($\sim$9500 K). In Fig. 5(c), the T_e([N II])/T_e([O III]) ratio illustrates that T_e([N II]) is always higher than T_e([O III]) but the ratio tends to be closer to one in the HH object and especially at HH 202-N where the density is higher. The uncertainties of the temperatures are about 600 K for T_e([N II]) and 250 K for T_e([O III]).

The Balmer continuum temperature, T_e(Bac), of the ionized gas has also been determined for most of the individual spaxels of the FOV; this is the first bidimensional T_e(Bac) map ever obtained for an ionized nebula. This temperature depends on the ratio between the Balmer jump (BJ) and the intensity of a given Balmer line. We have measured the BJ subtracting the continuum fitted at both sides of the Balmer discontinuity at 3646 Å (see Fig. 6). The continuum fitted at both sides of the BJ is defined over spectral ranges free of emission lines covering the possible maximum baseline. The errors associated with the continuum subtraction are included in the discontinuity measurements. Finally, we have computed T_e(Bac) in K from the ratio of the BJ to the H11 flux using the relation proposed by Liu et al. (2001):

$$T_e(\mathrm{Bac}) = 368\left(1 + 0.259y^{+} + 3.409y^{2+}\right)\left(\frac{\mathrm{BJ}}{\mathrm{H11}}\right)^{-(3/2)}, \qquad (1)$$

where y^+ and y^{2+} correspond to the He^+/H^+ and He^{2+}/H^+ ratios, respectively. We have assumed for y^+ the value derived by Esteban et al. (2004) for their slit position at the centre of the Orion Nebula and $y^{2+} = 0$ due to the lack of He II lines in our spectra. The effect of the interstellar extinction was taken into account in the calculations.

The T_e(Bac) map is shown in Fig. 7. The T_e(Bac) error was calculated by error propagation in equation (1), and it amounts to 22 per cent on average (i.e., 1100 to 1900 K). We can see that the lowest temperatures ($\sim$5500 K) are reached at the east half

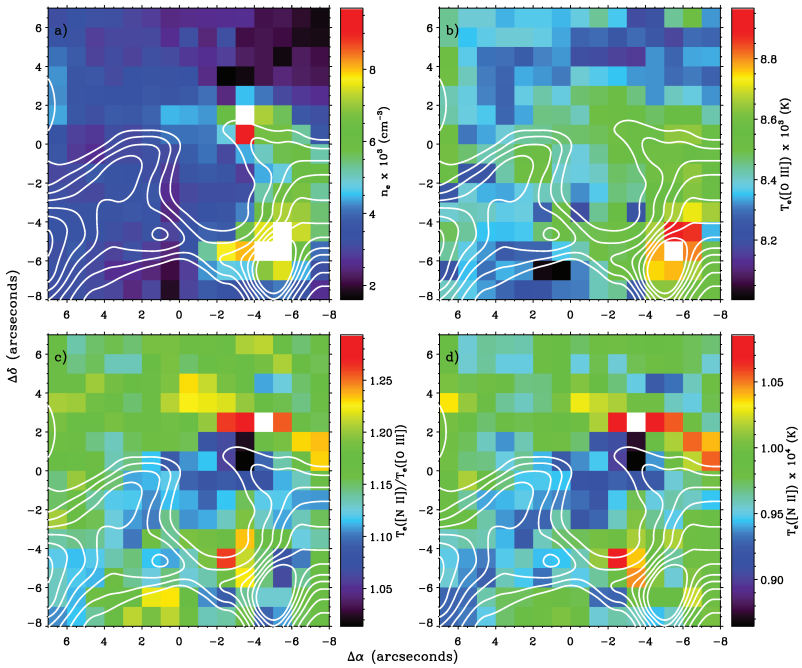

Figure 5. Physical conditions maps with Hα contours overplotted: (a) n_e([S II]), (b) T_e([O III]), (c) T_e([N II])/T_e([O III]) ratio and (d) T_e([N II]).

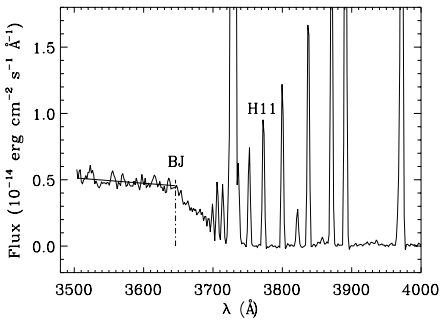

Figure 6. Section of a PMAS spectrum of the brightest spaxel at the apex (−5.5, −6.5). The fitted continuum contribution to the right-hand side of the BJ was subtracted to the whole range showed.

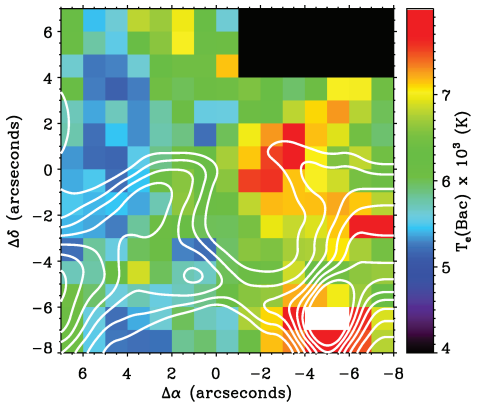

Figure 7. Balmer temperature map with Hα contours overplotted. The black rectangle on the north-west corner corresponds to an area masked due to the bad determination of T_e(Bac).

of the FOV, while the west half shows values of about 7000 K, encompassing HH 202-S and HH 202-N. From the comparison of Fig. 7 and the rest of the maps, we can see that the spatial distribution of T_e(Bac) is something similar that of T_e([O III]): both indicators show the maximum values at HH 202-S, HH 202-N and the arc connecting both features.

4.2 Chemical abundances

The IRAF package NEBULAR has been used to derive ionic abundances of N^+, O^+ and O^{2+} from the intensity of CELs. We have assumed no temperature fluctuations in the ionized gas ($t^2 = 0$) and a two-zone scheme: T_e([N II]) for N^+ and O^+ – the low ionization potential ions – and T_e([O III]) for O^{2+}. The errors in the ionic abundances have been calculated as a quadratic sum of the independent contributions of errors in flux, n_e and T_e. The spatial distributions of the O^{2+} and O^+ abundances are presented in Figs 8(b) and (d), respectively. In these figures, we can see that the spatial distributions of both abundances are completely different. The O^+/H^+ ratio reaches the highest values just on the bow shock, whereas O^{2+}/H^+ shows an inverse behaviour, reflecting the different ionization structure of the bow shock and the bulk of the background nebular gas. The

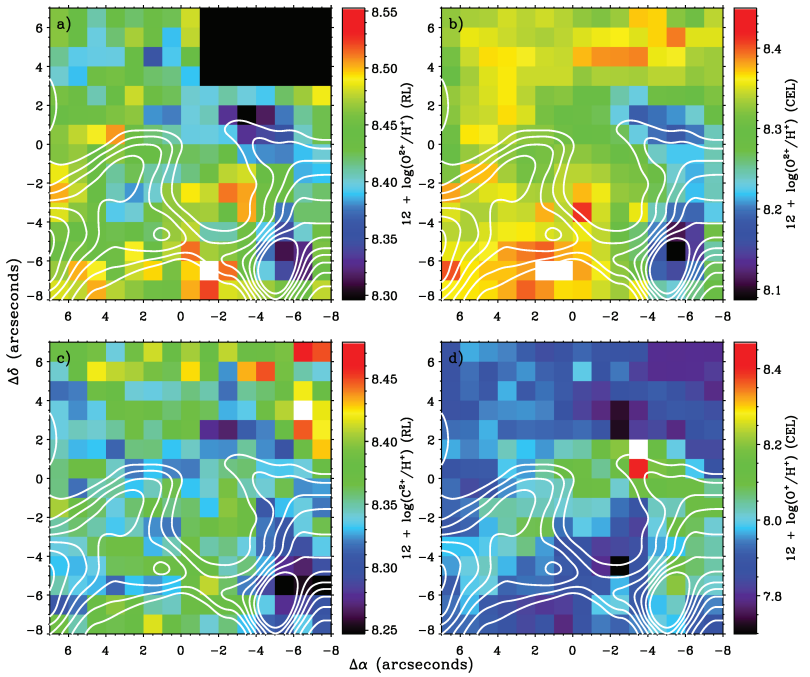

Figure 8. Ionic abundance maps with Hα contours overplotted: (a) $12 + \log(O^{2+}/H^{+})$ from RLs – the black rectangle on the north-west corner corresponds to an area masked due to the bad determination of the abundance, (b) $12 + \log(O^{2+}/H^{+})$ from CELs, (c) $12 + \log(C^{2+}/H^{+})$ from RLs and (d) $12 + \log(O^{+}/H^{+})$ from CELs.

higher O^{+}/O^{2+} ratio at the bow shock is probably produced by the higher densities in the shock gas, which increase the recombination rate of O^{2+}. The abundance map of N^{+} – not presented here – shows a very similar distribution to the O^{+} map.

The high signal-to-noise ratio of our spectra has permitted to detect and measure the weak RLs of O II and C II in all the spaxels of the PMAS FOV. These RLs have the advantage that their relative intensity with respect to a Balmer line is almost independent on T_e and n_e, largely unaffected by the possible presence of temperature fluctuations. In Fig. 2, we show a section of the spectra at spaxel (−5.5, −6.5) around the O II lines.

We have measured the blend of the O II 4649 and 4651 Å lines – the brightest individual lines of the O II multiplet 1 – in most of the spaxels of the FOV. In order to determine the O^{2+} abundance from this blend, we have combined equations (1) and (4) of Peimbert & Peimbert (2005) estimating the expected flux of all the lines of O II multiplet 1 flux with respect to Hβ, I(M1 O II)/I(Hβ). These relations were used in order to correct for the non-local thermodynamic equilibrium (NLTE) effects in the relative intensity of the individual lines of the multiplet, though these are rather small in the Orion Nebula due to its relatively large n_e. Then, the O^{2+}/H^{+} ratio is calculated by

$$\frac{O^{2+}}{H^{+}} = \frac{\lambda_{M1}}{4861}\frac{\alpha_{eff}(H\beta)}{\alpha_{eff}(M1)}\frac{I(M1\,O\,II)}{I(H\beta)}, \qquad (2)$$

where $\alpha_{eff}(H\beta)$ and $\alpha_{eff}(M1)$ are the effective recombination coefficients for Hβ and for the O II multiplet 1, respectively, and $\lambda_{M1} = 4651.5$ Å the representative mean wavelength of the whole multiplet. We can also obtain the C^{2+} abundance using an equation analogous to (2) but using the specific quantities for this ion. Both abundances have been calculated assuming T_e([O III]) and with the effective recombination coefficients available in the literature (Storey 1994 for O^{2+} assuming LS coupling, and Davey, Storey & Kisielius 2000 for C^{2+}). Typical ionic abundance errors are 0.10 dex for O^{2+} and 0.08 dex for C^{2+}. The ionic abundances obtained from RLs are shown in Figs 8(a) and (c).

The spatial distributions of the O^{2+} abundance obtained from CELs and RLs show that the lower values are found at the positions of HH 202-S, HH 202-N and the arc connecting both features. In contrast, the O^{2+} abundance map obtained from CELs shows especially large values in the zone inside the HH object at the bottom of the FOV. For a given spaxel, the O^{2+}/H^{+} ratios obtained from RLs are always higher than those obtained from CELs, with a typical difference of about 0.10 dex. Finally, the C^{2+} abundance map shows rather constant values of about 8.35 dex, with its minimum value also found at HH 202-S. The qualitative behaviour of this map is rather similar to the O^{2+} abundance spatial distribution.

For each spaxel, the ADF(O^{2+}) has been calculated from the difference between the O^{2+} abundances obtained from RLs and CELs. In Fig. 9, we show the spatial distribution of the ADF(O^{2+}), which shows the highest values at and around HH 202-S (up to 0.23 dex), the rest of the spaxels show values between 0.05 and 0.20 dex with a typical error value of 0.12 dex. Excluding the masked area showed in Fig. 9, we have calculated an average value of 0.13 dex with a standard deviation of 0.05 dex. Mesa-Delgado et al. (2008) also found a peak of the ADF(O^{2+}) of about 0.30 dex at the same zone of HH 202. Both values of the discrepancy are consistent within the uncertainties, but the value obtained by those authors is, in principle, more reliable because of the better signal-to-noise ratio of their spectra.

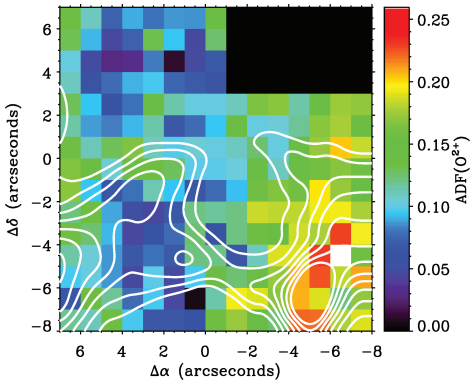

Figure 9. ADF(O^{2+}) map with Hα contours overplotted. The black rectangle on the north-west corner corresponds to an area masked due to the bad determination of the O^{2+} abundance from RLs.

5 DISCUSSION

5.1 Temperature fluctuations

One of the possible explanations for the AD problem in ionized nebulae is provided by the presence of temperature fluctuations (e.g. García-Rojas & Esteban 2007). Following Peimbert (1967), the temperature fluctuation over the observed volume of a nebula can be parametrized by

$$T_0 = \frac{\int T_e n_e n_i \, dV}{\int n_e n_i \, dV}, \quad (3)$$

where T_0 is the average temperature of the nebula and n_i is the ion density, and

$$t^2 = \frac{\int (T_e - T_0)^2 n_e n_i \, dV}{T_0^2 \int n_e n_i \, dV}, \quad (4)$$

where t^2 is the mean-square electron temperature fluctuation.

There are several methods to obtain t^2 and T_0 along the line of sight (see Peimbert et al. 2004). One possibility is to compare the T_e obtained from independent methods. Following Peimbert (1967), the temperature derived from the BJ depends on t^2 and T_0 as

$$T_e(\mathrm{Bac}) = T_0(1 - 1.70t^2), \quad (5)$$

and the temperatures derived from the ratio of CELs can be written as (Peimbert & Costero 1969)

$$T_e(\mathrm{h}) = T_0(\mathrm{h})\left[1 + \frac{1}{2}\left(\frac{91\,300}{T_0(\mathrm{h})} - 3\right)t^2(\mathrm{h})\right] \quad (6)$$

and

$$T_e(\mathrm{l}) = T_0(\mathrm{l})\left[1 + \frac{1}{2}\left(\frac{69\,000}{T_0(\mathrm{l})} - 3\right)t^2(\mathrm{l})\right], \quad (7)$$

where T_e(l) and T_e(h) are the electron temperatures for the low – T_e([N II]) – and high – T_e([O III]) – ionization zone, respectively. We can obtain the $t^2(O^{2+})$ and $T_0(O^{2+})$ combining equations (5) and (6), whereas $t^2(N^+)$ and $T_0(N^+)$ can be obtained combining equations (5) and (7). To obtain the mean-square temperature fluctuation for the entire volume, t^2, we have weighted the relative importance of $t^2(N^+)$ and $t^2(O^{2+})$ in the observed volume by using equation (16) of Peimbert, Peimbert & Luridiana (2002), assuming that in this region N^+ and O^+ co-exist in the same volume. In Figs 10(a), (c) and (e), the $t^2(O^{2+})$, $t^2(N^+)$ and t^2 maps are presented. Their associated error maps are also shown in Figs 10(b), (d) and (f).

The inspection of Figs 10(b), (c) and (e) indicates that the spatial distribution of t^2 values are rather similar, showing somewhat lower t^2 values at the positions of HH 202-S and HH 202-N. We have calculated the mean value of $\langle t^2 \rangle$ in the area where this quantity has been determined weighting the individual values of the fluctuation for each spaxel by its associated error, obtaining $\langle t^2 \rangle \approx 0.061 \pm 0.022$.

Another possibility to obtain the t^2 parameter is assuming that the ADF(O^{2+}) is produced by the presence of temperature fluctuations. Following this assumption, we have used equations (9), (10) and (11) from Peimbert et al. (2004) to derive the associated $t^2(O^{2+})$ for each spaxel that – as expected – shows a spatial distribution analogous to the ADF map shown in Fig. 9. In this case, the mean value of t^2 is only slightly lower than that obtained from the data of Fig. 10(a). A remarkable result is that the t^2 maps obtained from the two different methods – comparison of temperatures and from the ADF(O^{2+}) – are qualitatively different suggesting, in this case, that there is not a genetic relationship between t^2 and ADF(O^{2+}).

Finally, we have determined the t^2 in the plane of the sky, t^2_A, using equations (11) and (12) of Mesa-Delgado et al. (2008), averaging the bidimensional point-to-point variations of $T_e(O^{2+})$ and $T_e(N^+)$. The values obtained are $t^2_A(O^{2+}) \sim 0.0004$ and $t^2_A(N^+) \sim 0.0023$, in agreement with the long-slit results by Mesa-Delgado et al. (2008), and substantially lower than the t^2 values obtained with the methods described in the previous paragraphs, which correspond to the fluctuations along the line of sight.

5.2 Correlations between the ADF and other nebular properties

In this section, we investigate some relationships among physical properties derived in the HH 202 PMAS field. In Fig. 11 the possible correlations among the ADF(O^{2+}), T_e, n_e, $c(H\beta)$, t^2 and ionic abundances determined from CELs and RLs are presented.

The dependence of the ADF(O^{2+}) with respect to $c(H\beta)$, n_e, T_e([O III]), T_e(BJ), $t^2(O^{2+})$ and O^{2+}/O^+ ratio is shown from Figs 11(a)–(f). Fig. 11(a) – ADF(O^{2+}) versus $c(H\beta)$ – does not show a clear trend, indicating that the ADF does not depend on the amount of dust present in the line of sight of each spaxel of the PMAS field. As Mesa-Delgado et al. (2008) also obtained from their long-slit data, there seems to be no correlation between the ADF and n_e (see Fig. 11b) as well as between the ADF and the ionization degree of the gas (see Fig. 11f).

In Figs 11(c) and (d), we can see that positive correlations are obtained between ADF(O^{2+}) versus T_e([O III]) and ADF(O^{2+}) versus T_e(BJ), respectively. This is expected because these three quantities show larger values at HH 202-S. As we can see in Figs 11(c) and (d), these correlations do not seem very reliable considering the very narrow baseline of T_e([O III]) and T_e(BJ) covered by the data and the large error bars with respect to the baseline.

A rather unclear negative correlation between the ADF(O^{2+}) and the fluctuation parameter t^2 (O^{2+}) along the line of sight can be guessed in Fig. 11(e). However, the large error bars in both quantities do not permit to establish any correlation. This result suggests the ADF and t^2 may be independent.

In Figs 11(g), (h) and (i), we represent the O^{2+} abundances from RLs, O^{2+} abundances from CELs and C^{2+} abundances from RLs versus T_e([O III]), respectively. In the case of the abundances from

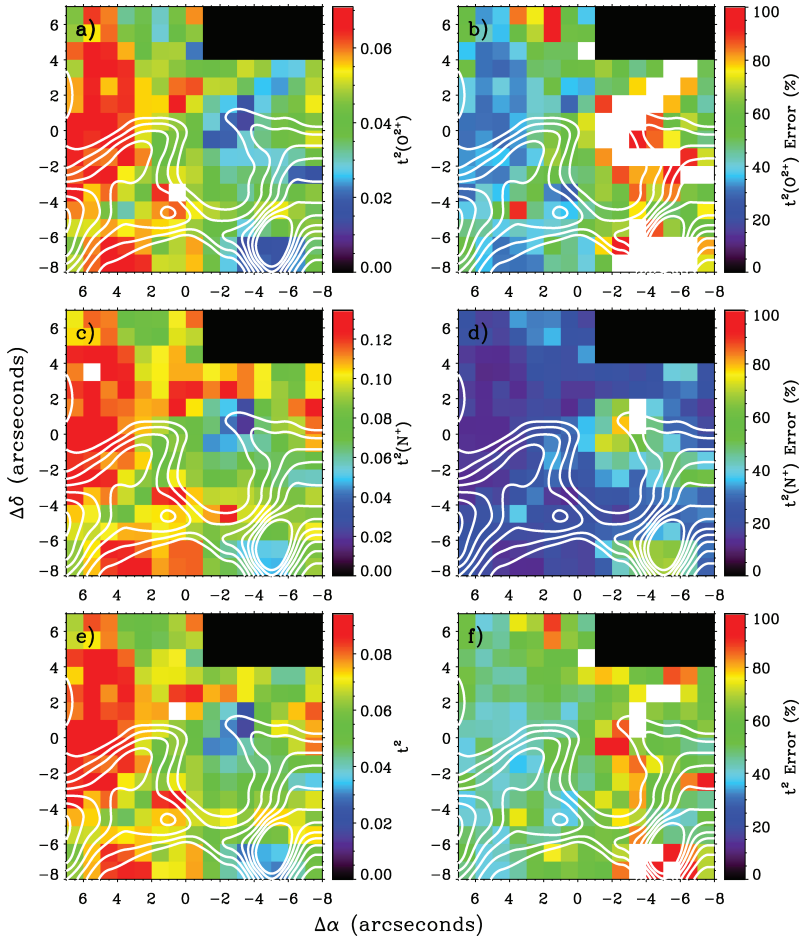

Figure 10. t^2 parameters and their respective error maps in percentage with Hα contours overplotted: (a) and (b) t^2 (O^{2+}) and its error, (c) and (d) t^2 (N^+) and its error, (e) and (f) t^2 and its error. The white areas are where the error is higher than the t^2 value. The black rectangle on the north-west corner corresponds to an area masked due to the bad determination of T_e(Bac).

RLs, we can observe negative correlations with rather low Spearman correlation coefficients ($\rho = -0.42$ and -0.28 for Figs 11g and i, respectively). This apparent trend is mainly produced by the behaviour observed at HH 202-S and HH 202-N, which are precisely the zones where the O^{2+} and C^{2+} abundances obtained from RLs are lower and T_e([O III]) is higher. From integral field spectroscopy, Tsamis et al. (2008) have found rather clear positive correlations between ionic abundances obtained from RLs and T_e in three PNe, exactly the opposite trend we observe in this FOV of the Orion Nebula. These authors argue that their results provide evidence for the existence of two distinct components of highly ionized gas at very different temperatures. However, in this case, we observe the expected natural behaviour of an ionized nebula – the O^{2+} abundance from RLs increases when the temperature decreases – due to the fact that O^{2+} is a dominant coolant in the gas phase and the presence of spatial changes of the O^{2+}/O^+ ratio across the FOV. Therefore, the presence of metal-rich droplets does not seem to be supported by our results. However, the O^{2+}/H^+ ratio from CELs shows a much tighter correlation with T_e([O III]) due to the lower uncertainties of these abundances. We have fitted the following linear relation:

$$12 + \log\left(\frac{O^{2+}}{H^+}\right) = (11.4 \pm 0.1) + (-3.6 \pm 0.1)T_4, \quad (8)$$

where T_4 is T_e([O III]) in units of 10^4 K and we have obtained a linear correlation coefficient $r = -0.90$.

6 CONCLUSIONS

In this paper, we present results from integral field spectroscopy of an area of 15×15 arcsec^2 covering the head of HH 202 in the Orion Nebula. The FOV comprises the bright regions known as HH 202-S and HH 202-N. We have obtained maps of relevant emission-line ratios, physical conditions and ionic abundances, including O^{2+} and C^{2+} abundances determined from RLs. Additionally, we have

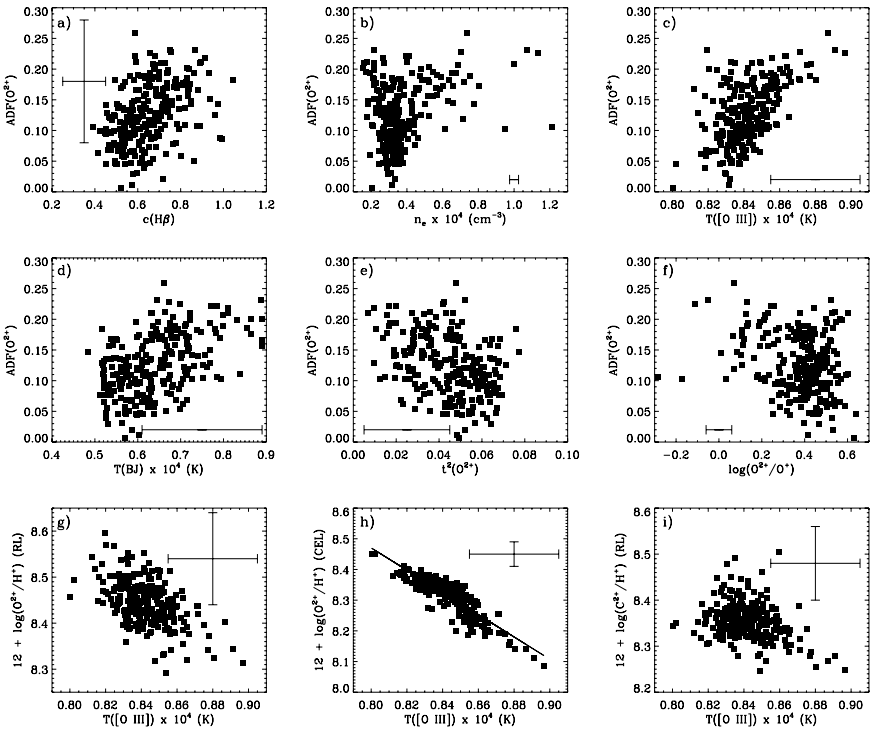

Figure 11. Correlations among different nebular properties obtained from PMAS maps. From (a)–(f) the ADF(O^{2+}) is represented with respect to $c(H\beta)$, n_e, T_e([O III]), T_e(BJ), t^2[O III] and log (O^{2+}/O^+). The mean error bar in the ADF(O^{2+}) is only shown in (a). From (g)–(i) the logarithmic abundances of O^{2+} from RLs, O^{2+} from CELs and C^{2+} from RLs are represented versus T_e([O III]).

obtained maps of other interesting nebular properties, as the temperature fluctuation parameter, t^2, and the ADF of O^{2+}, ADF(O^{2+}), which is defined as the difference between the O^{2+}/H^+ ratios determined from RLs and CELs.

We find that the flux distributions of the [O III] and O II lines are rather similar and that the HH object is comparatively much brighter in the lines of low-ionization potential ionic species and especially in [Fe III]. The n_e is about 4000 cm^{-3} in most of the FOV and higher – about 10 000 cm^{-3} – at HH 202-S and HH 202-N. The T_e([O III]) map shows a narrow range of variation, but the values are higher at HH 202-S. However, T_e([N II]) shows larger variations and a very different spatial distribution, being higher at the northern and eastern edges of HH 202-N and HH 202-S, respectively, a likely consequence of the ionization stratification or the presence of some shock excitation in the knots of the HH object. We have obtained – for the first time in an ionized nebula – the T_e(Bac) map, which follows closely that of T_e([O III]).

The O^+/H^+ ratio map reaches the highest values just on the arc that delineates the north of HH 202 from the east and west edges of the FOV, whereas the map of O^{2+} abundance obtained from CELs shows an inverse behaviour, probably produced by the higher densities in the shock gas that increase the recombination rate of O^{2+}. The spatial distributions of the O^{2+} abundance obtained from CELs and RLs agree in showing the lower values at the positions of HH 202-S, HH 202-N and the arc connecting both features. However, for a given spaxel, the O^{2+}/H^+ ratios obtained from RLs are always about 0.10 dex higher than those obtained from CELs. The map of the ADF(O^{2+}) shows the highest values at and around HH 202-S.

We have determined – for the first time in an ionized nebula – the t^2 map of the FOV from the comparison of T_e(Bac) and the other T_e values determined from CEL ratios, finding that it does not match the ADF(O^{2+}) map. This result supports that the AD and temperature fluctuations are independent phenomena.

Finally, we have found weak correlations between the ADF(O^{2+}) and T_e values of the different spaxels of the FOV and between the O^{2+}/H^+ ratios obtained from RLs and CELs and T_e([O III]). The negative correlation between the O^{2+} abundances obtained from RLs and T_e([O III]) does not support the predictions of the chemical inhomogeneity models of Tsamis & Péquignot (2005) and Stasińska et al. (2007).

ACKNOWLEDGMENTS

We thank Sebastián F. Sánchez and the personnel of Calar Alto Observatory for their help with the observations. We are grateful to M. Peimbert, G. Stasińska and W. Henney for several suggestions and discussions. We also thank the referee of the paper for his/her positive comments. This work has been funded by the Spanish Ministerio de Ciencia y Tecnología (MCyT) under project AYA2004-07466 and Ministerio de Educación y Ciencia (MEC) under project AYA2007-63030 and 64712.

REFERENCES

Blagrave K. P. M., Martin P. G., Rubin R. H., Dufour R. J., Baldwin J. A., Hester J. J., Walter D. K., 2007, ApJ, 655, 299

Cantó J., Goudis C., Johnson P. G., Meaburn J., 1980, A&A, 85, 128
Costero R., Peimbert M., 1970, Bol. Obs. Tonantzintla Tacubaya, 5, 229
Davey A. R., Storey P. J., Kisielius R., 2000, A&AS, 142, 85
Doi T., O'Dell C. R., Hartigan P., 2002, AJ, 124, 445
Doi T., O'Dell C. R., Hartigan P., 2004, AJ, 127, 3456
Esteban C., Peimbert M., Torres-Peimbert S., Escalante V., 1998, MNRAS, 295, 401
Esteban C., Peimbert M., García-Rojas J., Ruiz M. T., Peimbert A., Rodríguez M., 2004, MNRAS, 355, 229
García-Rojas J., Esteban C., 2007, ApJ, 670, 457
García-Rojas J., Esteban C., Peimbert A., Peimbert M., Rodríguez M., Ruiz M. T., 2005, MNRAS, 362, 301
Henney W. J., O'Dell C. R., 1999, AJ, 118, 2350
Liu X.-W., Storey P. J., Barlow M. J., Danziger I. J., Cohen M., Bryce M., 2000, MNRAS, 312, 585
Liu X.-W., Luo S.-G., Barlow M. J., Danziger I. J., Storey P. J., 2001, MNRAS, 327, 141
Liu X.-W., Barlow M. J., Zhang Y., Bastin R. J., Storey P. J., 2006, MNRAS, 368, 1959
Meaburn J., 1986, A&A, 164, 358
Mesa-Delgado A., Esteban C., García-Rojas J., 2008, ApJ, 675, 389
O'Dell C. R., Doi T., 2003, AJ, 125, 277
O'Dell C. R., Henney W. J., 2008, AJ, 136, 1566
O'Dell C. R., Wong K., 1996, AJ, 111, 846
O'Dell C. R., Yusef-Zadeh F., 2000, AJ, 120, 382
O'Dell C. R., Wen Z., Hester J. J., 1991, PASP, 103, 824
O'Dell C. R., Hartigan P., Lane W. M., Wong S. K., Burton M. G., Raymond J., Axon D. J., 1997, AJ, 114, 730
O'Dell C. R., Peimbert M., Peimbert A., 2003, AJ, 125, 2590
Oke J. B., 1990, AJ, 99, 1621
Peimbert M., 1967, ApJ, 150, 825
Peimbert M., Costero R., 1969, Bol. Obs. Tonantzintla Tacubaya, 5, 3
Peimbert A., Peimbert M., 2005, Rev. Mex. Astron. Astrofis. Ser. Conf., 23, 9
Peimbert A., Peimbert M., Luridiana V., 2002, ApJ, 565, 668
Peimbert M., Peimbert A., Ruiz M. T., Esteban C., 2004, ApJS, 150, 431
Roth M. M. et al., 2005, PASP, 117, 620
Rubin R. H., Martin P. G., Dufour R. J., Ferland G. J., Blagrave K. P. M., Liu X.-W., Nguyen J. F., Baldwin J. A., 2003, MNRAS, 340, 362
Sánchez S. F., Cardiel N., Verheijen M. A. W., Martín-Gordón D., Vilchez J. M., Alves J., 2007, A&A, 465, 207
Shaw R. A., Dufour R. J., 1995, PASP, 107, 896
Stasińska G., Tenorio-Tagle G., Rodríguez M., Henney W. J., 2007, A&A, 471, 193
Storey P. J., 1994, A&A, 282, 999
Storey P. J., Hummer D. G., 1995, MNRAS, 272, 41
Tenorio-Tagle G., 1996, AJ, 111, 1641
Tsamis Y. G., Péquignot D., 2005, MNRAS, 364, 687
Tsamis Y. G., Barlow M. J., Liu X.-W., Danziger I. J., Storey P. J., 2003, MNRAS, 345, 186
Tsamis Y. G., Barlow M. J., Liu X.-W., Storey P. J., Danziger I. J., 2004, MNRAS, 353, 953
Tsamis Y. G., Walsh J. R., Péquignot D., Barlow M. J., Danziger I. J., Liu X.-W., 2008a, MNRAS, 386, 22
Tsamis Y. G., Walsh J. R., Péquignot D., 2009, in Moorwood A., ed., Science with the VLT in the ELT Era, p. 61
Vasconcelos M. J., Cerqueira A. H., Plana H., Raga A. C., Morisset C., 2005, AJ, 130, 1707

This paper has been typeset from a TEX/LATEX file prepared by the author.

4

Propiedades del gas ionizado en HH 202. II: resultados a partir de espectrofotometría *echelle* con UVES

La tercera parte de esta tesis trata de analizar en profundidad las propiedades espectrales del nudo sur del objeto HH 202, HH 202-S. Los resultados presentados en los anteriores capítulos muestran que el ADF(O^{2+}) aumenta significativamente, respecto al fondo nebular, en la posición exacta en la que se encuentra dicho nudo, donde también se encuentra el máximo en velocidad de este flujo de gas.

En esta ocasión, las observaciones obtenidas con el espectrógrafo UVES (acrónimo de *Ultraviolet Visual echelle Spectrograph*), ubicado en el telescopio Kueyen de 8m del Observatorio de Cerro Paranal, a muy alta resolución espectral, nos han permitido un análisis físico-químico completo de las dos componentes cinemáticas observadas: una asociada al fondo nebular y la otra asociada al propio objeto HH. Con ello, hemos conseguido aislar la procedencia de la mayor contribución al ADF(O^{2+}) observada en los capítulos anteriores. Además, la alta señal a ruido que presenta el espectro nos ha permitido detectar un gran número de líneas emitidas por elementos refractarios tales como Ca, Fe, Ni y Cr, de forma que hemos podido analizar el grado de destrucción de polvo tras el paso de la onda de choque en el nudo HH 202-S.

Esta tercera parte de la tesis fue publicada en el artículo "Properties of the ionized gas in HH 202–II. Results from *echelle* spectrophotometry with Ultraviolet Visual *echelle* Spectrograph" de la revista *Monthly Notices of the Royal Astronomical Society*, Volumen 395, páginas 855 a 876, el cual se adjunta a continuación, tras el resumen.

Resumen: Presentamos resultados basados en espectrofotometría *echelle* profunda del nudo más brillante del objeto Herbig-Haro HH 202 de la Nebulosa de Orión –HH 202-S– utilizando el *Ultraviolet Visual echelle Spectrograph* en el rango espectral que abarca desde 3100 a 10400 Å. La alta resolución espectral de las observaciones nos ha permitido separar la componente asociada al gas nebular de la componente asociada al material a alta velocidad. Determinamos las temperaturas y densidades electrónicas a partir de diferentes diagnósticos

en ambas componentes, así como las abundancias químicas de algunos iones y elementos a partir de líneas excitadas colisionalmente, incluyendo las primeras determinaciones de las abundancias de Ca^+ y Cr^+ en la nebulosa de Orión. También calculamos las abundancias de He^+, C^{2+}, O^+ y O^{2+} a partir de líneas de recombinación. La diferencia entre las abundancias de O^{2+} calculadas a partir de líneas excitadas colisionalmente y líneas de recombinación –el conocido factor de discrepancia de abundancias– es 0.35 y 0.11 dex en la componente chocada y nebular, respectivamente. Suponiendo que la discrepancia de abundancias es debida a variaciones espaciales de la temperatura electrónica, obtenemos valores para el parámetro de fluctuación de temperatura, t^2, iguales a 0.050 y 0.016 para las componentes chocada y nebular, respectivamente. Es interesante destacar que obtenemos valores de t^2 muy similares para ambas componentes a partir del análisis de las líneas de He I. Encontramos importantes desviaciones en los cocientes de flujos de las líneas de Balmer y Paschen con mayor número cuántico principal, n, respecto a las predicciones para el caso B. Analizamos la estructura de ionización del HH 202-S, encontrando evidencias suficientes para concluir que el flujo de gas en HH 202-S ha comprimido el gas ambiente de la nebulosa generando en su interior un frente de ionización. Medimos también un gran aumento de las abundancias totales de niquel y hierro en la componente chocada, concluyendo que el patrón de abundancias observado y los resultados obtenidos a partir de modelos de fotoionización, son consistentes con la destrucción parcial de granos de polvo después del paso de la onda de choque en HH 202-S.

Mon. Not. R. Astron. Soc. **395,** 855–876 (2009) doi:10.1111/j.1365-2966.2009.14554.x

Properties of the ionized gas in HH 202 – II. Results from echelle spectrophotometry with Ultraviolet Visual Echelle Spectrograph★

A. Mesa-Delgado,[1]† C. Esteban,[1] J. García-Rojas,[2] V. Luridiana,[3] M. Bautista,[4] M. Rodríguez,[5] L. López-Martín[1] and M. Peimbert[2]

[1]*Instituto de Astrofísica de Canarias, E-38200 La Laguna, Tenerife, Spain*
[2]*Instituto de Astronomía, UNAM, Apdo. Postal 70-264, 04510 México D.F., Mexico*
[3]*Instituto de Astrofísica de Andalucía (CSIC), Apdo. Correos 3004, E-18080 Granada, Spain*
[4]*Deparment of Physics, Virginia Polytechnic and State University, Blacksburg, VA 24061, USA*
[5]*Instituto Nacional de Astrofísica, Óptica y Electrónica INAOE, Apdo. Postal 51 y 216, 7200 Puebla, Pue., Mexico*

Accepted 2009 January 23. Received 2008 December 23; in original form 2008 October 24

ABSTRACT

We present results of deep echelle spectrophotometry of the brightest knot of the Herbig–Haro object HH 202 in the Orion Nebula – HH 202-S – using the Ultraviolet Visual Echelle Spectrograph in the spectral range from 3100 to 10 400 Å. The high spectral resolution of the observations has permitted to separate the component associated with the ambient gas from that associated with the gas flow. We derive electron densities and temperatures from different diagnostics for both components, as well as the chemical abundances of several ions and elements from collisionally excited lines, including the first determinations of Ca^+ and Cr^+ abundances in the Orion Nebula. We also calculate the He^+, C^{2+}, O^+ and O^{2+} abundances from recombination lines. The difference between the O^{2+} abundances determined from collisionally excited and recombination lines – the so-called abundance discrepancy factor – is 0.35 and 0.11 dex for the shock and nebular components, respectively. Assuming that the abundance discrepancy is produced by spatial variations in the electron temperature, we derive values of the temperature fluctuation parameter, t^2, of 0.050 and 0.016 for the shock and nebular components, respectively. Interestingly, we obtain almost coincident t^2 values for both components from the analysis of the intensity ratios of He I lines. We find significant departures from case B predictions in the Balmer and Paschen flux ratios of lines of high principal quantum number n. We analyse the ionization structure of HH 202-S, finding enough evidence to conclude that the flow of HH 202-S has compressed the ambient gas inside the nebula trapping the ionization front. We measure a strong increase of the total abundances of nickel and iron in the shock component, the abundance pattern and the results of photoionization models for both components are consistent with the partial destruction of dust after the passage of the shock wave in HH 202-S.

Key words: ISM: abundances – dust, extinction – ISM: Herbig–Haro objects – ISM: individual: Orion Nebula – ISM: individual: HH 202.

1 INTRODUCTION

HH 202 is one of the brightest and most conspicuous Herbig–Haro (HH) objects of the Orion Nebula. It was discovered by Cantó et al. (1980). The origin of this outflow is not clear, though the radial velocity and proper motion studies suggest that this object forms a great complex together with HH 203, 204, 269, 529, 528 and 625, with a common origin in one or more sources embedded within the Orion Molecular Cloud 1 South (OMC 1S; see Rosado et al. 2002; O'Dell & Doi 2003; O'Dell & Henney 2008). Recently, Henney et al. (2007) have summarized the main characteristics of these outflows, and an extensive study of their kinematics can be found in García-Díaz et al. (2008). HH 202 shows a wide parabolic form with several bright knots of which HH 202-S is the brightest one (see Fig. 1).

The kinematic properties of HH 202-S have been studied by means of high spectral resolution spectroscopy by several authors.

★Based on observations collected at the European Southern Observatory, Chile, proposal number ESO 70.C-0008(A).

†E-mail: amd@iac.es

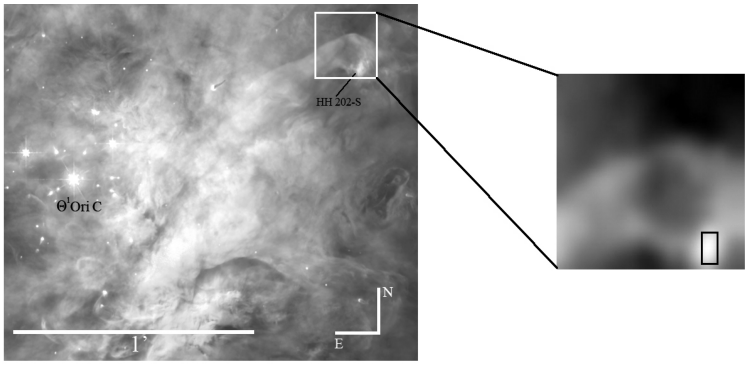

Figure 1. *HST* image of the central part of the Orion Nebula combined with Wide Field Planetary Camera 2 images in different filters (O'Dell & Wong 1996). The white square corresponds to the FOV of the PMAS and the separate close-up image at the right-hand side shows the rebinned Hα map presented in Paper I. Inside of this box, the black rectangle indicates the slit position and the area covered by the UVES spectrum analysed in this paper (1.5×2.5 arcsec^2).

Doi, O'Dell & Hartigan (2004) have found a radial velocity of -39 ± 2 km s^{-1}, in agreement with previous results by Meaburn (1986) and O'Dell, Wen & Hester (1991). O'Dell & Henney (2008) have determined a tangential velocity of 59 ± 8 km s^{-1}, which is in agreement with previous determinations by O'Dell & Doi (2003). O'Dell & Henney (2008) have calculated a spatial velocity of 89 km s^{-1} and an angle of the velocity vector of 48° with respect to the plane of the sky, similar to the values found by Henney et al. (2007). Imaging studies by O'Dell et al. (1997) with the *Hubble Space Telescope* (*HST*) of the HH objects in the Orion Nebula show an extended [O III] emission in HH 202 and a strong [O III] emission in HH 202-S. This fact, together with the closeness of HH 202 to the main ionization source of the Orion Nebula, θ^1 Ori C, indicates that the excitation of the ionized gas is dominated by photoionization in HH 202-S, though the observed radial velocities imply that some shocked gas can be mixed in the region (Cantó et al. 1980). Photoionization-dominated flows are a minority in the inventory of HH objects, which are typically excited by shocks. This kind of HH objects is also known as 'irradiated jets' (Reipurth et al. 1998), since they are excited by the ultraviolet (UV) radiation from nearby massive stars. Irradiated jets have been found in the Orion Nebula (e.g. Bally & Reipurth 2001; O'Dell et al. 1997; Bally et al. 2006), the Pelican Nebula (Bally & Reipurth 2003), the Carina Nebula (Smith, Bally & Brooks 2004), NGC 1333 (Bally et al. 2006) and the Trifid Nebula (Cernicharo et al. 1998; Reipurth et al. 1998).

Mesa-Delgado, Esteban & García-Rojas (2008) have obtained the spatial distributions of the physical conditions and the ionic abundances in the Orion Nebula using long-slit spectroscopy at spatial scales of 1.2 arcsec. The goal of that work was to study the possible correlations between the local structures observed in the Orion Nebula – HH objects, proplyds, ionization fronts – and the abundance discrepancy (AD) that is found in H II regions. The AD is a classical problem in the study of ionized nebulae: the abundances of a given ion derived from recombination lines (RLs) are often between 0.1 and 0.3 dex higher than those obtained from collisionally excited lines (CELs) in H II regions (see García-Rojas & Esteban 2007; Esteban et al. 2004; Tsamis et al. 2003). The difference between those independent determinations of the abundance defines the AD factor (ADF). The predictions of the temperature fluctuation paradigm proposed by Peimbert (1967) – and parametrized by the mean square of the spatial distribution of temperature, the t^2 parameter – seem to account for the discrepancies observed in H II regions (see García-Rojas & Esteban 2007). A striking result found in the spatially resolved study of Mesa-Delgado et al. (2008) is that the ADF of O^{2+}, ADF(O^{2+}), shows larger values at the locations of HH objects as is the case of HH 202. Using integral-field spectroscopy with intermediate spectral resolution and a spatial resolution of 1×1 arcsec^2, Mesa-Delgado et al. (2009, hereafter Paper I) have mapped the emission line fluxes, the physical properties and the O^{2+} abundances derived from RLs and CELs of HH 202. They have found extended [O III] emission and higher values of the electron density and temperature as well as an enhanced ADF(O^{2+}) in HH 202-S, confirming the earlier results of Mesa-Delgado et al. (2008).

HH 529 is another HH object that is photoionized by θ^1 Ori C and shows similar characteristics to those of HH 202. Blagrave, Martin & Baldwin (2006) have performed deep optical echelle spectroscopy of that object with a 4 m class telescope and have detected and measured about 280 emission lines. Their high spectral resolution spectroscopy allowed them to separate the kinematic components associated with the ambient gas and with the flow. They have determined the physical conditions and the ionic abundances of oxygen from CELs and RLs in both components. However, they do not find high ADF(O^{2+}) and t^2 values in neither component. Another interesting result of Blagrave et al. (2006) is that the ionization structure of HH 529 indicates that it is a matter-bounded shock.

Motivated by the results found by Mesa-Delgado et al. (2008), inspired by the work of Blagrave et al. (2006) and in order to complement the results presented in Paper I, we have isolated the emission of the flow of HH 202-S knot using high spectral resolution spectroscopy, presenting the first complete physical and chemical analysis of this knot.

In Section 2, we describe the observations of HH 202 and the reduction procedure. In Section 3, we describe the emission line measurements, identifications and the reddening correction, we also compare our reddening determinations with those available in the literature. In Section 4, we describe the determinations of the physical conditions, the chemical – ionic and total – abundances and the ADF for O^+ and O^{2+}. In Section 5, we discuss (i) some inconsistencies found in the Balmer decrement of the lines of higher principal quantum number, (ii) the ionization structure of HH 202-S, (iii) the radial velocity pattern of the lines of each kinematic component, (iv) the t^2 parameter obtained from different methods and its possible relation with the ADF and (v) the evidences of dust grain

destruction in HH 202-S. Finally, in Section 6 we summarize our main conclusions.

2 OBSERVATIONS AND DATA REDUCTION

HH 202 was observed on 2003 March 30 at Cerro Paranal Observatory, Chile, using the UT2 (Kueyen) of the Very Large Telescope (VLT) with the Ultraviolet Visual Echelle Spectrograph (UVES; D'Odorico et al. 2000). The standard settings of UVES were used covering the spectral range from 3100 to 10 400 Å. Some narrow spectral ranges could not be observed. These are: 5783–5830 and 8540–8650 Å, due to the physical separation between the CCDs of the detector system of the red arm and 10 084–10 088 and 10 252–10 259 Å, because the last two orders of the spectrum do not fit completely within the size of the CCD. Five individual exposures of 90 s – for the 3100–3900 and 4750–6800 Å ranges – and 270 s – for the 3800–5000 and 6700–10 400 Å ranges – were added to obtain the final spectra. In addition, exposures of 5 and 10 s were taken to obtain good flux measurements – i.e. non-saturated – for the brightest emission lines. The spectral resolution was $\lambda/\Delta\lambda \approx 30\,000$. This high spectral resolution enables us to separate two kinematic components: one corresponding to the ambient gas – which we will call *nebular component* and whose emission mainly arises from behind HH 202 and, therefore, could not entirely correspond to the pre-shock gas – and another one corresponding to the gas flow of the HH object, the post-shock gas, which we will call *shock component*.

The slit was oriented north–south, and the atmospheric dispersion corrector (ADC) was used to keep the same observed region within the slit regardless of the airmass value. The HH object was observed between airmass values of 1.20 and 1.35. The average seeing during the observation was 0.7 arcsec. The slit width was set to 1.5 arcsec as a compromise between the spectral resolution needed and the desired signal-to-noise ratio of the spectra. The slit length was fixed to 10 arcsec. The one-dimensional spectra were extracted for an area of 1.5×2.5 arcsec^2. This area covers the apex of HH 202, the so-called knot HH 202-S, as we can see in Fig. 1. This zone shows the maximum shift in velocity between the shock and nebular components (see Fig. 2) allowing us to appropriately separate and study the spectra of both kinematic components.

The spectra were reduced using the IRAF[1] echelle reduction package, following the standard procedure of bias subtraction, aperture extraction, flat-fielding, wavelength calibration and flux calibration. The standard stars EG 247, C-32 9927 (Hamuy et al. 1992, 1994) and HD 49798 (Turnshek et al. 1990; Bohlin & Lindler 1992) were observed to perform the flux calibration. The error of the absolute flux calibration was of the order of 3 per cent.

3 LINE MEASUREMENTS, IDENTIFICATIONS AND REDDENING CORRECTION

Line fluxes were measured applying a double Gaussian profile fit procedure over the local continuum. All these measurements were made with the SPLOT routine of IRAF.

All line fluxes of a given spectrum have been normalized to a particular bright emission line present in the common range of two consecutive spectra. For the bluest spectrum (3100–3900 Å), the reference line was H9 3835 Å. For the range from 3800 to 5000 Å, the reference line was Hβ. In the case of the spectrum covering 4750–6800 Å, the reference was [O III] 4959 Å. Finally, for the reddest spectrum (6700–10 400 Å), the reference line was [S II] 6731 Å. In order to produce a final homogeneous set of line flux ratios, all of them were rescaled to the Hβ flux. In the case of the bluest spectra, the ratios were rescaled by the H9/Hβ ratio obtained from the 3800–5000 Å range. The emission line ratios of the 4750–6800 Å range were multiplied by the [O III] 4959/Hβ ratio measured in the 3800–5000 Å range. In the case of the last spectral section, 6700–10 400 Å, the rescaling factor was the [S II] 6731/Hβ ratio obtained from the 4750–6800 Å spectrum. All rescaling factors were measured in the short exposure spectra in order to avoid the possible saturation of the brightest emission lines. This process was done separately for both the nebular and shock components.

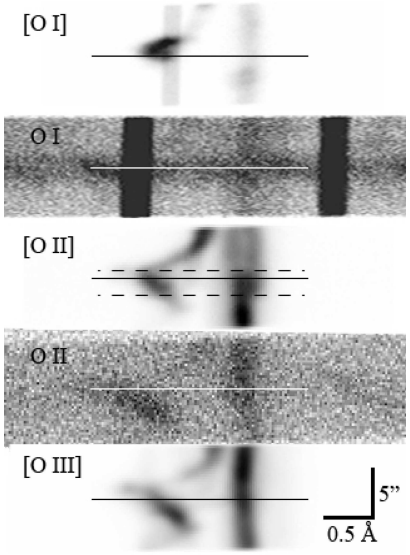

Figure 2. Sections of the bidimensional UVES spectrum showing the spatio-kinematic profiles of different oxygen lines: [O I] 6300 Å, O I 7772 Å, [O II] 3728 Å, O II 4649 Å and [O III] 4959 Å. Wavelength increases to the right and north points up. The solid straight lines in all the sections correspond to the slit centre and the dashed lines – only represented in the case of the [O II] 3728 Å profile – correspond to the extracted area 2.5 arcsec wide.

The spectral ranges present overlapping regions at the edges. The adopted flux of a line in the overlapping region was obtained as the average of the values obtained in both spectra. A similar procedure was considered in the case of lines present in two consecutive spectral orders of the same spectral range. The average of both measurements was considered for the adopted value of the line flux. In all cases, the differences in the line flux measured for the same line in different orders and/or spectral ranges do not show systematic trends and are always within the uncertainties.

The identification and laboratory wavelengths of the lines were obtained following a previous work on the Orion Nebula by Esteban et al. (2004), the compilations by Moore (1945) and the Atomic Line List v2.04.[2] The identification process and the measurement of line

[1] IRAF is distributed by National Optical Astronomy Observatories, which is operated by AURA (Association of Universities for Research in Astronomy), under cooperative agreement with NSF (National Science Foundation).

[2] Webpage at http://www.pa.uky.edu/~peter/atomic/.

fluxes were done simultaneously. The inspection of the line shapes at the bidimensional echelle spectrum was always used to identify which component – nebular or shock – was measured at each moment. The rather different spatial and spatio-kinematic structure of the two kinematic components is illustrated in Fig. 2. We have identified 360 emission lines in the spectrum of HH 202-S, 115 of them only show one component – eight belong to the nebular component and 107 belong to the shock one – and eight are dubious identifications.

For a given line, the observed wavelength is determined by the centroid of the Gaussian fit to the line profile. For lines measured in different orders and/or spectral ranges, the average of the different wavelength determinations has been adopted. From the adopted wavelength, the heliocentric velocity, $V_{\rm hel}$, has been calculated using the heliocentric correction appropriate for the coordinates of the object and the moment of observation. The typical error in the heliocentric velocity measured is about 1–2 km s^{-1}.

All line fluxes with respect to Hβ, $F(\lambda)/F(\mathrm{H}\beta)$, were dereddened using the typical relation,

$$\frac{I(\lambda)}{I(\mathrm{H}\beta)} = \frac{F(\lambda)}{F(\mathrm{H}\beta)} 10^{c(\mathrm{H}\beta) f(\lambda)}. \quad (1)$$

The reddening coefficient, c(Hβ), represents the amount of interstellar extinction which is the logarithmic extinction at Hβ, while $f(\lambda)$ is the adopted extinction curve normalized to $f(\mathrm{H}\beta) = 0$. The reddening coefficient was determined from the comparison of the observed flux ratio of Balmer and Paschen lines – those not contaminated by telluric or other nebular emissions – with respect to Hβ and the theoretical ones computed by Storey & Hummer (1995) for the physical conditions of $T_{\rm e} = 10\,000$ K and $n_{\rm e} = 1000$ cm^{-3}. As in Paper I, we have used the reddening function, $f(\lambda)$, normalized to Hβ derived by Blagrave et al. (2007) for the Orion Nebula. The use of this extinction law instead of the classical one (Costero & Peimbert 1970) produces slightly higher c(Hβ) values and also slightly different dereddened line fluxes depending on the spectral range (see Paper I). The final c(Hβ) values obtained for the two kinematic components were weighted averages of the values obtained for the individual lines: $c(\mathrm{H}\beta)_{\rm neb} = 0.41 \pm 0.02$ and $c(\mathrm{H}\beta)_{\rm sh} = 0.45 \pm 0.02$. Although not all the c(Hβ) values are consistent with each other (see Section 5.1), the average values obtained are quite similar and consistent within the uncertainties.

We can compare the reddening values with those obtained from integral-field spectroscopy data presented in Paper I in the same area of HH 202-S (see Fig. 1) and corresponding to the section $\Delta\alpha = [-4, -6]$ and $\Delta\delta = [-8, -5]$ (see fig. 3 of Paper I). The average c(Hβ) in this zone is 0.65 ± 0.15, which is higher than those determined for UVES data. However, if we recalculate the value of c(Hβ) from the UVES data using the same Balmer lines as in Paper I, we obtain a value 0.5 ± 0.1 in both kinematic components, a value consistent with the Potsdam Multi-Aperture Spectrograph (PMAS) one within the errors. These differences can be related to several systematical disagreements found between the c(Hβ) values obtained from different individual Balmer or Paschen lines (see Section 5.1).

In the most complete work on the reddening distribution across the Orion Nebula, O'Dell & Yusef-Zadeh (2000) obtain values of c(Hβ) between 0.2 and 0.4 in the zone around HH 202-S, somewhat lower than our reddening determinations. This can be due to the fact that O'Dell & Yusef-Zadeh use the extinction law by Costero & Peimbert (1970) which, as we discuss in Paper I, produces lower c(Hβ) values than the more recent extinction law (Blagrave et al. 2007). We have also recalculated c(Hβ) from our UVES spectra making use of the Costero & Peimbert law, and we obtain values about 0.3, being now in agreement with the determinations of O'Dell & Yusef-Zadeh (2000).

In Table 1, the final list of line identifications (Columns 1–3), $f(\lambda)$ values (Column 4), heliocentric velocities (Columns 5 and 8) and dereddened flux line ratios (Columns 6 and 9) for the nebular and shock components are presented. The observational errors associated with the line dereddened fluxes with respect to Hβ – in percentage – are also presented in Columns (7) and (10) of Table 1. These errors include the uncertainties in line flux measurement, flux calibration and error propagation in the reddening coefficient.

In Column (11) of Table 1, we present the shock-to-nebular line flux ratio for those lines in which both kinematic components have been measured. This ratio is defined as

$$\frac{I_{\rm sh}}{I_{\rm neb}} = \frac{[I(\lambda)/I(\mathrm{H}\beta)]_{\rm sh}}{[I(\lambda)/I(\mathrm{H}\beta)]_{\rm neb}} = \frac{I(\lambda)_{\rm sh}}{I(\lambda)_{\rm neb}} \times \frac{I(\mathrm{H}\beta)_{\rm neb}}{I(\mathrm{H}\beta)_{\rm sh}}, \quad (2)$$

where the integrated dereddened Hβ fluxes are $I(\mathrm{H}\beta)_{\rm neb} = (3.80 \pm 0.20) \times 10^{-12}$ and $I(\mathrm{H}\beta)_{\rm sh} = (6.00 \pm 0.20) \times 10^{-12}$ erg cm^{-2} s^{-1}. The $I_{\rm neb}/I_{\rm sh}$ ratios depend on each particular line. In general, they are close to 1 for H I lines but become less than 1 for higher ionized species – except Fe ions – and are typically greater than 1 for neutral species. A more extensive discussion on this particular issue will be presented in Section 5.2.

In Fig. 3, we show a section of our flux-calibrated echelle spectra around the lines of multiplet 1 of O II. It can be seen that both the nebular and the shock components are well separated and show a remarkable high signal-to-noise ratio.

4 RESULTS

4.1 Excitation mechanism of the ionized gas in HH 202-S

In their recent work, O'Dell & Henney (2008) argue that the presence of a variety of ionization stages in the ionized gas of HH 202 indicates that the flow also contains neutral material. They interpret that fact as due to the impact of the flow with pre-existing neutral material – perhaps of the foreground veil – or that the flow compresses the ambient ionized gas inside the nebula to such degree that it traps the ionization front. Our results provide some clues that can help to ascertain this issue. The value of some emission line ratios are good indicators of the presence of shock excitation in ionized gas, especially [S II]/Hα and [O I]/Hα. In our spectra, we find log([S II] 6717+31/Hα) values which are almost identical in both kinematic components (-1.49 and -1.44 for the nebular and shock components, respectively). These values are completely consistent with those expected for photoionized nebulae and far from the range of values between -0.5 and 0.5, which is the typical of supernova remnants and HH objects (see fig. 10 of Riera et al. 1989). On the other hand, the values of log([O I] 6300/Hα) that we obtain for the nebular and shock components are of -2.66 and -2.22, somewhat different in this case, but also far from the values expected in the case of substantial contribution of shock excitation (Hartigan, Raymond & Hartmann 1987). Finally, we have also used the diagnostic diagrams of Raga et al. (2008) where the [N II] 6548/Hα and [S II] 6717+31/Hα versus [O III] 5007/Hα ratios of HH 202 are found in the zone dominated by photoionized shocks. Therefore, the spectrum of HH 202-S seems to be consistent with the picture that the bulk of the emission in this area is produced by photoionization acting on compressed ambient gas that has trapped the ionization front inside the ionized bubble of the nebula. In the rest of the

Table 1. Identifications, reddening-corrected line ratios [$I(H\beta) = 100$] for an area of 1.5×2.5 arcsec^2 and heliocentric velocities for the nebular and shock components.

				Nebular component			Shock component				
λ_0 (Å)[a]	Ion[a]	Mult[a]	$f(\lambda)$[b]	V_{hel}[c]	$I(\lambda)$[d]	Error (per cent)[e]	V_{hel}[c]	$I(\lambda)$[d]	Error (per cent)[e]	I_{sh}/I_{neb}[f]	Notes
3187.74	He I	3	0.195	15	3.450	6	-34	3.682	6	1.067	
3239.74	[Fe III]	6F	0.194	–	–	–	−35	0.806	15	–	
3286.19	[Fe III]	6F	0.192	–	–	–	−35	0.206	15	–	
3319.21	[Fe III]	6F	0.191	–	–	–	−38	0.114	40	–	
3322.54	[Fe III]	5F	0.191	–	–	–	−48	0.744	9	–	
3334.90	[Fe III]	6F	0.190	–	–	–	−36	0.320	9	–	
3354.55	He I	8	0.189	14	0.148	10	−33	0.159	10	1.079	
3355.49	[Fe III]	6F	0.189	–	–	–	−37	0.189	10	–	
3356.57	[Fe III]	6F	0.189	–	–	–	−35	0.262	9	–	
3366.20	[Fe III]	6F	0.189	–	–	–	−35	0.119	40	–	
3371.41	[Fe III]	5F	0.188	–	–	–	−47	0.543	11	–	
3406.18	[Fe III]	5F	0.186	–	–	–	−48	0.250	11	–	
3447.59	He I	7	0.184	16	0.241	9	−34	0.246	9	1.019	
3498.66	He I	40	0.180	10	0.090	15	−36	0.054	18	0.595	
3512.52	He I	38	0.179	13	0.195	10	−38	0.176	10	0.901	
3530.50	He I	36	0.178	12	0.129	10	−34	0.147	10	1.136	
3554.42	He I	34	0.176	15	0.224	10	−36	0.219	10	0.976	
3587.28	He I	32	0.173	13	0.331	9	−36	0.339	9	1.024	
3613.64	He I	6	0.171	15	0.435	9	−37	0.462	9	1.061	
3634.25	He I	28	0.169	13	0.425	9	−35	0.464	9	1.090	
3664.68	H I	H28	0.166	13	0.172	10	−36	0.251	9	1.457	
3666.10	H I	H27	0.166	13	0.355	9	−36	0.347	9	0.977	
3667.68	H I	H26	0.166	13	0.414	9	−36	0.458	9	1.105	
3669.47	H I	H25	0.166	13	0.468	9	−36	0.502	9	1.072	
3671.48	H I	H24	0.165	13	0.543	9	−36	0.586	9	1.079	
3673.76	H I	H23	0.165	14	0.557	9	−36	0.645	9	1.157	
3676.37	H I	H22	0.165	15	0.661	9	−36	0.721	9	1.091	
3679.36	H I	H21	0.165	15	0.761	9	−36	0.841	9	1.105	
3682.81	H I	H20	0.164	14	0.822	9	−36	0.887	9	1.079	
3686.83	H I	H19	0.164	15	0.867	9	−36	0.993	9	1.146	
3691.56	H I	H18	0.163	14	1.106	9	−37	1.148	9	1.038	
3697.15	H I	H17	0.163	14	1.271	6	−36	1.312	6	1.032	
3703.86	H I	H16	0.162	13	1.409	6	−37	1.502	6	1.065	
3705.04	He I	25	0.162	10	0.646	9	−39	0.717	9	1.108	
3711.97	H I	H15	0.161	14	1.745	6	−36	1.834	6	1.050	
3721.83	[S III]	2F	0.160	10	4.041	6	−39	3.363	6	0.832	
3721.93	H I	H14									
3726.03	[O II]	1F	0.160	22	87.30	5	−34	70.12	5	0.803	
3728.82	[O II]	1F	0.160	18	52.04	5	−36	28.15	5	0.540	
3734.37	H I	H13	0.159	13	2.542	6	−36	2.581	6	1.015	
3750.15	H I	H12	0.158	14	3.081	6	−36	3.143	6	1.020	
3770.63	H I	H11	0.155	14	3.967	6	−36	4.087	6	1.030	
3797.63	[S III]	2F	0.152	35	5.240	5	−15	5.381	5	1.027	
3797.90	H I	H10									
3805.74	He I	58	0.152	12	0.063	15	−37	0.045	18	0.720	
3819.61	He I	22	0.150	14	1.129	9	−35	1.153	7	1.020	
3833.57	He I	62	0.149	14	0.067	15	−39	0.077	15	1.158	
3835.39	H I	H9	0.148	13	7.271	6	−37	7.242	6	0.996	
3856.02	Si II	1	0.146	16	0.211	10	−38	0.309	10	1.469	
3862.59	Si II	1	0.145	16	0.120	12	−38	0.175	12	1.450	
3868.75	[Ne III]	1F	0.145	12	12.94	5	−34	8.096	6	0.625	
3871.82	He I	60	0.144	10	0.084	15	−39	0.087	15	1.034	
3888.65	He I	2	0.142	16	6.717	6	−39	5.625	6	0.837	
3889.05	H I	H8	0.142	13	11.52	4	−45	9.043	6	0.784	
3918.98	C II	4	0.139	9	0.049	18	−39	0.062	18	1.267	
3920.68	C II	4	0.139	9	0.098	15	−39	0.106	15	1.086	
3926.53	He I	58	0.138	15	0.122	10	−36	0.135	10	1.102	
3964.73	He I	5	0.133	13	0.906	9	−36	0.937	9	1.034	
3967.46	[Ne III]	1F	0.133	13	3.866	6	−36	2.574	6	0.665	
3970.07	H I	H7	0.133	13	15.68	4	−37	15.93	4	1.016	
3993.06	[Ni II]	4F	0.130	28	0.033	20	−40	0.041	18	1.227	
4008.36	[Fe III]	4F	0.128	–	–	–	−42	0.587	9	–	*g*

Table 1 – *continued*

				Nebular component				Shock component				
λ_0 (Å)[a]	Ion[a]	Mult[a]	$f(\lambda)$[b]	V_{hel}[c]	$I(\lambda)$[d]	Error (per cent)[e]	V_{hel}[c]	$I(\lambda)$[d]	Error (per cent)[e]	I_{sh}/I_{neb}[f]	Notes
4009.22	He I	55	0.128	16	0.170	10	−35	0.222	10	1.312	*g*
4023.98	He I	54	0.126	16	0.028	20	−39	0.026	20	0.935	
4026.08	N II	40	0.126	13	2.195	6	−37	2.110	6	0.961	
4026.21	He I	18									
4046.43	[Fe III]	4F	0.123	–	–	–	−38	0.084	15	–	
4068.60	[S II]	1F	0.121	23	0.887	9	−35	5.318	6	5.996	
4069.62	O II	10	0.121	25	0.288	10	−28	0.197	15	0.683	*g*
4069.89	O II	10									
4072.15	O II	10	0.120	15	0.066	15	−38	0.045	18	0.683	
4076.35	[S II]	1F	0.120	23	0.362	9	−35	1.800	6	4.968	
4079.70	[Fe III]	4F	0.119	–	–	–	−42	0.154	10	–	
4089.29	O II	48	0.118	13	0.012	30	−38	0.021	28	1.754	
4092.93	O II	10	0.118	11	0.014	30	−34	0.008	35	0.595	
4096.61	[Fe III]	4F	0.117	9	0.028	40	−37	0.036	20	1.295	
4097.22	O II	20	0.117	15	0.025	25	−34	0.020	40	0.789	
4097.26	O II	48									
4101.74	H I	H6	0.117	14	24.75	4	−37	25.10	4	1.014	
4114.48	[Fe II]	23F	0.115	–	–	–	−42	0.083	15	–	
4119.22	O II	20	0.114	12	0.014	30	−40	0.019	28	1.355	
4120.82	He I	16	0.114	12	0.175	10	−35	0.199	10	1.134	*g*
4121.46	O II	19	0.114	7	0.031	20	−34	0.047	18	1.511	*g*
4132.80	O II	19	0.113	9	0.027	20	−45	0.051	18	1.881	
4143.76	He I	53	0.111	13	0.281	9	−37	0.304	9	1.082	
4153.30	O II	19	0.110	10	0.037	18	−42	0.042	18	1.141	
4156.36	N II	19	0.110	14	0.034	18	−37	0.030	20	0.896	*h*
4168.97	He I	52	0.108	18	0.052	18	−34	0.055	18	1.044	
4177.20	[Fe II]	21F	0.107	26	0.015	40	−41	0.041	20	2.695	
4178.96	[Fe II]	23F	0.107	–	–	–	−42	0.023	30	–	
4185.45	O II	36	0.106	11	0.026	20	−36	0.009	35	0.363	
4189.79	O II	36	0.105	10	0.024	20	−51	0.023	20	0.939	
4201.17	[Ni II]	4F	0.104	–	–	–	−40	0.015	30	–	
4211.10	[Fe II]	23F	0.103	–	–	–	−40	0.034	18	–	
4243.97	[Fe II]	21F	0.098	22	0.104	10	−41	0.275	9	2.649	
4251.44	[Fe II]	23F	0.097	–	–	–	−41	0.018	40	–	
4267.15	C II	6	0.095	15	0.247	9	−35	0.211	10	0.854	
4276.83	[Fe II]	21F	0.094	26	0.039	18	−40	0.147	10	3.776	
4287.39	[Fe II]	7F	0.093	27	0.083	15	−41	0.280	9	3.379	
4303.82	O II	53	0.091	10	0.027	20	−34	0.016	30	0.574	
4317.14	O II	2	0.089	9	0.021	28	−49	0.045	18	2.174	
4319.62	[Fe II]	21F	0.088	–	–	–	−41	0.077	15	–	
4326.24	[Ni II]	^{2}D-^{4}P	0.088	28	0.041	18	−28	0.311	:	7.603	
4340.47	H I	Hγ	0.086	13	46.21	4	−37	46.56	4	1.007	
4345.55	O II	63.01	0.085	11	0.035	18	−42	0.069	15	1.958	
4346.85	[Fe II]	21F	0.085	–	–	–	−41	0.056	18	–	
4349.43	O II	2	0.084	11	0.047	18	−37	0.051	18	1.088	
4352.78	[Fe II]	21F	0.084	26	0.027	40	−41	0.071	18	2.647	
4358.36	[Fe II]	21F	0.083	–	–	–	−41	0.046	15	–	
4359.34	[Fe II]	7F	0.083	26	0.060	15	−41	0.209	10	3.488	
4363.21	[O III]	2F	0.082	13	0.944	9	−36	0.934	9	0.989	
4366.89	O II	2	0.081	10	0.025	20	−41	0.046	18	1.843	
4368.19	O I	5	0.081	29	0.082	15	−29	0.030	20	0.361	
4368.25	O I	5									
4372.43	[Fe II]	21F	0.081	–	–	–	−41	0.032	20	–	
4387.93	He I	51	0.078	14	0.523	9	−37	0.563	9	1.076	
4413.78	[Fe II]	7F	0.073	28	0.055	15	−41	0.151	10	2.766	*g*
4414.90	O II	5	0.073	15	0.037	20	−32	0.024	20	0.638	*g*
4416.27	[Fe II]	6F	0.073	23	0.054	15	−41	0.237	9	4.412	*g*
4416.97	O II	5	0.073	13	0.021	28	−33	0.343	20	16.53	*g*
4432.45	[Fe II]	6F	0.070	–	–	–	−41	0.020	28	–	
4437.55	He I	50	0.069	14	0.063	15	−36	0.071	15	1.121	
4452.11	[Fe II]	7F	0.067	26	0.034	18	−42	0.095	15	2.764	
4452.38	O II	5									
4457.95	[Fe II]	6F	0.066	27	0.022	20	−42	0.102	10	4.599	

Table 1 – *continued*

				Nebular component			Shock component				
λ_0 (Å)[a]	Ion[a]	Mult[a]	$f(\lambda)$[b]	V_{hel}[c]	$I(\lambda)$[d]	Error (per cent)[e]	V_{hel}[c]	$I(\lambda)$[d]	Error (per cent)[e]	I_{sh}/I_{neb}[f]	Notes
4471.47	He I	14	0.064	15	4.303	6	−35	4.405	6	1.023	
4474.91	[Fe II]	7F	0.063	25	0.012	:	−42	0.044	18	3.655	
4488.75	[Fe II]	6F	0.061	–	–	–	−42	0.033	20	–	
4492.64	[Fe II]	6F	0.060	26	0.011	:	−41	0.032	20	3.025	
4509.60	[Fe II]	6F	0.057	–	–	–	−38	0.011	:	–	*h*
4514.90	[Fe II]	6F	0.056	–	–	–	−41	0.024	40	–	*h*
4528.38	[Fe II]	6F	0.054	–	–	–	−42	0.010	:	–	*h*
4563.18	[Cr III]?		0.048	–	–	–	−78	0.020	40	–	
4571.10	Mg I]	1	0.047	10	0.034	30	−41	0.215	9	6.377	
4581.14	[Cr II]?		0.045	–	–	–	−49	0.024	30	–	
4590.97	O II	15	0.044	14	0.016	40	−36	0.017	40	1.071	
4597.00	[Co IV]?		0.043	–	–	–	−39	0.122	10	–	
4601.48	N II	5	0.042	14	0.027	40	−42	0.020	40	0.753	
4607.13	[Fe III]	3F	0.041	13	0.065	15	−43	0.752	9	11.51	
4607.16	N II	5									
4628.05	[Ni II]	^{2}D-^{4}P	0.037	29	0.008	:	−39	0.014	40	1.685	
4630.54	N II	5	0.037	13	0.035	18	−37	0.041	18	1.178	
4638.86	O II	1	0.036	10	0.065	15	−41	0.044	18	0.678	
4641.81	O II	1	0.035	12	0.072	15	−39	0.077	15	1.065	
4641.85	N III	2									
4649.13	O II	1	0.034	13	0.102	10	−38	0.093	15	0.908	
4650.84	O II	1	0.034	15	0.049	18	−43	0.045	18	0.929	
4658.10	[Fe III]	3F	0.032	18	0.870	9	−39	10.98	5	12.62	
4661.63	O II	1	0.032	11	0.048	18	−38	0.059	15	1.207	
4667.01	[Fe III]	3F	0.031	9	0.047	30	−40	0.531	9	11.42	
4673.73	O II	1	0.030	13	0.008	35	−38	0.006	40	0.738	
4676.24	O II	1	0.030	11	0.024	20	−38	0.026	20	1.106	
4701.62	[Fe III]	3F	0.025	14	0.237	9	−43	3.915	6	16.52	
4711.37	[Ar IV]	1F	0.024	12	0.014	40	–	–	–	–	
4713.14	He I	12	0.023	15	0.570	9	−35	0.551	9	0.966	
4728.07	[Fe II]	4F	0.021	–	–	–	−41	0.054	15	–	
4733.93	[Fe III]	3F	0.020	14	0.125	10	−42	1.842	6	14.77	
4740.16	[Ar IV]	1F	0.019	15	0.016	40	–	–	–	–	
4754.83	[Fe III]	3F	0.017	13	0.167	10	−46	2.070	6	12.39	
4769.60	[Fe III]	3F	0.014	7	0.098	10	−48	1.391	6	14.21	
4774.74	[Fe II]	20F	0.014	24	0.007	:	−42	0.044	18	6.607	
4777.88	[Fe III]	3F	0.013	7	0.036	25	−51	0.901	9	24.92	
4814.55	[Fe II]	20F	0.007	26	0.071	15	−41	0.211	10	2.947	
4861.33	H I	Hβ	0.000	14	100.0	4	−37	100.0	4	1.000	
4874.48	[Fe II]	20F	−0.002	–	–	–	−41	0.039	18	–	
4881.00	[Fe III]	2F	−0.003	20	0.342	9	−38	5.776	6	16.86	
4889.70	[Fe II]	3F	−0.005	23	0.074	18	−45	0.159	10	2.171	
4902.65	Si II	7.23	−0.007	10	0.016	:	−39	0.010	30	0.642	*g*
4905.34	[Fe II]	20F	−0.007	19	0.031	:	−40	0.071	20	2.311	*g*
4921.93	He I	48	−0.010	13	1.195	6	−37	1.181	6	0.988	
4924.50	[Fe III]	2F	−0.010	21	0.063	20	−37	0.074	15	1.221	
4924.53	O II	28									
4930.50	[Fe III]	1F	−0.011	25	0.195	15	−32	0.527	9	2.706	*g*
4931.32	[O III]	1F	−0.011	11	0.038	22	−38	0.027	20	0.702	*g*
4947.38	[Fe II]	20F	−0.013	23	0.016	35	−39	0.031	20	2.309	
4950.74	[Fe II]	20F	−0.014	–	–	–	−40	0.030	19	–	
4958.91	[O III]	1F	−0.015	13	101.9	5	−35	71.55	5	0.702	
4973.39	[Fe II]	20F	−0.017	–	–	–	−41	0.029	20	–	
4985.90	[Fe III]	2F	−0.019	–	–	–	−44	0.045	40	–	
4987.20	[Fe III]	2F	−0.019	22	0.097	30	−38	1.069	6	11.07	
4987.38	N II	24									
5006.84	[O III]	1F	−0.022	13	303.8	5	−35	213.5	5	0.702	
5011.30	[Fe III]	1F	−0.023	18	0.182	15	−40	1.968	6	10.80	
5015.68	He I	4	−0.024	13	2.357	6	−37	2.396	6	1.016	
5020.23	[Fe II]	20F	−0.024	–	–	–	−39	0.035	25	–	
5041.03	Si II	5	−0.028	15	0.178	10	−37	0.141	10	0.792	
5043.52	[Fe II]	20F	−0.028	–	–	–	−40	0.020	:	–	
5047.74	He I	47	−0.028	–	–	–	−37	0.148	10	–	*g*

Table 1 – *continued*

				Nebular component			Shock component				
λ_0 (Å)[a]	Ion[a]	Mult[a]	$f(\lambda)$[b]	V_{hel}[c]	$I(\lambda)$[d]	Error (per cent)[e]	V_{hel}[c]	$I(\lambda)$[d]	Error (per cent)[e]	I_{sh}/I_{neb}[f]	Notes
5055.98	Si II	5	−0.030	17	0.224	9	−36	0.274	9	1.223	
5084.77	[Fe III]	1F	−0.034	–	–	–	−40	0.332	9	–	
5111.63	[Fe II]	19F	−0.038	–	–	–	−41	0.103	10	–	
5146.61	O I	28	−0.043	28	0.041	18	–	–	–	–	
5146.65	O I	28									
5158.00	[Fe II]	18F	−0.045	–	–	–	−41	0.061	15	–	*g*
5158.81	[Fe II]	19F	−0.045	25	0.077	15	−42	0.722	9	9.373	*g*
5163.95	[Fe II]	35F	−0.045	–	–	–	−40	0.044	18	–	
5181.95	[Fe II]	18F	−0.048	–	–	–	−39	0.023	25	–	
5191.82	[Ar III]	3F	−0.049	6	0.045	20	−41	0.059	20	1.303	
5197.90	[N I]	1F	−0.050	28	0.224	9	−32	0.037	18	0.164	*i*
5200.26	[N I]	1F	−0.051	28	0.111	10	−33	0.010	30	0.091	*i*
5220.06	[Fe II]	19F	−0.053	–	–	–	−40	0.073	18	–	
5261.61	[Fe II]	19F	−0.059	28	0.052	15	−40	0.318	9	6.083	
5268.88	[Fe II]	18F	−0.060	–	–	–	−40	0.022	20	–	
5270.40	[Fe III]	1F	−0.060	24	0.418	9	−33	6.378	6	15.24	
5273.38	[Fe II]	18F	−0.061	25	0.037	18	−42	0.160	10	4.374	
5296.83	[Fe II]	19F	−0.064	–	–	–	−41	0.032	25	–	
5298.89	O I	26	−0.064	25	0.030	30	–	–	–	–	
5299.04	O I	26									
5333.65	[Fe II]	19F	−0.069	23	0.028	40	−41	0.165	10	5.827	
5376.45	[Fe II]	19F	−0.075	–	–	–	−41	0.111	10	–	
5412.00	[Fe III]	1F	−0.080	23	0.054	40	−33	0.597	9	11.01	
5412.65	[Fe II]	17F	−0.080	–	–	–	−41	0.055	40	–	
5433.13	[Fe II]	18F	−0.082	–	–	–	−41	0.050	25	–	
5436.43	[Cr III]	2F	−0.083	–	–	–	−44	0.048	25	–	
5454.72	[Cr III]	2F	−0.085	–	–	–	−41	0.056	20	–	
5472.35	[Cr III]	2F	−0.088	–	–	–	−43	0.083	15	–	
5485.03	[Cr III]	2F	−0.089	–	–	–	−44	0.052	20	–	
5495.82	[Fe II]	17F	−0.091	–	–	–	−40	0.034	30	–	
5506.87	[Cr III]	2F	−0.092	–	–	–	−41	0.153	10	–	
5512.77	O I	25	−0.093	26	0.020	20	−42	0.012	30	0.618	
5517.71	[Cl III]	1F	−0.093	12	0.507	9	−36	0.271	9	0.535	
5527.34	[Fe II]	17F	−0.095	–	–	–	−41	0.173	10	–	
5537.88	[Cl III]	1F	−0.096	12	0.507	9	−39	0.555	9	1.095	
5551.96	[Cr III]	2F	−0.098	–	–	–	−45	0.278	9	–	
5554.83	O I	24	−0.098	34	0.041	18	–	–	–	–	
5555.03	O I	24									
5654.86	[Fe II]	17F	−0.111	–	–	–	−42	0.018	28	–	
5666.64	N II	3	−0.113	13	0.022	40	−37	0.017	40	0.765	
5679.56	N II	3	−0.114	13	0.024	40	−34	0.031	40	1.302	
5714.61	[Cr III]	1F	−0.119	–	–	–	−43	0.132	10	–	
5746.97	[Fe II]	34F	−0.123	–	–	–	−41	0.022	25	–	
5754.64	[N II]	3F	−0.124	21	0.646	9	−37	1.565	6	2.421	
5875.64	He I	11	−0.138	13	12.969	5	−37	13.024	5	1.004	
5885.88	[Cr III]	1F	−0.140	–	–	–	−45	0.106	18	–	
5887.67	[Mn II]?		−0.140	–	–	–	−32	0.039	25	–	*i*
5890.27	[Co II]	b^3P-c^3F	−0.140	–	–	–	−54	0.095	25	–	*i*
5931.78	N II	28	−0.145	25	0.027	18	−42	0.026	:	0.976	
5941.65	N II	28	−0.147	10	0.009	30	−39	0.024	:	2.554	
5957.56	Si II	4	−0.148	19	0.087	30	−39	0.102	15	1.177	
5958.39	O I	23	−0.149	31	0.037	:	–	–	–	–	
5958.58	O I	23									
5978.93	Si II	4	−0.151	19	0.129	15	−38	0.182	11	1.410	
5983.32	[Cr III]	1F	−0.152	–	–	–	−47	0.047	18	–	
5987.62	[Co II]	b^3P-c^3F	−0.152	–	–	–	−54	0.040	20	–	
6000.10	[Ni III]	2F	−0.154	–	–	–	−34	0.167	15	–	
6046.23	O I	22	−0.159	35	0.086	15	−27	0.023	25	0.268	
6046.44	O I	22									
6046.49	O I	22									
6300.30	[O I]	1F	−0.189	27	0.544	9	−32	1.691	6	3.106	*j*
6312.10	[S III]	3F	−0.191	14	1.700	6	−38	2.248	6	1.322	
6347.11	Si II	2	−0.195	18	0.194	12	−39	0.297	9	1.531	

Table 1 – *continued*

				Nebular component			Shock component				
λ_0 (Å)[a]	Ion[a]	Mult[a]	$f(\lambda)$[b]	V_{hel}[c]	$I(\lambda)$[d]	Error (per cent)[e]	V_{hel}[c]	$I(\lambda)$[d]	Error (per cent)[e]	I_{sh}/I_{neb}[f]	Notes
6363.78	[O I]	1F	−0.197	26	0.207	9	−32	0.554	9	2.676	*j*
6371.36	Si II	2	−0.198	15	0.107	15	−39	0.150	12	1.406	
6440.40	[Fe II]	15F	−0.206	–	–	–	−41	0.037	18	–	
6533.80	[Ni III]	2F	−0.217	–	–	–	−51	0.264	9	–	
6548.03	[N II]	1F	−0.218	24	15.60	5	−34	24.83	5	1.591	
6562.82	H I	Hα	−0.220	13	279.4	4	−38	283.1	4	1.013	
6576.30	[Co III]	a^4F-a^4P	−0.222	–	–	–	−48	0.049	20	–	
6578.05	C II	2	−0.222	13	0.196	12	−38	0.215	12	1.093	
6583.41	[N II]	1F	−0.223	24	46.67	5	−35	76.64	5	1.642	
6666.80	[Ni II]	8F	−0.232	–	–	–	−40	0.068	20	–	
6678.15	He I	46	−0.234	13	3.462	6	−37	3.532	6	1.020	
6682.20	[Ni III]	2F	−0.234	–	–	–	−53	0.085	15	–	
6716.47	[S II]	2F	−0.238	22	3.715	6	−36	3.211	6	0.864	
6730.85	[S II]	2F	−0.240	23	5.405	6	−36	7.041	6	1.302	
6739.80	[Fe IV]	–	−0.241	–	–	–	−37	0.015	30	–	
6747.50	[Cr IV]?	–	−0.242	–	–	–	−37	0.038	25	–	
6797.00	[Ni III]	2F	−0.247	–	–	–	−53	0.035	20	–	
6809.23	[Fe II]	31F	−0.249	–	–	–	−40	0.008	35	–	
6813.57	[Ni II]	8F	−0.249	–	–	–	−42	0.007	35	–	
6946.40	[Ni III]	2F	−0.265	–	–	–	−51	0.046	18	–	
6961.50	[Co III]	a^4F-a^4P	−0.266	–	–	–	−49	0.011	35	–	
7001.92	O I	21	−0.271	36	0.088	15	−25	0.053	15	0.603	*i*
7002.23	O I	21									
7035.30	[Co II]?	a^1D-c^3P	−0.275	–	–	–	−74	0.011	35	–	
7065.28	He I	10	−0.278	11	5.366	6	−40	4.677	6	0.871	
7078.10	[V II]?		−0.280	–	–	–	−33	0.010	40	–	
7088.30	[Cr III]?		−0.281	–	–	–	−33	0.026	30	–	
7125.74	[V II]?		−0.285	–	–	–	−63	0.009	30	–	
7135.78	[Ar III]	1F	−0.286	13	12.88	6	−37	14.46	6	1.122	
7152.70	[Co III]?	a^4F-a^4P	−0.288	–	–	–	−32	0.025	18	–	
7155.16	[Fe II]	14F	−0.289	25	0.057	15	−42	1.045	6	18.48	
7160.58	He I	1/10	−0.289	12	0.027	18	−38	0.023	18	0.847	
7172.00	[Fe II]	14F	−0.291	–	–	–	−43	0.286	9	–	
7231.34	C II	3	−0.297	12	0.081	15	−39	0.069	15	0.856	*i*
7236.42	C II	3	−0.298	12	0.164	12	−36	0.117	15	0.712	*i*
7254.15	O I	20	−0.300	34	0.133	11	−25	0.030	18	0.221	*i*
7254.45	O I	20									
7254.53	O I	20									
7281.35	He I	45	−0.303	14	0.594	9	−36	0.709	9	1.191	
7291.47	[Ca II]	1F	−0.304	–	–	–	−43	0.480	9	–	
7298.05	He I	1/9	−0.305	13	0.026	18	−39	0.024	18	0.918	*i*
7318.92	[O II]	2F	−0.307	28	0.880	6	−30	3.061	6	3.476	*g*, *i*
7319.99	[O II]	2F	−0.308	27	3.257	6	−32	10.19	5	3.129	*g*, *i*
7323.89	[Ca II]	1F	−0.308	–	–	–	−43	0.342	9	–	
7329.66	[O II]	2F	−0.309	23	1.589	6	−36	5.548	6	3.492	*g*, *i*
7330.73	[O II]	2F	−0.309	22	1.814	6	−36	5.502	6	3.032	*g*, *i*
7377.83	[Ni II]	2F	−0.314	29	0.070	11	−40	0.965	6	13.73	
7388.16	[Fe II]	14F	−0.315	–	–	–	−42	0.202	9	–	
7411.61	[Ni II]	2F	−0.318	28	0.026	18	−40	0.101	11	3.869	
7452.54	[Fe II]	14F	−0.323	25	0.021	20	−41	0.333	9	15.58	
7499.85	He I	1/8	−0.328	13	0.038	15	−37	0.038	15	0.990	
7637.54	[Fe II]	1F	−0.344	–	–	–	−43	0.120	20	–	
7686.94	[Fe II]	1F	−0.349	–	–	–	−43	0.108	18	–	
7751.10	[Ar III]	2F	−0.356	14	3.118	6	−37	3.488	6	1.118	*i*
7771.94	O I	1	−0.359	25	0.011	30	−42	0.012	28	1.115	*g*, *i*
7774.17	O I	1	−0.359	–	–	–	−43	0.026	18	–	*g*, *i*
7775.39	O I	1	−0.359	21	0.005	35	−42	0.006	35	1.115	*g*, *i*
7816.13	He I	1/7	−0.363	14	0.062	15	−37	0.051	15	0.830	
7889.90	[Ni III]	1F	−0.372	22	0.049	15	−35	0.736	6	15.13	
8000.08	[Cr II]	1F	−0.384	26	0.014	28	−43	0.053	15	3.704	
8125.30	[Cr II]	1F	−0.397	26	0.013	28	−41	0.045	15	3.383	
8260.93	H I	P36	−0.411	15	0.033	18	−37	0.046	15	1.400	
8264.28	H I	P35	−0.412	16	0.068	11	−34	0.064	11	0.936	

Table 1 – *continued*

				Nebular component				Shock component				
λ_0 (Å)[a]	Ion[a]	Mult[a]	$f(\lambda)$[b]	V_{hel}[c]	$I(\lambda)$[d]	Error (per cent)[e]	V_{hel}[c]	$I(\lambda)$[d]	Error (per cent)[e]	I_{sh}/I_{neb}[f]	Notes
8267.94	H I	P34	−0.412	15	0.053	15	−37	0.067	11	1.245	
8271.93	H I	P33	−0.413	14	0.067	11	−39	0.068	11	1.009	
8276.31	H I	P32	−0.413	14	0.076	11	−38	0.086	11	1.127	
8281.12	H I	P31	−0.414	23	0.057	15	−36	0.104	11	1.831	
8286.43	H I	P30	−0.414	10	0.075	11	−46	0.042	15	0.563	*i*
8292.31	H I	P29	−0.415	13	0.091	11	−37	0.111	11	1.221	
8298.83	H I	P28	−0.415	12	0.101	11	−38	0.112	11	1.104	*i*
8300.99	[Ni II]	2F	−0.416	–	–	–	−38	0.040	15	–	*g*
8306.11	H I	P27	−0.416	15	0.120	11	−36	0.129	11	1.075	*g*
8308.49	[Cr II]	1F	−0.416	–	–	–	−41	0.027	18	–	*g*
8314.26	H I	P26	−0.417	14	0.131	11	−37	0.154	9	1.173	
8323.42	H I	P25	−0.418	15	0.151	9	−36	0.171	9	1.138	
8333.78	H I	P24	−0.419	14	0.153	9	−38	0.173	9	1.131	
8345.55	H I	P23	−0.420	15	0.185	9	−36	0.189	9	1.026	*i*
8357.64	[Cr II]	1F	−0.422	–	–	–	−39	0.011	28	–	*g*
8359.00	H I	P22	−0.422	15	0.214	9	−37	0.241	9	1.128	*g*
8361.67	He I	1/6	−0.422	16	0.094	11	−35	0.091	11	0.968	*g*
8374.48	H I	P21	−0.423	15	0.233	9	−37	0.242	9	1.039	
8392.40	H I	P20	−0.425	14	0.248	9	−37	0.277	9	1.116	
8413.32	H I	P19	−0.427	14	0.277	9	−37	0.327	9	1.178	*g*, *i*
8437.96	H I	P18	−0.430	15	0.338	9	−37	0.353	9	1.045	
8446.25	O I	4	−0.431	30	0.566	9	−38	0.035	15	0.061	
8446.36	O I	4									
8446.76	O I	4	−0.635	27	0.279	9	–	–	–	–	
8446.76	O I	4	−0.431	27	0.282	9	–	–	–	–	
8467.25	H I	P17	−0.433	14	0.398	9	−37	0.403	9	1.012	*g*, *i*
8499.60	[Ni III]	1F	−0.436	–	–	–	−37	0.280	9	–	
8502.48	H I	P16	−0.436	15	0.453	9	−37	0.486	9	1.071	*i*
8665.02	H I	P13	−0.453	14	0.840	7	−38	0.835	7	0.994	
8728.90	[Fe III]	8F	−0.459	–	–	–	−37	0.105	11	–	*i*
8728.90	N I	21									
8733.43	He I	6/12	−0.459	13	0.033	15	−37	0.035	15	1.082	*g*
8736.04	He I	7/12	−0.460	15	0.010	28	−40	0.012	28	1.209	*g*
8750.47	H I	P12	−0.461	15	1.028	7	−37	1.032	7	1.004	
8838.20	[Fe III]	8F	−0.469	–	–	–	−41	0.064	11	–	*g*, *i*
8845.38	He I	6/11	−0.470	13	0.050	15	−36	0.054	15	1.068	
8848.05	He I	7/11	−0.470	6	0.023	18	−40	0.020	18	0.852	*g*, *i*
8862.79	H I	P11	−0.472	14	1.327	7	−37	1.311	7	0.987	
8891.91	[Fe II]	13F	−0.475	–	–	–	−41	0.397	9	–	
8914.77	He I	2/7	−0.477	13	0.022	18	−38	0.017	20	0.778	
8996.99	He I	6/10	−0.484	13	0.057	11	−38	0.059	11	1.022	
9014.91	H I	P10	−0.486	10	1.545	7	−37	1.764	7	1.141	*g*, *i*
9033.50	[Fe II]	13F	−0.488	–	–	–	−42	0.135	9	–	
9051.95	[Fe II]	13F	−0.489	–	–	–	−42	0.266	9	–	
9063.29	He I	4/8	−0.490	14	0.056	15	−36	0.053	15	0.944	
9068.60	[S III]	1F	−0.491	26	34.83	6	−28	37.41	6	1.074	
9123.60	[Cl II]	1F	−0.485	27	0.025	25	−35	0.078	15	3.117	
9210.28	He I	6/9	−0.494	14	0.078	11	−36	0.094	11	1.193	
9213.20	He I	7/9	−0.494	12	0.020	18	−39	0.033	15	1.710	
9226.62	[Fe II]	13F	−0.495	–	–	–	−42	0.233	9	–	
9229.01	H I	P9	−0.496	15	2.293	7	−37	2.330	7	1.015	
9267.56	[Fe II]	13F	−0.499	–	–	–	−42	0.168	9	–	*g*, *i*
9399.04	[Fe II]	13F	−0.512	–	–	–	−43	0.037	15	–	
9444.60	[Co III]	b^4P-b^4D	−0.517	–	–	–	−49	0.049	15	–	
9463.57	He I	1/5	−0.518	13	0.095	11	−37	0.127	9	1.341	
9526.16	He I	6/8	−0.524	14	0.094	11	−36	0.114	11	1.205	
9530.60	[S III]	1F	−0.525	26	80.05	6	−26	94.51	6	1.180	
9545.97	H I	P8	−0.526	15	3.301	7	−40	2.524	7	0.764	*i*
9701.20	[Fe III]	11F	−0.540	–	–	–	−27	0.214	9	–	
9705.30	[Ti III]	2F	−0.540	–	–	–	−34	0.019	18	–	
9903.46	C II	17.02	−0.557	14	0.048	40	−33	0.045	40	0.947	
9960.00	[Fe III]	8F	−0.562	–	–	–	−42	0.022	30	–	
10027.7	He I	6/7	−0.567	14	0.152	9	−36	0.159	9	1.048	

Table 1 – *continued*

				Nebular component			Shock component				
λ_0 (Å)[a]	Ion[a]	Mult[a]	$f(\lambda)$[b]	V_{hel}[c]	$I(\lambda)$[d]	Error (per cent)[e]	V_{hel}[c]	$I(\lambda)$[d]	Error (per cent)[e]	I_{sh}/I_{neb}[f]	Notes
10 031.2	He I	7/7	−0.568	11	0.045	15	−38	0.054	11	1.185	
10 049.4	H I	P7	−0.569	13	5.425	7	−38	5.016	7	0.924	
10 320.5	[S II]	3F	−0.590	22	0.194	9	−37	1.016	7	5.234	
10 336.4	[S II]	3F	−0.591	22	0.216	9	−38	0.891	7	4.117	
10 370.5	[S II]	3F	−0.593	–	–	–	−38	0.396	9	–	

[a]Identification of each line: laboratory wavelength, ion and multiplet. Dubious identifications are marked with '?'.
[b]Value of the extinction curve adopted (Blagrave et al. 2007).
[c]Heliocentric velocity in units of km s^{-1}, the typical error is 1–2 km s^{-1}.
[d]Dereddened fluxes with respect to $I(H\beta) = 100$.
[e]Error of the dereddened flux ratios. Colons indicate errors larger than 40 per cent.
[f]Shock-to-nebular line flux ratio. See definition in equation (2).
[g]Line blended with another line and deblended via Gaussian fitting.
[h]Contaminated by 'ghost'.
[i]Contaminated by telluric emissions and not deblended.
[j]Deblended from telluric emissions.

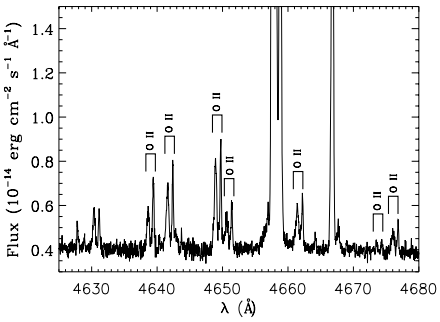

Figure 3. Section of the echelle spectrum of HH 202-S showing the shock (left-hand side) and nebular (right-hand side) components of each emission line of multiplet 1 of O II.

paper, we will provide and discuss further indications that HH 202-S contains an ionization front.

4.2 Physical conditions

We have computed physical conditions of the two kinematic components using several ratios of CELs following the same methodology as in Paper I and in Mesa-Delgado et al. (2008). The electron temperatures, T_e, and densities, n_e, are presented in Table 2.

We have determined n_e from [O II], [S II], [Cl III] and [Ar IV] line ratios using the NEBULAR package (Shaw & Dufour 1995). In the case of the n_e obtained from [Fe III] lines, we have used flux ratios of 31 and 12 lines for the shock and nebular components, respectively, following the procedure described by García-Rojas et al. (2006). For the nebular component, we have adopted the average value of n_e([O II]), n_e([S II]) and n_e([Cl III]) excluding n_e([Fe III]) and n_e([Ar IV]) due to their discrepant values and very large uncertainties. For the shock component, we have adopted the average of n_e([O II]), n_e([Cl III]) and n_e([Fe III]), while n_e([S II]) has not been included because the [S II] line ratio is out of the range of validity of the indicator. As we can see in Table 2, the density of the shock component (∼17 000 cm^{-3}) is much higher than the density of the nebular one (∼3000 cm^{-3}).

Table 2. Physical conditions.

Indicator		Nebular component	Shock component
n_e (cm^{-3})	[O II]	3490 ± 810	18 810 ± 8280
	[S II]	2350 ± 910	>14 200
	[Cl III]	2470 ± 1240	23 780 ± 13 960
	[Fe III]	11 800 ± 9000	17 100 ± 2500
	[Ar IV]	5800 :[a]	–
	Adopted	2890 ± 550	17 430 ± 2360
T_e (K)	[N II]	9610 ± 390	9240 ± 300
	[O II]	8790 ± 250	9250 ± 280
	[S II]	8010 ± 440	8250 ± 540
	[O III]	8180 ± 200	8770 ± 240
	[S III]	8890 ± 270	9280 ± 300
	[Ar III]	7920 ± 450	8260 ± 410
	He I	8050 ± 150	7950 ± 200

[a]Error larger than 60 per cent.

However, the bulk of the emission of the nebular component might come from behind HH 202, and the electron density that we have found for that component might not be the true one of the pre-shock gas. In fact, taking into account that the velocity of the gas flow is 89 km s^{-1} (O'Dell & Henney 2008) and the typical speed of sound in an ionized gas is about 10–20 km s^{-1}, we have adopted a Mach number, M, for HH 202 of about 5 and, thus, the shock compression ratio should be $M^2 \sim 25$. Using the density of the shock component (see Table 2), we obtain a pre-shock density ∼17 430/25 ≈ 700 cm^{-3}. This value is lower than the 2890 cm^{-3} determined for the nebular component. Therefore, it seems clear that the bulk of the nebular component does not refer to the gas in the immediate vicinity of HH 202 as we have mentioned in Section 2.

Electron temperatures have been derived from the classical CEL ratios of [N II], [O II], [S II], [O III], [S III] and [Ar III]. Under the two-zone ionization scheme, we have adopted T_e([N II]) as representative for the low-ionization zone and T_e([O III]) for the high-ionization zone. We have also derived T_e(He I) using the method of Peimbert, Peimbert & Luridiana (2002) and state-of-the-art atomic data (see Section 4.4).

We have compared these temperature determinations with those obtained from the integral field unit (IFU) data presented in Paper I.

We have determined the mean T_e values of the spaxels of the section of the field of view (FOV) of the PMAS data that encompasses the area covered by our UVES spectrum, finding $\langle T_e([O\,III])\rangle = 8760 \pm 260$ K and $\langle T_e([N\,III])\rangle = 9730 \pm 590$ K. These values are in agreement within the errors with those obtained in this paper (see Table 2). The average density from the IFU data, obtained from the [S II] line ratio, is 7300 ± 3000 cm^{-3}, a value between the n_e adopted for each kinematic component from the UVES data.

As we can see in Table 2, the T_e values are quite similar in both components with differences of the order of a few 100 K. The temperatures derived from [N II] lines are higher than those derived from [O III] lines, which is a typical result observed in previous works on the Orion Nebula (e.g. Rubin et al. 2003; Mesa-Delgado et al. 2008) as well as in Paper I. This is a likely result of the ionization stratification in the nebula. It is interesting to note that the difference between both temperatures is smaller in the case of the shock component, in this case all the emission comes from a – probably – much narrower slab of ionized gas.

The relatively low uncertainties in the physical conditions are due to the high signal-to-noise ratio of the emission lines used in the diagnostics. Blagrave et al. (2006) computed the physical conditions for HH 529 and they obtained similar results – higher densities in the shock component but similar temperatures in both components – though with comparatively larger errors.

4.3 Ionic abundances from CELs

Ionic abundances of N^+, O^+, O^{2+}, Ne^{2+}, S^+, S^{2+}, Cl^+, Cl^{2+}, Ar^{2+} and Ar^{3+} have been derived from CELs under the two-zone scheme and $t^2 = 0$, using the NEBULAR package. All abundances were calculated for the shock and nebular components, except for Ar^{3+}, which were not detected in the spectrum of the shock component. The atomic data for Cl^+ are not implemented in the NEBULAR routines, so we have used an old version of the five-level atom program of Shaw & Dufour (1995) – FIVEL – that is described by De Robertis, Dufour & Hunt (1987). This program uses the atomic data for this ion compiled by Mendoza (1983).

We have also measured [Ca II], [Cr II], [Fe II], [Fe III], [Fe IV], [Ni II] and [Ni III] lines. The abundances of these ions are also presented in Table 3. They were computed assuming the appropriate temperature under the two-zone scheme and the procedures indicated below. In addition and only in the shock component, we have detected a substantial number of lines of other quite rare heavy-element ions as [Cr III], [Co II], [Co III], [Ti III] and, possibly, [Cr IV], [Co IV], [Mn II] and [V II]. Unfortunately, we cannot derive abundances from these lines due to the lack of atomic data for these ions.

Two [Ca II] lines at 7291 and 7324 Å were detected in the shock component. In order to derive the Ca^+ abundance, we solved a five-level model atom using the single atomic data set available for this ion (Meléndez, Bautista & Badnell 2007). Note that this is the first determination of the Ca^+ abundance in the Orion Nebula and this poses a lower limit to the gas-phase Ca/H ratio in this object.

Two and four [Cr II] lines were measured in the nebular and shock components, respectively, although those at 8309 and 8368 Å are very faint. [Cr II] lines can be affected by continuum or starlight fluorescence as is also the case for the [Fe II] and [Ni II] lines. We have computed the Cr^+ abundances using a 180-level model atom that treat continuum fluorescence excitation as in Bautista, Peng & Pradhan (1996) and include the atomic data of Bautista et al. (2009). In order to consider the continuum fluorescence excitation, we have assumed that the incident radiation field derives entirely from the dominant ionization star θ^1 Ori C. As Bautista et al. (1996), we have calculated a dilution factor assuming a $T_{\rm eff}$ = 39 000 K, $R_{\rm star} = 9.0\,R_\odot$ (see Section 5.3) and a distance to the Orion Nebula of 414 pc (Menten et al. 2007). In Table 3, we include the Cr^+/H^+ ratio for the nebular and shock components. This is the first estimation of the Cr^+ abundance in the Orion Nebula.

Table 3. Ionic abundances and AD factors.

	Nebular component		Shock component	
	Ionic abundances from CELs			
	$t^2 = 0$	$t^2 > 0$	$t^2 = 0$	$t^2 > 0$
C^{2+}	7.87[b]	–	–	–
N^+	7.02 ± 0.04	7.07 ± 0.05	7.35 ± 0.03	7.52 ± 0.04
O^+	8.00 ± 0.06	8.05 ± 0.09	8.29 ± 0.06	8.48 ± 0.08
O^{2+}	8.35 ± 0.03	8.46 ± 0.04	8.08 ± 0.03	8.43 ± 0.05
Ne^{2+}	7.46 ± 0.11	7.58 ± 0.12	7.13 ± 0.10	7.51 ± 0.11
S^+	5.50 ± 0.07	5.54 ± 0.08	6.03 ± 0.04	6.22 ± 0.05
S^{2+}	6.90 ± 0.25	6.98 ± 0.25	6.89 ± 0.22	7.16 ± 0.21
Cl^+	3.99 ± 0.09	4.04 ± 0.10	4.52 ± 0.06	4.68 ± 0.06
Cl^{2+}	5.13 ± 0.04	5.23 ± 0.05	5.05 ± 0.05	5.38 ± 0.06
Ar^{2+}	6.30 ± 0.04	6.39 ± 0.04	6.26 ± 0.05	6.56 ± 0.04
Ar^{3+}	3.73 ± 0.11	3.85 ± 0.12	–	–
Ca^+	–	–	3.86 ± 0.07	4.03 ± 0.07
Cr^+	2.88 ± 0.11	2.92 ± 0.11	3.75 ± 0.07	3.91 ± 0.07
Fe^+	5.18 ± 0.26	5.23 ± 0.27	5.82 ± 0.03	6.01 ± 0.06
Fe^{2+}	5.66 ± 0.13	5.72 ± 0.13	6.77 ± 0.09	6.96 ± 0.10
Fe^{3+}	–	–	5.87 ± 0.16	6.16 ± 0.20
Ni^+	3.83 ± 0.10	3.88 ± 0.11	4.78 ± 0.09	4.96 ± 0.09
Ni^{2+}	4.42 ± 0.14	4.47 ± 0.15	5.60 ± 0.09	5.77 ± 0.09
	Ionic abundances from RLs			
He^+	10.94 ± 0.01		10.93 ± 0.01	
C^{2+}	8.32 ± 0.07		8.25 ± 0.08	
O^+	8.01 ± 0.12		8.25 ± 0.16	
O^{2+}	8.46 ± 0.03		8.44 ± 0.03	
	ADFs			
C^{2+}	0.45		-	
O^+	0.01 ± 0.17		−0.04±0.14	
O^{2+}	0.11 ± 0.04		0.35 ± 0.05	

[a] In units of $12 + \log(X^{+n}/H^+)$.
[b] Average value from positions 8b and 11 of Walter et al. (1992).

Several [Fe II] lines have been detected in our spectra. As in the case of [Cr II] lines, most of them are affected by continuum fluorescence (see Rodríguez 1999; Verner et al. 2000). Following the same procedure as for Cr^+, we considered a 159 model atom in order to compute the Fe^+ abundances using the atomic data presented in Bautista & Pradhan (1998).

Many [Fe III] lines have been detected in the two kinematic components and their flux is not affected by fluorescence. For the calculations of the Fe^{2+}/H^+ ratio, we have implemented a 34-level model atom that uses collision strengths taken from Zhang (1996) and the transition probabilities of Quinet (1996) as well as the new transitions found by Johansson et al. (2000). The average value of the Fe^{2+} abundance has been obtained from 31 and 12 individual emission lines for the shock and nebular components, respectively.

One [Fe IV] line has been detected in the shock component at 6740 Å. The Fe^{3+}/H^+ ratio has been derived using a 33-level model atom where all collision strengths are those calculated by Zhang & Pradhan (1997) and the transition probabilities recommended by Froese Fischer & Rubin (2004).

Several [Ni II] lines have been measured in both kinematic components but they are strongly affected by continuum fluorescence (see Lucy 1995). As for the Cr^+ and Fe^+ ions, we have used a 76-level model that includes continuum fluorescence excitation and

the new collisional data of Bautista (2004) in order to compute the Ni^+ abundances.

We have measured several [Ni III] lines in the shock and nebular components. These lines are not expected to be affected by fluorescence. The Ni^{2+}/H^+ ratio has been derived using a 126-level model atom and the atomic data of Bautista (2001).

The final adopted values of the ionic abundances are listed in Columns (1) and (3) of Table 3 for the nebular and shock components, respectively. Columns (2) and (4) correspond to the ionic abundances of both components assuming the presence of temperature fluctuations (see Section 5.5). In this table, we have also included the C^{2+}/H^+ ratio obtained from UV CELs by Walter, Dufour & Hester (1992). We have taken the average of the values corresponding to their slit positions 8b and 11, the nearest positions to HH 202. The uncertainties shown in the table are the quadratic sum of the independent contributions of the error in the density, temperature and line fluxes.

The abundance determinations presented in Table 3 show the following behaviour: ionic abundances determined from CELs of once ionized species are always higher in the shock than in the nebular component; the twice-ionized species of elements lighter than Ne (included) show lower abundances in the shock than in the nebular component and the twice-ionized species of elements heavier than Ne show similar abundances in both components except for iron, chromium and nickel abundances that show substantially larger abundances in the shock component, something that can be explained if a significant dust destruction occurs in this component (see Section 5.6).

Finally, we have compared our abundance determinations from UVES data with those obtained in the HH 202-S region from the IFU data presented in Paper I. Integrating the spaxels of the section of the FOV indicated in Section 3, we obtain $12 + \log(O^{2+}/H^+) = 8.18 \pm 0.07$ from CELs, which is in good agreement with the numbers presented in Table 3 for both kinematic components. On the other hand, the average value of the O^+ abundance from CELs is 8.06 ± 0.14. However, considering the large density dependence of this ionic abundance, we have recalculated the O^+/H^+ ratio adopting the physical conditions measured in the shock component from UVES, finding a value of 8.26 ± 0.09, which is in better agreement with the UVES determinations for the shock component, the brightest one in the [O II] line emission.

4.4 Ionic abundances from RLs

We have measured several He I emission lines in the spectra of HH 202, both in the nebular and in the shock components. These lines arise mainly from recombination, but they can be affected by collisional excitation and self-absorption effects. We have used the effective recombination coefficients of Storey & Hummer (1995) for H I and those computed by Porter et al. (2005), with the interpolation formulae provided by Porter, Ferland & MacAdam (2007) for He I. The collisional contribution was estimated from Sawey & Berrington (1993) and Kingdon & Ferland (1995), and the optical depth in the triplet lines was derived from the computations by Benjamin, Skillman & Smits (2002). We have determined the He^+/H^+ ratio from a maximum likelihood method (MLM, Peimbert, Peimbert & Ruiz 2000; Peimbert, Peimbert & Luridiana 2002).

To self-consistently determine n_e(He I), T_e(He I), He^+/H^+ and the optical depth in the He I 3889 line, τ_{3889}, we have used the adopted density obtained from the CEL ratios for each component as n_e(He I) (see Table 2) and a set of 16 He I lines (at 3614, 3819, 3889, 3965, 4026, 4121, 4388, 4471, 4713, 4922, 5016, 5048, 5876, 6678, 7065 and 7281 Å). We have discarded the He I 5048 Å line in the nebular component because it is affected by charge transfer in the CCD. So, for the nebular component of HH 202, we have a total of 16 observational constraints (15 lines plus n_e), and for the shock component we have 17 observational constraints (16 lines plus n_e). Finally, we have obtained the best value for the three unknowns and t^2 by minimizing χ^2. The final χ^2 parameters we have obtained are 7.53 for the nebular component and 12.34 for the shock component, which indicate very good fits, taking into account the degrees of freedom. The final adopted value of the He^+/H^+ ratio for each component is included in Table 3.

We have detected C II lines of multiplets 2, 3, 4, 6 and 17.02. The brightest of these lines is C II 4267 Å, which belongs to multiplet 6 and can be used to derive a proper C^{2+}/H^+ ratio. The rest of the C II lines are affected by fluorescence, like multiplets 2, 3 and 4 (see Grandi 1976) or are very weak, as in the case of the line multiplet 17.02 that has an uncertainty of 40 per cent in the line flux.

We have derived the O^+/H^+ ratio from RLs for the shock and nebular components. The O I lines of multiplet 1 are very weak and they are partially blended with bright telluric emission. In order to obtain the best possible abundance determination, we have used different lines for each component: O I 7775 Å for the nebular component and O I 7772 Å for the shock one, these are precisely the lines least affected by line blending.

The high signal-to-noise ratio of the spectra allowed us to detect and measure seven lines of the multiplet 1 of O II as we can see in Fig. 3. These lines are affected by non-local thermal equilibrium (NLTE) effects (Ruiz et al. 2003), therefore to obtain a correct O^{2+} abundance it is necessary to observe the eight lines of the multiplet. However, these effects are rather small in the Orion Nebula – as well as in the observed components – due to its relatively large density. Then, assuming LTE, the O^{2+} abundance from RLs has been calculated considering the abundances obtained from the flux of each line of multiplet 1 and the abundance from the estimated total flux of the multiplet (see Esteban et al. 1998).

The abundance determinations in Table 3 show that the He^+/H^+, C^{2+}/H^+ and O^{2+}/H^+ ratios derived from RLs are always very similar in both shock and nebular components. In the case of O^+ abundances, the nominal values determined for both components seem to be somewhat different (about 0.24 dex), but they are marginally in agreement considering the large uncertainties of this ion abundance.

As in the previous section, we have compared our abundance determinations from RLs with those obtained for HH 202-S in Paper I. From the data of Paper I, we obtain $12 + \log(O^{2+}/H^+) = 8.39 \pm 0.13$ and $12 + \log(C^{2+}/H^+) = 8.29 \pm 0.11$, values which are in good agreement with those obtained in this paper.

4.5 Abundance discrepancy factors

We have calculated ionic abundances from two kinds of lines – RLs and CELs – for three ions: C^{2+}, O^+ and O^{2+}. We present their values for the two components in Table 3. We have computed the ADF for these ions using the following definition:

$$\mathrm{ADF}(X^{+i}) = \log\left(\frac{X^{+i}}{H^+}\right)_{RL} - \log\left(\frac{X^{+i}}{H^+}\right)_{CEL}. \quad (3)$$

In the case of the ADF(C^{2+}), it can only be estimated for the nebular component and from the comparison of our determination from RLs and those from CELs for nearby zones taken from the literature. The value of the ADF(C^{2+}) amounts to 0.45 dex.

On the one hand, the ADF(O^+) can also be estimated in our spectrum and shows values very close to zero. However, these ADF

values are rather uncertain. On the other hand, as we can see in Table 3, the O^{2+} abundance from RLs is the same for both components while that from CELs is lower in the shock component, probably because the recombination rate increases in the shock one. This fact produces an ADF(O^{2+}) about 0.2 dex higher in the shock component than in the nebular one. This striking result will be discussed in Section 5.5.

The values of the ADFs of C^{2+} and O^{2+} for the nebular component are in good agreement with those obtained by Esteban et al. (2004) for a zone closer to the Trapezium cluster than HH 202. In the case of the ADF(O^{+}), both determinations disagree, Esteban et al. (2004) report a much larger value (0.39 dex).

4.6 Total abundances

In order to derive the total gaseous abundances of the different elements present in our spectrum, we have to correct for the unseen ionization stages by using a set of ionization correction factors (ICFs). The adopted ICF values are presented in Table 4 and the total abundances in Table 5. As in the case of the ionic abundances from CELs, these tables include values under the assumption of $t^2 = 0$ (Columns 1 and 3) and under the presence of temperature fluctuations (see Section 5.5; Columns 2 and 4).

The total helium abundance has been corrected for the presence of neutral helium using the expression proposed by Peimbert, Torres-Peimbert & Ruiz (1992) based on the similarity of the ionization potentials (IPs) of He^0 (24.6 eV) and S^+ (23.3 eV):

$$\frac{He}{H} = \left(1 + \frac{S^+}{S - S^+}\right) \times \frac{He^+}{H^+} = ICF(He^0) \times \frac{He^+}{H^+}. \quad (4)$$

For C, we have adopted the ICF(C^+) derived from photoionization models of Garnett et al. (1999) for the shock and nebular components. In order to derive the total abundance of nitrogen, we have used the usual ICF:

$$\frac{N}{H} = \frac{O^+ + O^{2+}}{O^+} \times \frac{N^+}{H^+} = ICF(N^{2+}) \times \frac{N^+}{H^+}. \quad (5)$$

Table 4. Adopted ICF values.

		Nebular component		Shock component	
Elements	Unseen ion	$t^2 = 0$	$t^2 > 0$	$t^2 = 0$	$t^2 > 0$
He	He^0	1.04 ± 0.02	1.03 ± 0.02	1.12 ± 0.06	1.08 ± 0.04
C[a]	C^+	1.31 ± 0.46		1.50 ± 0.47	
N	N^{2+}	3.21 ± 0.54	3.82 ± 0.83	1.62 ± 0.27	2.29 ± 0.46
Ne	Ne^+	1.45 ± 0.15	1.35 ± 0.19	2.61 ± 0.31	1.78 ± 0.26
S	S^{3+}	1.01 ± 0.01	1.01 ± 0.01	1.09 ± 0.03	1.03 ± 0.01
Ar[b]	Ar^+	1.33	–	–	–
Ar[c]	Ar^+	1.20 ± 0.36	1.16 ± 0.36	2.00 ± 0.51	1.71 ± 0.46
Fe[d]	Fe^{3+}	2.71 ± 0.46	3.16 ± 0.69	1.52 ± 0.25	2.02 ± 0.41
Ni	Ni^{3+}	3.21 ± 0.54	3.82 ± 0.83	1.62 ± 0.27	2.29 ± 0.46

[a]From photoionization models by Garnett et al. (1999).
[b]Mean of Orion Nebula models.
[c]From correlations obtained by Martín-Hernández et al. (2002).
[d]From photoionization models by Rodríguez & Rubin (2005).

Table 5. Total abundances.[a]

	Nebular component		Shock component	
	$t^2 = 0$	$t^2 > 0$	$t^2 = 0$	$t^2 > 0$
He	10.95 ± 0.01	10.95 ± 0.02	10.98 ± 0.03	10.98 ± 0.02
C[b]	8.07	–	–	–
C[c]	8.43 ± 0.17		8.43 ± 0.16	
N	7.53 ± 0.08	7.62 ± 0.11	7.56 ± 0.08	7.81 ± 0.10
O	8.51 ± 0.03	8.60 ± 0.04	8.50 ± 0.04	8.76 ± 0.05
O[c]	8.59 ± 0.05		8.65 ± 0.05	
Ne	7.62 ± 0.12	7.72 ± 0.13	7.54 ± 0.11	7.83 ± 0.12
S	6.92 ± 0.24	7.00 ± 0.24	6.98 ± 0.19	7.23 ± 0.19
Cl	5.16 ± 0.04	5.26 ± 0.05	5.16 ± 0.04	5.46 ± 0.05
Ar[d]	6.42 ± 0.04	6.52 ± 0.04	–	–
Ar[e]	6.38 ± 0.19	6.46 ± 0.14	6.56 ± 0.21	6.79 ± 0.12
Fe[f]	–	–	6.86 ± 0.07	7.06 ± 0.08
Fe[g]	6.10 ± 0.15	6.19 ± 0.16	6.95 ± 0.12	7.19 ± 0.13
Ni	5.03 ± 0.14	5.12 ± 0.15	5.87 ± 0.11	6.11 ± 0.12

[a]In units of $12 + \log(X^{+n}/H^+)$.
[b]Average value from positions 8b and 11 of Walter et al. (1992).
[c]Value derived from RLs.
[d]Adopting the ICF from the mean of Orion Nebula models.
[e]Adopting the ICF from *ISO* observations (Martín-Hernández et al. 2002).
[f]From $Fe^+ + Fe^{2+} + Fe^{3+}$.
[g]Assuming the ICF of equation (6).

This expression gives very different values of the ICF(N^{2+}) for both components due to their rather different ionization degree.

The total abundance of oxygen is calculated as the sum of O^+ and O^{2+} abundances. The absence of He II lines in the spectra, and the similarity between the IPs of He^+ and O^{2+}, implies the absence of O^{3+}. In Table 5, we present the O abundances from RLs and CELs.

The only measurable CELs of Ne in the optical range are those of Ne^{2+} but the fraction of Ne^+ can be important in the nebula. We have adopted the usual expression (Peimbert & Costero 1969) to obtain the total Ne abundance:

$$\frac{\mathrm{Ne}}{\mathrm{H}} = \frac{\mathrm{O}^+ + \mathrm{O}^{2+}}{\mathrm{O}^{2+}} \times \frac{\mathrm{Ne}^{2+}}{\mathrm{H}^+} = \mathrm{ICF}(\mathrm{Ne}^+) \times \frac{\mathrm{Ne}^{2+}}{\mathrm{H}^+}. \quad (6)$$

We have measured CELs of two ionization stages of S: S^+ and S^{2+}. Then, we have used an ICF to take into account the presence of S^{3+} (Stasińska 1978) which is based on photoionization models of H II regions,

$$\frac{\mathrm{S}}{\mathrm{H}} = \left[1 - \left(\frac{\mathrm{O}^+}{\mathrm{O}^+ + \mathrm{O}^{2+}}\right)^3\right]^{-1/3} \frac{\mathrm{S}^+ + \mathrm{S}^{2+}}{\mathrm{H}^+} = \\ = \mathrm{ICF}(\mathrm{S}^{3+}) \times \frac{\mathrm{S}^+ + \mathrm{S}^{2+}}{\mathrm{H}^+}. \quad (7)$$

Following Esteban et al. (1998), we expect that the amount of Cl^{3+} is negligible in the Orion Nebula. Therefore, the total abundance of chlorine is simply the sum of Cl^+ and Cl^{2+} abundances.

For argon, we have determinations of Ar^{2+} and Ar^{3+} but some contribution of Ar^+ is expected. In Table 4, we present the values obtained from two ICF schemes: one obtained from correlations between N^{2+}/N^+ and Ar^{2+}/Ar^+ from *Infrared Space Observatory* (*ISO*) observations of compact H II regions by Martín-Hernández et al. (2002) and another one – following Osterbrock, Tran & Veilleux (1992) – derived as the mean of Orion Nebula models by Rubin et al. (1991) and Baldwin et al. (1991).

We have measured lines of three ionization stages of iron in the shock component – Fe^+, Fe^{2+} and Fe^{3+} – and two stages of ionization in the nebular component – Fe^+ and Fe^{2+}. For the shock component, we can derive the total Fe abundance from the sum of the three ionization stages. For the nebular component – and also for the shock one in order to compare – we have used an ICF scheme based on photoionization models of Rodríguez & Rubin (2005) to obtain the total Fe/H ratio using only the Fe^{2+} abundances, which is given by

$$\frac{\mathrm{Fe}}{\mathrm{H}} = 0.9 \times \left(\frac{\mathrm{O}^+}{\mathrm{O}^{2+}}\right)^{0.08} \times \frac{\mathrm{Fe}^{2+}}{\mathrm{O}^+} \times \frac{\mathrm{O}}{\mathrm{H}}. \quad (8)$$

Finally, there is no ICF available in the literature to correct for the presence of Ni^{3+} in order to calculate the total Ni abundance. Nevertheless, we have applied a first-order ICF scheme based on the similarity between the IPs of Ni^{3+} (35.17 eV) and O^{2+} (35.12 eV):

$$\frac{\mathrm{Ni}^{3+}}{\mathrm{Ni}} = \frac{\mathrm{O}^{2+}}{\mathrm{O}}. \quad (9)$$

Therefore,

$$\frac{\mathrm{Ni}}{\mathrm{H}} = \frac{\mathrm{O}}{\mathrm{O}^+} \times \left(\frac{\mathrm{Ni}^+}{\mathrm{H}^+} + \frac{\mathrm{Ni}^{2+}}{\mathrm{H}^+}\right). \quad (10)$$

In general, the total abundances shown in Columns (1) and (3) of Table 5 are quite similar for the shock and nebular components within the errors, except for the nickel and iron abundances, which are much larger in the shock component – see Section 5.6 for a possible explanation. The set of abundances for the nebular component are in very good agreement with previous results of Esteban et al. (2004). We have also compared our Ni abundance values with the previous determination of Osterbrock et al. (1992) finding that our Ni/H ratio for the nebular component is an order of magnitude lower. This difference is due to the large uncertainties in the atomic data used by those authors (see Bautista 2001).

5 DISCUSSION

5.1 Differences between the $c(\mathrm{H}\beta)$ coefficient determined with different lines

A puzzling feature of our UVES data is that the $c(\mathrm{H}\beta)$ values determined with different lines ratios appear to be inconsistent with each other, even with observational errors taken into account. Possible explanations are either a bias in the extinction curve or an extra mechanism, in addition to extinction, altering the individual line intensities from case B predictions.

Fig. 4 shows the $c(\mathrm{H}\beta)$ values measured for individual line ratios in the Balmer and Paschen series. The bizarre pattern followed by the curve, and particularly the steep slope it reaches in the proximity of the Balmer and Paschen limits, strongly suggests that the solution cannot be a bias in the extinction law.

We can test the second hypothesis by considering how the line intensity ratios relative to case B ratios depend on the principal quantum number n of the level where each line originates. Such dependence, plotted in Fig. 5 for the two kinematic components, shows a definite trend with n for both series. This strongly supports the second of our hypotheses, namely that an extra mechanism is acting to deviate level populations away from case B predictions. Indeed, detailed photoionization modelling indicates that this behaviour is the result of two independent but concomitant mechanisms: ℓ-changing collisions with $|\Delta\ell| > 1$ and pumping of Balmer and Paschen lines by absorption of stellar continuum photons at the Lyman wavelengths. Both mechanisms are neglected in case B calculations (Storey & Hummer 1995) but included in our models, which take advantage of a new model hydrogen atom with fully resolved levels (CLOUDY, version C08.00; Porter, Ferland, van Hoof, & Williams, in preparation; see also appendix A in Luridiana et al. 2009); both alter the n, ℓ populations, resulting in enhanced intensities of the high-n lines.

As for the first mechanism, at low n it has a negligible effect if compared to other depopulation mechanisms, such as

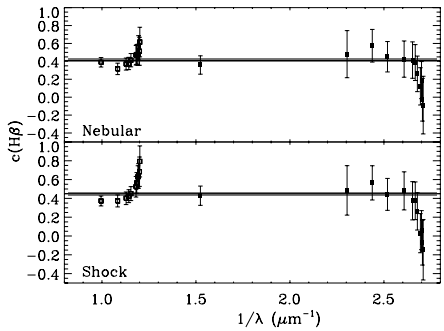

Figure 4. $c(\mathrm{H}\beta)$ values obtained from different line ratios versus the inverse of the wavelength in μm for the nebular (up) and shock component (down). The filled and non-filled squares correspond to the $c(\mathrm{H}\beta)$ values derived from Balmer and Paschen lines, respectively. The horizontal line is the weighted average value adopted and the grey band its error.

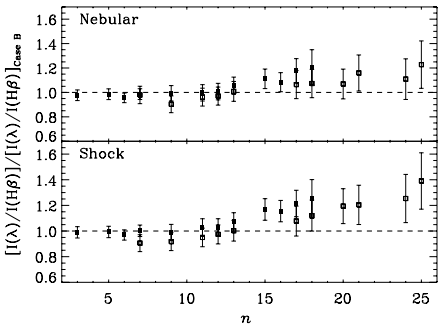

Figure 5. Dereddened fluxes of Balmer (filled squares) and Paschen (non-filled squares) lines to their theoretical flux under the case B prediction ratio versus the principal quantum number n for the nebular (up) and shock components (down).

energy-changing collisions and horizontal collisions with $|\Delta\ell| = 1$; at high n, it becomes increasingly important. Case B calculations neglect this mechanism by construction, so a discrepancy is doomed to appear whenever high-n lines are compared to case B results.

The effectiveness of the second mechanism strongly depends on the availability of the exciting photons, i.e. on the stellar flux at the Lyman wavelengths; the results of Luridiana et al. (2009) and further preliminary calculations (Luridiana et al., in preparation) suggest that its impact on line intensities might increase with n.

A full account of both processes in H II regions can be found in Luridiana et al. (2009) and Luridiana et al. (in preparation).

5.2 Comparison of line ratios in the shock and nebular components and the ionization structure

To maximize the shock-to-nebula ratio, the echelle spectra were extracted over the area where the shock component is brighter and the velocity separation with respect to the nebular background gas is maximum (see Fig. 2).

In Fig. 6, we present the weighted average shock-to-nebular ratio for different ionic species, $I(\lambda)_{sh}/I(\lambda)_{neb}$ – which was defined in equation (1) – with respect to the IP needed to create the associated originating ion. In general, as we can see in this figure, the line ratios of the shock component relative to those of the ambient gas

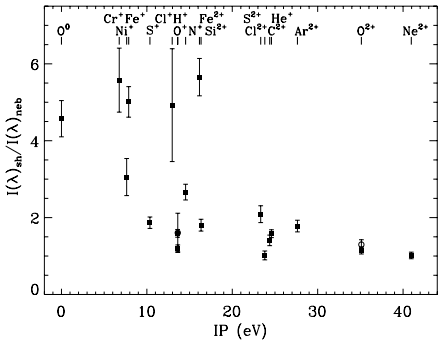

Figure 6. Weighted average of shock-to-nebular line ratios versus the IP needed to create the associated originating ion. Non-filled circles correspond to ratios measured from RLs (only for O^+ and O^{++}). Smaller error bars are of about 3 per cent.

are between 1 and 2 for most ionic species with IP above 10 eV and close to one for the most ionized species as O^{2+} and Ne^{2+}. Since the illumination of the shock should be approximately the same as that of the nebula at this particular zone of the slit, shock-to-nebular ratios of the order of one imply that the shock should be ionization-bounded. This is exactly the opposite situation that Blagrave et al. (2006) find in HH 529, where the shock-to-nebular ratios are clearly lower than 1 indicating that the shock associated to HH 529 is matter-bounded.

As we have commented above and can be seen in Fig. 6, the shock-to-nebular ratio varies from 1 to 2 for species with an IP higher than 10 eV except in two cases: (i) Fe^{2+}, whose lines show a substantial enhancement in the shock component, probably due to dust destruction (see Section 5.6) and (ii) Cl^+, but this can be accidental because this ionic abundance is derived from a single rather faint line with a very large uncertainty. Ionic species with an IP lower than 10 eV show a shock-to-nebular ratio always higher than 2 in Fig. 6. In particular, Fe^+, Ni^+ and Cr^+ show ratios larger than 2 and these ions may be also affected by an increase of the gas-phase abundance due to dust destruction.

Neutral species like O^0 or N^0 are associated with the presence of an ionization front. In the case of O^0, the shock-to-nebular ratio has been calculated from the [O I] 6300 and 6363 Å lines that are contaminated by telluric emissions but only in the shock component. We extracted the telluric emissions from the zone free of shock emission along the slit and subtracted this feature to the shock component. The shock-to-nebular ratio of [O I] lines is the largest one for those ions which are not heavily affected by possible dust destruction. This is a further indication of the presence of an ionization front in HH 202-S. In the case of [N I] lines, those belonging to the nebular component are also contaminated by telluric emission but, in this case, it was impossible to deblend properly these lines.

In Fig. 2, we can see the spatio-kinematic profiles of lines of different ionization stages of oxygen: O^0, O^+ and O^{2+}, including RLs and CELs. In the shock component, we can clearly distinguish a stratification in the location of the ions: the bulk of the O^{2+} emission is located at the south of the extracted area, O^0 at the north and O^+ is located approximately at the centre of the extracted area. Another interesting feature that can be seen in Fig. 2 is that the emissions from RLs and CELs of the same ion seem to show the same spatio-kinematic profiles. These profiles provide further indication that HH 202-S is an ionization-bounded shock.

The peak emission of the spatio-kinematic profiles of ions with IP lower or similar to the one of O^+: Cr^+, Ni^+, S^+, Fe^+ or H^+ is located to the north of HH 202-S, as in the case of O^+. Ions as He^+, C^{2+} or Fe^{2+} show their peak emission about the centre of the aperture, while the ions with the highest IP, as Ne^{2+} or Ar^{3+}, show spatio-kinematic profiles similar to that of O^{2+}.

5.3 Width of the ionized slab and the physical separation between θ^1Ori C and HH 202-S

An interesting result of this paper is the claim that HH 202-S contains an ionization front as we have shown in Sections 4.1 and 5.2. Due to this fact, we can estimate the width of the ionized slab of HH 202-S and its physical separation with respect to the main ionization source of the Trapezium cluster, θ^1Ori C.

On the one hand, from the maximum emission of the shock component in the spatio-kinematic profiles of O^{2+} and O^0 shown in Fig. 2, we can measure an angular distance on the plane of the sky of about 3.9 ± 0.5 arcsec. Using the distance to the Orion Nebula obtained by Menten et al. (2007), $d = 414 \pm 7$ pc, and

the inclination angle of HH 202-S with respect to the plane of the sky calculated by O'Dell & Henney (2008), $\theta = 48^{\circ}$, we estimate $(11.7 \pm 1.5) \times 10^{-3}$ pc for the width of the ionized slab.

On the other hand, to trap the ionization front in HH 202-S, the incident Lyman continuum flux must be balanced by the recombinations in the ionized slab, i.e.

$$F_{\rm Ly} = \frac{Q(H^0)}{4\pi D^2} = n_{\rm sh}^2 \alpha_B(H^0, T) L, \quad (11)$$

where D is the physical separation between HH 202-S and θ^1Ori C, $Q(H^0)$ is the ionizing photon rate, $n_{\rm sh}$ the density in the shock component, $\alpha_B(H^0, T)$ is the case B recombination coefficient for H and L is the width of the slab. In order to estimate $Q(H^0)$, we have used a spectral energy distribution of FASTWIND code with the stellar parameters for θ^1Ori C obtained by Simón-Díaz et al. (2006) – $T_{\rm eff} = 39\,000 \pm 1000$ K and $\log g = 4.1 \pm 0.1$ dex – and the distance to the Orion Nebula calculated by Menten et al. (2007). Then, the output parameters have been: the stellar radius $R = (9.0 \pm 1.3)$ $R_{\odot}$, the stellar luminosity $\log L = 38.80 \pm 0.14$ dex and the ionizing photon rate $Q(H^0) = (6.30 \pm 2.00) \times 10^{48}$ s^{-1}. Taking a value for the recombination coefficient, $\alpha_B = 2.59 \times 10^{-13}$ cm^{-3} s^{-1} at 10^4 K, we have finally calculated a physical separation of $D = 0.14 \pm 0.05$ pc. This result suggests that HH 202 is quite embedded within the body of the Orion Nebula and, therefore, discards the origin of the ionized front as result of the interaction of the gas flow with the veil (see Section 4.1), which is between 1 and 3 pc in front of the Trapezium cluster (see Abel et al. 2004).

5.4 Radial velocity analysis

In Fig. 7, we show the average heliocentric velocity of the lines that belong to a given ionic species as a function of the IP needed to create the associated originating ion. We have used two separate graphs to distinguish between the behaviour of the nebular and the shock components. The nebular component shows the typical velocity gradient that has been observed in other positions of the Orion Nebula and other H II regions (e.g, Bautista & Pradhan 1998; Esteban & Peimbert 1999), with a velocity difference of the order of -15 km s^{-1} between the neutral and the most ionized species. This gradient is likely produced by the presence of flows of ionized gas originating from the ionization front inside the nebula. In contrast, the ions in the shock component show a rather similar radial velocity independently of their IP. This indicates that the bulk of the ionized gas at the HH 202-S is moving at approximately the same velocity with respect to the rest of the nebula. The H II lines (Balmer and Paschen series) of the shock component are shifted by -50.7 ± 1.0 km s^{-1} relative to the H II lines of the nebular component and -64.8 ± 1.0 km s^{-1} relative to the velocity of the photon-dominated region (PDR,+28 km s^{-1}; Goudis 1982). The zone covered by our UVES slit (see Fig. 1) coincides with position 117–256 of Doi et al. (2004). These authors detect two radial velocity components belonging to the shock gas in this zone, a fast component (-57 km s^{-1}) and a slower brighter one (-31 km s^{-1}). Our value of the radial velocity for the shock component of HH 202 (-36.8 ± 1.0 km s^{-1}) is somewhat more negative than the slower velocity component of Doi et al. (2004), probably our shock component corresponds to the unresolved blend of the two velocity systems detected by those authors.

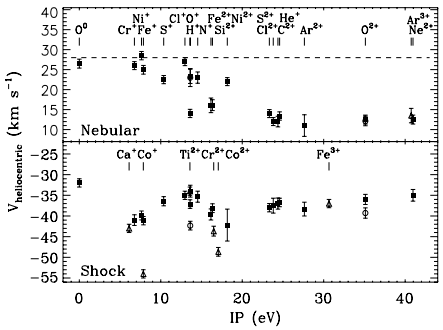

Figure 7. Heliocentric velocities of the nebular (up) and shock (down) components emission lines versus the IP needed to create the associated originating ion. The velocity of the PDR (dashed horizontal line) is also shown. Non-filled triangles correspond to ions observed in only one kinematic component. Non-filled circles correspond to heliocentric velocities measured from RLs (only for O^+ and O^{++}).

5.5 The abundance discrepancy and temperature fluctuations

Assuming the validity of the temperature fluctuations paradigm and that this phenomenon produces the AD, we can estimate the values of the t^2 parameter from the ADFs obtained for each component and ion (see Table 3). In Table 6, we include the t^2 values that produce the agreement between the abundance determinations obtained from CELs and RLs of O^{2+} and C^{2+}. These calculations have been made following the formalism outlined by Peimbert & Costero (1969). Adopting the t^2 value obtained for O^{2+} zone, $t^2(O^{2+})$, we have calculated the ionic abundances, the ICFs and the total abundances under the presence of temperature fluctuations and they are presented in Tables 3–5, respectively.

As we can see in Table 5, the high $t^2(O^{2+})$ value used to derive the abundances for the shock component implies that the total abundances obtained from CELs considering $t^2 > 0$ are higher in the shock component than in the nebular one for all the elements. On the other hand, the abundances of C and O obtained from RLs are very similar in both components. Moreover, the O/H ratio computed from CELs for $t^2 > 0$ is higher than that obtained from RLs. However, for the nebular component, we find that the total abundance of oxygen determined from CELs considering $t^2 > 0$ agrees with the oxygen abundance from RLs.

These results can suggest that, perhaps, the t^2 value we have found for the shock component is too high and, therefore, that the

Table 6. Estimates of the t^2 parameter.

	HH 202		HH 529[a]		
Ion	Nebular component	Shock component	Nebular component	Shock component	Esteban et al. (2004)
O^{2+}	0.016 ± 0.006	0.050 ± 0.007	0.009 ± 0.004	0.010 ± 0.010	0.022 ± 0.002
C^{2+}	0.040	–	–	–	0.039 ± 0.011
He^+	0.014 ± 0.013	0.049 ± 0.011	–	–	–

[a]Blagrave et al. (2006).

t^2 paradigm is not applicable in this case. However, we have to consider that we have used a t^2 value representative of the high-ionization zone for all the ions. The increase of the O^+/O^{2+} ratio in the shock component with respect to the nebular one, due to an enhanced recombination rate, makes the O^+ zone more extended in this component and a lower $t^2(O^+)$ would lead to a better agreement between the O abundances of both components. We have also computed the t^2 parameter for the He^+ zone using a MLM (see Section 4.4). The determination of the $t^2(He^+)$ weighs the O^+ and the O^{2+} zones depending on their extension. It is remarkable that the t^2 values obtained from different methods, such as the He^+ lines and the ADF(O^{2+}), which assume the presence of temperature fluctuations in the observed volume, produce almost identical values in both components, though $t^2(He^+)$ has large uncertainties. These ones can reconcile the total abundances of both components for $t^2 > 0$ considering that the MLM depends strongly on the He I 3889 Å line flux and that the shock components of this line and H8 are severely blended.

In Table 6, we have also included the values of t^2 obtained by Blagrave et al. (2006) from the ADF(O^{2+}) that they estimate for the nebular and shock components of HH 529 and those obtained by Esteban et al. (2004) from the ADF of O^{2+} and C^{2+}. The data of Esteban et al. (2004) correspond to a zone free of high-velocity flows and can be considered as representative of the nebular component but closer to the Trapezium. The values of the t^2 obtained for the nebular component of HH 202-S are quite consistent with those obtained by Esteban et al. (2004). The $t^2(O^{2+})$ of the nebular component of HH 529 obtained by Blagrave et al. (2006) is lower than the two other determinations, but still consistent with our values within the uncertainties. As has been commented above, the t^2 values found in the shock component of HH 202 are much higher than those of the nebular component and the value determined by Blagrave et al. (2006) for the shock component of HH 529.

The effect of temperature fluctuations in the spectra of ionized nebulae and their existence has been a controversial problem from the first work of Peimbert (1967). Peimbert (1995), Esteban (2002), Peimbert & Peimbert (2006) have reviewed the possible mechanisms that could produce such temperature fluctuations. Among the possible sources of temperature fluctuations, we can list the deposition of mechanics energy by shocks and the gas compression due to turbulence. Peimbert, Sarmiento & Fierro (1991) have studied the effect of shock waves in H II regions using shock models by Hartigan et al. (1987). They found that high t^2 values can be explained by the presence of shocks with velocities larger than 100 km s^{-1}. In the case of the flow of 89 km s^{-1} that produces HH 202, this effect should produce very small t^2 values. Therefore, another process or other formalisms of the problem should be taken into account in this case. Further discussion of this problem is beyond the scope of this article.

5.6 Dust destruction

As indicated in Section 5.2, the emission lines of refractory elements as Fe, Ni or Cr are much brighter in the gas flow than in the ambient gas. Moreover, the shock component shows relatively bright [Ca II] lines which are not detected in the spectrum of the ambient gas. On the other hand, in Section 4.1 we have stated that HH 202-S does not contain a substantial contribution of shock excitation and, therefore, we need other mechanisms to explain those abnormally high line fluxes. It is well known that Fe, Ni, Cr and Ca are expected to be largely depleted in neutral and molecular interstellar clouds as well as in H II regions. However, theoretical studies have shown that fast shocks – as those typical in HH objects and supernova remnants – should efficiently destroy grains by thermal and non-thermal sputtering in the gas behind the shock front and by grain–grain collisions (McKee, Chernoff & Hollenbach 1984; Jones et al. 1994; Mouri & Taniguchi 2000). Several works have shown that some non-photoionized HH flows show a decrease in the amount of Fe depletion as determined from the analysis of [Fe II] lines (Beck-Winchatz, Bohm & Noriega-Crespo 1996; Böhm & Matt 2001; Nisini et al. 2005). On the other hand, HH 399 is the first precedent of a fully ionized HH object where an overabundance in Fe was detected and this one was related with dust destruction (Rodríguez 2002).

In Table 7, we compare the values of the C, O, Fe, Ni and Cr^+ abundances and the Fe/Ni ratios of the Sun (Grevesse, Asplund & Sauval 2007) and the nebular and shock components for $t^2 = 0$ and $t^2 > 0$. In the case of Fe and Ni, we can see that the difference between the abundances of the shock and nebular components are of the order of 0.85 dex for $t^2 = 0$ and 1.00 dex for $t^2 > 0$. This result indicates that the gas-phase abundance of Fe and Ni increases by a factor between 7 and 10 after the passage of the shock wave. The fact that the Fe/Ni ratio is the same in both

Table 7. Comparison of abundances and depletion factors.

		Nebular component		Shock component	
	Sun[a]	$t^2 = 0$	$t^2 > 0$	$t^2 = 0$	$t^2 > 0$
C	8.39 ± 0.05	8.43 ± 0.17		8.43 ± 0.16	
O	8.66 ± 0.05	8.59 ± 0.05		8.65 ± 0.05	
Fe	7.45 ± 0.05	6.10 ± 0.15	6.19 ± 0.16	6.95 ± 0.12	7.19 ± 0.13
Ni	6.23 ± 0.04	5.03 ± 0.14	5.12 ± 0.15	5.87 ± 0.11	6.11 ± 0.12
Fe/Ni	1.22 ± 0.06	1.07 ± 0.23	1.07 ± 0.25	1.08 ± 0.17	1.08 ± 0.19
Cr^+	-	2.88 ± 0.11	2.92 ± 0.11	3.75 ± 0.07	3.91 ± 0.07
	Shock−Nebular		Nebular−Sun		Shock−Sun	
	$t^2 = 0$	$t^2 > 0$	$t^2 = 0$	$t^2 > 0$	$t^2 = 0$	$t^2 > 0$
C	0.00 ± 0.27		0.04 ± 0.19		0.04 ± 0.18	
O	0.06 ± 0.07		-0.07 ± 0.07		-0.01 ± 0.07	
Fe	0.85 ± 0.13	1.00 ± 0.14	-1.35 ± 0.05	-1.26 ± 0.05	-0.50 ± 0.06	-0.26 ± 0.09
Ni	0.84 ± 0.12	0.99 ± 0.13	-1.20 ± 0.04	-1.11 ± 0.04	-0.36 ± 0.06	-0.12 ± 0.10
Fe/Ni	–	–	–	–	–	–
Cr^+	0.87 ± 0.07	0.99 ± 0.07	–	–	–	–

[a] Grevesse et al. (2007).

components – because the increase of the gas-phase abundance of both elements is the same – and consistent with the solar Fe/Ni ratio within the errors suggests that the abundance pattern we see in HH 202-S is the likely product of dust destruction. In fact, observations of Galactic interstellar clouds indicate that Fe, Ni – as well as Cr – have the same dust-phase fraction (Savage & Sembach 1996b; Jones 2000). It is also remarkable that, although it could be modulated by ionization effects, the behaviour of the Cr^+ abundance is also consistent with the dust-destruction scenario. The increase of the Cr^+/H^+ ratio between the nebular and shock components is identical to that of Fe and Ni.

Considering the solar Fe/H ratio as the reference ($12 + \log(Fe/H) = 7.45 \pm 0.05$; Grevesse et al. 2007) – which is almost identical to the Fe/H ratio determined for the B-type stars of the Orion association ($12 + \log(Fe/H) = 7.44 \pm 0.04$; Przybilla, Nieva & Butler 2008) – we estimate that the Fe dust-phase abundance decreases by about 30 per cent for $t^2 = 0$ and about 53 per cent for $t^2 > 0$ after the passage of the shock wave in HH 202-S. This result is in good agreement with the predictions of the models of Jones et al. (1994) and Mouri & Taniguchi (2000). In particular, for the velocity determined for HH 202 (89 km s^{-1}; O'Dell & Henney 2008), Jones et al. (1994) obtain a level of destruction of iron dust particles of the order of 40 per cent. On the other hand, the Fe gas-phase abundance we measure in HH 202-S follows closely the empirical correlation obtained by Böhm & Matt (2001) from [Fe II] and [Ca II] emission line fluxes of several non-photoionized HH flows. Further evidence that the dust is not completely destroyed in HH 202 is the detection of 11.7 μm emission coincident with the bright ionized gas around HH 202-S (Smith et al. 2005). As we can see in Table 7, the depletion factors of Fe and Ni in the nebular component are similar to those found in warm neutral interstellar environments and those at HH 202-S of the order of the depletions observed in the Galactic halo (see Welty et al. 1999 and references therein).

In the cases of C and O, the effect of dust destruction in their gas-phase abundance is more difficult to estimate. First, these elements are far less depleted in dust grains than Fe or Ni in neutral interstellar clouds and in H II regions. Secondly, there is still a controversy about the correct solar abundance of these two elements (see Holweger 2001; Grevesse et al. 2007). Finally, chemical evolution models predict some increase in the C/H and O/H ratios in the 4.6 Gyr since the formation of the Sun (0.28 and 0.13 dex; Carigi et al. 2005). All these problems make impossible to estimate confident values of the depletion factors for C and O.

Considering the data gathered in Table 7, the C abundance is virtually the same in the nebular and shock components, although any possible small difference may be washed out due to the intrinsic relatively large error of the abundance determination of this element. In any case, only a slight increase of the C gas-phase abundance would be expected after the passage of the shock wave for a shock velocity of about 89 km s^{-1} (Jones et al. 1994).

The uncertainties in the determination of the O abundances are much lower than in the case of C and its determination does not depend on the selection of an appropriate ICF scheme. In Table 7, we see an increase of 0.06 dex in the O abundance in the shock component with respect to the nebular one. These results suggest a possible moderate decrease of the depletion for this element in the shocked material. Very recent detailed determinations of the O abundance of B-type stars in the Orion association (Simón-Díaz, in preparation) indicate that the mean O/H ratio in this zone is 8.76 ± 0.04. In principle, one would expect that this is a better reference for estimating the dust depletion in the Orion Nebula than the solar one because it corresponds to the *actual* O abundance at the same location. If we take the B-type stars determination as a reference for the total O/H ratio, the amount of O depletion in the ambient gas would be -0.17 ± 0.06 dex and -0.11 ± 0.06 dex in the gas flow. Therefore, a 30 per cent of the O tied up into dust grains would be destroyed after the passage of the shock front.

There are two other alternative methods to estimate the oxygen depletion factor. The first one can be drawn following Esteban et al. (1998). This one is based on the fact that Mg, Si and Fe form molecules with O which are trapped in dust grains. We have used Mg, Si and Fe depletions in order to obtain the fraction of O trapped in dust grains. These depletions are estimated considering the Orion gas abundances of Mg and Si given by Esteban et al. (1998), our Fe abundance for $t^2 > 0$, the O abundances derived from RLs, the stellar abundances of the Orion association of Si ($12 + \log(Si/H) = 7.41 \pm 0.10$) from Simón-Díaz (in preparation) and Mg and Fe from Przybilla et al. (2008). By assuming that O is trapped in olivine $(Mg, Fe)_2SiO_4$, pyroxene $(Mg, Fe)SiO_3$ and several oxides like MgO, Fe_2O_3 and Fe_3O_4 (see Savage & Sembach 1996a and references therein), we have estimated an O depletion factor of -0.10 ± 0.04 dex for the nebular component. If we consider the older stellar abundances of Si and Fe from Cunha & Lambert (1994) and the Mg/Fe ratio from Grevesse et al. (2007), this value becomes -0.08 ± 0.05, which is almost identical to that computed from the new stellar Mg, Si and Fe abundances.

The last method to obtain O depletion factors assumes that oxygen and iron are destroyed in the same fraction. The fraction of iron dust particles is calculated using the Fe abundances for $t^2 > 0$ presented in Table 7 and Fe abundance of B-type stars of the Orion association. From this assumption, and taking into account the O abundance from RLs, we have derived a depletion factor of $-0.11^{+0.11}_{-0.14}$ dex in the nebular component. Finally, we have calculated the average of the values obtained from the three methods, finding that the O depletion factor of the ambient gas is -0.12 ± 0.03. In all cases, the depletion becomes larger by about 0.08 dex if we adopt abundances for $t^2 = 0$. Additionally, the depletion factor in the shock component is smaller than in the ambient gas, probably due to gas destruction.

5.7 Photoionization models for HH 202-S

To test the role of dust destruction both in the temperature structure observed in the shock component and in the iron abundance in the gas, we have run some simple photoionization models for the nebular and the shock components. The models were constructed using CLOUDY (Ferland et al. 1998), version 07.02, and assuming a plane–parallel open geometry with density equal to the value adopted from the observations (see Table 2). We used a WM-basic (Pauldrach, Hoffmann & Lennon 2001) model stellar atmosphere, with $T_{\rm eff} = 39\,000$ K and $\log\ g = 4.0$, values very similar to those derived by Simón-Díaz et al. (2006) for θ^1 Ori C. The number of ionizing photons entering the ionized slab was specified using the ionization parameter, U, the ratio of hydrogen-ionizing photons to the hydrogen density. We changed the value of this parameter till the degrees of ionization (given by O^+/O^{2+}) derived for the models were close to the observed ones. The final values used for U imply similar numbers of hydrogen-ionizing photons in the nebular and shock models, with a difference of ∼40 per cent.

We have used the CLOUDY 'H II region' abundances, based on the abundances derived by Baldwin et al. (1991), Rubin et al. (1991) and Osterbrock et al. (1992) in the Orion Nebula, for all elements except iron, which we have rescaled in order to reproduce the observed [Fe III] 4658/Hβ line ratios. The models also have 'Orion' type

Table 8. Input parameters for photoionization models.

Parameter	Nebular model	Shock model A	Shock model B	Shock model C
$\log(n_e)$ (cm^{-3})	3.46	4.24	4.24	4.24
$\log(U)$	−1.95	−2.53	−2.53	−2.53
Dust	Orion	Orion	Orion	0.5 × Orion
$(Fe/H)_{gas}$	2.1×10^{-6}	2.1×10^{-6}	1.5×10^{-5}	1.5×10^{-5}

Table 9. Results of photoionization models.

Constraint	Nebular Obs.	Nebular Mod.	Shock Obs.	Shock model A	Shock model B	Shock model C
n_e (cm^{-3})	2890 ± 550	2960	17 430 ± 2360	17 540	17 670	17 650
T_e([N II]) (K)	9610 ± 390	9340	9240 ± 300	9510	9220	9210
T_e([O III]) (K)	8180 ± 200	8230	8770 ± 240	8810	8670	8640
$\log(O^+/O^{2+})$	−0.35±0.07	−0.37	0.20 ± 0.07	0.21	0.23	0.22
I([Fe III] 4658)/I(Hβ)	0.009 ± 0.001	0.010	0.110 ± 0.006	0.017	0.111	0.107

dust: graphite and silicate grains with the Orion size distribution (deficient in small grains; see Baldwin et al. 1991) and an original dust to gas mass ratio of 0.0055. For each model, we used the calculated line intensities to derive the physical conditions and the O^+ and O^{2+} abundances, following a similar procedure to the one used to derive the observational results.

We computed three shock models. Model A has similar characteristics to the nebular model except for the density, and can be used to assess the influence of this parameter on the electron temperatures. Model B has the same input parameters as model A, but with the Fe abundance multiplied by a factor of 7. Model C has the same input parameters as model B but with half the amount of dust. The input model parameters are listed in Table 8. Table 9 shows a comparison for observations and models of the physical conditions, the degree of ionization given by O^+/O^{2+}, and the [Fe III] 4658/Hβ line ratio. We can see that the nebular model reproduces well the observational constraints. As for the shock models, the increment in the density of model A is enough to explain the temperatures found for the shock component, but does not reproduce the [Fe III] flux, whereas the higher Fe abundance of model B reproduces well this flux. Model C illustrates that a reduction in the amount of dust does not change significantly the values of the chosen constraints. The introduction of grains smaller than the ones considered in the Orion size distribution of CLOUDY will lead to higher temperatures through photoelectric heating, but we do not know what grain size distribution would be suitable for the shock component.

The iron abundances in those models that reproduce the observed [Fe III] line fluxes are somewhat higher than the ones derived from the observations, but they reproduce the value of the shock to nebular abundance ratio. This can be considered a confirmation of the increment in the iron abundance in the shock component, which is most probably due to dust destruction. As it has been discussed in Section 5.6, dust destruction could also increase the gaseous abundances of other elements like carbon or oxygen and this increment will change the amount of cooling and hence the electron temperature. We ran a model where the abundances of O and C were increased by 14 per cent and found that the derived temperatures decrease by about 200 K.

6 CONCLUSIONS

We have obtained deep echelle spectrophotometry of HH 202-S, the brightest knot of the HH object HH 202. Our high spectral resolution has permitted to separate two kinematic components: the nebular component – associated with the ambient gas – and the shock one – associated with the gas flow. We have detected and measured 360 emission lines of which 352 lines were identified.

We have found a clear disagreement between the individual $c(H\beta)$ values obtained from different Balmer and Paschen lines. We outline a possible solution for this problem based on the effects of Ly-continuum pumping and ℓ-changing collisions with protons.

We have analysed the ionization structure of HH 202-S concluding that the dominant excitation mechanism in HH 202-S is photoionization. Moreover, the dependence of the $I(\lambda)_{sh}/I(\lambda)_{neb}$ ratios and the IP, the comparison of the spatio-kinematic profiles of the emission of different ions as well as the physical separation estimated of 0.14 ± 0.05 pc between HH 202-S and θ^1Ori C indicate that an ionization front is trapped in HH 202-S due to compression of the ambient gas by the shock.

We have derived a high n_e, about 17 000 cm^{-3}, and similar T_e for the low- and high-ionization zones for the shock component, while for the ambient gas we obtain an n_e of about 3000 cm^{-3}, and a higher T_e in the low-ionization zone than in the high-ionization one. We have estimated that the pre-shock gas in the immediate vicinity of HH 202 has a density of about 700 cm^{-3}, indicating that the bulk of the emission of the ambient gas comes from the background behind HH 202.

We have derived chemical abundances for several ions and elements from the flux of CELs. In particular, we have determined the Ca^+ and Cr^+ abundances for the first time in the Orion Nebula but only for the shock component. The abundance of C^{2+}, O^+ and O^{2+} have been determined using RLs for both components. The AD factor for O^{2+}, ADF(O^{2+}), is 0.35 dex in the shock component and much lower in the ambient gas component.

Assuming that the ADF and temperature fluctuations are related phenomena, we have found a $t^2(O^{2+})$ of 0.050 for the shock component and 0.016 for the nebular one. The high t^2 value of the shock component produces some apparent inconsistencies between the total abundances in both components that cast some doubts on the suitability of the t^2 paradigm, at least for the shock component. However, the fact that the values of the t^2 parameter determined from the analysis of the He I line ratios are in complete agreement with those obtained from the ADF(O^{2+}) supports that paradigm.

Finally, the comparison of the abundance patterns of Fe and Ni in the nebular and shock components and the results of photoionzation models of both components indicate that a partial destruction of dust

grains has been produced in HH 202-S after the passage of the shock wave. We estimate that the percentage of destruction of iron dust particles is of the order of 30–50 per cent.

ACKNOWLEDGMENTS

We are very grateful to the referee of this paper, J. Bally, for his comments, which have improved the scientific content of the paper. We also thank S. Simón-Díaz for providing us the stellar parameters for θ^1 Ori C. This work has been funded by the Spanish Ministerio de Ciencia y Tecnología (MCyT) under project AYA2004-07466 and Ministerio de Educación y Ciencia (MEC) under project AYA2007-63030. VL acknowledges support from MEC under project AYA2007-64712. JGR is supported by an UNAM postdoctoral grant. MR acknowledges support from Mexican CONACYT project 50359-F.

REFERENCES

Abel N. P., Brogan C. L., Ferland G. J., O'Dell C. R., Shaw G., Troland T. H., 2004, ApJ, 609, 247
Baldwin J. A., Ferland G. J., Martin P. G., Corbin M. R., Cota S. A., Peterson B. M., Slettebak A., 1991, ApJ, 374, 580
Bally J., Reipurth B., 2001, ApJ, 546, 299
Bally J., Reipurth B., 2003, AJ, 126, 893
Bally J., Licht D., Smith N., Walawender J., 2006, AJ, 131, 473
Bautista M. A., 2001, A&A, 365, 268
Bautista M. A., 2004, A&A, 420, 763
Bautista M. A., Pradhan A. K., 1998, ApJ, 492, 650
Bautista M. A., Peng J., Pradhan A. K., 1996, ApJ, 460, 372
Bautista M. A., Ballance C., Gull T., Lodders K., Martínez M., Meléndez M., 2009, MNRAS, 393, 1503
Beck-Winchatz B., Bohm K.-H., Noriega-Crespo A., 1996, AJ, 111, 346
Benjamin R. A., Skillman E. D., Smits D. P., 2002, ApJ, 569, 288
Blagrave K. P. M., Martin P. G., Baldwin J. A., 2006, ApJ, 644, 1006
Blagrave K. P. M., Martin P. G., Rubin R. H., Dufour R. J., Baldwin J. A., Hester J. J., Walter D. K., 2007, ApJ, 655, 299
Bohlin R. C., Lindler D., 1992, STScI Newsletter, 9, 19
Böhm K.-H., Matt S., 2001, PASP, 113, 158
Cantó J., Goudis C., Johnson P. G., Meaburn J., 1980, A&A, 85, 128
Carigi L., Peimbert M., Esteban C., García-Rojas J., 2005, ApJ, 623, 213
Cernicharo J. et al., 1998, Sci, 282, 462
Costero R., Peimbert M., 1970, Bol. Obser., 5, 229
Cunha K., Lambert D. L., 1994, ApJ, 426, 170
De Robertis M. M., Dufour R. J., Hunt R. W., 1987, J. R. Astron. Soc. Can., 81, 195
D'Odorico S., Cristiani S., Dekker H., Hill V., Kaufer A., Kim T., Primas F., 2000, in Bergeron J., ed., Proc. SPIE, Vol. 4005, Discoveries and Research Prospects from 8- and 10-Meter-Class Telescopes. SPIE, Bellingham, WA, p. 121
Doi T., O'Dell C. R., Hartigan P., 2004, AJ, 127, 3456
Esteban C., 2002, in Henney W. J., Franco J., Martos M., eds, Rev. Mex. Astron. Astrofis. Conf. Ser. Vol. 12, Ionized Gaseou Nebulae. UNAM, Mexico City, p. 56
Esteban C., Peimbert M., 1999, A&A, 349, 276
Esteban C., Peimbert M., Torres-Peimbert S., Escalante V., 1998, MNRAS, 295, 401
Esteban C., Peimbert M., García-Rojas J., Ruiz M. T., Peimbert A., Rodríguez M., 2004, MNRAS, 355, 229
Ferland G. J., Korista K. T., Verner D. A., Ferguson J. W., Kingdon J. B., Verner E. M., 1998, PASP, 110, 761
Froese Fischer C., Rubin R. H., 2004, MNRAS, 355, 461
García-Díaz M. T., Henney W. J., López J. A., Doi T., 2008, Rev. Mex. Astron. Astrofis., 44, 181
García-Rojas J., Esteban C., 2007, ApJ, 670, 457
García-Rojas J., Esteban C., Peimbert M., Costado M. T., Rodríguez M., Peimbert A., Ruiz M. T., 2006, MNRAS, 368, 253
Garnett D. R., Shields G. A., Peimbert M., Torres-Peimbert S., Skillman E. D., Dufour R. J., Terlevich E., Terlevich R. J., 1999, ApJ, 513, 168
Goudis C., 1982, The Orion complex: A case study of interstellar matter. Reidel, Dordrecht
Grandi S. A., 1976, ApJ, 206, 658
Grevesse N., Asplund M., Sauval A. J., 2007, Space Sci. Rev., 130, 105
Hamuy M., Walker A. R., Suntzeff N. B., Gigoux P., Heathcote S. R., Phillips M. M., 1992, PASP, 104, 533
Hamuy M., Suntzeff N. B., Heathcote S. R., Walker A. R., Gigoux P., Phillips M. M., 1994, PASP, 106, 566
Hartigan P., Raymond J., Hartmann L., 1987, ApJ, 316, 323
Henney W. J., O'Dell C. R., Zapata L. A., García-Díaz M. T., Rodríguez L. F., Robberto M., 2007, AJ, 133, 2192
Holweger H., 2001, in Wimmer-Schweingruber R. F., ed., Solar and Galactic Composition. Springer, Berlin, p. 23
Johansson S., Zethson T., Hartman H., Ekberg J. O., Ishibashi K., Davidson K., Gull T., 2000, A&A, 361, 977
Jones A. P., 2000, J. Geophys. Res., 105, 10257
Jones A. P., Tielens A. G. G. M., Hollenbach D. J., McKee C. F., 1994, ApJ, 433, 797
Kingdon J., Ferland G. J., 1995, ApJ, 442, 714
Lucy L. B., 1995, A&A, 294, 555
Luridiana V., Simón-Díaz S., Cerviño M., González Delgado R. M., Porter R. L., Ferland G. J., 2009, ApJ, 691, 1712
McKee C. F., Chernoff D. F., Hollenbach D. J., 1984, in Kessler M. F., Phillips J. P., eds, Galactic and Extragalactic Infrared Spectroscopy. Reidel, Dordrecht, p. 103
Martín-Hernández N. L. et al., 2002, A&A, 381, 606
Meaburn J., 1986, A&A, 164, 358
Meléndez M., Bautista M. A., Badnell N. R., 2007, A&A, 469, 1203
Mendoza C., 1983, in Flower D. R., ed., Proc. IAU Symp. 103, Planetary Nebulae. D. Reidel Publishing Co., Dordrecht, p. 143
Menten K. M., Reid M. J., Forbrich J., Brunthaler A., 2007, A&A, 474, 515
Mesa-Delgado A., Esteban C., García-Rojas J., 2008, ApJ, 675, 389
Mesa-Delgado A., López-Martín L., Esteban C., García-Rojas J., Luridiana V., 2009, MNRAS, 394, 693 (Paper I)
Moore C. E., 1945, A Multiplet Table of Astrophysical Interest. Princeton Univ. Obs., Princeton, NJ, p. 20
Mouri H., Taniguchi Y., 2000, ApJ, 534, L63
Nisini B., Bacciotti F., Giannini T., Massi F., Eislöffel J., Podio L., Ray T. P., 2005, A&A, 441, 159
O'Dell C. R., Doi T., 2003, AJ, 125, 277
O'Dell C. R., Henney W. J., 2008, AJ, 136, 1566
O'Dell C. R., Wen Z., Hester J. J., 1991, PASP, 103, 824
O'Dell C. R., Wong K., 1996, AJ, 111, 846
O'Dell C. R., Yusef-Zadeh F., 2000, AJ, 120, 382
O'Dell C. R., Hartigan P., Lane W. M., Wong S. K., Burton M. G., Raymond J., Axon D. J., 1997, AJ, 114, 730
Osterbrock D. E., Tran H. D., Veilleux S., 1992, ApJ, 389, 305
Pauldrach A. W. A., Hoffmann T. L., Lennon M., 2001, A&A, 375, 161
Peimbert M., 1967, ApJ, 150, 825
Peimbert M., 1995, in Williams R., Livio M., eds, The Analysis of Emission Lines. Cambridge Univ. Press, Cambridge, p. 165
Peimbert M., Costero R., 1969, Bol. Obs. Tonantzintla y Tacubaya, 5, 3
Peimbert M., Peimbert A., 2006, in Barlow M. J., Méndez R. H., eds, Proc. IAU Symp. 234, Planetary Nebulae in our Galaxy and Beyond. Cambridge Univ. Press, Cambridge, p. 227
Peimbert M., Sarmiento A., Fierro J., 1991, PASP, 103, 815
Peimbert M., Peimbert A., Ruiz M. T., 2000, ApJ, 541, 688
Peimbert A., Peimbert M., Luridiana V., 2002, ApJ, 565, 668
Peimbert M., Torres-Peimbert S., Ruiz M. T., 1992, Rev. Mexicana Astron. Astrofis., 24, 155
Porter R. L., Bauman R. P., Ferland G. J., MacAdam K. B., 2005, ApJ, 622, L73
Porter R. L., Ferland G. J., MacAdam K. B., 2007, ApJ, 657, 327
Przybilla N., Nieva F. M., Butler K., 2008, ApJ, 688, L103

Quinet P., 1996, A&AS, 116, 573
Raga A. C., Cantó J., De Colle F., Esquivel A., Kajdic P., Rodríguez-González A., Velázquez P. F., 2008, ApJ, 680, L45
Reipurth B., Bally J., Fesen R. A., Devine D., 1998, Nat, 396, 343
Riera A., Mampaso A., Vilchez J. M., Phillips J. P., 1989, A&A, 210, 351
Rodríguez M., 1999, A&A, 348, 222
Rodríguez M., 2002, A&A, 389, 556
Rodríguez M., Rubin R. H., 2005, ApJ, 626, 900
Rosado M., de La Fuente E., Arias L., Le Coarer E., 2002, Rev. Mexicana Astron. Astrofis. Conf. Ser., 13, 90
Rubin R. H., Simpson J. P., Haas M. R., Erickson E. F., 1991, ApJ, 374, 564
Rubin R. H., Martin P. G., Dufour R. J., Ferland G. J., Blagrave K. P. M., Liu X.-W., Nguyen J. F., Baldwin J. A., 2003, MNRAS, 340, 362
Ruiz M. T., Peimbert A., Peimbert M., Esteban C., 2003, ApJ, 595, 247
Savage B. D., Sembach K. R., 1996a, ARA&A, 34, 279
Savage B. D., Sembach K. R., 1996b, ApJ, 470, 893
Sawey P. M. J., Berrington K. A., 1993, At. Data Nucl. Data Tables, 55, 81
Shaw R. A., Dufour R. J., 1995, PASP, 107, 896
Simón-Díaz S., Herrero A., Esteban C., Najarro F., 2006, A&A, 448, 351
Smith N., Bally J., Brooks K. J., 2004, AJ, 127, 2793
Smith N., Bally J., Shuping R. Y., Morris M., Kassis M., 2005, AJ, 130, 1763
Stasińska G., 1978, A&A, 66, 257
Storey P. J., Hummer D. G., 1995, MNRAS, 272, 41
Tsamis Y. G., Barlow M. J., Liu X.-W., Danziger I. J., Storey P. J., 2003, MNRAS, 338, 687
Turnshek D. A., Bohlin R. C., Williamson R. L., Lupie O. L., Koornneef J., Morgan D. H., 1990, AJ, 99, 1243
Verner E. M., Verner D. A., Baldwin J. A., Ferland G. J., Martin P. G., 2000, ApJ, 543, 831
Walter D. K., Dufour R. J., Hester J. J., 1992, ApJ, 397, 196
Welty D. E., Hobbs L. M., Lauroesch J. T., Morton D. C., Spitzer L., York D. G., 1999, ApJS, 124, 465
Zhang H., 1996, A&AS, 119, 523
Zhang H. L., Pradhan A. K., 1997, A&AS, 126, 373

This paper has been typeset from a TEX/LATEX file prepared by the author.

5

Variaciones de las propiedades nebulares y la discrepancia de abundancias en tres regiones H II a pequeña escala espacial

En esta última parte de la tesis presentamos el estudio de las distribuciones espaciales de las propiedades nebulares del gas ionizado en tres regiones H II galácticas brillantes y relativamente cercanas: M8, M17 y NGC 7635. El estudio que aquí se realiza es análogo al llevado a cabo en el capítulo §2 en la Nebulosa de Orión y, por tanto, persigue los mismos objetivos: analizar la variación espacial del ADF y comprobar si existe alguna correlación con la presencia de subestructuras morfológicas embebidas dentro de las nebulosas. En estas regiones H II se observaron: dos posiciones de rendija en M8 y una posición de rendija en M17 y NGC 7635. Todas las observaciones se llevaron a cabo con el telescopio WHT del Observatorio del Roque de los Muchachos y su instrumento ISIS.

Al igual que en los trabajos anteriores, y haciendo uso de las tareas desarrolladas en el análisis de la Nebulosa de Orión, se han determinado las distribuciones espaciales de un amplio número de variables: flujos de líneas, coeficiente de extinción, temperaturas y densidades electrónicas, abundancias químicas de varios iones y el ADF(O^{2+}).

Esta cuarta parte de la tesis fue publicada en el artículo "Small-spatial-scale variations of nebular properties and the abundance discrepancy in three Galactic H II regions" de la revista *Monthly Notices of the Royal Astronomical Society*, actualmente en prensa y sin números de volumen y páginas asignados, el cual se adjunta a continuación, tras el resumen.

Resumen: Presentamos resultados de espectroscopia de rendija larga en varias posiciones que cubren diferentes estructuras morfológicas de las partes centrales de tres regiones H II galácticas: M8, M17 y NGC 7635. Estudiamos las distribuciones espaciales de un gran número de parámetros nebulares tales como el coeficiente de extinción, los flujos de líneas de emisión, las condiciones físicas y las abundancias químicas a la máxima resolución espacial alcanzable con nuestra instrumentación. Particularmente, nuestro objetivo es el estudio del comportamiento del factor de discrepancia de abundancias de O^{2+} [ADF(O^{2+})], definido como la diferencia logarítmica de las abundancias de O^{2+} determinadas a partir de líneas

de recombinación y líneas excitadas colisionalmente. Encontramos que el ADF(O^{2+}) se mantiene básicamente constante a lo largo de las posiciones de rendija que cubren M8 y M17. Para NGC 7635 únicamente detectamos las líneas de recombinación de O II en el espectro integrado, donde el ADF(O^{2+}) alcanza un valor muy grande de 0.59 dex. Comparamos también los resultados encontrados aquí con los anteriores resultados obtenidos para la Nebulosa de Orión. Hallamos evidencias que sugieren la presencia de un candidato a objeto Herbig-Haro en M8.

Monthly Notices of the ROYAL ASTRONOMICAL SOCIETY

Mon. Not. R. Astron. Soc. (2010) doi:10.1111/j.1365-2966.2010.16664.x

Small-spatial-scale variations of nebular properties and the abundance discrepancy in three Galactic H II regions⋆

A. Mesa-Delgado† and C. Esteban

Instituto de Astrofísica de Canarias, E-38200 La Laguna, Tenerife, Spain
Departamento de Astrofísica, Universidad de La Laguna, E-38205 La Laguna, Tenerife, Spain

Accepted 2010 March 8. Received 2010 March 1; in original form 2009 December 14

ABSTRACT

We present the results of long-slit spectroscopy in several slit positions that cover different morphological structures of the central parts of three bright Galactic H II regions: M8, M17 and NGC 7635. We study the spatial distributions of a large number of nebular parameters, such as the extinction coefficient, line fluxes, physical conditions and ionic abundances at the maximum spatial resolution attainable with our instrumentation. Particularly, our goal is to study the behaviour of the abundance discrepancy factor of O^{2+} [ADF(O^{2+})], defined as the logarithmic difference of the O^{2+} abundances derived from collisionally excited and recombination lines. We find that ADF(O^{2+}) remains fairly constant along the slit positions of M8 and M17. For NGC 7635, we only detect the O II recombination lines in the integrated spectrum along the whole slit, where ADF(O^{2+}) reaches a remarkably high value of about 0.59 dex. We compare our results with previous results obtained for the Orion Nebula. We find much evidence to suggest the presence of a candidate Herbig–Haro object in M8.

Key words: ISM: abundances – H II regions – ISM: individual objects: M8 – ISM: individual objects: M17 – ISM: individual objects: NGC 7635.

1 INTRODUCTION

The study of the elemental abundances in H II regions is an essential tool for our knowledge of the chemical evolution of the Universe. Traditionally, ionic abundances relative to elements heavier than He have been determined from strong collisionally excited lines (CELs). More than 20 yr ago, French (1983) obtained the first determination of the C^{2+}/H^+ ratio derived from the faint recombination line (RL) C II 4267 Å for a planetary nebula (PN), finding that it was several orders of magnitude larger than the abundance obtained from the CELs of this ion. Later, this result was confirmed in other PNe (e.g. Rola & Stasinska 1994; Mathis & Liu 1999). A similar qualitative result was also found by Peimbert, Storey & Torres-Peimbert (1993a) for the O^{2+}/H^+ ratio in the Orion Nebula; the abundances obtained from the flux of the faint RLs were higher than those derived using the standard method based on CELs. Currently, this observational fact is a classical problem in the understanding of the physics of photoionized nebulae known as the abundance discrepancy (AD) problem. This disagreement is quantified by means of the abundance discrepancy factor (ADF), which can be defined as the ratio, or the logarithmic difference, between the abundances of a same ion derived from RLs and CELs. In the case of the O^{2+}/H^+ ratio, the ADF has similar values between 0.1 and 0.3 dex for extragalactic and Galactic H II regions (e.g. García-Rojas et al. 2005; García-Rojas & Esteban 2007; Esteban et al. 2009), while for PNe the ADF shows a much wider range of values, becoming substantially larger in some objects (e.g. Liu et al. 2000, 2006; Tsamis et al. 2004, 2008).

What causes the AD problem is nowadays debated. On the one hand, the predictions of the temperature fluctuation paradigm proposed by Peimbert (1967), and characterized by the mean square of the spatial distribution of temperature – the so-called temperature fluctuation parameter, t^2 – seems to explain the ADF observed in H II regions, as argued by García-Rojas & Esteban (2007). Under this scheme, the AD problem is a direct consequence of the different temperature dependence of the emissivities of the lines used. In the case of CELs, it depends exponentially on the electron temperature, T_e, of the ionized gas, while the emissivity of RLs has a power-law temperature dependence, similar to those of the Balmer lines used as reference to determine the ionic abundance ratio relative to H^+. On the other hand, the hypothesis suggested by Liu et al. (2000), where most of the emission of RLs comes from a cold hydrogen-poor component immersed in the ambient gas, which emits the bulk of CELs, seems to solve the AD problem in PNe with high ADF values. This hypothesis is based on the observed fact that certain PNe contain well-resolved H-deficient knots, which are strong metallic RL emitters (e.g. Abell 30; Harrington & Feibelman 1984).

⋆Based on observations made with the 4.2-m William Herschel Telescope (WHT) operated on the island of La Palma by the Isaac Newton Group in the Spanish Observatorio del Roque de los Muchachos of the Instituto de Astrofísica de Canarias.

†E-mail: amd@iac.es

The existence and origin of the temperature fluctuations is controversial because high values of the t^2 parameter are not reproduced by standard photoionization models (Kingdon & Ferland 1995; Rodríguez & García-Rojas 2010). Additional mechanisms are proposed in order to explain the presence of temperature fluctuations (see revisions of Esteban 2002; Peimbert & Peimbert 2006). In the same way, new scenarios are used to try to find a solution to the AD problem in H II regions, putting forward new physical mechanisms. This is the case of the hypothesis presented by Tsamis & Péquignot (2005) and Stasińska et al. (2007). Based on the chemical model for the heavy-element mixing of Tenorio-Tagle (1996), these authors proposed the presence of two components of different chemical composition and physical conditions in H II regions. The component responsible for most of the emission of RLs consists of cold metal-rich droplets from supernova ejecta still not mixed with the ambient gas of the H II region where most of the CEL emission would be produced. Then, note that assuming a chemically inhomogeneous model in H II regions in order to explain the AD problem, the abundance derived from RLs and CELs would be upper and lower limits, respectively, of the real abundance of the ionized gas (Stasińska et al. 2007). Recently, a new scenario has been proposed by Ercolano (2009) based on the existence of high-density quasi-neutral clumps – embedded in the nebular gas ionized by the extreme-ultraviolet (EUV) radiation – which are ionized mainly by the X-ray emission from the central star. Under this scheme, the CEL emission mainly comes from the region ionized by the EUV radiation (E region), while the RLs are emitted in different proportions from the clumps (X region) and the E region. In this sense, the abundances of the E region would be representative of the nebula and those from CELs would be easier to correct than RL ones. Contrary to the model proposed by Tsamis & Péquignot (2005) and Stasińska et al. (2007), the nebular model of Ercolano (2009) has homogeneous abundances.

In a previous paper (Mesa-Delgado, Esteban & García-Rojas 2008), we explored the behaviour of the AD at small spatial scales and its dependence on different nebular parameters and physical conditions in the Orion Nebula in order to shed light on the origin of the AD problem. In that study, we used long-slit spectroscopy at spatial scales of 1.2 arcsec, finding high ADF(O^{2+}) values related to the presence of Herbig–Haro (HH) objects and temperature spikes at the position of the protoplanetary discs (proplyds). A subsequent detailed analysis of HH 202 was carried out by Mesa-Delgado et al. (2009a) using integral field spectroscopy, confirming a high ADF(O^{2+}) value at the main knot of HH 202, in agreement with the results of Mesa-Delgado et al. (2008). Another important result of Mesa-Delgado et al. (2009a) was that we obtained – for the first time in an H II region – a map of the Balmer temperature and of the temperature fluctuations in the observed field, finding no correlation between the ADF(O^{2+}) and the t^2 parameter.

Following the same goals and methodology of Mesa-Delgado et al. (2008), in this paper we have used long-slit spectroscopy at intermediate spectral resolution in order to study the spatial distribution of the ADF(O^{2+}) and other main nebular properties, as well as their relation with the local morphological structures (e.g. density condensations, ionization fronts or HH objects) in other bright Galactic H II regions, namely, M8, M17 and NGC 7635.

After the Orion Nebula, M8 and M17 are probably the most studied Galactic H II regions. M8 forms a blister of photoionized material on the surface of a giant molecular cloud. Near the optical centre, the region with the highest surface brightness of the nebula is found, the Hourglass (HG) region. This region is mainly ionized by the O star, Herschel 36 (Her 36), while the stars HD 165052 and 9 Sgr ionize the rest of the nebula (Woodward et al. 1986). M17 is a cavity with a V shape and the V opening in the line of sight. The main ionization source of M17 is a group of O3–O4 stars, which belong to the open cluster NGC 6618, located in the dark bay of the nebula (Hanson & Conti 1995). A singular characteristic of M17 is its high ionization degree – O^{2+}/O^{+} ratio – in comparison with other Galactic H II regions. The chemical compositions of M8 and M17 have been widely studied by several authors in all spectral ranges from low to high spectral resolution (e.g. Peimbert & Costero 1969; Rubin 1969; Sánchez & Peimbert 1991; Esteban et al. 1998; Rodríguez 1999; Tsamis et al. 2003). Based on high-resolution and deep echelle spectrophotometry, García-Rojas et al. (2007) have provided a complete revision of the chemical abundances of these H II regions using CELs and RLs. Nevertheless, we have not found in the literature detailed studies about the spatial behaviour of the nebular properties of these regions, excluding that of Peimbert, Torres-Peimbert & Ruiz (1992) along 17 areas of M17 at low spectral resolution. Our third region, NGC 7635, is not a classical H II region. This nebula is an interstellar bubble formed by the interaction of the stellar wind of the O6.5 IIIf star, BD+60 2522, with the surrounding interstellar medium. Recently, it has been assumed that the ram pressure of the stellar wind is balanced by the surrounding gas pressure because of the similarity between the velocities of the molecular cloud and the bright nebulosity places of the nebula (Christopoulou et al. 1995; Moore et al. 2002). The study of physical conditions and chemical abundances in NGC 7635 has been restricted to some selected zones (Talent & Dufour 1979; Rodríguez 1999; Moore et al. 2002). Moore et al. (2002) were the first to explore the spatial distributions of several bright emission lines – [O III] 5007 Å, Hα and [N II] 6584 Å – along the set of knots located north-west of the central star and the rim of the bubble. These authors also obtained the first density spatial profile along the slit position that covered the knots.

In Section 2, we describe the observations of the Galactic H II regions, the reduction procedure and the extraction of the one-dimensional spectra. In Section 3, we enumerate the selected emission lines and describe the procedure used to measure the fluxes and the extinction correction applied for each nebula. In Section 4, we describe the method used to determine the physical conditions and the ionic abundances from both types of lines, CELs and RLs. In Section 5, we present and discuss the spatial distributions along the slit positions of several nebular quantities for each nebula. In Section 6, we show the physical conditions and the ionic abundances for the individual extractions of NGC 7635, as well as discussing the puzzling abundance pattern found in this object. In Section 7, we compare the results in the light of the different lineal spatial resolution attained in this paper with that of the observations of Mesa-Delgado et al. (2008) in the case of the Orion Nebula. We also present several arguments for the presence of a new HH object in M8, and discuss the possible causes of the high ADF(O^{2+}) found in NGC 7635. Finally, in Section 8, we summarize the main conclusions of the paper.

2 OBSERVATIONS, DATA REDUCTION AND EXTRACTION OF THE ONE-DIMENSIONAL SPECTRA

Long-slit spectra at intermediate spectral resolution were obtained on 2007 July 18 and 2008 May 11 using the intermediate dispersion spectrograph and imaging system (ISIS) of the 4.2-m William Herschel Telescope (WHT) at the Observatorio del Roque de los Muchachos (La Palma, Spain). Two different CCDs were used at

the blue and red arms of the spectrograph: an EEV12 CCD with a configuration 4096 × 2048 pixels with a size of 13.5 μm per pixel in the blue arm and a REDPLUS CCD with 4096 × 2048 pixels with a pixel size of 15 μm in the red arm. The spatial scales were 0.20 and 0.22 arcsec pixel^{-1} in the blue and red arms, respectively. The slit length was 3.8 arcmin and the slit width was fixed to 0.98 arcsec. The R1200B grating was used in the blue arm and the R316R grating in the red arm. These gratings gave effective spectral resolutions of 0.86 and 3.81 Å for the blue and red arms, respectively. The blue spectra covered the spectral range from 4220 to 5080 Å and the red from 5320 to 8100 Å. The observation nights were photometric and the seeing during both observations was between 0.5 and 0.8 arcsec.

The Galactic H II region M8 and the wind-blown nebula NGC 7635 were observed on 2007 July 18. In the case of M8, we observed two slit positions (POS1 and POS2) centred at the HG region with different position angles (PAs; see Fig. 1, where the HG region is indicated by a grey section over the slit of POS1). These positions were chosen in order to cover different morphological structures, such as a candidate proplyd (Stecklum et al. 1998), marked as UC in Fig. 1, and the prominent HH 870. Unfortunately, during the analysis of these data, we noticed that probably the proplyd was not covered by the slit as we expected because of the difficulty of positioning the slit so close to the bright star Her 36. In the case of NGC 7635, a single slit position was used to cover the bright knots K1 and K2 as well as the rim of the bubble (see Fig. 1). On 2008 May 11 a single slit position was observed over the Galactic H II region M17 covering a high surface brightness zone. For all objects, large and short exposures were taken at each slit position and spectral range in order to achieve a good signal-to-noise ratio in the faint C II and O II RLs and to avoid saturation of the brightest emission lines. The journal of observations can be found in Table 1 where we present the coordinates (RA, Dec.) and the PA of each slit position observed as well as the total exposure times.

All CCD frames were reduced using the standard IRAF[1] TWODSPEC reduction package to perform bias correction, flat-fielding, cosmic-ray rejection, wavelength and flux calibration. The wavelength calibration was carried out with a CuNe+CuAr lamp. The absolute flux calibration was achieved by observations of the standard stars BD+33 2642, BD+28 4211 and BD+25 4655 for the first night and BD+25 3941, Feige 34 and BD+33 2642 for the second. The error of the flux calibration is of the order of 5 per cent.

The extraction of the one-dimensional spectra was carried out using an IRAF script based on the APALL task, following the procedure explained in Mesa-Delgado et al. (2008). We extracted the apertures for each region applying the bi-dimensional fit to the spectra of a standard star (with positional coordinates more similar to the object) used for flux calibration on the bi-dimensional image. In all cases, we adjusted a third-order Chebyshev polynomial obtaining a typical rms between 0.05 and 0.08 pixels. The slit centre in the red arm was some pixels displaced with respect to the slit centre in the blue arm; this effect was also corrected in the extraction procedure, and later verified from the alignment of Hα and Hβ spatial profiles, ensuring the same spatial coverage in both ranges. We also discarded apertures located at the edges of the CCD.

For M8, we extracted apertures of 6 pixels in the blue arm, and 5.45 pixels in the red arm, in the spatial direction, which corresponds to an effective spatial resolution of 1.2 arcsec. This size was chosen as a compromise to have the maximum attainable spatial resolution (only slightly larger than the mean seeing of the night) and a good signal-to-noise ratio in the auroral lines of [O III] and [N II]. However, larger extractions of 4.8-arcsec angular size were necessary to achieve a good flux measurement in the fainter O II RLs. Then, for the slit position 1 and considering the discarded apertures, we have obtained a final number of 150 apertures with a spatial resolution of 1.2 × 0.98 arcsec^2 and 38 apertures with a resolution of 4.8 × 0.98 arcsec^2 for the measurements of O II RLs. Similarly, a total number of 146 and 37 apertures were extracted, respectively, for the slit position 2. The smaller number of apertures obtained in this slit position is because we discarded four apertures that were severely contaminated by stellar emission from Her 36.

For the NGC 7635 slit position, we extracted apertures with an angular size of 3 arcsec. A total of 30 apertures with an area of 3.0 × 0.98 arcsec^2 were used. We also extracted individual integrated spectra of knots K1 and K2, and the rim of the bubble with areas of 12.4 × 0.98, 8.5 × 0.98 and 10.4 × 0.98 arcsec^2, respectively. We notice the detection of the C II 4267 Å RL in the three extractions.

For M17, apertures extracted with an angular size of 1.2 arcsec were sufficient to obtain a high signal-to-noise ratio in the auroral lines and RLs. We have obtained a total number of 185 apertures extracted with an individual area of 1.2 × 0.98 arcsec^2.

Additionally, for each slit position, we extracted a one-dimensional spectra collapsing the whole slit – the sum of all the individual apertures. These are designated as 'whole slit' spectra. The area covered by the 'whole slit', and therefore the total extraction area, is shown in Fig. 1.

3 EMISSION-LINE MEASUREMENTS AND REDDENING CORRECTION

The emission lines considered in our analysis were selected according to the following criteria:

(i) H I lines (Hα, Hβ and Hγ), which are used to compute the reddening correction and to rescale the line flux ratios of the red spectral range with respect to the blue;

(ii) CELs of several species in order to compute the physical conditions, such as the auroral lines [O III] 4363 Å and [N II] 5755 Å used to derive the electron temperatures, [S II] 6717, 6731 Å and [Cl III] 5718, 5738 Å used to calculate the electron density;

(iii) other CELs needed to derive different ionic abundances (N^+, O^+, O^{2+}, S^+, S^{2+}, Cl^{2+} and Ar^{2+});

(iv) faint RLs of C II and O II, which are used to derive the C^{2+} and O^{2+} abundances and to compute the abundance discrepancy factor, ADF, for O^{2+} (via a comparison with the O^{2+} abundances derived from CELs).

Line fluxes were measured applying a single or a multiple Gaussian profile fit procedure over a local continuum. All these measurements were made with the SPLOT routine of the IRAF package and using our own scripts to automatize the process. Because of the local variations of the continuum around O II RLs and their faintness, these lines were measured manually.

Following Mesa-Delgado et al. (2008), to accurately compute the line fluxes we need to define the adjacent continuum of each line using the SPLOT routine. For each selected line, we define two small spectral zones at each side of the line as close as possible and free of any spectral feature. Then, the routine fits the

[1] IRAF is distributed by the National Optical Astronomical Observatories, operated by the Associated Universities for Research in Astronomy, under cooperative agreement with the National Science Foundation.

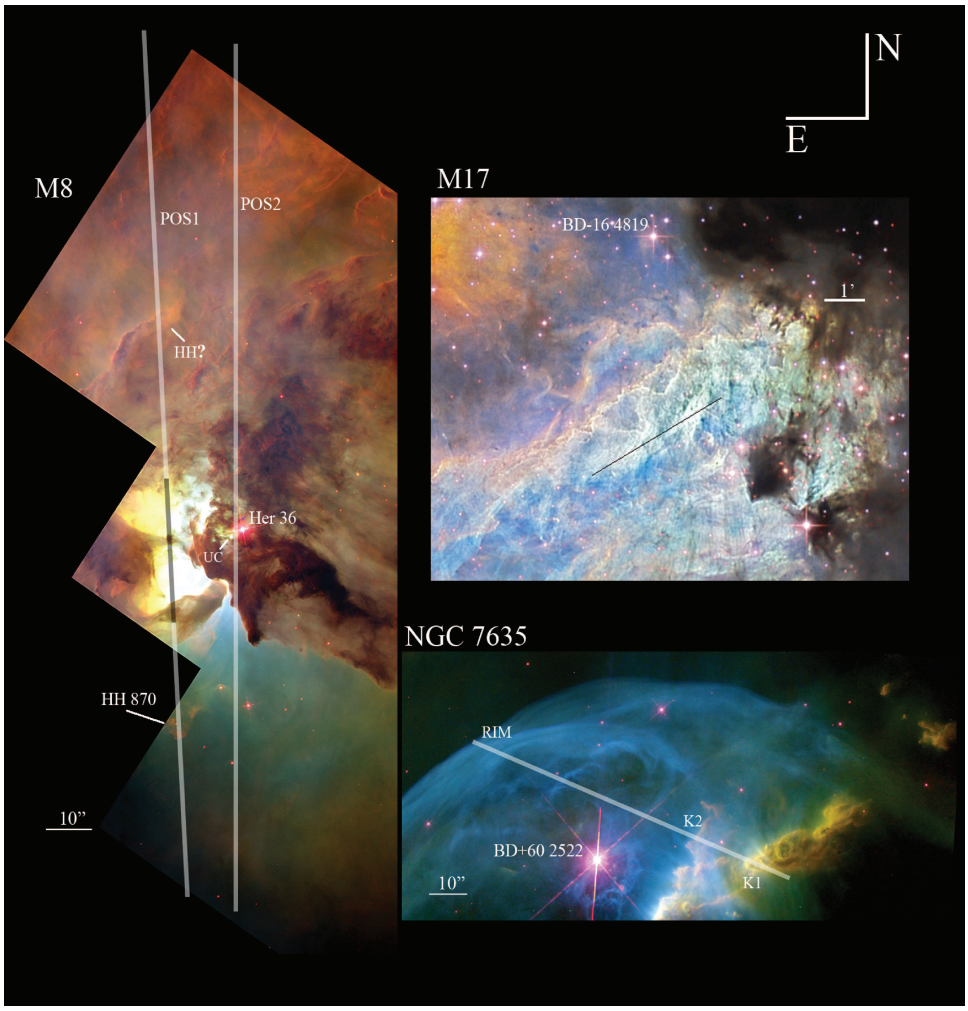

Figure 1. Observed slit positions over the central parts of the three Galactic H II regions. The slits only show the total extraction area, while the total slit length is 3.8 arcmin. The positions of the candidate proplyd (Stecklum et al. 1998) and HH object (see Section 7.3) are indicated as UC and HH?, respectively. The images are combinations of exposures taken with different narrow-band filters. For all regions, emission from [O III] is shown in blue, emission from Hα is shown in green and emission from [S II] is shown in red. The M8 (Caulet 1997) and NGC 7635 (Moore et al. 2002) images are sections of combinations of Wide Field Planetary Camera 2 images. The M17 image is a section of the original mosaic obtained by the amateur astronomer I. de la Cueva Torregrosa.

Table 1. Journal of observations.

Target	RA[a]	Dec.[a]	PA (°)	Exposure time (s) Blue arm	Red arm
M8 POS1	$18^h03^m41\overset{s}{.}40$	$-24°22'42\overset{''}{.}7$	3	7 × 1200,60	36 × 180,60
M8 POS2	$18^h03^m40\overset{s}{.}42$	$-24°22'42\overset{''}{.}7$	0	7 × 1200,60	36 × 180,60
M17	$18^h20^m42\overset{s}{.}98$	$-16°10'02\overset{''}{.}4$	120	5 × 1800,60	15 × 500,60
NGC 7635	$23^h20^m44\overset{s}{.}36$	$+61°11'56\overset{''}{.}0$	67.5	5 × 1200,60	8 × 600,60

[a]Coordinates of the slit centre (J2000.0).

continuum between both zones and the line profile to obtain the flux. The observational errors associated with the flux measurements were estimated following the criteria of Mesa-Delgado et al. (2008). The final error of a line flux was computed as the quadratic sum of the error in its flux measurement and the error in the flux calibration. All line fluxes for a given aperture were normalized to an H I line of reference, Hβ and Hα for the blue and red ranges, respectively.

The observed fluxes with respect to their H I line of reference were dereddened using the usual relation:

$$\frac{I(\lambda)}{I(\lambda_{\rm ref})} = \frac{F(\lambda)}{F(\lambda_{\rm ref})} 10^{c(\mathrm{H}\beta)[f(\lambda)-f(\lambda_{\rm ref})]}. \quad (1)$$

Here, the reddening coefficient, $c(\mathrm{H}\beta)$, represents the amount of interstellar extinction, $f(\lambda)$ the adopted extinction curve normalized to $f(\mathrm{H}\beta) = 0$, and $\lambda_{\rm ref}$ the H I line of reference. The reddening coefficient was determined from the comparison of the observed flux ratio of Hγ and Hα with respect to Hβ and the case B theoretical ones computed by Storey & Hummer (1995) for the physical conditions $T_{\rm e} = 10\,000$ K and $n_{\rm e} = 1000\,{\rm cm}^{-3}$. The final $c(\mathrm{H}\beta)$ was the weighted average of the values obtained from each line. In Appendix A, we present the dereddened emission-line ratios and their associated errors of the main emission lines per slit position as well as the observed Hβ flux and the mean $c(\mathrm{H}\beta)$ coefficient.

In all regions we have assumed the extinction law derived by Cardelli, Clayton & Mathis (1989), which is parametrized by the ratio of total to selective extinction, $R_V = A_V/E(B–V)$. In the case of M17, NGC 7635 and the position 2 of M8, we have used the typical value in the diffuse interstellar medium, $R_V = 3.1$. For the position 1 of M8, we have adopted different values of R_V depending on the zones covered by the slit. It is well known that the main ionization source of HG is Her 36 (Woodward et al. 1986) and that it shows a considerably higher extinction than the other zones of M8, which are mainly ionized by 9 Sgr and most of their reddening is a result of foreground interstellar dust. Consequently, following Sánchez & Peimbert (1991) we have adopted $R_V = 5.0$ to correct the apertures of position 1 that cover the HG region (the area indicated by a darker grey band in the slit position 1 of M8 shown in Fig. 1) and the typical value $R_V = 3.1$ in the other zones. The use of a higher total to selective extinction produces significant changes in the $c(\mathrm{H}\beta)$ values, while the line flux ratios remain almost unaffected by deviations from the classical extinction law. In the case of the 'whole slit' spectra, we have also assumed the typical R_V value for the interstellar medium. Finally, in order to produce a final homogeneous set of dereddened flux ratios, all of them were rescaled to Hβ. The rescaling factor used in the red spectra was the theoretical Hα/Hβ ratio for the physical conditions of $T_{\rm e} = 10\,000$ K and $n_{\rm e} = 1000\,{\rm cm}^{-3}$. The final error associated with the line dereddened fluxes includes the uncertainties in the flux measurements, flux calibration and the error propagation in the reddening coefficient.

In the different panels of Fig. 2 we present the spatial profiles of the $c(\mathrm{H}\beta)$ determinations as a function of the positional measurement along the slit in arcsec. Hereafter, each positional measurement represents the position on the slit of a given quantity obtained for an individual extraction with origin in the south edge of the original slit in the case of M8, in the north-west edge for M17 and in the south-west edge for NGC 7635. In all cases, we have found good agreement between our determinations and those available in the literature, considering that the measurements do not correspond exactly to the same spatial zone and the areas covered by the slits are also different. On the one hand, Figs 2(a) and (b) show the spatial distribution of $c(\mathrm{H}\beta)$ for slit positions 1 and 2 of M8, respectively, where we notice higher $c(\mathrm{H}\beta)$ values associated with the HG region and the zones near Her 36. These values are in agreement with previous $c(\mathrm{H}\beta)$ determinations carried out in the HG region

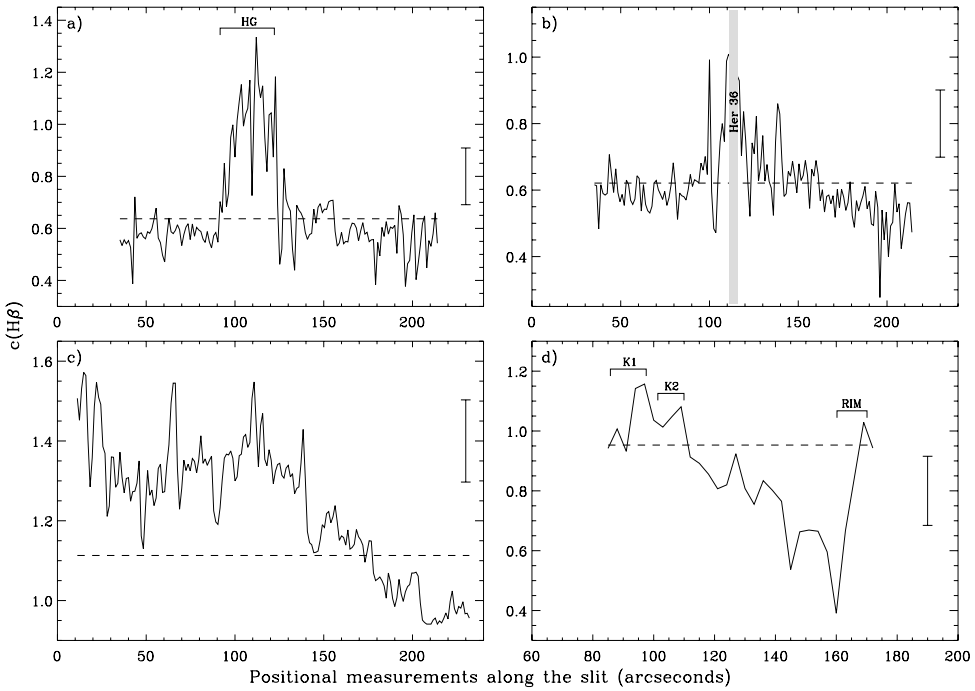

Figure 2. Spatial profiles of the reddening coefficient, $c(\mathrm{H}\beta)$, along the slit positions (a) M8 POS1, (b) M8 POS2, (c) M17 and (d) NGC 7635. The position of the HG region as well as of the knots K1 and K2 and the rim of the bubble of NGC 7635 are indicated. The grey band in (b) corresponds to apertures contaminated by stellar emission from Her 36. Positional measurements along the slits go from south to north in the two positions of M8 and from west to east for M17 and NGC 7635. The dashed horizontal line represents the $c(\mathrm{H}\beta)$ value obtained for the 'whole slit' spectra. The typical error bar is also included.

by Sánchez & Peimbert (1991), Esteban et al. (1999b) and García-Rojas et al. (2007), who found values between 0.85 and 1.0 dex. On the other hand, in Fig. 2(c) we present the spatial distribution of $c(\mathrm{H}\beta)$ along the slit position of M17. We have compared our determinations with those performed by Peimbert et al. (1992), whose slit positions 3 and 13 approximately coincide with the positional measurements 60 and 125 arcsec, respectively. For those positions, Peimbert et al. (1992) obtained values of about 1.72 and 1.45 dex, which are in agreement with our determinations, considering the uncertainties in the $c(\mathrm{H}\beta)$ determination. Fig. 2(d) presents the $c(\mathrm{H}\beta)$ spatial profile of NGC 7635. In this panel, we can see higher $c(\mathrm{H}\beta)$ values related to the knots and the rim. We have compared our values with previous determinations obtained by Talent & Dufour (1979) and Moore et al. (2002) at different parts of the nebula. Positions 3 and 5 of Talent & Dufour (1979) coincide with the positions of the knot K1 and the rim indicated in Fig. 2(d). Talent & Dufour (1979) measured $c(\mathrm{H}\beta)$ values at those positions of about 1.21 and 1.07 dex, respectively, which are in agreement with our determinations. However, Moore et al. (2002) obtained a similar value, 1.25 dex, from their slit position that covers the knots K1 and those located to the south of K1, but measured a value of about 1.46 dex for the rim of the bubble, which is higher than our determination and that of Talent & Dufour (1979) at the same position. The typical error in the $c(\mathrm{H}\beta)$ coefficient presented in Fig. 2 is of about 0.1 dex for all regions.

The results shown in Fig. 2 indicate that an important fraction of the extinction should come from dust located inside the objects, and that the distribution of such absorbing material is not homogeneous.

4 PHYSICAL CONDITIONS AND CHEMICAL ABUNDANCES

4.1 Physical conditions

We have determined the physical conditions – electron densities and temperatures – from the usual CEL ratios and using the IRAF task TEMDEN of the NEBULAR package (Shaw & Dufour 1995) with updated atomic data (see Liu et al. 2000; García-Rojas et al. 2005). We have computed the electron density, n_e, from the [S II] 6717/6731 line ratio and the electron temperatures, T_e, from the nebular to auroral [O III] (4959+5007)/4363 and [N II] (6548+6584)/5755 line ratios. Although we detect the [Cl III] doublet in several apertures, we do not use these lines to obtain density values because of their large associated errors. The spatial distributions of the physical conditions are presented and discussed for each region in Section 5.

Following the same methodology as Mesa-Delgado et al. (2008) for the determination of the physical conditions, a representative initial $T_\mathrm{e} = 10\,000$ K is assumed in order to derive a first approximation of n_e([S II]) – hereafter n_e. Then, we calculate T_e([O III]) and T_e([N II]), and iterate until convergence to compute the finally adopted values using T_e([N II]) in the density calculations. The errors in the physical conditions were computed by error propagation on the analytical expressions of n_e by Castañeda, Vilchez & Copetti (1992) and those of T_e given by Osterbrock & Ferland (2006) (their equations 5.4 and 5.5). Although the expression derived by Castañeda et al. (1992) is only valid to a limited range of densities lower than 10^4 cm^{-3}, and uses the old atomic data for S^+ from the compilation by Mendoza (1983), it seems adequate for an estimation of the errors in the physical conditions.

4.2 Ionic abundances from CELs and RLs

We used the IRAF package NEBULAR to derive ionic abundances of N^+, O^+, O^{2+}, S^+, S^{2+}, Cl^{2+} and Ar^{2+} from CELs. We have assumed no temperature fluctuations in the ionized gas ($t^2 = 0$) and a two-zone scheme, adopting T_e([N II]) to derive the abundances of singly ionized species and T_e([O III]) in the case of doubly ionized species. The electron density obtained from the [S II] line ratio was adopted for all ionic species. The errors in the ionic abundance determinations were calculated as the quadratic sum of the independent contributions of temperature, density and line flux uncertainties. The spatial distributions of the ionic abundances of some species are presented and discussed for each region in Section 5.

The wavelength range covered with the blue arm did not include the bright [O II] 3726, 3729 Å lines. In the case of NGC 7635, it was necessary to determine the O^+ abundance (see Section 6); to do this, we performed a proper subtraction of the telluric emission in the [O II] 7320, 7330 Å lines. The subtraction was achieved using rescaled pure telluric measurements from sky extractions of different sizes of long-exposure spectra of a compact H II region observed during the same night (the data of this object were published in Martín-Hernández et al. 2008). This procedure adds an uncertainty between 6 and 8 per cent higher in the flux measurements of [O II] lines. However, in the cases of M8 and M17 we do not consider it necessary to determine the O^+ abundance for our aims.

We have detected and measured pure RLs of the multiplet 1 of O II (see Fig. 3) and C II 4267 Å. The abundance of a heavy element X in the ionization state $i + 1$, which emits a RL at wavelength λ, is given by

$$\frac{N(\mathrm{X}^{i+1})}{N(\mathrm{H}^+)} = \frac{\lambda(\text{Å})}{4861}\frac{\alpha_\mathrm{eff}(\mathrm{H}\beta)}{\alpha_\mathrm{eff}(\lambda)}\frac{I(\lambda)}{I(\mathrm{H}\beta)}. \quad (2)$$

Here, $I(\lambda)/I(\mathrm{H}\beta)$ is the dereddened flux ratio, $\alpha_\mathrm{eff}(\lambda)$ and $\alpha_\mathrm{eff}(\mathrm{H}\beta)$ are the effective recombination coefficients for the RL and Hβ, respectively. Because of the similar temperature dependence of the emissivities of RLs, the $\alpha_\mathrm{eff}(\mathrm{H}\beta)/\alpha_\mathrm{eff}(\lambda)$ ratio is almost independent of the adopted temperatures. In our case, under the two-zone scheme, we have assumed T_e([O III]) to calculate the C^{2+} and O^{2+} abundances.

We have detected the C II line at 4267 Å in most of the apertures extracted at 1.2 arcsec in M17 and M8, and in the integrated spectra for the 'whole slit', the knots and the rim of the bubble of NGC 7635 (see Section 6). C^{2+} abundances from RLs have been calculated using the atomic data of Davey, Storey & Kisielius (2000).

The O^{2+} abundances were derived when at least four lines of multiplet 1 were measured in a given one-dimensional spectrum using the effective recombination coefficients from Storey (1994) and the same method that is detailed in Esteban et al. (1998). We have determined the O^{2+} abundances correcting for the departure from local thermodynamic equilibrium (LTE) of the upper levels of the transitions of multiplet 1 of O II for densities lower than 10 000 cm^{-3} using the empirical formulation proposed by Peimbert & Peimbert (2005). Abundances determined assuming LTE for the population of the levels do not differ more than 2 per cent from the NLTE ones because we use several of the brightest lines of the multiplet. We have computed the O^{2+}/H^+ ratio for 89 per cent of the apertures extracted at 1.2 arcsec in M17, for all the apertures extracted at 4.8 arcsec in both slit positions of M8, and in the 'whole slit' spectrum of NGC 7635 (see Section 6).

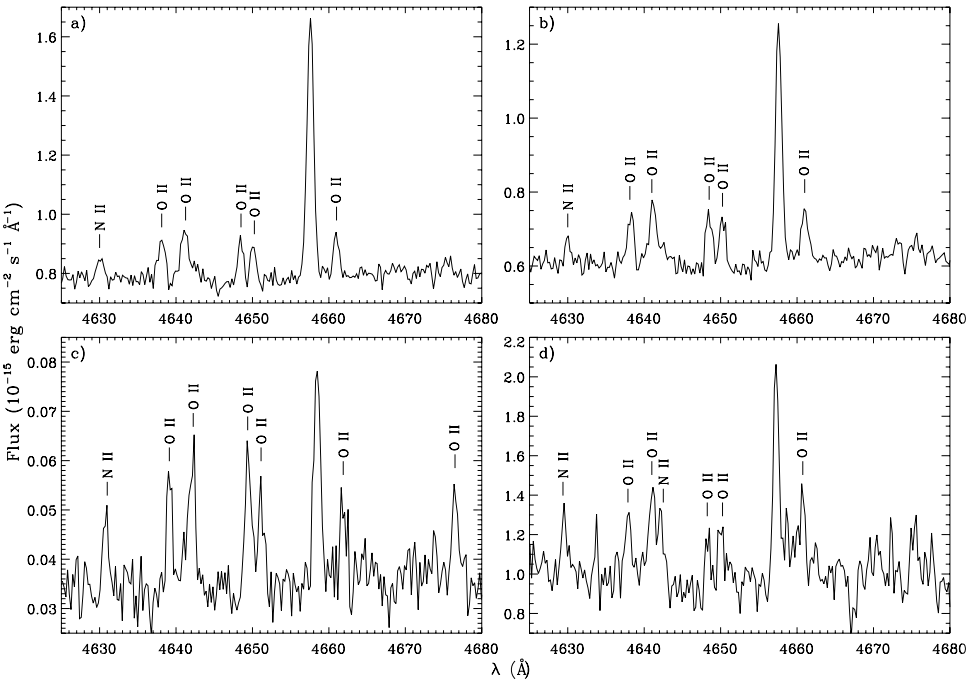

Figure 3. Sections of the spectrum around the emission lines of multiplet 1 of O II. (a) and (b) correspond to apertures of 4.8 arcsec wide extracted from slit positions 1 and 2 of M8, respectively, extending from positional measurements 137.2 to 142 arcsec. (c) corresponds to a 1.2 arcsec wide aperture extracted from the slit position of M17, which covers from 153.4 to 154.6 arcsec. (d) shows a section of the 'whole slit' spectrum of NGC 7635.

5 SPATIAL PROFILES ALONG THE SLIT POSITIONS

In the following sections, we present the spatial profiles of several nebular properties along the slit positions of each H II region. The selected parameters are n_e, T_e([N II]), T_e([O III]), the flux of several selected lines ([Fe III] 4658 Å, C II 4267 Å, O II 4649 Å and [O III] 4959 Å) and the O^{2+} abundances obtained from CELs and RLs.

5.1 M8

In Figs 4 and 5, we show the spatial variations of the nebular properties for the slit positions 1 and 2 of M8, respectively.

The spatial profiles of n_e along the slits show a wide range of variation with a maximum associated with the HG region in position 1 (see Fig. 4a) and the apertures near Her 36 in the case of position 2 (see Fig. 5a). The density peak in Fig. 4(a) associated with HH 870 reaches a value higher than 800 cm^{-3}. Following the nomenclature proposed by Arias et al. (2006), this peak would be more specifically related to the knot B of this object. At the HG region, we find densities between 2600 and 3500 cm^{-3}, values that are in agreement with previous determinations by García-Rojas et al. (2007) and Peimbert, Torres-Peimbert & Dufour (1993b), who derive densities between 1800 and 3700 cm^{-3}. We have noticed a slight localized enhancement of about 300 cm^{-3} in the density profile of position 1 around the positional measurement 155.2 arcsec (indicated as HH? in Figs 1 and 4). This feature coincides in Fig. 1 with a relatively bright rim crossed by the slit and located about 45 arcsec to the north of the centre of the HG region. In Section 7.3 we argue that this feature may be a candidate HH object. In Fig. 5(a), the highest density value is related to an ionization front located at 15.3 arcsec S and 1.5 arcsec E from Her 36. In this slit position, we have also detected local maxima at the positional measurements 65.2, 79.6, 151.6 and 192.4 arcsec. On the one hand, the first two maxima coincide in Fig. 1 with gaseous arcs that surround faint stars located approximately at 34 and 49 arcsec to the south of Her 36. On the other hand, the other maxima are related to high-density filaments located approximately at 40 and 80 arcsec to the north of Her 36. The average value of both slit position 1 and 2 obtained from the 'whole slit' spectrum, and included in Figs 4(a) and 5(a) with a dashed line, amounts to 1140 ± 220 and 750 ± 150 cm^{-3}, respectively.

The spatial profiles of T_e([O III]) and T_e([N II]) are presented in Figs 4(b) and 5(b) for the slit positions 1 and 2, respectively. We do not find relevant features in these profiles, excluding perhaps very slight enhancement of both temperature indicators at the HG region. However, the temperature rises at these positional measurements are of the order of the error bar. We also present the T_e([N II])/T_e([O III]) ratio in the bottom panels of Figs 4(b) and 5(b), which is basically constant along the slits showing spatial variations of the order of the observational errors. In general, T_e([N II]) is slightly higher than T_e([O III]), a typical result obtained for H II regions as a consequence of the hardening of the radiation field in the low ionization zones (e.g. Stasińska 1980).

One of the main spectral properties of HH objects is their strong emission in [Fe III] lines as a result of the destruction of dust grains (Mesa-Delgado et al. 2009b) or changes in the ionization conditions (Blagrave, Martin & Baldwin 2006). In Figs 4(c) and 5(c) we have plotted the spatial profile of the dereddened flux of [Fe III] 4658 Å with respect to Hβ for the slit positions 1 and 2, respectively. In

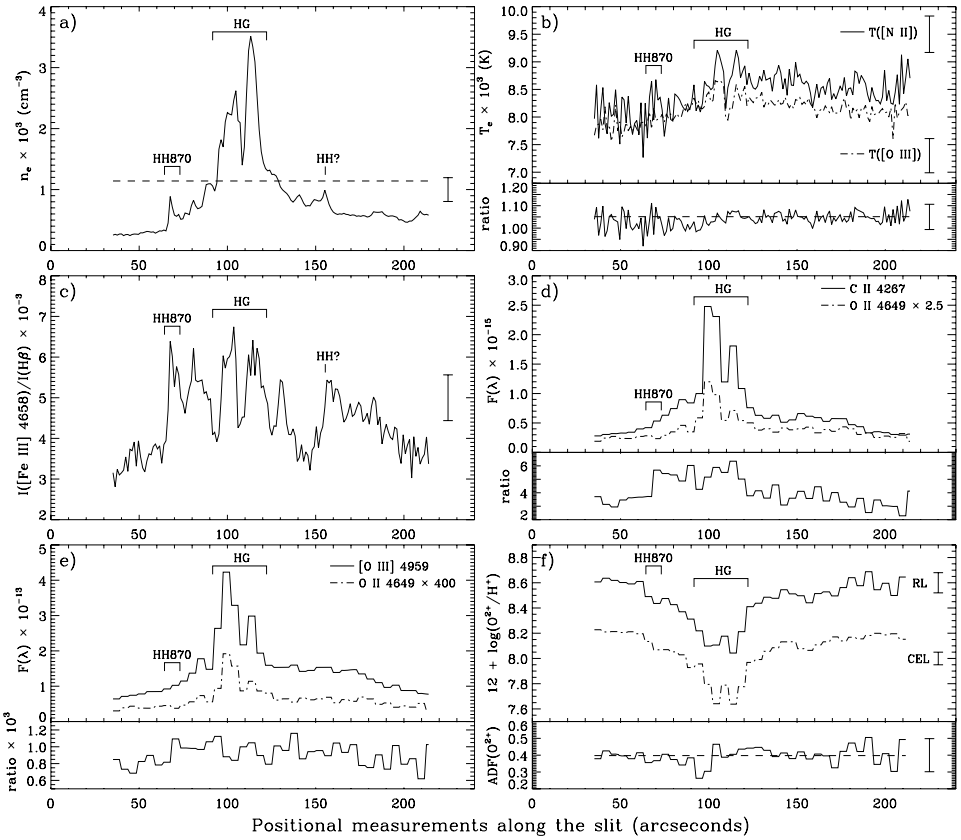

Figure 4. Spatial profiles of several nebular parameters along the slit position 1 of M8. Positional measurements along the slit go from south to north (see Fig. 1). The position of the HG region and the HH object 870 are indicated as well as the typical error of some variables. The possible candidate HH object (see Section 7.3) is also marked as HH? in (a) and (c). The horizontal dashed line in some panels indicates the value obtained for the 'whole slit' spectrum. (a) Profile of n_e. (b) Top, profiles of T_e([N II]) (solid line) and T_e([O III]) (dash-dotted line); bottom, profile of the T_e([N II])/T_e([O III]) ratio. (c) Profile of the dereddened flux ratio of [Fe III] 4658 Å. (d) Top, observed flux of C II 4267 Å (solid line) and O II 4649 Å (dash-dotted line); bottom, profile of the F(C II 4267 Å)/F(O II 4649 Å) ratio. (e) Top, observed flux of [O III] 4959 Å (solid line) and O II 4649 Å (dash-dotted line); bottom, profile of the F([O III] 4959 Å)/F(O II 4649 Å) ratio. (f) Top, O^{2+} abundances from RLs (solid line) and CELs (dash-dotted line); bottom, profile of ADF(O^{2+}). All observed fluxes have units of erg cm^{-2} s^{-1}. Note that from (a) to (c) the profiles correspond to extractions of 1.2 arcsec. From (d) to (f) the spatial increments are 4.8 arcsec wide.

the slit position 1 we can see a clear rise of the flux at the position of HH 870, which increases by a factor of ∼2 with respect to the adjacent background gas. This factor seems to extend along the HG region where the ionization degree decreases and the electron density increases. As in the density spatial profile of slit position 1, we have found in Fig. 4(c) an enhancement of the [Fe III] emission line at the positional measurement 155.2 arcsec where a possible candidate HH object is located (see Section 7.3). In the case of the slit position 2, we have found no evidence of important localized increase in the [Fe III] emission, only a decrease of a factor of 2 around Her 36.

In Figs 4(d), 5(d), 4(e) and 5(e) the spatial profiles of the observed flux of C II 4267 Å, O II 4649 Å and [O III] 4959 Å lines along the slit positions are shown, as well as their ratio in the bottom panels of the same figures. It should be remembered that the extractions of the O II line are 4.8 arcsec wide. Then, each extracted aperture represents the average value of four apertures extracted with a spatial size of 1.2 arcsec. In order to perform a proper comparison, we have also plotted the observed fluxes of C II and [O III] lines with extractions 4.8 arcsec wide. The spatial distributions of the pure RLs are similar in each slit position. However, we can note a slight rise of the F(C II 4267 Å)/F(O II 4649 Å) ratio at the HG and HH 870 regions (see Fig. 4d). We have observed a similar enhancement of the ratio of emission lines of species with similar ionization potential to C^{2+} (24.4 eV), such as Ar^{2+} (27.6 eV) or Cl^{2+} (23.8 eV), with respect to [O III] 4959 Å and O II 4649 Å. In order to explore the reason for this enhancement, we have determined the spatial distribution of the ionization degree, which presents an inverse behaviour to the C II/O II ratio. Although we have not subtracted the telluric emissions from the [O II] 7320, 7330 Å lines in M8, we have observed that the O^{2+}/O^{+} decreases between the positional measurements at 70 and 130 arcsec, where the HG region is located, reaching values of about −0.4 dex lower than in the rest of the slit position. Therefore, this indicates that the variation in the C II/O II ratio can be simply a result of the decrease of the ionization degree in that zone. However, the point-to-point comparison of the spatial profiles of [O III] 4959 Å and O II 4649 Å (see Figs 4e and 5e) does not show clear tendencies.

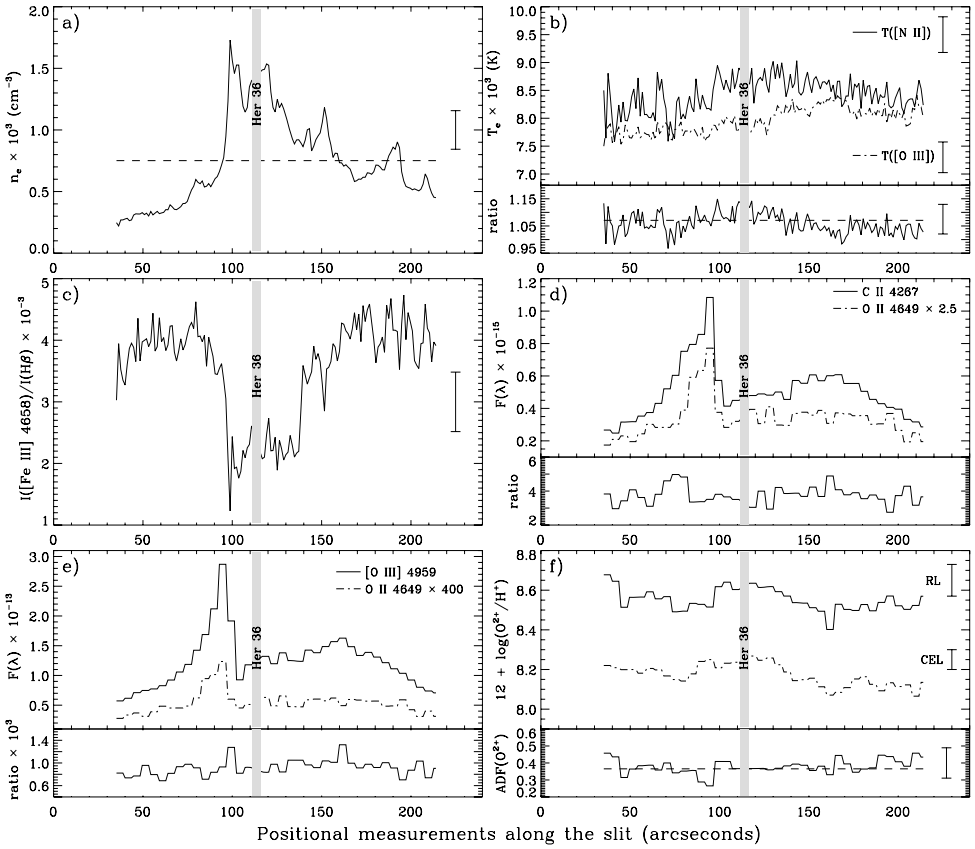

Figure 5. Same as Fig. 4 for slit position 2 of M8. The grey vertical band covers the apertures affected by stellar features from the emission of Her 36.

The [O III] spatial distribution of the slit positions 1 and 2 of M8 suggests that the gas covered by both slits might not be ionized by the same source. Slit position 1 shows an [O III] emission distribution rather similar to the density distribution, but position 2 does not. In fact, the [O III] emission shows a peak at the ionization front at the south of Her 36 (positional measurement ∼95 arcsec) and remains almost constant toward the north of the slit. This area coincides with the dark zone around Her 36. It seems that while the HG region and the area at the south of the positional measurement ∼95 arcsec of the slit position 2 are ionized by Her 36, the rest of the position 2 is ionized by another star, perhaps 9 Sgr. This hypothesis is consistent with the results from previous works of Woodward et al. (1986) and Sánchez & Peimbert (1991).

Finally, Figs 4(f) and 5(f) show the spatial variation of the O^{2+} abundances derived from RLs and CELs, as well as the AD factor of this ion – ADF(O^{2+}) – defined in its logarithmic form as

$$\mathrm{ADF}(O^{2+}) = \log(O^{2+}/H^{+})_{\mathrm{RLs}} - \log(O^{2+}/H^{+})_{\mathrm{CELs}}. \quad (3)$$

As in Figs 4(d), 4(e), 5(d) and 5(e), we present the spatial profile for the extractions 4.8 arcsec wide of the O^{2+}/H^{+} ratio obtained from RLs and CELs. The ADF(O^{2+}) remains fairly constant along the slit positions 1 and 2 with average values of 0.40 ± 0.11 and 0.37 ± 0.09 dex, respectively. These are in agreement with previous determinations obtained by Esteban et al. (1999a), 0.34 dex, and García-Rojas et al. (2007), 0.37 dex. The only relevant variation detected in the O^{2+} abundance profiles is at the HG region, where the O^{2+} abundance decreases up to 7.6 dex because of the decrease of the ionization degree.

5.2 M17

Fig. 6 shows the spatial distributions of several nebular properties along the slit position that covers two bright areas of M17 (see Fig. 1). The density profile (Fig. 6a) shows a peak between the positional measurements 30 and 90 arcsec, a constant value between 90 and 180 arcsec and a decrease at the eastern edge. We have found good agreement between our density determinations and those at the positions 3 and 13 studied by Peimbert et al. (1992), which coincide with our positional measurements 60 and 125 arcsec (see Section 3). In the case of the temperature distributions (see Fig. 6b), we have only found variations of the order of our error bar. In the case of the T_e([O III]), we have found values similar to those derived by Peimbert et al. (1992) in their slit positions. However, the T_e([N II]) obtained by those authors shows a higher value at their position 3, which amounts to 11 600 K. However, Esteban et al. (1999a) also explored the physical conditions at position 3 of Peimbert et al. (1992) and found a T_e([N II]) of about 8990 K, which is in agreement with our determinations within the errors. In Fig. 6(c), we can find the spatial profile of the [Fe III] 4658 Å

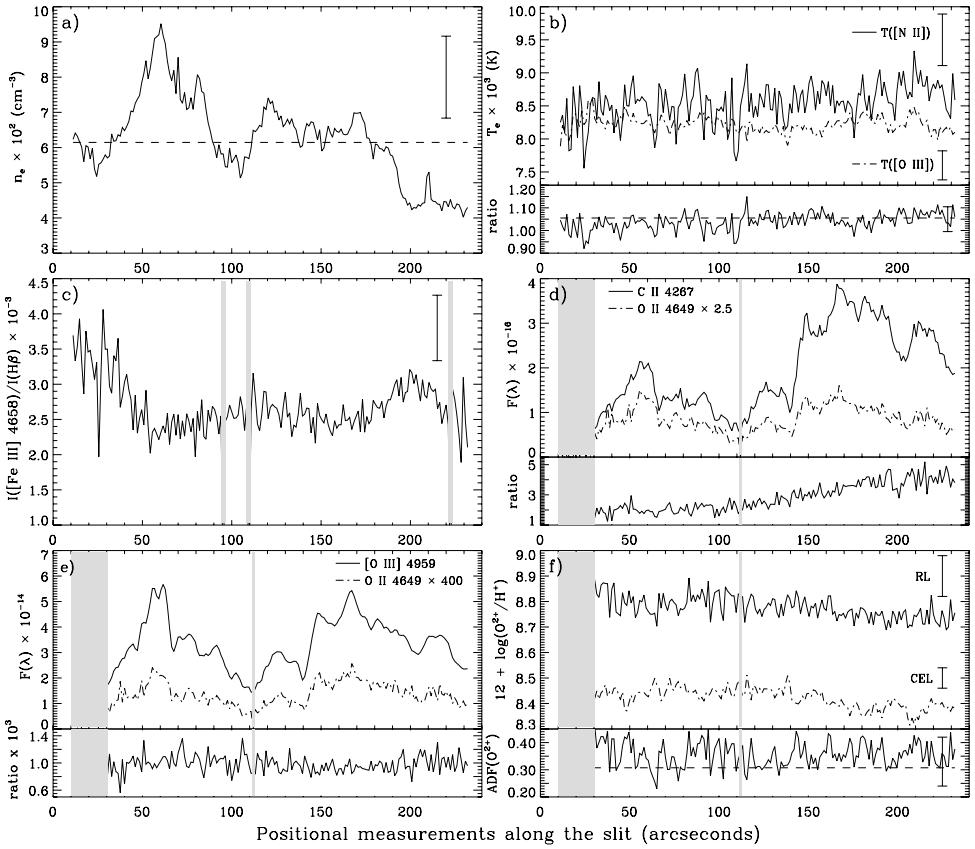

Figure 6. Same as Fig. 4 for the slit position of M17. The grey bands cover apertures where [Fe III] 4658 Å (c) and O II 4649 Å (d)–(f) were not detected. Positional measurements along the slit go from west to east (see Fig. 1).

line flux with respect to Hβ, where we do not find any localized enhancement, which may be related to the presence of HH objects.

The spatial distributions of C II 4267 Å and O II 4649 Å are presented in Fig. 6(d), where we can notice an increase of the C II emission flux to the east of the positional measurement 140 arcsec. This rise can be related to a decrease of the ionization degree. In fact, Peimbert et al. (1992) find a change in the O^{2+}/O^{+} ratio between their slit positions 3 and 13 of about 0.40 dex. The comparison of the [O III] and O II emission-line fluxes in Fig. 6(e) does not show relevant features, and their ratio remains essentially constant along the slit.

Finally, Fig. 6(f) shows the spatial profiles of the O^{2+} abundances derived from RLs and CELs, as well as their ratio, ADF(O^{2+}). As we can see, both abundance determinations show a similar decrease along the slit, while the ADF(O^{2+}) distribution presents a constant value of about 0.37 $\pm$ 0.09 dex. This value is higher than that obtained in the 'whole slit' spectrum, which amounts to 0.31 $\pm$ 0.07 dex, although the difference is consistent within the errors.

5.3 NGC 7635

The spatial distributions of nebular properties along the slit position of NGC 7635 are presented in Fig. 7. Each positional measurement corresponds to an area of 3 × 0.98 arcsec. The results obtained for the integrated spectra covering separately the bright knots at the west of the central star, K1 and K2, and the rim of the bubble (see Fig. 1) are presented in Section 6.

In Fig. 7(a) the density profile shows its highest value at the position of knot K1, where it reaches a value of about 2600 cm^{-3}. Rodríguez (1999) obtained the density in three zones of NGC 7635 and her position 1 coincides with our K1, as well as the slit position 3 of Talent & Dufour (1979). Rodríguez (1999) derived a density value of about 2800 cm^{-3}, which is in agreement with our results, while Talent & Dufour (1979) derived a density value of about 4200 cm^{-3}. Moreover, Moore et al. (2002) also obtained higher density values on the knots and the rim, but with larger uncertainties. Two local maxima can also be seen at the positional measurements corresponding to the knot K2 and the rim. Between the knots and the rim, the density remains constant with an average value of about 100 cm^{-3} and a standard deviation of about 20 cm^{-3}.

In Fig. 7(b), we can see that the electron temperatures do not show strong variations along the slit and are of the order of the error bar. The average values of both temperatures amount to 8600 K for T_e([O III]) and 8100 K for T_e([N II]) with standard deviations of about 390 and 420 K, respectively. Their ratio shows an average value of 0.94 with a standard deviation of about 0.05. Our temperature determinations are in agreement with the results of Rodríguez (1999), Talent & Dufour (1979) and Moore et al. (2002).

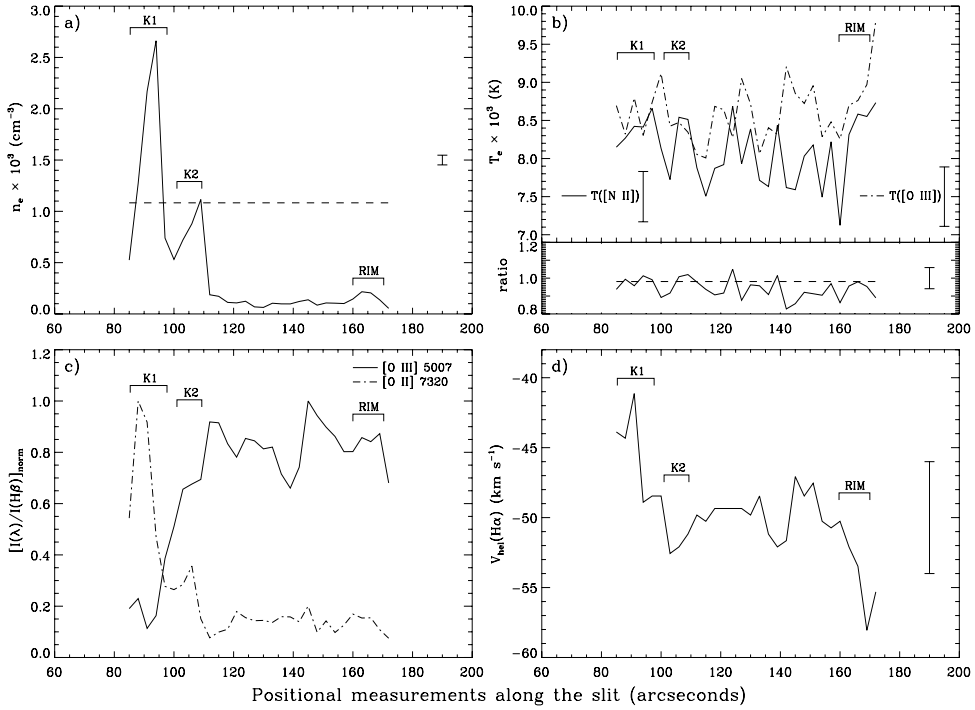

Figure 7. Spatial profiles of several nebular properties along the slit position of NGC 7635. Positional measurements along the slit go from west to east (see Fig. 1). The position of the knots, K1 and K2, and the rim are indicated as well as the typical error of some variables. The horizontal dashed line in some panels gives the value obtained from the 'whole slit' spectrum. (a) Profile of n_e. (b) Top, profiles of T_e([N II]) (solid line) and T_e([O III]) (dash-dotted line); bottom, profile of the T_e([N II])/T_e([O III]) ratio. (c) Profile of the dereddened fluxes with respect to Hβ of [O III] 5007 Å (solid line) and [O II] 7320 Å (dash-dotted line) normalized to their respective maximum. (d) Heliocentric velocity profile obtained from the centroid of Hα.

Fig. 7(c) shows the spatial profiles of the dereddened fluxes of [O III] 5007 Å and [O II] 7320 Å with respect to Hβ and normalized to their respective maximum emission. On the one hand, the [O II] spatial profile shows its maximum values at the position of the knot K1 decreasing progressively up to the positional measurement 110 arcsec. On the other hand, the [O III] distribution presents an inverse pattern with a progressive increase until the same positional measurement. Beyond this point, both spatial profiles do not show strong variations. A similar result can be seen in the *Hubble Space Telescope* (*HST*) images of Moore et al. (2002). The behaviour shown in Fig. 7(c) is a result of the dramatic change of the ionization degree. The knots have a lower ionization degree than the gas beyond the positional measurement 110 arcsec, which corresponds to the bubble.

Finally, Fig. 7(d) shows the heliocentric radial velocity, V_{hel}, spatial distribution obtained from the Gaussian fit of the Hα line profile. We have obtained the most negative velocity at the position of the rim, which is about -54 ± 4 and in agreement with the mean heliocentric velocity found by Christopoulou et al. (1995) for NGC 7635. This value is also similar to that of the molecular cloud associated with the bubble and the S162 complex (see Christopoulou et al. 1995, and references therein). The expansion of the bubble is very slow, with velocities between 4 and 25 km s^{-1}, and therefore our spectral resolution did not allow us to resolve the line splitting of the expanding bubble. In fact, the velocity profile along the slit shown in Fig. 7(d) does not show any remarkable feature or velocity differences substantially larger than the uncertainties.

6 CHEMICAL ABUNDANCES OF SELECTED ZONES OF NGC 7635

In this section, we present the physical conditions and ionic and elemental abundances – derived from CELs and RLs – obtained from the integrated spectra that cover the knots K1 and K2, the rim of the bubble as well as the 'whole slit' spectrum. The results are shown in Tables 2 and 3.

The physical conditions derived from the ratios of CELs are shown in Table 2. These values are in agreement with those obtained from the 3-arcsec extractions presented in Fig. 7, as well as with the different determinations from the literature that we have cited in Section 5.3. We can see that the temperatures calculated from the different indicators are very similar within the errors, in agreement with the result obtained from the temperature spatial distribution along the slit position (see Fig. 7b). The electron density and temperatures found for the 'whole slit' spectra are basically averages of the knots and the rim values.

We have derived ionic abundances of several ions (see Table 2). The O^+/H^+ ratio was obtained by removing the telluric contamination from the [O II] 7320, 7330 Å lines, as explained in Section 4.2. A proper determination of the O^+ abundances has allowed us to explore the strong variation of the ionization degree between the knots and the rim. As we can see in Table 2, the ions with low ionization potential, such as N^+, O^+ and S^+, show a gradual decrease in their abundance following the sequence: K1, K2 and the rim. As expected, this decrease is accompanied by an increase of the

Table 2. Physical conditions and ionic abundances[a] of selected zones of NGC 7635.

	K1	K2	Rim	'Whole slit' $t^2=0$	'Whole slit' $t^2>0$
n_e([S II]) (cm^{-3})	1900 ± 150	890 ± 70	180 ± 30	1080 ± 90	
T_e([N II]) (K)	8450 ± 320	8150 ± 300	8680 ± 430	8420 ± 330	
T_e([O III]) (K)	8830 ± 800	8140 ± 290	8640 ± 320	8580 ± 320	
C^{2+b}	8.21 ± 0.14	8.46 ± 0.08	8.40 ± 0.12	8.44 ± 0.12	
N^+	7.55 ± 0.04	7.27 ± 0.04	6.87 ± 0.05	7.32 ± 0.04	7.66 ± 0.06
O^+	8.39 ± 0.10	8.28 ± 0.10	7.97 ± 0.12	8.24 ± 0.10	8.45 ± 0.17
O^{2+}	7.32 ± 0.10	8.07 ± 0.05	8.08 ± 0.05	7.89 ± 0.05	8.48 ± 0.08
O^{2+b}	–	–	–	8.48 ± 0.09	
S^+	6.37 ± 0.04	6.06 ± 0.04	5.53 ± 0.04	6.10 ± 0.04	6.43 ± 0.06
S^{2+}	6.69 ± 0.20	6.90 ± 0.09	6.71 ± 0.09	6.77 ± 0.09	7.40 ± 0.12
N^+/O^+	-0.84 ± 0.11	-1.02 ± 0.11	-1.10 ± 0.13	-0.91 ± 0.11	-0.79 ± 0.18
O^{2+}/O^+	-1.07 ± 0.15	-0.21 ± 0.11	0.11 ± 0.13	-0.34 ± 0.11	0.03 ± 0.19
S^+/O^+	-2.02 ± 0.11	-2.23 ± 0.11	-2.44 ± 0.13	-2.14 ± 0.11	-2.02 ± 0.18

[a]In units of $12 + \log(X^{+i}/H^+)$.
[b]Determined from RLs.

Table 3. Elemental abundances[a] in NGC 7635.

		C	N	O	S
K1		9.00 ± 0.20	7.58 ± 0.14	8.42 ± 0.09	6.86 ± 0.14
K2		8.77 ± 0.14	7.47 ± 0.12	8.49 ± 0.06	6.96 ± 0.08
Rim		8.59 ± 0.18	7.23 ± 0.15	8.33 ± 0.06	6.77 ± 0.09
'Whole slit'	$t^2=0$	8.80 ± 0.17	7.49 ± 0.13	8.40 ± 0.08	6.87 ± 0.08
	$t^2>0$	8.65 ± 0.23	7.98 ± 0.20	8.76 ± 0.09	7.46 ± 0.11
Abundances expected from abundance gradients					
Shaver et al. (1983)		–	7.67 ± 0.15	8.60 ± 0.15	–
Afflerbach et al. (1997)		–	7.76 ± 0.08	8.56 ± 0.11	6.67 ± 0.07
Deharveng et al. (2000)		–	–	8.46 ± 0.07	–
Esteban et al. (2005)[b]		8.45 ± 0.20	–	8.64 ± 0.12	–
Carigi et al. (2005)[c]		–	7.74 ± 0.20	–	–
Solar abundances					
Asplund et al. (2009)		8.43 ± 0.05	7.83 ± 0.05	8.69 ± 0.05	7.12 ± 0.03

[a]In units of $12 + \log(X/H)$.
[b]Determined from RLs.
[c]Determined from CELs assuming $t^2 > 0$.

abundances of ions of high ionization potential; however, the differences between K2 and the rim are not large in this case. In Fig. 8 we present the spatial distribution of several emission lines of ions with different ionization potentials: S^+ (10.4 eV), H^+ (13.6 eV) and O^{2+} (35.1 eV). The profiles are centred around the knots (Fig. 8a) and the rim (Fig, 8b). As shown in Fig. 8(a), the [O III] profile shows a completely different behaviour with respect to the other ions showing a progressive decrease from the positional measurement 110 arcsec towards the west (left in Fig. 8a). This behaviour is produced because most ionizing photons that are able to convert O^+ to O^{2+} are exhausted between the positional measurement 105 and 110 arcsec, and therefore they do not penetrate the inner surface of K1, which is facing the ionizing star. Then, K1 is a wall of dense material that maintains the nebula ionization-bounded at that precise location. In the case of K2, the spatial profiles of the three emission lines are similar, indicating that this feature is matter-bounded or, conversely, it is an ionization front whose surface is perpendicular to the line of sight. Finally, the behaviour of the line profiles at the rim – whose surface is tangential to the line of sight – indicates that it is a matter-bounded feature. This is also consistent with the fact that T_e([O III]) and T_e([N II]) are so similar at the rim.

It is important to note that we have detected and measured the faint C II 4267 Å RL (see Fig. 9) in all the integrated spectra, as well as five of the eight RLs of the multiplet 1 of O II (see Fig. 3d) in the 'whole slit' spectrum, allowing us to derive C^{2+} and O^{2+} abundances from RLs. Several authors have previously determined the C^{2+} abundance in NGC 7635. Rodríguez (1999) obtained values between 8.11 and 8.23 dex in her two slit positions, which cover the group of knots at the south of K1. On the bubble rim, Moore et al. (2002) obtained a C^{2+} abundance of 8.63 dex. Our determinations lie in between these values. In addition, Moore et al. (2002) obtained the first determination of the O^{2+}/H^+ ratio from RLs on the rim bubble. They found a value of 8.47 dex and a moderate ADF(O^{2+}) = 0.2 dex. However, from our 'whole slit' spectrum we obtain an ADF(O^{2+}) of about 0.59 ± 0.10 dex, the highest value found so far in an H II region (see Section 7.1).

In order to derive the total gaseous abundances of the different elements, we have corrected for the unseen ionization stages by using a set of ionization correction factors (ICFs). Both total abundances and adopted ICF values are presented in Tables 3 and 4, respectively. For carbon, we have adopted the photoionization models of Garnett et al. (1999) to estimate the ICF(C^+). For oxygen and nitrogen, we

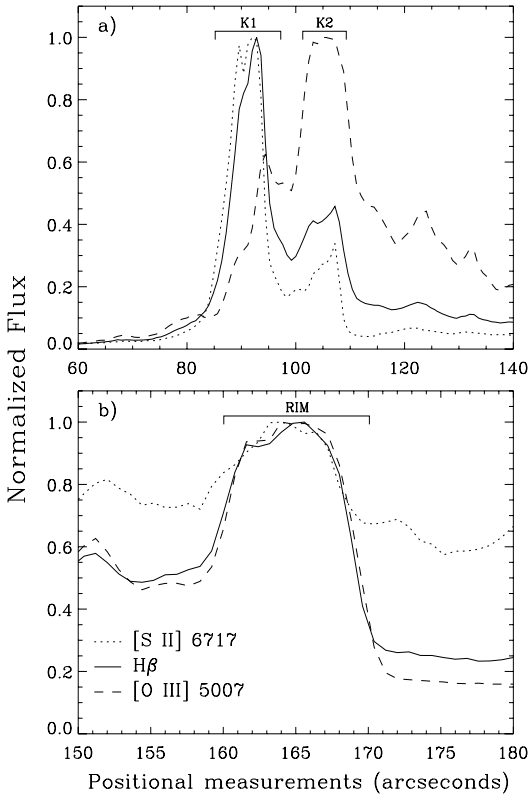

Figure 8. Spatial profiles of several emission lines obtained from extractions with a size of 0.8 arcsec (the average seeing during the observations) around (a) the knots and (b) the rim.

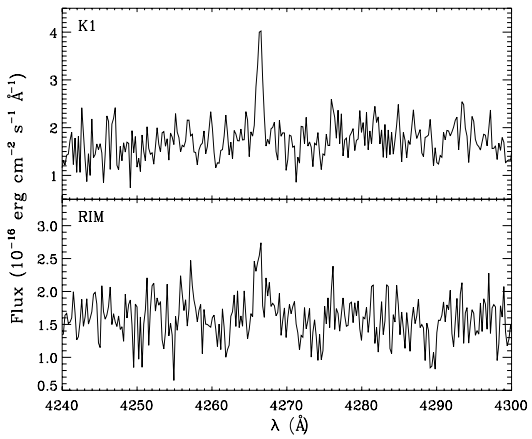

Figure 9. Sections of the integrated spectra around the emission line C II 4267 Å for the knot K1 (top panel) and the rim (bottom panel) of NGC 7635.

considered the classical assumptions $O = O^+ + O^{2+}$ and $N^+/N = O^+/O$, respectively. Finally, we have used the relation proposed by Stasińska (1978) to derive the ICF(S^{3+}) and the S abundances. In general, the total abundances derived for K1 and K2 are similar considering the uncertainties – except perhaps in the case of carbon – but higher than those derived for the spectrum of the rim. For the knots, Rodríguez (1999), Talent & Dufour (1979) and Moore et al. (2002) have determined total O abundances of about 8.42, 8.72 and 8.78, respectively. Our O abundance determinations for K1 and K2 are only consistent with those of Rodríguez (1999). For the rim, our O/H ratio is lower than those of Talent & Dufour (1979) and Moore et al. (2002); both obtain a $12 + \log(O/H) = 8.49$. The largest differences of abundances between the knots and the rim are found for carbon. The relative contribution of C^+ – and therefore the uncertainty of the total C/H ratio – is far larger in the case of K1. One of the possible reasons for such a difference may be the very different ionization degree of the knots and the rim, especially between K1 and the rim, where the O^{2+}/O^+ ratio differs in more than 1 dex (see Table 2). This strong change in the ionization degree, because of the ionization-bounded structure of the knots, involves an important variation in the ICF(C^+) (see Table 4). This fact could be affecting the suitability of this ICF.

7 DISCUSSION

7.1 Abundance pattern of NGC 7635

Assuming the validity of the temperature fluctuation hypothesis proposed by Peimbert (1967) and that this phenomenon is related to the AD problem (see García-Rojas & Esteban 2007), we have estimated a t^2 parameter from the ADF(O^{2+}) found for the 'whole slit' spectra, following the formalism outlined by Peimbert & Costero (1969) and equations (8)–(11) of Peimbert et al. (2004). The value of the t^2 parameter representative of the O^{2+} zone is 0.071 ± 0.009. We have adopted this t^2 parameter in order to calculate the ionic abundances, the same set of ICFs (see Section 6) and the total abundances for the 'whole slit' spectrum under the presence of temperature fluctuations. These values are also included in Tables 2–4.

The 'whole slit' abundances can be considered as the representative average values for NGC 7635, and therefore it seems appropriate to compare them with those expected from the Galactic abundance gradients. We have included in Table 3 the expected abundances obtained from some of the gradients determinations available in the literature, as well as the solar values. Using the distance to NGC 7635 of 2.4 ± 0.2 kpc adopted by Moore et al. (2002) and assuming a galactocentric distance of the Sun of 8.0 ± 0.5 kpc (Reid 1993), we estimate a galactocentric distance of about 9.2 ± 0.5 kpc for NGC 7635. As we can see in Table 3, the comparison of the total abundances for both possible values of t^2 and the abundance gradients is puzzling. First, the C/H ratio obtained from the C II 4267 Å RL is larger than expected by the Galactic abundance gradient of this element derived from observations of H II regions (Esteban et al. 2005) for any of the two values of the t^2 parameter considered in the table. The difference between our C abundance determinations and the expectations of the abundance gradients is especially large for the knots, but marginally consistent within the errors for the rim. This could suggest that (as we outlined in Section 6) this disagreement may be because of the unsuitability of the ICF(C^+) used, at least in the case of the knots. For the 'whole slit' spectrum, the C^{2+}/O^{2+} ratio with respect to the excitation degree (O^{2+}/O^+ ratio) of the ionized gas is similar to the values reported for other Galactic H II regions, as S 311 (García-Rojas et al. 2005), and therefore the ICF(C^+) seems not to be the reason for the large C/H ratio in this particular case. The

Table 4. Set of ICFs adopted in NGC 7635.

Elements	Unseen ion	K1	K2	Rim	'Whole slit' $t^2 = 0$	'Whole slit' $t^2 > 0$
C	C^+	6.20 ± 1.94	2.03 ± 0.55	1.56 ± 0.50	2.34 ± 0.66	1.64 ± 0.74
N	N^{2+}	1.09 ± 0.33	1.61 ± 0.43	2.28 ± 0.73	1.45 ± 0.40	2.08 ± 0.93
S	S^{3+}	1.00 ± 0.01	1.02 ± 0.01	1.07 ± 0.04	1.01 ± 0.01	1.05 ± 0.05

expected values of the Galactic O/H and N/H gradients are just in between our determinations for $t^2 = 0$ and $t^2 > 0$. In particular, the O abundance expected in the abundance gradient of Esteban et al. (2005) – based on the flux of O II RLs – is marginally consistent with our determinations for $t^2 > 0$ within the errors. Finally, the S/H ratio calculated for any value of the t^2 parameter is always larger than that expected from the S gradient of Afflerbach, Churchwell & Werner (1997).

The lack of consistency between our abundance determinations and the Galactic abundance gradient expectations for NGC 7635 suggests that perhaps the standard methods for deriving physical conditions and chemical abundances are not giving the correct values for this object. The problem seems to affect the spectra of all selected areas: the knots, the rim and the 'whole slit' spectrum. First, the carbon abundance is too high. It is very unlikely that the nebula has suffered a pollution of C processed by the ionizing central star because it is still in the main sequence. However, because K1 and K2 also show a very intense C II 4267 Å RL and high C^{2+}/H^+ ratios, the hypothetical chemical pollution event should also affect these structures that belong to the larger emission complex S162 (Moore et al. 2002), which is outside the bubble of NGC 7635. Another possibility of a local increase of C may be a result of the destruction of carbon-rich dust by the shock associated with the expanding windblown bubble, a possibility that has already been suggested by Moore et al. (2002). Esteban et al. (1998) estimated that the destruction of all the carbon locked up on dust grains in the Orion Nebula would increase the measured gas-phase C/H ratio by only about 0.1 dex. An increase of such magnitude would alleviate somehow the difference between the observed values and those expected by the abundance gradients, but does not account for it completely. All these problems with the flux of the C II 4267 Å RL and the high C/H ratio, especially at K1, make us consider that the emission flux of that line is enhanced by an unknown mechanism. We speculate that perhaps this mechanism could be related to the strong photoevaporative flow from the surfaces of the knots found by Moore et al. (2002) from *HST* images of NGC 7635. For these authors, structures such as K1 are the ionized edge of a mass of neutral material associated with the S162 complex, which is ionized by the central Of-type star. The photoevaporative flow seems to be interacting with the stellar wind, as suggested by the presence of an emission loop between the knots and the central star (Moore et al. 2002). Further deeper and higher spectral resolution spectroscopical observations of these features would be needed to shed light on this problem.

7.2 Comparison with the Orion Nebula

The Orion Nebula is the nearest H II region and therefore the most suitable object to explore the spatial variations of the nebular properties as well as the abundance discrepancy problem at the highest spatial resolution. Mesa-Delgado et al. (2008) obtained the spatial distributions of several quantities over five slit positions in the Orion Nebula with an angular resolution set to 1.2 arcsec. They found significant small-spatial-scale variations of density and temperature as well as the ADF(O^{2+}), most of these related to the presence of morphological structures such as HH objects, proplyds and ionization fronts such as the Orion bar.

In this study, we have tried to obtain a similar data set for other bright, but more distant, Galactic H II regions. However, the inventories of proplyds and HH objects in M8 and M17 are far less complete than for the Orion Nebula. Because of its different nature, there is no detection of these objects in NGC 7635. Discovering proplyds in other H II regions (apart from the Orion Nebula) is a difficult task, considering their larger distances and the problems related to the discrimination between true proplyds and fragmented portions of molecular clouds (see De Marco et al. 2006). The single candidates to proplyds in M8 and M17 have been reported by Stecklum et al. (1998) (marked as UC in Fig. 1) and De Marco et al. (2006), analysing narrow-band images taken with the *HST*. However, HH objects are direct manifestations of the interaction of gas ejected by a young star with its surroundings. The existence of HH objects in M8 was first mentioned by Reipurth (1981), who discovered HH 213 from images with the 1-m telescope class at Las Campanas Observatory. More recently, the catalogue of HH objects in M8 has increased with the spectroscopic confirmation of HH 870 (Arias et al. 2006) and the five new outflows reported by Barbá & Arias (2007) using optical narrow-band imaging with the Wide Field Imager at the 2.2-m telescope at La Silla Observatory. In the case of M17, there is no available literature about the presence of HH objects in this H II region, excluding a possible microjet found by De Marco et al. (2006).

Assuming a distance to the Orion Nebula of 436 pc (O'Dell & Henney 2008), the linear sizes of the proplyds and HH objects located at the Huygens region lie between 0.003 and 0.007 pc and 0.006 and 0.02 pc, respectively. The extractions analysed by Mesa-Delgado et al. (2008) had an angular size of 1.2 arcsec, which corresponds to a linear resolution of 0.0025 pc. Given this resolution, Mesa-Delgado et al. (2008) could obtain enough spatial sampling to detect the spatial variations of the nebular properties associated with these morphological structures. However, the H II regions we analyse in this paper are at larger distances than the Orion Nebula: 1.25 kpc (M8; Arias et al. 2006), 1.6 kpc (M17; Povich et al. 2007) and 2.4 kpc (NGC 7635; Moore et al. 2002). At these distances and with the size of the extractions used for each H II region in this work, the minimum linear sizes we can resolve are 0.0072, 0.0093 and 0.035 pc for M8, M17 and NGC 7635, respectively. As we can see, the linear resolutions that we achieve in our spatial analysis are factors of 3, 4 and 14, respectively, lower than in the case of the Orion Nebula. It is clear that spatial variations of the physical and chemical properties associated with proplyds with linear sizes similar to those of the Orion Nebula are very unlikely to be detected with our observations, except perhaps in the case of M8, where very large proplyds are of the order of our small extractions. With these comparatively large resolution elements, the emission of the

proplyds (and any associated variation of the local properties of the ionized gas, if they exist) would be diluted with the emission of the ambient nebular gas. In the case of HH objects, structures similar to those observed in the Orion Nebula would be resolved with the size of the extractions used in the cases of M8 and M17. For example, knot B of HH 870 in M8 has a diameter of about 0.015 pc, similar to those found in the Orion Nebula.

If these objects are present in all H II regions, we have estimated that the spatial resolution needed to resolve proplyds similar to those of the Orion Nebula should be about 0.42 arcsec for M8, 0.33 arcsec for M17 and 0.22 arcsec for NGC 7635, which are of the order of or smaller than the best seeing attainable with ground-based telescopes.

7.3 A possible candidate HH object in M8

In Section 5.1 we have presented evidence to suggest the presence of a new HH object in M8. It is located approximately 16 arcsec east and 44 arcsec north from Her 36, and can be seen as a diffuse relatively bright arc near an ionization front (HH? in Fig. 1). This candidate HH object presents a density 1.4 times larger than the adjacent background, lower than the density contrast found for the much prominent HH 870, which amounts to 2.3.

As mentioned in Section 5.1, HH objects typically show a strong emission of lines emitted by low ionization potential ions, such as Fe^{2+}, S^{+} or O^{+}. The spatial distribution of [Fe III] 4658 Å shown in Fig. 4(c) indicates that this line is enhanced by a factor of 1.3 with respect to the surrounding background gas. This increase of the dereddened flux of [Fe III] 4658 Å is also lower than that shown by HH 870. The [S II]/Hα ratio is a good indicator to discriminate between shock-excited and photoionized gas. Arias et al. (2006) obtained a map of the [S II]/Hα ratio of the central part of the M8 nebula, where they reported high values of this indicator at the three nebular knots associated with HH 870. Using our data, we find that the [S II]/Hα ratio increases by a factor of 1.8 at the position of HH 870. In the case of our candidate HH object, we have obtained an increment of about 1.3, similar to what we can estimate from the map of Arias et al. (2006). In fact, the shape of the possible HH object can be well identified in the [S II] and [S II]/Hα maps of Arias et al. (2006), while it cannot be seen in their Hα map. This behaviour is different to what we can observe in the ionization front near the candidate, which can be clearly seen in all maps. Further spectroscopic observations at a higher spectral resolution would be necessary to study the kinematics of this object in order to confirm its true nature.

8 CONCLUSIONS

In this paper, we have carried out long-slit spectrophotometry at an intermediate spectral resolution of the Galactic H II regions M8, M17 and NGC 7635. The one-dimensional spectra were extracted with a resolution of 1.2 arcsec for M8 and M17, and 3 arcsec for NGC 7635. Additional extractions with a spatial size of 4.8 arcsec were necessary in order to measure the faint C II and O II RLs in M8. We have studied the spatial distributions of a large number of nebular quantities along several slit positions covering different morphological structures such as HH objects, ionization fronts or bright knots. The studied quantities were $c(\mathrm{H}\beta)$, n_e, T_e([O III]), T_e([N II]), the observed and dereddened flux of several emission lines ([Fe III] 4658 Å, C II 4267 Å, O II 4649 Å, [O III] 4959,5007 Å and [O II] 7320 Å) and the O^{2+} abundances derived from CELs and RLs, as well as the difference of both determinations, ADF(O^{2+}).

The density spatial distributions show a large range of variation across the different slit positions. We have found local maxima associated with the HG region, HH 870, knots and regions with a high surface brightness. However, the temperature spatial profiles do not show important variations related to the cited structures. The temperatures obtained from the different indicators present the classical behaviour for M8 and M17; those derived from [N II] lines are higher than those derived from [O III] lines, as expected for ionization-bounded nebulae. For NGC 7635, both temperatures seem to be very similar considering the error due to the structure of the Bubble nebula, which is matter-bounded. We have also explored the spatial behaviour of the ADF(O^{2+}) along the slit positions of M8 and M17, which remains constant, finding values between 0.3 and 0.5 dex with an average error of about 0.1 dex.

We have analysed the physical conditions and chemical composition of four additional extractions of NGC 7635: three centred on the knots K1 and K2 and the rim of the bubble, and one corresponding to the 'whole slit' spectrum. The comparison of the O^{2+}/H^{+} ratio determined from CELs and RLs in the 'whole slit' spectrum produces an ADF(O^{2+}) of about 0.59 dex. Assuming that the AD problem is related to temperature fluctuations, we have obtained a t^2 parameter of 0.071. We have found a puzzling pattern in the total abundances derived for NGC 7635. The total abundances obtained for the knots are slightly higher than those of the rim. The total abundances were compared with those expected by the Galactic abundance gradients, finding that there are discrepancies, especially in the case of C. We suspect that C II 4267 Å RL may be abnormally enhanced in NGC 7635 because of an unknown physical process, whose investigation is outside the scope of this paper but deserves further more detailed observations.

Comparing our observations with those of Mesa-Delgado et al. (2008), we conclude that proplyds (and the associated variations of the local properties of the gas) with linear sizes similar to those found in the Orion Nebula cannot be resolved with the observations reported in this paper. Angular resolutions of the order of or smaller than the minimum seeing reached from ground-based telescopes would be needed to distinguish the presence of proplyds.

Finally, we have found evidence that points to a possible new candidate HH object in M8. This new object is located 16 arcsec east and 44 arcsec north from Her 36, where we have found enhancements in the spatial profile of [Fe III] 4658 Å and in the [S II]/Hα map presented by Arias et al. (2006).

ACKNOWLEDGMENTS

We are very grateful to the referee of the paper for his/her comments and suggestions. We thank J. García-Rojas, V. Luridiana and S. Simón-Díaz for their helpful suggestions. This work has been funded by the Spanish Ministerio de Ciencia y Tecnología (MCyT) under project AYA2004-07466 and Ministerio de Educación y Ciencia (MEC) under project AYA2007-63030.

REFERENCES

Afflerbach A., Churchwell E., Werner M. W., 1997, ApJ, 478, 190
Arias J. I., Barbá R. H., Maíz Apellániz J., Morrell N. I., Rubio M., 2006, MNRAS, 366, 739
Asplund M., Grevesse N., Sauval A. J., Scott P., 2009, ARA&A, 47, 481
Barbá R. H., Arias J. I., 2007, A&A, 471, 841
Blagrave K. P. M., Martin P. G., Baldwin J. A., 2006, ApJ, 644, 1006
Cardelli J. A., Clayton G. C., Mathis J. S., 1989, ApJ, 345, 245
Carigi L., Peimbert M., Esteban C., García-Rojas J., 2005, ApJ, 623, 213
Castañeda H. O., Vilchez J. M., Copetti M. V. F., 1992, A&A, 260, 370
Caulet A., 1997, Space Telesc. Europ. Coord. Fac. Newsl., 24, 12

Christopoulou P. E., Goudis C. D., Meaburn J., Dyson J. E., Clayton C. A., 1995, A&A, 295, 509
Davey A. R., Storey P. J., Kisielius R., 2000, A&AS, 142, 85
Deharveng L., Peña M., Caplan J., Costero R., 2000, MNRAS, 311, 329
De Marco O., O'Dell C. R., Gelfond P., Rubin R. H., Glover S. C. O., 2006, AJ, 131, 2580
Ercolano B., 2009, MNRAS, 397, L69
Esteban C., 2002, in Henney W. J., Franco J., Martos M., eds, RevMexAA Ser. Conf., 12, 56
Esteban C., Peimbert M., Torres-Peimbert S., Escalante V., 1998, MNRAS, 295, 401
Esteban C., Peimbert M., Torres-Peimbert S., García-Rojas J., 1999a, RevMexAA Ser. Conf., 35, 65
Esteban C., Peimbert M., Torres-Peimbert S., García-Rojas J., Rodríguez M., 1999b, ApJS, 120, 113
Esteban C., García-Rojas J., Peimbert M., Peimbert A., Ruiz M. T., Rodríguez M., Carigi L., 2005, ApJ, 618, L95
Esteban C., Bresolin F., Peimbert M., García-Rojas J., Peimbert A., Mesa-Delgado A., 2009, ApJ, 700, 654
French H. B., 1983, ApJ, 273, 214
García-Rojas J., Esteban C., 2007, ApJ, 670, 457
García-Rojas J., Esteban C., Peimbert A., Peimbert M., Rodríguez M., Ruiz M. T., 2005, MNRAS, 362, 301
García-Rojas J., Esteban C., Peimbert A., Rodríguez M., Peimbert M., Ruiz M. T., 2007, Revista Mexicana de Astronomia y Astrofisica, 43, 3
Garnett D. R., Shields G. A., Peimbert M., Torres-Peimbert S., Skillman E. D., Dufour R. J., Terlevich E., Terlevich R. J., 1999, ApJ, 513, 168
Hanson M. M., Conti P. S., 1995, ApJ, 448, L45
Harrington J. P., Feibelman W. A., 1984, ApJ, 277, 716
Kingdon J., Ferland G. J., 1995, ApJ, 450, 691
Liu X.-W., Storey P. J., Barlow M. J., Danziger I. J., Cohen M., Bryce M., 2000, MNRAS, 312, 585
Liu X.-W., Barlow M. J., Zhang Y., Bastin R. J., Storey P. J., 2006, MNRAS, 368, 1959
Martín-Hernández N. L., Esteban C., Mesa-Delgado A., Bik A., Puga E., 2008, A&A, 482, 215
Mathis J. S., Liu X.-W., 1999, ApJ, 521, 212
Mendoza C., 1983, in Flower D. R., ed., Proc. IAU Symp. 103, Planetary Nebulae. Kluwer, Dordrecht, p. 143
Mesa-Delgado A., Esteban C., García-Rojas J., 2008, ApJ, 675, 389
Mesa-Delgado A., López-Martín L., Esteban C., García-Rojas J., Luridiana V., 2009a, MNRAS, 394, 693
Mesa-Delgado A., Esteban C., García-Rojas J., Luridiana V., Bautista M., Rodríguez M., López-Martín L., Peimbert M., 2009b, MNRAS, 395, 855
Moore B. D., Walter D. K., Hester J. J., Scowen P. A., Dufour R. J., Buckalew B. A., 2002, AJ, 124, 3313
O'Dell C. R., Henney W. J., 2008, AJ, 136, 1566
Osterbrock D. E., Ferland G. J., 2006, Astrophysics of Gaseous Nebulae and Active Galactic Nuclei, 2nd edn. University Science Books, Sausalito, CA
Peimbert M., 1967, ApJ, 150, 825
Peimbert M., Costero R., 1969, Bol. Observatorios Tonantzintla y Tacubaya, 5, 3
Peimbert A., Peimbert M., 2005, RevMexAA Ser. Conf., 23, 9
Peimbert M., Peimbert A., 2006, in Barlow M. J., Méndez R. H., eds, Proc. IAU Symp. 234, Planetary Nebulae in our Galaxy and Beyond. Kluwer, Dordrecht, p. 227
Peimbert M., Torres-Peimbert S., Ruiz M. T., 1992, RevMexAA, 24, 155
Peimbert M., Storey P. J., Torres-Peimbert S., 1993a, ApJ, 414, 626
Peimbert M., Torres-Peimbert S., Dufour R. J., 1993b, ApJ, 418, 760
Peimbert M., Peimbert A., Ruiz M. T., Esteban C., 2004, ApJS, 150, 431
Povich M. S. et al., 2007, ApJ, 660, 346
Reid M. J., 1993, ARA&A, 31, 345
Reipurth B., 1981, A&AS, 44, 379
Rodríguez M., 1999, A&A, 351, 1075
Rodríguez M., García-Rojas J., 2010, ApJ, 708, 1551
Rola C., Stasinska G., 1994, A&A, 282, 199
Rubin R. H., 1969, ApJ, 155, 841
Sánchez L. J., Peimbert M., 1991, RevMexAA, 22, 285
Shaver P. A., McGee R. X., Newton L. M., Danks A. C., Pottasch S. R., 1983, MNRAS, 204, 53
Shaw R. A., Dufour R. J., 1995, PASP, 107, 896
Stasińska G., 1978, A&A, 66, 257
Stasińska G., 1980, A&A, 85, 359
Stasińska G., Tenorio-Tagle G., Rodríguez M., Henney W. J., 2007, A&A, 471, 193
Stecklum B., Henning T., Feldt M., Hayward T. L., Hoare M. G., Hofner P., Richter S., 1998, AJ, 115, 767
Storey P. J., 1994, A&A, 282, 999
Storey P. J., Hummer D. G., 1995, MNRAS, 272, 41
Talent D. L., Dufour R. J., 1979, ApJ, 233, 888
Tenorio-Tagle G., 1996, AJ, 111, 1641
Tsamis Y. G., Péquignot D., 2005, MNRAS, 364, 687
Tsamis Y. G., Barlow M. J., Liu X.-W., Danziger I. J., Storey P. J., 2003, MNRAS, 338, 687
Tsamis Y. G., Barlow M. J., Liu X.-W., Storey P. J., Danziger I. J., 2004, MNRAS, 353, 953
Tsamis Y. G., Walsh J. R., Péquignot D., Barlow M. J., Danziger I. J., Liu X.-W., 2008, MNRAS, 386, 22
Woodward C. E. et al., 1986, AJ, 91, 870

APPENDIX A: EMISSION-LINE FLUXES

In Table A1 (available in the electronic version of the journal – see Supporting Information), we present the aperture number (column 1), Hβ observed fluxes in units of erg cm^2 s^{-1} (column 2), dereddened flux line ratios of the main emission lines (columns 3–14) per slit position in units of $I(\mathrm{H}\beta) = 100$ and the average extinction coefficient (last row of each slit position). Several notes should be considered in order to understand Table A1.

(i) The aperture number (Ap) is the identification number of each one-dimensional spectra extracted and it is related to the positional measurement in arcsec as $\mathrm{Ap}_{\mathrm{initial}} + \mathrm{Ap}_{\mathrm{size}} \times \mathrm{Ap}$. $\mathrm{Ap}_{\mathrm{initial}}$ corresponds to the position in arcsec after the edges of the CCD were discarded for the extraction of one-dimensional spectra (see extraction procedure in Section 3). $\mathrm{Ap}_{\mathrm{initial}}$ amounts to 34 arcsec in M8 POS1 and POS2, 10 arcsec in M17 and 82 arcsec in NGC 7635. $\mathrm{Ap}_{\mathrm{size}}$ is the extraction size in arcsec along the spatial direction (see the selected sizes in Section 3).

(ii) In order to interpret correctly the Ap column in M8 POS2 we should consider that apertures 65, 66, 67 and 68 were removed in this position as a result of contamination by stellar emission (see Section 3).

(iii) We have not included the errors associated with Hβ observed fluxes, which remain between 3 and 5 per cent among the different slit positions.

(iv) We have only listed [O III] 4959 Å and [N II] 6548 Å nebular lines. [O III] 5007 Å and [N II] 6583 Å can be obtained from the first ones using their theoretical relations:

$$I([\mathrm{O\,III}]5007)/I([\mathrm{O\,III}]4959) = 2.88 \quad \text{(A1)}$$

and

$$I([\mathrm{N\,II}]6583)/I([\mathrm{N\,II}]6548) = 2.92. \quad \text{(A2)}$$

(v) For M8 POS1 and POS2, it should be noted that additional extractions of 4.8 arcsec wide were obtained to achieve proper flux measurements of O II RLs (see Section 3). In this sense, an aperture of 4.8 arcsec wide represents the average value of four apertures extracted with an angular size of 1.2 arcsec. The vertical lines on the left-hand side of the O II RLs cover the four apertures of 1.2 arcsec wide.

SUPPORTING INFORMATION

Additional Supporting Information may be found in the on-line version of this article:

Table A1. Hβ observed flux – $F(\mathrm{H}\beta)$ – in units of erg cm^2 s^{-1}, reddening-corrected line ratios in units of $I(\mathrm{H}\beta) = 100$ of the main emission lines and their errors per slit position, and average extinction coefficients – $\langle c(\mathrm{H}\beta)\rangle$.

Please note: Wiley-Blackwell are not responsible for the content or functionality of any supporting materials supplied by the authors. Any queries (other than missing material) should be directed to the corresponding author for the article.

This paper has been typeset from a TEX/LATEX file prepared by the author.

6

Conclusiones y perspectivas

En esta tesis se ha explorado, principalmente, el comportamiento de las distribuciones espaciales de las condiciones físicas, las abundancias químicas y el factor de discrepancia de abundancias, a pequeñas escalas espaciales, en cuatro de las regiones H II galácticas más brillantes y cercanas (la Nebulosa de Orión, M8, M17 y NGC 7635). También se han estudiado las propiedades físico-químicas del gas ionizado del objeto Herbig-Haro HH 202, de la Nebulosa de Orión, haciendo uso de espectroscopia de campo integral y *echelle* de muy alta resolución espectral. A lo largo del presente capítulo, resumimos las principales conclusiones obtenidas a partir de las diferentes estrategias observacionales utilizadas en este trabajo, así como las perspectivas futuras en la presente línea de investigación.

Conclusiones

Espectroscopia de rendija larga

- Presentamos espectroscopia de rendija larga ($4'$), de resolución espectral intermedia en el rango espectral de 4200 a 7500 Å, que cubre diferentes estructuras morfológicas de las regiones H II de la muestra y con resolución angular entre $1''$ y $3''$. Observamos un total de 9 posiciones de rendija larga: 5 en la Nebulosa de Orión, 2 en M8 y 1 en M17 y NGC 7635. A partir de los espectros bidimensionales, extrajimos y analizamos un total de 1316 espectros unidimensionales. Para cada uno de estos espectros, medimos entre 25 y 30 líneas de emisión, que incluyen las débiles LRs de O II. Con ello, hemos llevado a cabo un estudio novedoso del problema de la DA en regiones H II, hasta ahora únicamente realizado en la región extragaláctica 30 Doradus a una resolución angular de $3''.7$.

- Para cada uno de los espectros unidimensionales, hemos calculado los coeficientes de extinción, las condiciones físicas, las abundancias químicas de varios iones, a partir de LECs (N^+, O^+, O^{2+}, S^+, S^{2+}, Cl^{2+} y Ar^{2+}) y LRs (C^{2+} y O^{2+}), y el factor de discrepancia de abundancias del O^{2+}, ADF(O^{2+}). Para cada posición de rendija, obtuvimos y analizamos el comportamiento de las distribuciones espaciales de cada una de estas variables, así como de los flujos de algunas de las líneas de emisión

medidas.

- En todas las regiones H II, las distribuciones en densidad muestran un amplio rango de variación, con máximos locales asociados a diferentes estructuras morfológicas donde los rangos de variación respecto al fondo nebular pueden ir desde ∼1000 cm^{-3} hasta ∼30000 cm^{-3}. En la Nebulosa de Orión, dichos máximos están asociados a los discos protoplanetarios, los objetos Herbig-Haro (HH), la Barra de Orión y la Barra Compacta de Orión al suroeste del cúmulo del Trapecio. En M8, los máximos se encuentran asociados a la región del Reloj de Arena y el objeto HH 870. En el caso de M17, dichos picos se encuentran en una zona de gran brillo superficial. Por último, en NGC 7635, los máximos locales están relacionados con los nudos K1 y K2 al este de la estrella central.

- Los perfiles espaciales de las temperaturas –T_e([O III]) y T_e([N II])– no muestran variaciones importantes relacionadas con las estructuras locales en las posiciones analizadas en M8, M17 y NGC 7635. En cambio, en la Nebulosa de Orión, la T_e([N II]) presenta picos relacionados con los discos protoplanetarios y los objetos HH. En el primer caso, dichos aumentos pueden explicarse por las desexcitaciones colisionales que pueden sufrir las líneas nebulares utilizadas en el cálculo de las temperaturas, debido a la alta densidad de los discos protoplanetarios y la baja densidad crítica de los niveles de partida de estas líneas. En el segundo caso, el calentamiento por choques puede estar incrementando la T_e([N II]) en los objetos HH. Los distintos resultados obtenidos para la Nebulosa de Orión y el resto de regiones H II pueden estar relacionados con la pérdida de resolución espacial debido a la gran distancia, respecto a la Tierra, a la que se encuentran M8, M17 y NGC 7536 en comparación con Orión. Debido a ello, las posibles variaciones a pequeña escala en la estructura de temperaturas asociadas a subestructuras morfológicas pueden haberse diluido con la emisión del gas de ambiente.

- Contrariamente a lo observado en trabajos previos llevados a cabo en nebulosas planetarias (NPs), en las regiones H II estudiadas en este trabajo, las distribuciones espaciales de las líneas de O II y [O III] son similares a lo largo de las posiciones de rendija.

- Como resultado general, el comportamiento del ADF(O^{2+}), a lo largo de todas las posiciones de rendija, es básicamente constante –con un error promedio de 0.1 dex– y valores que se sitúan en los rangos de: 0.15 a 0.20 dex en la Nebulosa de Orión; y 0.2 a 0.5 dex en M8 y M17. Fuera de este rango de valores, hay que destacar los aumentos localizados del ADF(O^{2+}) encontrados en la posición de los objetos HH de la Nebulosa de Orión (HH 202, HH 203 y HH 204). En el objeto HH 870 de M8, no encontramos aumentos del ADF(O^{2+}), aunque es muy probable que la emisión de dicho objeto HH se haya diluido con la emisión del gas de fondo, debido a la menor resolución espacial alcanzada en este objeto.

- Dada la homogeneidad de los valores de ADF(O^{2+}), no hemos encontrado correlaciones positivas entre el ADF(O^{2+}) y el resto de parámetros nebulares estudiados,

excluyendo una correlación muy débil entre el ADF y la T_e([O III]) en la Nebulosa de Orión.

- En la Nebulosa de Orión hemos podido obtener la distribución radial del ADF(O^{2+}) y de las temperaturas electrónicas respecto a la principal fuente de ionización, θ^1Ori C. Por un lado, las temperaturas disminuyen conforme nos alejamos de la fuente de ionización; por otro lado, el ADF(O^{2+}) se mantiene básicamente constante en toda la nebulosa, salvo en 40″ alrededor de θ^1Ori C, donde parece aumentar conforme nos acercamos a dicha estrella.

- También en la Nebulosa de Orión calculamos el valor para las fluctuaciones de temperatura sobre el plano del cielo. Encontramos valores mucho más pequeños que los hallados en la literatura a lo largo de la línea de visión. Concluimos que si las hipotéticas inhomogeneidades térmicas existen, estas deberían ser más pequeñas que nuestro límite de resolución espacial (1.″2).

- Hemos analizado las condiciones físicas y composición química de varias extracciones individuales en la región NGC 7635: dos centradas en los nudos K1 y K2, otra centrada en el borde de la burbuja (RIM), y la última correspondiente a la extracción de la rendija completa. Por un lado, a partir del estudio del espectro de rendija completa, hemos obtenido el mayor ADF(O^{2+}) registrado en regiones H II: 0.59±0.10 dex; por otro lado, en el estudio de los nudos y el RIM, hemos encontrado un extraño patrón de abundancias: (1) las abundancias totales de los nudos son ligeramente mayores que las del RIM; y (2) las abundancias totales difieren de las abundancias esperadas según los gradientes galácticos, sobre todo en el caso del carbono, tanto si consideramos la presencia de fluctuaciones de temperatura como si no. Varios autores han sugerido que la sobreabundancia de C puede ser debida a la destrucción de granos de polvo ricos en carbono.

- En la región H II M8 hemos encontrado evidencias (aumentos significativos en la densidad electrónica, la emisión de [Fe III] y en el cociente de líneas [S II]/Hα) sobre la presencia de un candidato a objeto HH. Dicho objeto se encuentra a 16″ al este y 44″ norte de la estrella Her 36.

Espectroscopia de campo integral

- Presentamos espectroscopia de campo integral de resolución espectral intermedia, en el rango de 3500 a 7200 Å, del objeto HH 202 de la Nebulosa de Orión, en un área de 16″×16″ con un muestreo espacial de 1″×1″. Este tipo de datos nos ha permitido mapear los flujos de algunas líneas de emisión, las condiciones físicas y las abundancias iónicas, incluidas las abundancias de O^{2+} y C^{2+} determinadas a partir de LRs. Por tanto, hemos hecho uso de una técnica observacional que se encuentra en sus inicios en el estudio de la DA en nebulosas ionizadas, y de la que existen pocos trabajos disponibles en la literatura.

- Como ocurrió en el análisis de rendija larga, encontramos que las distribuciones de los flujos de las líneas de O II y [O III] son muy similares. También hallamos que

HH 202 es mucho más brillante en las líneas emitidas por especies con bajo potencial de ionización. En cuanto a las distribuciones de las condiciones físicas, observamos: (1) picos de densidad asociados a los nudos norte, HH 202-N, y sur, HH 202-S, del objeto; y (2) mayor rango de variación en la T_e([N II]) que en la T_e([O III]), así como diferente estructura espacial en ambas distribuciones de temperatura.

- Hemos obtenido, por primera vez para una región H II, los mapas de la temperatura de Balmer, del parámetro t^2 y del ADF(O^{2+}). El resultado más relevante es que el máximo valor de ADF(O^{2+}), 0.23±0.12 dex, se encuentra en la posición del nudo sur del HH 202, exactamente donde el flujo de gas alcanza su máxima velocidad.

- No hemos encontrado ninguna correlación entre el ADF(O^{2+}) y t^2, lo que indica la independencia de ambas variables. Por otro lado, hemos encontrado una correlación positiva entre la T_e([O III]) y el cociente O^{2+}/H^+, tanto a partir de LRs como LECs. Este resultado, esperado por los modelos de fotoionización, es diferente del hallado en NPs por Tsamis et al. (2008) y, por tanto, parece no apoyar las predicciones de los modelos basados en inhomogeneidades químicas.

Espectroscopia *echelle*

- Presentamos espectroscopia *echelle* de muy alta resolución del nudo sur del objeto HH 202, HH 202-S, en el rango espectral de 3100 a 10400 Å. La alta resolución espectral nos ha permitido resolver la componente cinemática asociada al gas de ambiente –denominada componente nebular– de la componente asociada al flujo de gas –denominada componente de choque–. Se detectaron y midieron 360 líneas de emisión, de las cuales 115 presentaban una única componente cinemática, y 8 no se consiguieron identificar.

- Encontramos un claro desacuerdo entre los coeficientes de extinción, $c(H\beta)$, individuales obtenidos a partir de las diferentes líneas de Balmer y Paschen, que provienen de niveles superiores con alto número cuántico orbital n. Proponemos, como posible solución, la acción conjunta de dos efectos: fluorescencia por continuo Lyman y cambios en el momento angular l debido a colisiones con protones.

- Hemos analizado la estructura de ionización del HH 202-S, encontrando que el mecanismo predominante es la fotoionización. Concluimos que, debido a la compresión del gas de ambiente, HH 202-S contiene un frente de ionización en su interior. Los resultados que sostienen esta conclusión son: (1) la dependencia encontrada entre el potencial de ionización de varios iones, y el cociente entre componentes cinemáticas de los flujos de las líneas emitidas por esos iones; (2) la estructura observada en los perfiles espacio-cinemáticos; y (3) la distancia calculada entre θ^1Ori C y HH 202-S.

- Hemos determinado las condiciones físicas de las componentes cinemáticas a partir de diferentes diagnósticos. La componente de choque presenta una densidad mucho mayor que la componente nebular. Estimamos la densidad del gas pre-chocado en la vecindad del HH 202, que es inferior a la densidad de la componente nebular, y nos

permite concluir que la mayor parte de la emisión de la componente nebular proviene del gas de ambiente localizado detrás de HH 202-S.

- Calculamos las abundancias químicas de un gran número de iones en las dos componentes cinemáticas. Particularmente, es importante destacar las primeras determinaciones de las abundancias de Cr^+ y Ca^+ en la Nebulosa de Orión, aunque las abundancias de estos iones únicamente fueron determinadas en la componente de choque. Obtenemos también las abundancias de C^+, O^+ y O^{2+} en ambas componentes a partir de LRs.

- Encontramos valores para el ADF(O^{2+}) que ascienden a 0.11±0.04 y 0.35±0.05 dex en la componente nebular y la componente de choque, respectivamente. Este es uno de los principales resultados de la presente tesis doctoral, ya que es la primera evidencia observacional que muestra que los flujos de gas a alta velocidad pueden –y decimos pueden, porque únicamente tenemos información de este objeto HH en particular– estar contribuyendo a la generación de la DA.

- Suponiendo válida la relación entre el ADF y la presencia de fluctuaciones de temperatura, hemos calculado los valores de t^2 para las dos componentes cinemáticas. El alto valor hallado para la componente de choque produce algunas inconsistencias en las abundancias totales de dicha componente y, por tanto, puede que el paradigma de t^2 no sea aplicable, al menos en esta componente. Sin embargo, hemos de tener en cuenta que hemos aplicado un valor de t^2 representativo de la zona ocupada por iones con alto potencial de ionización a todas las especies iónicas observadas. Un valor de t^2 menor y representativo de la zona de bajo potencial de ionización podría ayudar a conciliar el desacuerdo encontrado en las abundancias totales. Por otro lado, hemos encontrado valores de t^2 muy parecidos en las dos componentes cinemáticas a partir de la comparación de las abundancias de O^{2+} y a partir de la comparación de temperaturas de T_e(He I) y T_e([O III]). Este hecho apoyaría la validez de dicho paradigma.

- Finalmente, la comparación de los patrones de abundancias totales de Fe y Ni en la componente nebular y de choque, así como los resultados de los modelos de fotoionización aplicados a ambas componentes, apuntan a que hay destrucción parcial de granos de polvo en HH 202-S, tras el paso de la onda de choque. Estimamos que el porcentaje de destrucción de partículas de polvo que contienen hierro asciende a un 30-50%.

Perspectivas futuras

Los resultados encontrados en esta tesis son sólo una pequeña contribución que nos permitirá seguir investigando sobre el origen de la DA. Contamos ya con nuevos datos y nuevas estrategias observacionales que nos ayudarán a profundizar aún más en la raíz de dicho problema. A continuación, describimos brevemente las observaciones adicionales disponibles, las nuevas estrategias y los objetivos que se pretenden conseguir con el análisis de estos nuevos datos.

- Nos encontramos en la fase final del análisis de nuevos datos espectroscópicos de campo integral obtenidos con el instrumento PMAS a escalas espaciales de $1''$, de estructuras morfológicas adicionales en la Nebulosa de Orión. Tales estructuras son: discos protoplanetarios, la barra de Orión y un campo de control. La motivación de estas observaciones es relacionar las variaciones que puede sufrir el ADF(O^{2+}) con las estructuras morfológicas embebidas en el gas ionizado. En el análisis previo hemos encontrado aumentos significativos del ADF(O^{2+}) relacionados con frentes de choque que surgen de la interacción del viento estelar y los flujos provenientes de los discos protoplanetarios. Estos nuevos campos, junto con el análisis del HH 202, aumentan significativamente la muestra de puntos disponibles, y ayudan a reforzar la principal conclusión de esta tesis (la relación entre los flujos de gas a alta velocidad y los aumentos en el ADF).

- Creemos que es crucial, y una línea prometedora, aumentar la muestra de objetos HH observados a muy alta resolución espectral (R$\geq$30000), con el fin de resolver las componentes cinemáticas y llevar a cabo un análisis físico-químico minucioso de cada una de las componentes resueltas. Estos estudios pueden servirnos para establecer correlaciones entre las velocidades de los flujos de gas y el ADF, o estudiar observacionalmente el grado de destrucción de polvo después del paso de las ondas de choque. Además, este tipo de observaciones, junto con la construcción de modelos combinados de fotoionización y choques, también nos podrían ayudar a discernir cuáles son las líneas, LRs o LECs, que se ven afectadas por la presencia de los flujos de gas y, por tanto, cuáles aportan las abundancias químicas más representativas. La confirmación del candidato a objeto HH encontrado en M8 también sería plausible con observaciones de estas características.

- La combinación ideal de los puntos anteriores consistiría en observaciones espectroscópicas de campo integral a muy alta resolución espectral. Hasta la fecha, el único instrumento que permite tales observaciones en el rango óptico de 3000 a 10000 Å es FLAMES, ubicado en uno de los telescopios de 8 metros del Observatorio de Cerro Paranal (Chile). Este tipo de estudio, centrado en los objetos HH de Orión, presentaría como ventaja la localización espacial precisa de la emisión, a distintas longitudes de onda, de las componentes cinemáticas que podamos resolver.

- Por último, observaciones espectroscópicas de rendija larga desde el telescopio espacial Hubble, y su instrumento STIS, resolverían el problema de muestreo que hemos encontrado en el análisis de las regiones H II M8, M17 y NGC 7635. A las escalas angulares accesibles desde el telescopio espacial, conseguiríamos un muestreo espacial del orden,al que se puede alcanzar en la Nebulosa de Orión desde telescopios terrestres, o incluso mejor. De tal modo que el muestreo de las condiciones físicas, las abundancias químicas, y demás parámetros nebulares de los posibles discos protoplanetarios y objetos HH, que presumiblemente pueblan una gran parte de las regiones H II, sería mucho más plausible. Hasta hoy, Rubin et al. (2003) han sido los únicos en aplicar esta técnica en la Nebulosa de Orión para investigar las posibles variaciones en la estructura de temperaturas, aunque las observaciones llevadas a cabo por estos autores son muy poco profundas y los perfiles de temperaturas obtenidos presentan

grandes errores. Dados los resultados de espectroscopia de rendija larga presentados aquí en el análisis de la Nebulosa de Orión, parece necesario repetir las observaciones de Rubin et al. (2003) con mayores tiempos de exposición para así también detectar las débiles LRs de O II. El telescopio espacial Hubble nos permitiría muestrear la temperatura y el ADF(O^{2+}) a escalas angulares de $0\farcs1$, algo no realizado aún a escalas tan pequeñas.

Bibliografía

Abel, N. P., Brogan, C. L., Ferland, G. J., et al. 2004, ApJ, 609, 247

Aller, L. H., ed. 1984, Physics of Thermal Gaseous Nebulae (edited by L.H. Aller; Astrophysics y Space Science Library vol. 112)

Aller, L. H. y Menzel, D. H. 1945, ApJ, 102, 239

Bautista, M. A., Peng, J., y Pradhan, A. K. 1996, ApJ, 460, 372

Binette, L., Ferruit, P., Steffen, W., y Raga, A. C. 2003, Rev. Mexicana Astron. Astrofis., 39, 55

Blagrave, K. P. M., Martin, P. G., Rubin, R. H., et al. 2007, ApJ, 655, 299

Bowen, I. S. 1934, PASP, 46, 146

Brocklehurst, M. 1971, MNRAS, 153, 471

Cardelli, J. A., Clayton, G. C., y Mathis, J. S. 1989, ApJ, 345, 245

Costero, R. y Peimbert, M. 1970, Boletín de los Observatorios Tonantzintla y Tacubaya, 5, 229

De Robertis, M. M., Dufour, R. J., y Hunt, R. W. 1987, J. R. Astron. Soc. Can., 81, 195

Dinerstein, H. L., Lester, D. F., y Werner, M. W. 1985, ApJ, 291, 561

Ercolano, B. 2009, MNRAS, 397, L69

Ercolano, B., Wesson, R., Zhang, Y., et al. 2004, MNRAS, 354, 558

Esteban, C. 2002, en Revista Mexicana de Astronomía y Astrofísica Conference Series, Vol. 12, ed. W. J. Henney, J. Franco, y M. Martos, 56

Esteban, C., Bresolin, F., Peimbert, M., et al. 2009, ApJ, 700, 654

Esteban, C., García-Rojas, J., Peimbert, M., et al. 2005, ApJ, 618, L95

Esteban, C., Peimbert, M., García-Rojas, J., et al. 2004, MNRAS, 355, 229

Esteban, C., Peimbert, M., Torres-Peimbert, S., y Escalante, V. 1998, MNRAS, 295, 401

Esteban, C., Peimbert, M., Torres-Peimbert, S., y García-Rojas, J. 1999a, Rev. Mexicana Astron. Astrofis., 35, 65

Esteban, C., Peimbert, M., Torres-Peimbert, S., García-Rojas, J., y Rodríguez, M. 1999b, ApJS, 120, 113

Esteban, C., Peimbert, M., Torres-Peimbert, S., y Rodríguez, M. 2002, ApJ, 581, 241

Ferland, G. J. 2001, PASP, 113, 41

Ferland, G. J. 2003, ARA&A, 41, 517

Ferland, G. J. 2009, en IAU Symposium, Vol. 259, IAU Symposium, 25

French, H. B. 1983, ApJ, 273, 214

García-Rojas, J. y Esteban, C. 2007, ApJ, 670, 457

García-Rojas, J., Esteban, C., Peimbert, A., et al. 2005, MNRAS, 362, 301

García-Rojas, J., Esteban, C., Peimbert, A., et al. 2007, Revista Mexicana de Astronomia y Astrofisica, 43, 3

García-Rojas, J., Esteban, C., Peimbert, M., et al. 2006, MNRAS, 368, 253

García-Rojas, J., Esteban, C., Peimbert, M., et al. 2004, ApJS, 153, 501

García-Rojas, J., Peña, M., y Peimbert, A. 2009, A&A, 496, 139

Garnett, D. R. y Dinerstein, H. L. 2001, ApJ, 558, 145

Giammanco, C. y Beckman, J. E. 2005, A&A, 437, L11

Grandi, S. A. 1976, ApJ, 206, 658

Gruenwald, R. B. y Viegas, S. M. 1992, ApJS, 78, 153

Guerrero, M. A., Chu, Y., Gruendl, R. A., y Meixner, M. 2005, A&A, 430, L69

Harrington, J. P. y Feibelman, W. A. 1984, ApJ, 277, 716

Harrington, J. P., Lutz, J. H., Seaton, M. J., y Stickland, D. J. 1980, MNRAS, 191, 13

Henney, W. J. y Stasińska, G. 2010, ApJ, 711, 881

Huggins, P. J. y Frank, A. 2006, en IAU Symp. 234, Planetary Nebulae in our Galaxy and Beyond (San Francisco: ASP), ed. M. J. Barlow y R. H. Méndez, 271

Kaler, J. B. 1986, ApJ, 308, 337

Kingdon, J. B. y Ferland, G. J. 1995, ApJ, 450, 691

Kingdon, J. B. y Ferland, G. J. 1998, ApJ, 506, 323

Krabbe, A. C. y Copetti, M. V. F. 2006, A&A, 450, 159

Liu, X. 1997, en ESA Special Publication, Vol. 419, The first ISO workshop on Analytical Spectroscopy, ed. A. M. Heras, K. Leech, N. R. Trams, y M. Perry, 87

Liu, X.-W. 1998, MNRAS, 295, 699

Liu, X.-W. 2002, en Revista Mexicana de Astronomía y Astrofísica Conference Series, Vol. 12, ed. W. J. Henney, J. Franco, y M. Martos, 70

Liu, X.-W. 2003, en IAU Symp. 209, Planetary Nebulae: Their Evolution and Role in the Universe (San Francisco: ASP), ed. S. Kwok, M. Dopita, y R. Sutherland, 339

Liu, X.-W. 2006, en IAU Symposium, Vol. 234, Planetary Nebulae in our Galaxy and Beyond, ed. M. J. Barlow y R. H. Méndez, 219

Liu, X.-W., Barlow, M. J., Zhang, Y., Bastin, R. J., y Storey, P. J. 2006, MNRAS, 368, 1959

Liu, X.-W., Luo, S.-G., Barlow, M. J., Danziger, I. J., y Storey, P. J. 2001, MNRAS, 327, 141

Liu, X.-W., Storey, P. J., Barlow, M. J., y Clegg, R. E. S. 1995, MNRAS, 272, 369

Liu, X.-W., Storey, P. J., Barlow, M. J., et al. 2000, MNRAS, 312, 585

López-Sánchez, A. R., Esteban, C., García-Rojas, J., Peimbert, M., y Rodríguez, M. 2007, ApJ, 656, 168

Lucy, L. B. 1995, A&A, 294, 555

Luo, S.-G., Liu, X.-W., y Barlow, M. J. 2001, MNRAS, 326, 1049

Luridiana, V., Cerviño, M., y Binette, L. 2001, A&A, 379, 1017

Maciejewski, W., Mathis, J. S., y Edgar, R. J. 1996, ApJ, 462, 347

Mathis, J. S. 1976, ApJ, 207, 442

Mathis, J. S. y Liu, X.-W. 1999, ApJ, 521, 212

Mathis, J. S., Torres-Peimbert, S., y Peimbert, M. 1998, ApJ, 495, 328

Menzel, D. H. y Aller, L. H. 1941, ApJ, 94, 30

Miller, J. S. 1968, ApJ, 154, L57+

O'Dell, C. R. y Wen, Z. 1994, ApJ, 436, 194

Osterbrock, D. E. y Ferland, G. J. 2006, Astrophysics of gaseous nebulae and active galactic nuclei (2nd. ed. Sausalito, CA: University Science Books)

Peimbert, A. 2003, ApJ, 584, 735

Peimbert, A., Peimbert, M., y Ruiz, M. T. 2005, ApJ, 634, 1056

Peimbert, M. 1967, ApJ, 150, 825

Peimbert, M. 1975, ARA&A, 13, 113

Peimbert, M. 1995, en The Analysis of Emission Lines, ed. R. Williams y M. Livio, 165

Peimbert, M. y Costero, R. 1969, Boletín de los Observatorios Tonantzintla y Tacubaya, 5, 3

Peimbert, M. y Peimbert, A. 2006, en IAU Symposium, Vol. 234, Planetary Nebulae in our Galaxy and Beyond, ed. M. J. Barlow y R. H. Méndez, 227–234

Peimbert, M., Peimbert, A., y Ruiz, M. T. 2000, ApJ, 541, 688

Peimbert, M., Peimbert, A., Ruiz, M. T., y Esteban, C. 2004, ApJS, 150, 431

Peimbert, M., Sarmiento, A., y Fierro, J. 1991, PASP, 103, 815

Peimbert, M., Storey, P. J., y Torres-Peimbert, S. 1993, ApJ, 414, 626

Peimbert, M., Torres-Peimbert, S., y Luridiana, V. 1995, Rev. Mexicana Astron. Astrofis., 31, 131

Peimbert, M., Torres-Peimbert, S., y Ruiz, M. T. 1992, Rev. Mexicana Astron. Astrofis., 24, 155

Pérez, E. 1997, MNRAS, 290, 465

Robertson-Tessi, M. y Garnett, D. R. 2005, ApJS, 157, 371

Rodríguez, M. 1998, Tesis doctoral, Universidad de La Laguna

Rodríguez, M. 1999, A&A, 348, 222

Rodríguez, M. y García-Rojas, J. 2010, ApJ, 708, 1551

Rola, C. y Stasińska, G. 1994, A&A, 282, 199

Rubin, R. H., Martin, P. G., Dufour, R. J., et al. 2003, MNRAS, 340, 362

Ruiz, M. T., Peimbert, A., Peimbert, M., y Esteban, C. 2003, ApJ, 595, 247

Sánchez, S. F., Cardiel, N., Verheijen, M. A. W., et al. 2007, A&A, 465, 207

Savage, B. D. y Mathis, J. S. 1979, ARA&A, 17, 73

Seaton, M. J. 1979, MNRAS, 187, 73P

Shaw, R. A. y Dufour, R. J. 1995, PASP, 107, 896

Simpson, J. P., Colgan, S. W. J., Rubin, R. H., Erickson, E. F., y Haas, M. R. 1995, ApJ, 444, 721

Stasińska, G. 1978, A&A, 66, 257

Stasińska, G. 2004, en Comochemistry. The melting Pot of the Elements, ed. C. Esteban, R. J. G. López, A. Herrero, y F. Sánchez (Cambridge University Press), 115–161

Stasińska, G. 2005, A&A, 434, 507

Stasińska, G. y Szczerba, R. 2001, A&A, 379, 1024

Stasińska, G., Tenorio-Tagle, G., Rodríguez, M., y Henney, W. J. 2007, A&A, 471, 193

Storey, P. J. y Hummer, D. G. 1995, MNRAS, 272, 41

Tenorio-Tagle, G. 1996, AJ, 111, 1641

Torres-Peimbert, S., Dufour, R. J., Peimbert, M., y Pena, M. 1997, en IAU Symp. 180: Planetary Nebulae, ed. H. J. Habing y H. J. G. L. M. Lamers, 281

Torres-Peimbert, S. y Peimbert, M. 1977, Rev. Mexicana Astron. Astrofis., 2, 181

Torres-Peimbert, S. y Peimbert, M. 2003, en IAU Symp. 209, Planetary Nebulae: Their Evolution and Role in the Universe (San Francisco: ASP), ed. S. Kwok, M. Dopita, y R. Sutherland, 363

Torres-Peimbert, S., Peimbert, M., y Daltabuit, E. 1980, ApJ, 238, 133

Torres-Peimbert, S., Peimbert, M., y Pena, M. 1990, A&A, 233, 540

Trumpler, R. J. 1930, PASP, 42, 214

Tsamis, Y. G., Barlow, M. J., Liu, X.-W., Danziger, I. J., y Storey, P. J. 2003a, MNRAS, 345, 186

Tsamis, Y. G., Barlow, M. J., Liu, X.-W., Danziger, I. J., y Storey, P. J. 2003b, MNRAS, 338, 687

Tsamis, Y. G., Barlow, M. J., Liu, X.-W., Storey, P. J., y Danziger, I. J. 2004, MNRAS, 353, 953

Tsamis, Y. G. y Péquignot, D. 2005, MNRAS, 364, 687

Tsamis, Y. G., Walsh, J. R., y Péquignot, D. 2009, en Science with the VLT in the ELT Era, ed. A. Moorwood, 61

Tsamis, Y. G., Walsh, J. R., Péquignot, D., et al. 2008, MNRAS, 386, 22

Viegas, S. M. y Clegg, R. E. S. 1994, MNRAS, 271, 993

Walsh, J. R. y Rosa, M. R. 1999, en Chemical Evolution from Zero to High Redshift, ed. J. R. Walsh y M. R. Rosa, 68

Wesson, R., Liu, X.-W., y Barlow, M. J. 2005, MNRAS, 362, 424

Whitford, A. E. 1958, AJ, 63, 201

Wyse, A. B. 1942, ApJ, 95, 356

Zhang, Y., Liu, X.-W., Liu, Y., y Rubin, R. H. 2005, MNRAS, 358, 457